Two-Craft Coulomb Formation Study about Circular Orbits and Libration Points

by

Ravi Kishore Inampudi

B.S., Mechanical Engineering, Osmania University, India, 1991

M.S., Industrial and Computer Engineering, University of Nebraska-Lincoln, 1995

M.S., Aerospace Engineering, University of Colorado, 2008

A thesis submitted to the

Faculty of the Graduate School of the

University of Colorado in partial fulfillment

of the requirements for the degree of

Doctor of Philosophy

Department of Aerospace Engineering Sciences

2010

This thesis entitled:
Two-Craft Coulomb Formation Study about Circular Orbits and Libration Points
written by Ravi Kishore Inampudi
has been approved for the Department of Aerospace Engineering Sciences

Hanspeter Schaub (Chair)

Penina Axelrad

George Born

Elizabeth Bradley

Dan Moorer

Date: ____________________

The final copy of this thesis has been examined by the signatories, and we find that both the content and the form meet acceptable presentation standards of scholarly work in the above mentioned discipline.

Inampudi, Ravi Kishore (Ph.D., Aerospace Engineering Sciences)

Two-Craft Coulomb Formation Study about Circular Orbits and Libration Points

Thesis directed by Associate Professor Hanspeter Schaub (Chair)

This dissertation investigates the dynamics and control of a two-craft Coulomb formation in circular orbits and at libration points; it addresses relative equilibria, stability and optimal reconfigurations of such formations.

The relative equilibria of a two-craft tether formation connected by line-of-sight elastic forces moving in circular orbits and at libration points are investigated. In circular Earth orbits and Earth-Moon libration points, the radial, along-track, and orbit normal great circle equilibria conditions are found. An example of modeling the tether force using Coulomb force is discussed. Furthermore, the non-great-circle equilibria conditions for a two-spacecraft tether structure in circular Earth orbit and at collinear libration points are developed. Then the linearized dynamics and stability analysis of a 2-craft Coulomb formation at Earth-Moon libration points are studied. For orbit-radial equilibrium, Coulomb forces control the relative distance between the two satellites. The gravity gradient torques on the formation due to the two planets help stabilize the formation. Similar analysis is performed for along-track and orbit-normal relative equilibrium configurations. Where necessary, the craft use a hybrid thrusting-electrostatic actuation system. The two-craft dynamics at the libration points provide a general framework with circular Earth orbit dynamics forming a special case. In the presence of differential solar drag perturbations, a Lyapunov feedback controller is designed to stabilize a radial equilibrium, two-craft Coulomb formation at collinear libration points.

The second part of the thesis investigates optimal reconfigurations of two-craft Coulomb formations in circular Earth orbits by applying nonlinear optimal control techniques. The objective of these reconfigurations is to maneuver the two-craft formation between two charged equilibria configurations. The reconfiguration of spacecraft is posed as an optimization problem using the calculus of variations approach. The optimality criteria are minimum time, minimum acceleration of the separation distance, minimum Coulomb and electric propulsion fuel usage, and minimum electrical power consumption. The continuous time problem is discretized using a pseudospectral method, and the resulting finite dimensional problem is solved using a sequential quadratic programming algorithm. The software package, DIDO, implements this approach. This second part illustrates how pseudospectral methods significantly simplify the solution-finding process.

DEDICATION

To the memory of my dear father

ACKNOWLEDGMENTS

I am deeply indebted to my advisor, Dr. Hanspeter Schaub, for his clear direction and steadfast support throughout this dissertation work. Dr. Schaub has taught and encouraged me to meet challenges that I had never before thought possible. I truly appreciate his time, effort and guidance. I would also like to extend my gratitude to Dr. Penina Axelrad who laid the foundation for my research interest in astrodynamics. I thank each member of my dissertation committee, Dr. Penina Axelrad, Dr. George Born, Dr. Elizabeth Bradley and Dr. Dan Moorer, for their valuable comments and suggestions. I thank Dr. Dale Lawrence for his insightful discussions on robust control techniques. For solving optimal control problems, I would also like to acknowledge DIDO software of Dr. Michael Ross at the Naval Postgraduate School.

I wish to thank all the past and present members of Dr. Schaub's research team for their constructive feedback during the research meetings. Particularly, I thank Rajtilok Chakravarty for informing about Dr. Schaub's research work, Shuquan Wang for clarifying questions related to Coulomb control and Carl Seubert for helping me crosscheck Coulomb power computations.

I owe gratitude to many of my colleagues at Rogue Wave Software for helping me to grow personally and professionally. Thanks to past and present directors and managers, Terry Hurly, Roberto Bigliani, Tim Adams and Benjamin Gmez who always encouraged me to pursue professional goals. I am pleased to have worked with some of the finest people in the field of object oriented analysis and design. I thank the company for financially supporting me during the doctoral program. Also, thanks to my friends Dr. Vani Cheruvu and Andreas Low for interesting discussions on mathematical and numerical analysis.

Earnest thanks to several brilliant people who are a constant source of inspiration and who changed the course of my life: Rogue Wave Software founder and former President

Tom Keffer, philosopher and teacher Swami Chinmayananda, space scientist and former President of India Abdul Kalam, and father of modern problem solving George Polya. My father Kesava Rao Inampudi who instilled in me the significance of education and the values of life was only able to witness the beginnings of this endeavor. I miss him dearly and thank him for all what he has done for me.

Thanks to God who equipped me with the necessary skills and persistence required to complete this effort. I wish to thank my loving wife Chaitali for her continual support and understanding through this long task. Finally, I am thankful to the lovely children Praneetha, Aryaman and Aman for helping me relax, rejoice and rejuvenate.

TABLE OF CONTENTS

LIST OF TABLES

LIST OF FIGURES

Figure Number Page

Chapter 1

INTRODUCTION

1.1 Motivation

Close proximity formation flying missions are envisioned as an attractive alternative to traditional large space structures so that the feasibility, accuracy and robustness of the mission is increased. Such missions fly spacecrafts in formation with separation distances ranging from 100's of meters to multiple kilometers. In order to maintain a desired cluster configuration, one of the most important technological hurdles is to develop an active fuel efficient micropropulsion system for relative positional control.[1] These requirements have led to a new and emerging field of study on Coulomb propulsion. Coulomb forces as a fuel efficient method for short-distance actuation in geostationary regions is discussed in Reference 3 in 1966. References 1 and 2 present a novel method of exploiting Coulomb forces for formation flying control with separation distance on the order of dozens of meters. Here active charge control is proposed to electrostatically inflate a large reflecting structure. The basic idea of Coulomb propulsion of free-flying vehicles is to control the spacecraft formation shape and size using the inter-spacecraft forces created by electrostatically charging the spacecraft to different potentials; a four-craft formation is shown in Figure 1.1. This control is achieved by varying the charge of the spacecraft by emitting either positive ions or negative electrons. As a consequence, changes in inter-spacecraft Coulomb forces actuate the relative motion control of the spacecraft as illustrated in Figure 1.2. For tight formation control of spacecraft separation distances on the order of 100 meters or less, this propellant-less thrusting is an attractive solution over conventional electric propulsion or chemical thrusting. For instance, at small separation distances between spacecraft, electric propulsion can cause thruster plume contamination of the neighbouring spacecraft. However, Coulomb propulsion is a highly

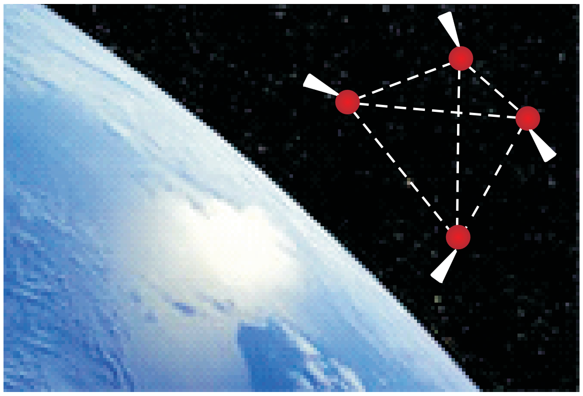

Figure 1.1: Coulomb Formation Flying

efficient system with a renewable energy source and I_{sp} values ranging up to 10^{13} seconds. Furthermore, it has very little electrical power requirements (one Watt or less) and has a very high bandwidth for relative motion control with charge transition times on the order of milli-seconds.[1] These advantages enable high precision formation flying with very little fuel consumption, increase the lifetime of the mission, and thus, the probability of mission success.

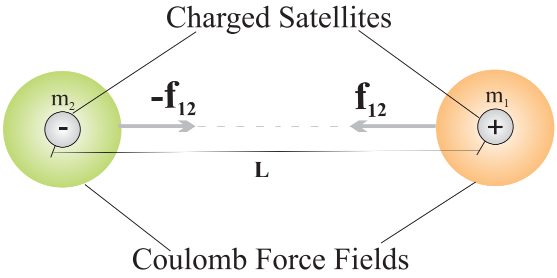

Figure 1.2: Two Charged Craft Coulomb Force Interaction

A Coulomb tether formation has several potential applications in space technologies, for example, high accuracy wide-field-of-view optical interferometry missions with geostationary orbits (GEO), spacecraft cluster control, rendezvous and docking maneuvers, as well as deployment or retrieval of dedicated sensors using Coulomb forces. As illustrated in Figure 1.3, Separated Spacecraft Interferometry (SSI) consists of an interferometer instrument distributed over multiple spacecraft collecting the light from a distant object in order to obtain information with very high angular resolution. Since the angular resolution of an interferometer is inversely proportional to the separation of its apertures, angularly fine objects can only be detected using SSI. For instance, using an SSI system, visible Earth imaging from GEO with meter level surface resolution would be possible. Therefore, the Coulomb concept is well suited to such wide-field-of-view planetary imaging with unprecedented resolution. Figure 1.4 illustrates the cluster Coulomb formation flying concept where the Coulomb forces not only keep the satellites bounded, but also keep them from colliding with each other. A potential application for a two-craft Coulomb formation is to deploy and retrieve a small free-flying camera or probe from a large geostationary communication satellite using Coulomb forces. This concept illustrated in Figure 1.5 allows the main satellite to carry sophisticated instruments which might be affected by high charging.

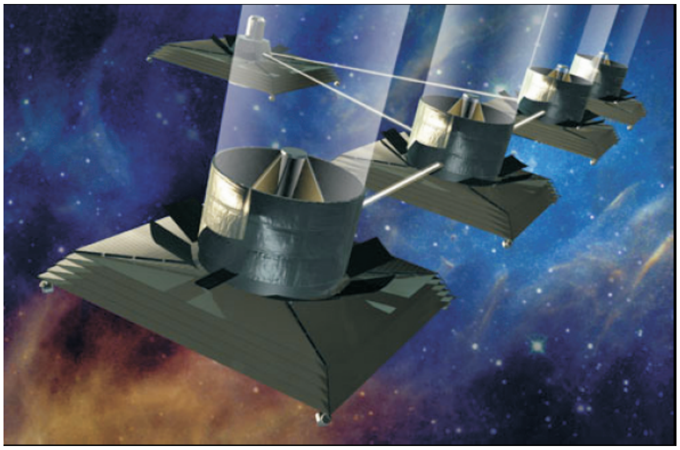

Figure 1.3: Separated Spacecraft Interferometry[a]

A three-body gravitational system consists of a spacecraft formation near two large celestial objects who are rotating around their common center of mass. Due to the rotation of the system, there are five equilibrium points as illustrated in Figure 1.6; these equilibrium points are the libration points (L_1-L_5) of the three-body system. For the Earth-Moon system the three collinear points L_1-L_3 are unstable, while the two equilateral triangle points L_4-L_5

---

[a] Courtesy NASA/JPL-Caltech, http://eis.jpl.nasa.gov/planetquest/gallery/tpfBrowseImages.cfm

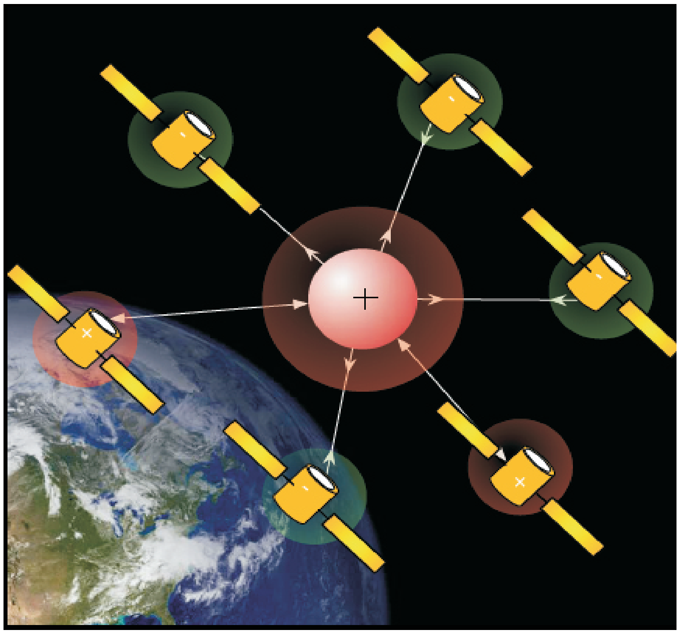

Figure 1.4: Cluster Coulomb Formation Flying[5]

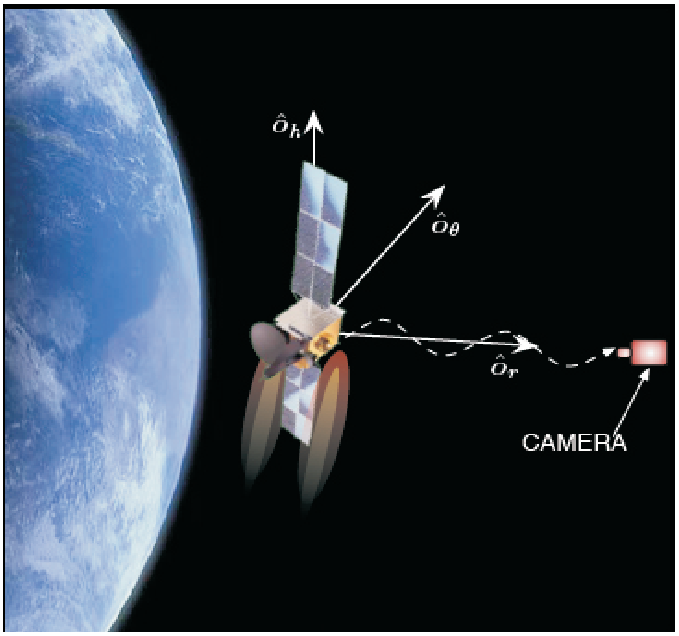

Figure 1.5: Deployment or Retrieval of a Camera using the Coulomb forces[5]

are stable. Virtual Coulomb structures at the libration points are useful for remote-sensing missions to establish a long baseline imaging capability, or for ensuring better stationkeeping configurations.

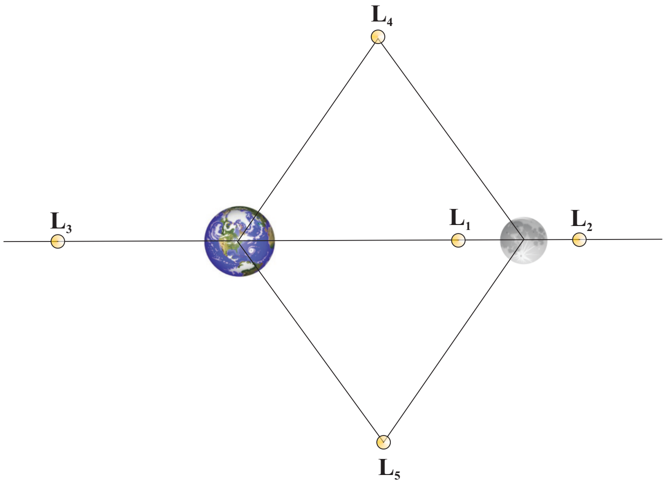

Figure 1.6: Libration Points

In spite of the many advantages of Coulomb propulsion, there are a few drawbacks. The formation dynamics is highly coupled and nonlinear; nonhomogeneous absolute spacecraft charging at geostationary altitudes may cause arcing; dependence of the inter-spacecraft Coulomb forces of the whole formation on each and every spacecraft's position and charge; and feasibility of Coulomb formation flying concept in less dense plasma environments at geostationary orbit (GEO) altitudes or higher. Moreover, as the electrostatic forces are internal to the formation, Coulomb forces cannot be used to reorient a full formation to a new orientation. Because these Coulomb forces cannot be used to control the center of mass of the formation and thus to change the total inertial formation angular momentum vector. Therefore, to reorient a Coulomb formation, external forces such as thrusters or differential gravity gradient torques must be used. Also, Coulomb formation flying requires a careful balance between the inter-craft forces and the relative orbital dynamics. Furthermore, in the presence of plasma, the Coulomb interaction between the craft is scaled by the Debye length parameter. The Debye length parameter is a measure of how strongly the plasma is shielding the electrostatic charge of a craft. For a fixed spacecraft separation distance, a lower Debye length implies a stronger plasma shielding and a weaker Coulomb interaction between charged crafts. Typically at Geostationary Orbits (GEO) the Debye length vary between 80-1400 m, with a mean of about 180 m.[7] Since the Debye length is small at LEO the use of electrostatic forces is not favorable in this region. However, with reasonable Debye lengths at GEO and interplanetary space environments,[1] electrostatic forces can be exploited in these regions for Coulomb spacecraft formations. While Coulomb propulsion is nearly propellantless, the non-affine nature of the charge actuation and the strongly coupled non-linear equations of motion result in a challenging and interesting control design problem.

1.2 Literature Review

In 1966, Cover et al[3] introduced Coulomb actuation of a membrane surface at GEO, and discussed the benefits of using Coulomb forces as a fuel efficient method for short-distance actuation. In 2002, in the context of formation flying, Parker and King presented the Coulomb propulsion concept in References 1 and 2. Ever since their work on Coulomb propulsion, there have been many interesting investigations on the dynamics and control problems of Coulomb formation. Parker and King[1,2] present analytic solutions for Hill-frame invariant static Coulomb formations with symmetry assumptions. The analytic open-loop solutions are for three and five craft formations, and the numerical solutions are for a six-craft formation. The charges required to maintain the formation shape are held constant and the spacecraft are placed at pre-defined locations in the rotating Hill frame. As a result, the Coulomb forces perfectly cancel all relative motion of the charged spacecraft, causing the static Coulomb formation to appear fixed as seen in the Hill frame. References 8–10 present more systematic analytic solutions for two, three, and four spacecraft formations. Furthermore, Berryman and Schaub[8] numerically demonstrate that charged equilibria with as many as 9 craft are possible in GEO orbits. The open-loop static Coulomb formations are all dynamically unstable without a feedback control law to stabilize the motion. Using a noncanonical Hamiltonian formulation of the Coulomb formation dynamics, Reference 11 formulates necessary conditions to achieve such static Coulomb formations with constant charges. These necessary conditions are derived for a virtual Coulomb structure where the orbital motion is decoupled from the attitude motion and these Hamiltonian formulations are equivalent to finding rigid body equilibrium conditions in orbit. Reference 12 applies a similar noncanonical Hamiltonian approach to examine the relative equilibria of a rigid satellite in a circular Keplerian orbit.

In the context of a restricted two-body problem, the existence of great-circle relative equilibria for a satellite (spherically symmetric rigid body) implies that the center of the circular orbit coincides with the center of the gravitational field.[12,13] The dynamics of the satellite's center of mass is exactly that of the Keplerian point mass model. If the satellite is assumed to be an arbitrary rigid body, and making a first order approximation of the gravitational force acting on the rigid body assuming that the orbital motion is decoupled from the attitude motion, the classical rigid-body attitude equilibrium study reveals that all three rigid body principal axes must line up with the LVLH (Local vertical/local horizontal) frame axes.[14] However, Reference 13 uses the exact potential function expression and proves the existence of nongreat-circle relative equilibria where the radius vector from the center of the gravitational field to the center of mass of the satellite traces a cone rather than a disk. Large variations in orientation from the classical regular motions are verified numerically for a finite rigid body.[13]

Specifically, Reference 15 discusses the relative equilibria and relative stability of a system of two spring-connected point masses moving in a central gravitational field. The paper shows that nongreat-circle equilibria exist for this simple spring system, and, for long tethers of approximately 3500 km at LEO, the attitude deflection from the vertical can reach tens of degrees. Such differences in orientation between great-circle and nongreat-circle solutions are particularly noticeable if the mass distribution of the formation is as asymmetric as possible. The spring system possesses $\boldsymbol{SO}(3)$ symmetry and such symmetry in geometric mechanics induces certain reduced dynamics which facilitates the computation of relative equilibria conditions. To obtain the conditions for relative equilibria, the principle of symmetric criticality is applied.[15] In order to gain further insights on the effects of nongreat-circle relative equilibria and mass asymmetry on a two spacecraft formation, the tether is modeled using a Coulomb force in this thesis. The Coulomb formation has $\boldsymbol{SO}(3)$ symmetry as well.

References 8–10 search for static Coulomb structure solutions using genetic algorithms. Here the simple principle axes condition of rigid body equilibria are used to speed up the genetic search algorithms. Thus, the open-loop equilibrium charges cause the virtual structure to assume a constant shape as seen by the rotating orbit frame. Some of these Coulomb concepts can have very asymmetric mass distributions. For example, consider the case of a small free-flying camera in the proximity of a large geostationary communication satellite. Because earlier work has shown that asymmetric bodies facilitate nongreat-circle equilibria, it is of interest how this impacts the 2-craft Coulomb virtual structure studies.

In the context of a restricted three-body problem, Reference 16 considers the equilibrium configurations of a rigid tethered system near all five libration points and carries out the stability analysis when it is near the translunar libration point. Reference 17 presents the attitude dynamics and stability of a small rigid satellite in the vicinity of Lagrangian points. The paper also investigates the attitude dynamics of a satellite while it is in Lyapunov and halo orbits. Also, the NIAC report in Reference 1 analyzes the suitability of Coulomb control for a static collinear five-vehicle formation at Earth-Sun Lagrange points where the formation local dynamics ignore gravity. Furthermore, Reference 18 presents compatibility results of using Coulomb satellites with electric propulsion and autonomous path planning techniques at the libration points for formation keeping and reconfiguration of swarms of satellites. In the interplanetary space at a distance of 1 AU from the Sun, the Debye length is much smaller than that in a GEO environment (highest Debye length of approximately 40 m); therefore, this constrains the maximum possible formation length, but despite the low value of the Debye length, multi-craft equilibrium formations are reported to exist at the Earth-Sun L_1 Lagrange point.[18]

Changing the position or orientation of a space structure using Coulomb propulsion is an important application. Reference 19 develops a charge control law to reposition a charged body using three charged drones. The control law neglects the orbital mechanics and considers only Coulomb attraction as the dominant force acting on a system. Reference 37 explores

---

[b] $\boldsymbol{SO}(3)$ rotation group concept is explained in Appendix A

a different Coulomb force deployment technique in which a chief satellite repositions small deputy spacecraft from an initial configuration near the chief to a specified shape outward from the chief. References 18 and 20 propose a distributed navigation technique called Equilibrium Shaping (ES) to drive a swarm of satellites to a desired configuration in space. This method exploits a decentralized path-planning algorithm requiring a small amount of communication between the satellites and gives each satellite the autonomous ability to decide a position in the target formation. The method is demonstrated though numerical simulations and suitable for very large swarms of spacecraft; however, each spacecraft pursues suboptimal maneuvers due to the highly decentralized scheme, and the control algorithm does not have analytical stability guarantees.

Stabilization techniques of two-craft virtual Coulomb structure in equilibrium configurations (radial, along-track, and orbit normal) are studied in Reference 5. About an orbit radial direction, to stabilize the relative separation distance a charge feedback law is used exploiting the differential gravitational attraction to stabilize the in-plane attitude. Along the orbit-normal and the along-track directions, the charge feedback law and the differential gravitational accelerations are inadequate to stabilize the in-plane motion. Therefore, for asymptotic in-plane stabilization, hybrid feedback control laws are used which combine conventional thrusters and Coulomb forces. Furthermore, Reference 5 investigates the linear dynamics and stability analysis of reconfiguration maneuvers for all three equilibrium configurations using linearized time-varying dynamical models. In such reconfiguration maneuvers as shown in Figure 1.7(a), varying electrostatic Coulomb forces can increase or decrease the relative distance between the two satellites. These Coulomb tether expansion and contraction rates affect the stability of the virtual structure within particular limits, and the reconfigurations thus obtained are suboptimal. Moreover, such linearized models could not be used in the nonlinear regime to perform reconfigurations such as a radial to along-track reconfiguration shown in Figure 1.7(b). Therefore, optimal control techniques could provide an alternative direction to determine optimized reconfiguration maneuvers for constrained nonlinear systems.

Optimal control problems concerning deployment/retrieval of a tethered subsatellite using

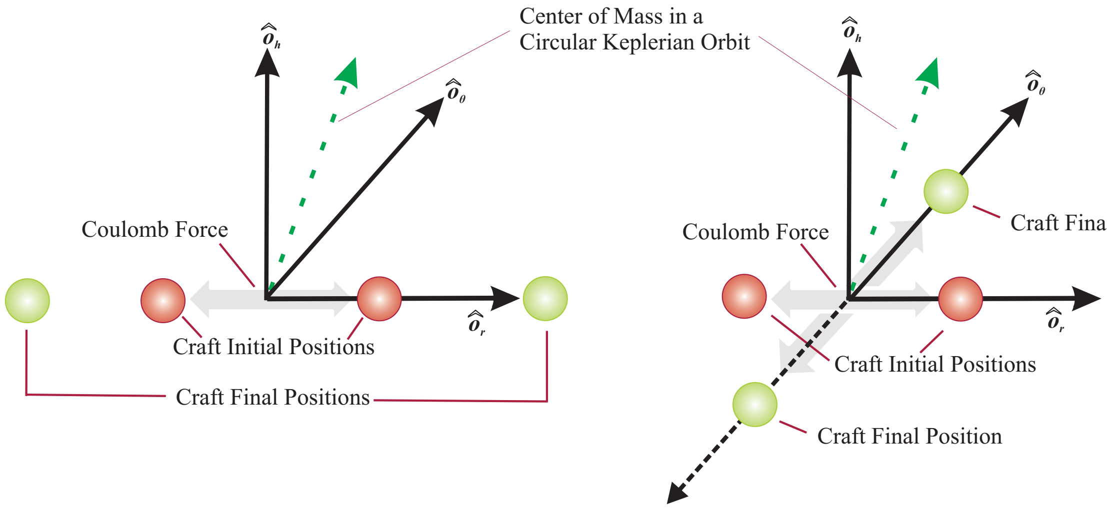

a) Radial to Radial

b) Radial to Along-track

Figure 1.7: Two-Craft Reconfiguration Maneuvers

various performance metrics are considered in References 21, 22 and 23. However, such solutions are not unique and depend on the performance index chosen to solve the optimal control problem. Reference 23 provides a comprehensive study of the effect of different performance indices on the optimal deployment and retrieval dynamics. For example, for a rigid tether, minimizing the length acceleration or minimizing functions of the tension acceleration appear to give good trajectories in terms of the maximum variations in the states and accelerations. Furthermore, optimal design problems in space applications almost always imply minimizing fuel use, which dictates the engineering feasibility of any mission.[24] Also, Reference 24 discusses how to choose proper minimum-fuel cost functions for correct problem formulation, and if a zero-cost (no fuel use needed) optimal trajectory is found, then it is the globally optimal solution. Using the pseudo-spectral method, a successful numerical implementation of an optimal control problem is demonstrated in Reference 25, where minimum-time reorientation of an asymmetric rigid body is considered. Therefore, prior work[21–25] motivates to explore the problems of repositioning or reorientation of Coulomb space structures using optimal control techniques.

Optimal control problems can rarely be solved analytically, and numerical methods are needed in such cases to solve them.[26] The first step is to discretize the problem, which is to define the system at discrete points which results in a finite number of variables because the system variables are only defined at the discrete points. The number of variables for the optimal control problem is then the number of variables in the system times the number of discretization points. The numerical techniques to solve optimal control problems are either indirect or direct methods.[27,28,33] Indirect methods are based on the calculus of variations and the necessary conditions are derived from Pontryagin's principles. Direct methods discretize the optimal control problem and solve the resulting large-scale finite-dimensional optimization problem. In recent years, developing direct algorithms using Legendre pseudospectral methods has become a very active research field.[30–32] Legendre pseudo-spectral methods posses the property that the solution satisfies the necessary optimality conditions and eliminates traditional difficulties in solving for the costates in the optimal control problem.[32] Also, Pontryagin's Minimum Principle verifies the extremality of these solutions.[33] Recent references show several interesting applications that use pseudospectral (PS) methods. Examples range from, spacecraft attitude control,[25] low-thrust orbit transfers,[34,35] tethered satellite system control,[36] and many more. Based on pseudo-spectral optimal control theory, DIDO is a powerful computational tool that generates spectrally accurate solutions.[33] Moreover, this tool can solve non-smooth problems that have state/control discontinuities where these discontinuities can be seen in bang-bang controls. For instance, Reference 25 considers a minimum-time reorientation of an asymmetric rigid body and demonstrates a successful implementation of the pseudo-spectral method using DIDO.

1.3 Dissertation Objectives

The primary goals of the thesis are to study the relative equilibria of a two spacecraft line-of-sight tether formation moving in circular orbits and at libration points, to stabilize a 2-craft Coulomb formation at Earth-Moon libration points, and to determine optimal reconfigurations of a two-craft Coulomb formation in circular Earth orbits. Figure 1.8 illustrates the research overview with the solid lines indicating previous research work and the dashed lines showing the work pertaining to this thesis.

The goals of this thesis are summarized below.

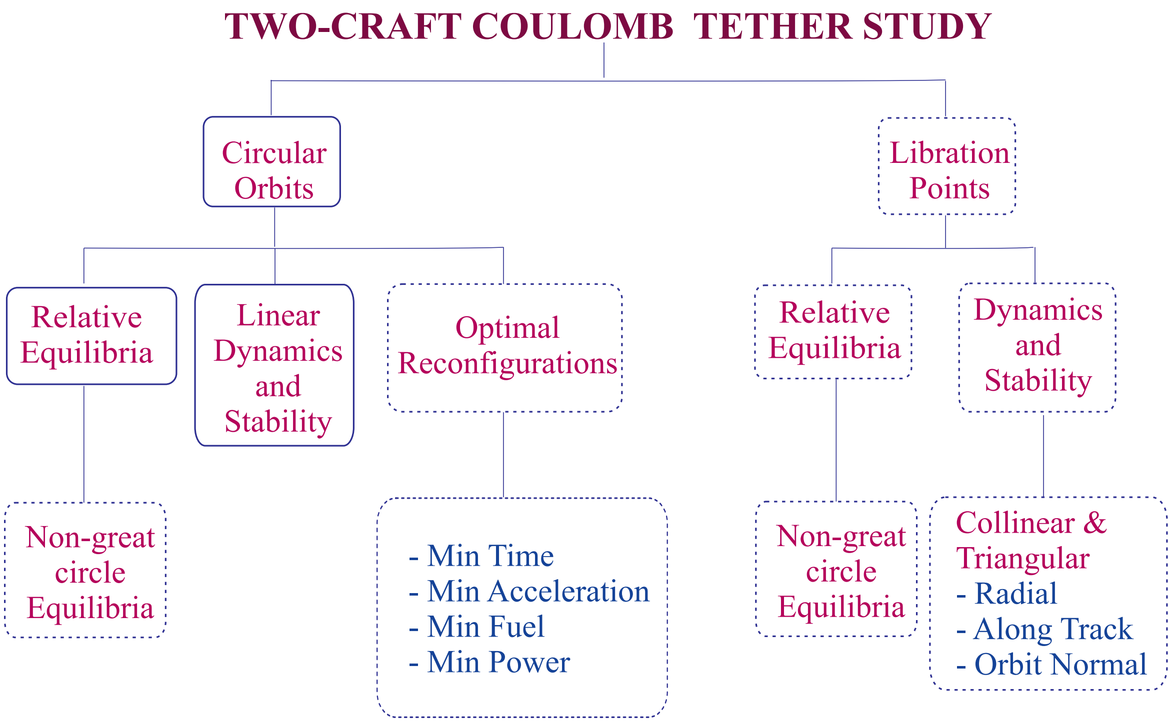

Figure 1.8: Research Overview

1.3.1 Two-Craft Tether Formation Relative Equilibria about Circular Orbits and Libration Points

The relative equilibria of a two spacecraft tether formation connected by line-of-sight elastic forces moving in the context of a restricted two-body system and a circularly restricted three-body system are investigated. For a two-spacecraft formation moving in a central gravitational field, a common assumption is that the center of the circular orbit is located at the primary mass and the center of mass of the formation orbits around the primary in a great-circle orbit. The relative equilibrium is called great-circle if the center of mass of the formation moves on the plane with the center of the gravitational field residing on it; otherwise, it is called a nongreat-circle orbit. Previous research shows that nongreat-circle equilibria in low Earth orbits exhibit a deflection of about a degree from the great-circle equilibria when spacecraft with unequal masses are separated by 350 km. This thesis studies these equilibria (radial, along-track and orbit-normal in circular Earth orbit and Earth-Moon

Libration points) for a range of inter-craft distances and semi-major axes of the formation center of mass. Furthermore, the nongreat-circle equilibria conditions for a two-spacecraft tether structure at the Lagrangian Libration points are developed. The relative equilibria computations use exact gravitational and tether potentials. The solution analysis considers the effect of mass asymmetry of the formation as well.

1.3.2 Dynamics and Stability Analysis of Two-Craft Coulomb Formation at Libration Points

The linearized radial, along-track and orbit-normal dynamics and stability of a 2-craft Coulomb tether formation at Earth-Moon libration points are investigated. The assumption for the linearized study is that the sunlit areas of the two-craft are equal such that the differential solar radiation pressure on the formation is zero. The relative distance between the two satellites of the Coulomb tether is controlled using electrostatic Coulomb forces. The separation distance between the satellites is stabilized with a charge feedback law which maintains the relative distance at a constant value. The electrostatic virtual tether between the two craft is capable of both tensile and compressive forces. In the orbit radial direction, the gravity gradient torques on the formation due to the two celestial objects is exploited to stabilize the Coulomb tether formation. Controlling the separation distance stabilizes the in-plane rotation angle; however, the out-of-plane rotational motion is not affected by the spacecraft charge control law. Similarly, control laws are developed for stabilizing the formation along the other two equilibrium configurations (along-track and orbit-normal). Since the gravity gradient torques alone are not sufficient to stabilize the Coulomb tether length and the formation attitude in these two equilibrium configurations, hybrid feedback control laws which combine conventional thrusters and Coulomb forces are necessary. The new two-craft dynamics at the libration points provide a general framework with circular Earth orbit dynamics forming a special case. In the presence of differential solar drag perturbations, a Lyapunov feedback controller stabilizes a radial equilibrium two-craft Coulomb formation at collinear libration points.

1.3.3 Optimal Reconfigurations of Two-Craft Coulomb Formation in Circular Orbits

Optimal reconfigurations of two-spacecraft Coulomb formations in circular Earth orbits are determined by applying nonlinear optimal control techniques. The objective of these reconfigurations is to maneuver the two-craft formation between two charged equilibria configurations. The four optimality criteria considered are minimum reconfiguration time, minimum acceleration of the separation distance, minimum electric propulsion fuel usage, and minimum electrical power consumption. Various optimal reconfigurations of 2-craft Coulomb virtual tether formations are considered. In a radial relative equilibrium reconfiguration, the Coulomb force alone is sufficient for controlling the in-plane motion and steering the satellites from their initial to their final radial position. In this reconfiguration maneuver, the gravity gradient torque stabilizes the in-plane motion. Other equilibrium-to-equilibrium reconfigurations require hybrid controls. For instance, reconfigurations in along-track or orbit normal equilibrium locations use Coulomb force to vary the separation distance and use inertial micro-thrusters for transverse direction control. Radial to along-track and radial to orbit-normal maneuvers are investigated as well. The goal is to determine optimal reconfigurations maximizing the use of Coulomb propulsion while minimizing the electric propulsion usage. The two-point boundary value problem optimization formulation is numerically solved via pseudo-spectral methods. Pontryagin's Minimum Principle verifies the open loop solutions' optimality.

In this thesis, the following assumptions are made:

1. The inter-spacecraft force undergoes both tensile and compressive forces along the line-of-sight direction between the two spacecraft.

2. The gravitational attraction between the two spacecraft masses is neglected.

3. For the three-body system, the spacecraft formation motion is in the primary bodies' plane of motion.

1.4 Dissertation Outline

This dissertation is organized as follows. Chapter 1 gives an outline of this thesis which presents the research background and the dissertation objectives. The second chapter presents the relative equilibria of a two spacecraft static tether structure using the exact gravitational and tether potentials in the context of a restricted two-body system and a circularly restricted three-body system. It also discusses the non-great circle effects in circular orbits on any two-craft formation existing from low Earth orbits (LEO) to geostationary orbits (GEO) as well as at collinear libration points. Chapter 3 presents the study of a two-craft Coulomb virtual tether that aligns along the orbit-radial (nadir) direction at any of the five libration points. It derives linear feedback laws for asymptotically stabilizing this formation along the orbit radial axis for a particular shape. To overcome solar drag perturbations on a two-craft Coulomb formation, a Lyapunov feedback controller is also designed for stabilizing a radial equilibrium formation at collinear libration points. Chapter 4 develops hybrid feedback control laws for asymptotically stabilizing the formation in the along-track and orbit-normal equilibrium configurations at any of the five libration points. Chapter 5 discusses optimal reconfigurations of a two spacecraft Coulomb formation. The derivation of two-craft nonlinear equations of motion and optimal control problem formulations are presented. For the reconfiguration optimal control problem, three discretization schemes and their solution methods are described as well. Four performance measures are used to study optimal two-craft reconfigurations: minimum-time, minimum-acceleration, minimum-fuel, and minimum-power. The goal is to maximize Coulomb propulsion usage for longitudinal maneuvers utilizing minimum electric propulsion for transverse maneuvers. For determining optimal reconfigurations of two-craft formations, pseudospectral methods are applied. The open-loop numerical solutions of two-craft reconfigurations in GEO circular orbits are presented and verified with Pontryagin's necessary conditions in this chapter. Finally, Chapter 6 provides a summary of the main contributions of this dissertation and indicates future avenues of research.

Chapter 2

TWO-CRAFT TETHER FORMATION RELATIVE EQUILIBRIA ABOUT CIRCULAR ORBITS AND LIBRATION POINTS

The objective of this chapter is to study the relative equilibria of a two spacecraft tether formation connected by line-of-sight elastic forces moving in the context of a restricted two-body system and a circularly restricted three-body system using the exact gravitational and tether potentials. An example of modeling the tether force using Coulomb force is discussed. The necessary conditions for a virtual Coulomb structure where the orbital motion is decoupled from the attitude motion are discussed in Reference 11. References 8–10 search for static Coulomb structure solutions using genetic algorithms. Here the simple principle axes condition of rigid body equilibria are used to speed up the genetic search algorithms. In this chapter, the validity of this assumption is investigated for Coulomb tether applications taking non-great-circle equilibria conditions into account. The goal is to identify for what formation dimension and altitudes these non-great circle effects become significant. The system dynamics and the notion of $\boldsymbol{SO}(3)$ symmetry applied to an elastic tether formation moving in a central gravitational field as well as for a restricted three-body system are discussed. The principle of symmetric criticality is applied to determine the conditions of relative equilibria of such static structures. For the restricted two-body system, the reduced dynamics identifies the classical great-circle equilibria; radial, along-track and orbit-normal equilibria. Also, the nongreat-circle effects in circular orbits for two-craft formations existing from LEO to GEO are investigated. Furthermore, relative equilibria solutions for a two-spacecraft formation are derived at the libration points. Finally, the nongreat-circle equilibria effects of such formations are presented at collinear libration points.

2.1 System Description and SO(3) Symmetry

In the following sections, fundamental concepts are introduced related to the dynamics of a system of N spacecrafts moving in a central gravitational field (restricted two-body system) and moving under the mutual gravitation of two bodies (restricted three-body system).

2.1.1 Restricted Two-body System

The spacecrafts shown in the Figure 2.1 are considered to be point masses moving in a central gravitational field. With the static virtual tether structure the system of spacecrafts behaves equivalently to a rigid body in orbit because the constant elastic inter-spacecraft forces cancel perfectly the differential gravitational forces acting across the cluster. Let $\boldsymbol{F}_t$ be the tether force acting between the two masses, and $\boldsymbol{r}_i$ be the inertial position vector of a single craft of mass m_i. Then the center of mass position vector $\boldsymbol{r}_c$ of this formation is defined as

$$\boldsymbol{r}_c = \frac{1}{M}\sum_{i=1}^{N} m_i \boldsymbol{r}_i \tag{2.1}$$

with $M = \sum_{i=1}^{N} m_i$ being the total formation mass. Let O be the center of the inverse square

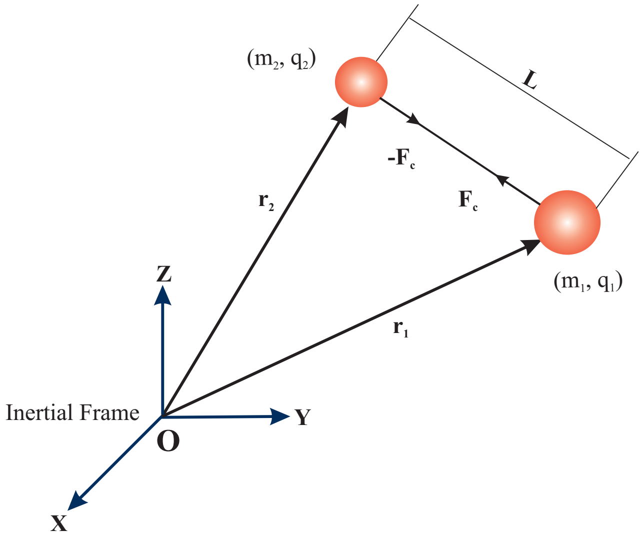

Figure 2.1: Two-Craft Coulomb Spacecraft Formation (Restricted Two-body System)

field and the origin of the inertial frame, while the formation's center of mass and center of gravity are denoted by C and G, respectively. The inertial position vectors of C and G are $\boldsymbol{r}_c$ and $\boldsymbol{r}_g$ and are related by

$$\boldsymbol{r}_g - \boldsymbol{r}_c = \boldsymbol{r} \tag{2.2}$$

where $\boldsymbol{r}$ is the constant vector between C and G.

From Newton's laws of gravitation the following relation relating the formation center of gravity and the individual inertial vectors is obtained as

$$\frac{\boldsymbol{r}_g}{\|\boldsymbol{r}_g\|^3} = \frac{1}{M}\sum_{i=1}^{N}\frac{\boldsymbol{r_i}}{\|\boldsymbol{r_i}\|^3}m_i \tag{2.3}$$

Using the two-body relative equations of motion with respect to G, the inertial second derivative of the vector $\boldsymbol{r}_g$ is

$$\frac{d^2\boldsymbol{r}_g\left(t\right)}{dt^2} + \frac{\mu\boldsymbol{r}_g\left(t\right)}{\|\boldsymbol{r}_g\left(t\right)\|^3} = 0 \tag{2.4}$$

where μ is the gravitational constant. Therefore, from Eqs. (2.2) and (2.4), the inertial second derivatives of the vectors $\boldsymbol{r}_c$ and $\boldsymbol{r}_g$ are related by

$$\frac{d^2\boldsymbol{r}_c\left(t\right)}{dt^2} + \frac{\mu\boldsymbol{r}_g\left(t\right)}{\|\boldsymbol{r}_g\left(t\right)\|^3} = 0 \tag{2.5}$$

Let m_1 and m_2 denote the mass of each craft with inertial position vectors $\boldsymbol{r_1}$ and $\boldsymbol{r_2}$, while each craft is assumed to have electrostatic (Coulomb) charges q_1 and q_2. The kinetic energy of the system is then given by

$$T\left(\dot{\boldsymbol{r}}_1, \dot{\boldsymbol{r}}_2\right) = \frac{m_1}{2}\|\dot{\boldsymbol{r}}_1\|^2 + \frac{m_2}{2}\|\dot{\boldsymbol{r}}_2\|^2 \tag{2.6}$$

The potential energy of the system is

$$V\left(\boldsymbol{r_1}, \boldsymbol{r_2}\right) = V_g\left(\boldsymbol{r_1}, \boldsymbol{r_2}\right) + V_t\left(\|\boldsymbol{r_1} - \boldsymbol{r_2}\|\right) \tag{2.7}$$

where $V_g(\boldsymbol{r_1}, \boldsymbol{r_2})$ is the gravitational potential energy of both the point masses in orbit defined as

$$V_g(\boldsymbol{r_1}, \boldsymbol{r_2}) = -\frac{\mu m_1}{\|\boldsymbol{r_1}\|} - \frac{\mu m_2}{\|\boldsymbol{r_2}\|} \tag{2.8}$$

$V_t(\|\boldsymbol{r_1} - \boldsymbol{r_2}\|)$ is the elastic tether potential energy and is a function of separation distance $\|\boldsymbol{r_1} - \boldsymbol{r_2}\|$ between the two spacecraft. For example, if a Coulomb tether is assumed between two spacecraft then $V_t = V_c$ with the Coulomb potential energy V_c given by

$$V_c(\|\boldsymbol{r_1} - \boldsymbol{r_2}\|) = k_c \frac{q_1 q_2}{\|\boldsymbol{r_1} - \boldsymbol{r_2}\|} e^{-\frac{\|\boldsymbol{r_1} - \boldsymbol{r_2}\|}{\lambda_d}} \tag{2.9}$$

where $k_c = 8.99 \times 10^9 \ Nm^2/C^2$ is the Coulomb's constant. The exponential term depends on the Debye length parameter λ_d which controls the electrostatic field strength of plasma shielding between the craft. At Geostationary Orbits (GEO) the Debye length vary between 80-1400 m, with a mean of about 180 m.[7] The Coulomb spacecraft formations are typically assumed to be orbiting on high Earth orbits. However, the tether spacecraft formations studied in this chapter are assumed to be orbiting from low to high Earth orbits.

In this chapter, the relative equilibria of a formation with two spacecraft subjected to elastic tether forces is considered where there are no external forces acting on the system. The relative equilibrium of the spacecraft formation is introduced by defining a uniformly rotating frame located at the origin O which has a constant orbital angular velocity of $\boldsymbol{\xi}$. A formation moving in a circular orbit that is stationary relative to this uniformly rotating frame exhibits symmetry with respect to the special orthogonal rotation group $\boldsymbol{SO}(3)$. The $\boldsymbol{SO}(3)$ rotation group and other group theoretic concepts used in this chapter are briefly explained in Appendix A.

As an example of an elastic tether, a Coulomb formation possesses $\boldsymbol{SO}(3)$ symmetry because both the kinetic and potential energies are invariant under the $\boldsymbol{SO}(3)$ group actions. This $\boldsymbol{SO}(3)$ symmetry reduces the dynamics of the spacecraft formation, and the equilibrium of the reduced dynamics is the relative equilibrium of the formation. If the center of mass of the formation moves on a great-circle orbit, then the relative equilibrium is called the great-circle relative equilibrium. This implies that $\boldsymbol{r}_c \cdot \boldsymbol{\xi} = 0$; if $\boldsymbol{r}_c \cdot \boldsymbol{\xi} \neq 0$ it is called the nongreat-circle relative equilibrium[13] as shown in Figure 2.2.

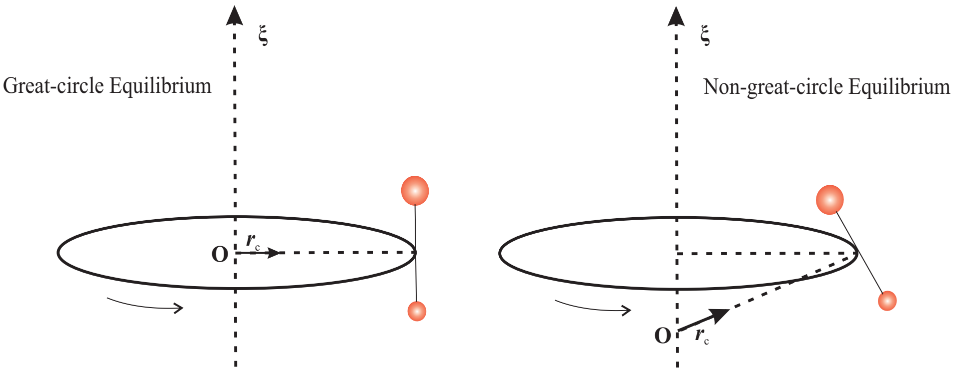

Figure 2.2: Great-circle and Non-great-circle Equilibria

Using the properties of the Lie algebra $\boldsymbol{g}^*$ of $\boldsymbol{SO}(3)$, at relative equilibria there exist two constant inertial vectors $\boldsymbol{r}_{co}$ and $\boldsymbol{r}_{go}$ with respect to O such that $\boldsymbol{r}_c\left(t\right) = e^{\hat{\boldsymbol{\xi}}t}\boldsymbol{r}_{co}$ and $\boldsymbol{r}_g\left(t\right) = e^{\hat{\boldsymbol{\xi}}t}\boldsymbol{r}_{go}$. Therefore at relative equilibrium Eq.(2.5) is reduced to

$$\hat{\boldsymbol{\xi}}\hat{\boldsymbol{\xi}}\boldsymbol{r}_{co} + \frac{\mu\boldsymbol{r}_{go}}{\|\boldsymbol{r}_{go}\|^3} = 0 \tag{2.10}$$

Taking an inner product of Eq. (2.10) with $\boldsymbol{\xi}$ gives $\boldsymbol{r}_{go} \cdot \boldsymbol{\xi} = 0$. Consequently, at relative equilibria, the center of gravity of a spacecraft formation moving in a central gravitational field traces a great-circle.

2.1.2 Restricted Three-body System

In a three-body system, as shown in Figure 2.3, the spacecrafts are considered to be point masses moving around the barycenter O under the mutual gravitation of two bodies M_1 and M_2. The relative equilibrium of the spacecraft formation is introduced by defining a uniformly rotating frame located at the barycenter O which has a constant orbital angular velocity of $\boldsymbol{\xi}$. A formation moving in a circular orbit that is stationary relative to this uniformly rotating frame exhibits symmetry with respect to $\boldsymbol{SO}(3)$. If m_1 and m_2 denote the mass of each craft with inertial position vectors $\boldsymbol{R}_{11}$, $\boldsymbol{R}_{12}$, $\boldsymbol{R}_{21}$ and $\boldsymbol{R}_{22}$ then using the three-body relative equations of motion, the inertial second derivative of the vector $\boldsymbol{r}_g$ is

$$M\ddot{\boldsymbol{r}}_g = -\mu_1\left(\frac{m_1}{R_{11}^3}\boldsymbol{R}_{11} + \frac{m_2}{R_{21}^3}\boldsymbol{R}_{21}\right) - \mu_2\left(\frac{m_1}{R_{12}^3}\boldsymbol{R}_{12} + \frac{m_2}{R_{22}^3}\boldsymbol{R}_{22}\right) \tag{2.11}$$

where M is the total formation mass, and μ_1 and μ_2 are the gravitational parameters of the two planets. The inertial position vectors $\boldsymbol{R}_{11}$, $\boldsymbol{R}_{12}$, $\boldsymbol{R}_{21}$ and $\boldsymbol{R}_{22}$ are expressed in rotating coordinates (synodic frame at the barycenter O) such that the distances are invariant under rotation. The synodic frame $S : \{\hat{\boldsymbol{e}}_r, \hat{\boldsymbol{e}}_\theta, \hat{\boldsymbol{e}}_h\}$ is rotating around the axis Oz with the constant angular velocity Ω defined as

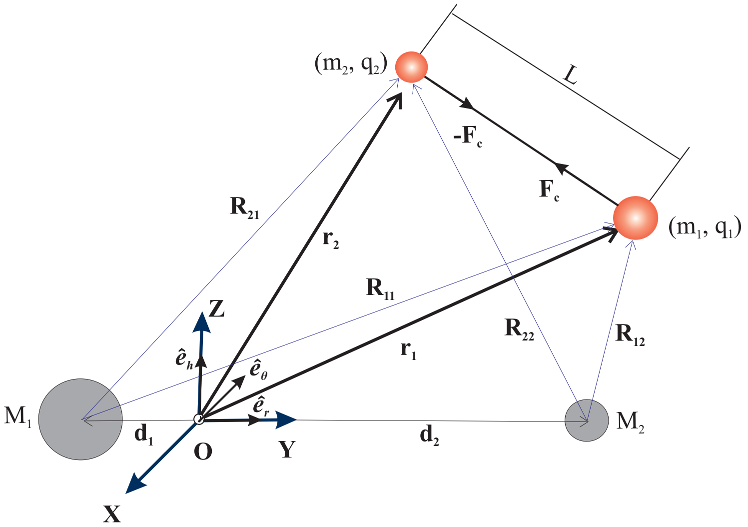

Figure 2.3: Two-Craft Coulomb Spacecraft Formation (Restricted Three-body System)

$$\Omega = \sqrt{\frac{G\left(M_1 + M_2\right)}{d^3}} \tag{2.12}$$

where G is the gravity constant and d is the distance between the two planets. The primaries are at rest in the synodic frame at positions $M_1(-d_1, 0, 0)$ and $M_2(d_2, 0, 0)$. Also, the kinetic energy of the system is still given by Eq. 2.6 with rotating position vectors $\boldsymbol{r_1}$ and $\boldsymbol{r_2}$ of the craft. In the potential energy expression in Eq. 2.7, the elastic tether potential energy remains the same, however, the gravitational potential energy $V_g\left(\boldsymbol{r_1}, \boldsymbol{r_2}\right)$ of the system becomes

$$V_g\left(\boldsymbol{r_1}, \boldsymbol{r_2}\right) = -\mu_1\left(\frac{m_1}{\|\boldsymbol{r_1} - \boldsymbol{d}_1\|} + \frac{m_2}{\|\boldsymbol{r_2} - \boldsymbol{d}_1\|}\right) - \mu_2\left(\frac{m_1}{\|\boldsymbol{r_1} - \boldsymbol{d}_2\|} + \frac{m_2}{\|\boldsymbol{r_2} - \boldsymbol{d}_2\|}\right) \tag{2.13}$$

Since the kinetic and potential energy are invariant under $\boldsymbol{SO}(3)$ actions, the elastic tether formation moving around the barycenter has $\boldsymbol{SO}(3)$ symmetry. This symmetry helps in the reduced dynamics by the $\boldsymbol{SO}(3)$ group action and the equilibrium of the reduced dynamics is the relative equilibrium of the spacecraft formation in the three-body system. Therefore, similar to the definitions for a two-body system, in a three-body system $\boldsymbol{r}_c \cdot \boldsymbol{\xi} = 0$ implies that the center of mass of the formation moves on a great-circle orbit and hence the relative equilibrium is called the great-circle relative equilibrium. And, if $\boldsymbol{r}_c \cdot \boldsymbol{\xi} \neq 0$ it is called the nongreat-circle relative equilibrium. Specifically, the elastic tether is modeled using Coulomb forces and Coulomb tether formations are feasible at Earth-Sun or Earth-Moon Lagrange points.[1] However, in the interplanetary space at a distance of 1 AU from the Sun, the Debye length is much smaller than that in a GEO environment (highest Debye length of approximately 40 m); therefore, this constrains the maximum possible formation length but despite the low value of the Debye length, multi-craft equilibrium formations are reported to exist at the Earth-Sun L1 Lagrange point.[18]

2.2 Relative Equilibria of the Static Two-Craft Tether Formation

Since the static two-craft tether formation possesses $\boldsymbol{SO}(3)$ symmetry, the dynamics in the original phase space of the system is reduced. The relative equilibria of the reduced dynamics facilitates finding the equilibrium configurations. Given a simple mechanical system with symmetry (Q, T, V, G), where Q is the configuration space with G-invariant Riemannian metric K on Q, T is the G-invariant kinetic energy and V is the G-invariant potential function, and G is the symmetry (Lie) group, then we have the following useful theorem based on the principle of symmetric criticality.[15]

Theorem : For a simple dynamical system with symmetry (Q, T, V, G) and the metric

$$K\left(\boldsymbol{q}\right)\left(\boldsymbol{v_q}, \boldsymbol{v_q}\right) = 2T\left(\boldsymbol{v_q}\right) \text{ with } \boldsymbol{v_q} \in TQ \tag{2.14}$$

define the augmented potential $V_\xi : Q \to \mathbf{R}$,

$$V_\xi(\boldsymbol{q}) = V(\boldsymbol{q}) - \frac{1}{2}K(\boldsymbol{q})\left(\boldsymbol{\xi}_Q(\boldsymbol{q}), \boldsymbol{\xi}_Q(\boldsymbol{q})\right) \tag{2.15}$$

where $\boldsymbol{\xi}_Q$ is the infinitesimal generator associated with $\boldsymbol{\xi}$. Then, at relative equilibrium, $\boldsymbol{q_e}$ is a critical point of V_ξ for some $\boldsymbol{\xi} \in \boldsymbol{g}^*$.

Therefore, for the two-craft tether formation the *augmented* potential function V_ξ is

$$V_\xi(\boldsymbol{r_1}, \boldsymbol{r_2}) = V(\boldsymbol{r_1}, \boldsymbol{r_2}) - \frac{m_1}{2}\langle \boldsymbol{\xi} \times \boldsymbol{r_1}, \boldsymbol{\xi} \times \boldsymbol{r_1} \rangle - \frac{m_2}{2}\langle \boldsymbol{\xi} \times \boldsymbol{r_2}, \boldsymbol{\xi} \times \boldsymbol{r_2} \rangle \tag{2.16}$$

where $\boldsymbol{\xi} \in \mathbf{R^3}$ is an arbitrary constant vector. According to the principle of symmetric criticality, the relative equilibria corresponding to some $\boldsymbol{\xi}$ is characterized by the critical points of the augmented potential V_ξ.

2.3 Relative Equilibria in the Restricted Two-body System

For the tether spacecraft formation with $\boldsymbol{SO}(3)$ symmetry, the relative equilibrium is one in a uniformly rotating frame. If the vector $\boldsymbol{\xi}$ denotes the angular velocity of the uniformly rotating frame, the augmented potential for the two spacecraft formation is,

$$\begin{aligned} V_\xi(\boldsymbol{r_1}, \boldsymbol{r_2}) = &-\frac{\mu m_1}{\|\boldsymbol{r_1}\|} - \frac{\mu m_2}{\|\boldsymbol{r_2}\|} + V_t(\|\boldsymbol{r_1} - \boldsymbol{r_2}\|) \\ &- \frac{m_1}{2}\langle \boldsymbol{\xi} \times \boldsymbol{r_1}, \boldsymbol{\xi} \times \boldsymbol{r_1} \rangle - \frac{m_2}{2}\langle \boldsymbol{\xi} \times \boldsymbol{r_2}, \boldsymbol{\xi} \times \boldsymbol{r_2} \rangle \end{aligned} \tag{2.17}$$

Then the relative equilibria of the system are characterized by the critical points of the augmented potential V_ξ. The first variation of V_ξ taken component wise with respect to $\boldsymbol{q} = (\boldsymbol{r_1}, \boldsymbol{r_2})$ is

$$\begin{aligned} \boldsymbol{D}V_\xi(\boldsymbol{r_1}, \boldsymbol{r_2}) \cdot (\delta\boldsymbol{r_1}, \delta\boldsymbol{r_2}) = &\, \mu m_1 \frac{\boldsymbol{r_1}}{\|\boldsymbol{r_1}\|^3} \cdot \delta\boldsymbol{r_1} + \mu m_2 \frac{\boldsymbol{r_2}}{\|\boldsymbol{r_2}\|^3} \cdot \delta\boldsymbol{r_2} \\ &+ V_t'(\|\boldsymbol{r_1} - \boldsymbol{r_2}\|) \frac{\boldsymbol{r_1} - \boldsymbol{r_2}}{\|\boldsymbol{r_1} - \boldsymbol{r_2}\|} \cdot (\delta\boldsymbol{r_1} - \delta\boldsymbol{r_2}) \\ &+ m_1\left(\hat{\boldsymbol{\xi}}\hat{\boldsymbol{\xi}}\boldsymbol{r_1}\right) \cdot \delta\boldsymbol{r_1} + m_2\left(\hat{\boldsymbol{\xi}}\hat{\boldsymbol{\xi}}\boldsymbol{r_2}\right) \cdot \delta\boldsymbol{r_2} \end{aligned} \tag{2.18}$$

If $V_t = V_c$, the Coulomb potential, then $V_c^{'}$ denotes the derivative of Coulomb potential with respect to $\|\boldsymbol{r_1} - \boldsymbol{r_2}\|$, which represents the Coulomb force acting between the two crafts. From Eq. (2.9), $V_c^{'}$ becomes

$$V_c^{'}\left(\|\boldsymbol{r_1} - \boldsymbol{r_2}\|\right) = -k_c \frac{q_1 q_2}{\|\boldsymbol{r_1} - \boldsymbol{r_2}\|^2} e^{-\frac{\|\boldsymbol{r_1} - \boldsymbol{r_2}\|}{\lambda_d}} \left[1 + \frac{\|\boldsymbol{r_1} - \boldsymbol{r_2}\|}{\lambda_d}\right] \tag{2.19}$$

Setting $DV_\xi\left(\boldsymbol{r_{1e}}, \boldsymbol{r_{2e}}\right) = 0$ we arrive at the following conditions of relative equilibria:

$$\frac{\mu m_1 \boldsymbol{r_{1e}}}{r_{1e}^3} + m_1 \hat{\boldsymbol{\xi}} \hat{\boldsymbol{\xi}} \boldsymbol{r_{1e}} + V_t^{'} \frac{\boldsymbol{r_{1e}} - \boldsymbol{r_{2e}}}{\|\boldsymbol{r_{1e}} - \boldsymbol{r_{2e}}\|} = 0 \tag{2.20a}$$

$$\frac{\mu m_2 \boldsymbol{r_{2e}}}{r_{2e}^3} + m_2 \hat{\boldsymbol{\xi}} \hat{\boldsymbol{\xi}} \boldsymbol{r_{2e}} - V_t^{'} \frac{\boldsymbol{r_{1e}} - \boldsymbol{r_{2e}}}{\|\boldsymbol{r_{1e}} - \boldsymbol{r_{2e}}\|} = 0 \tag{2.20b}$$

where $r_{1e} = \|\boldsymbol{r_{1e}}\|$ and $r_{2e} = \|\boldsymbol{r_{2e}}\|$. These equations are valid for any elastic tether type formations and are analogous to those developed in Reference 15 for a spring connected system. Therefore, the mathematical development to solve for relative equilibria with line-of-sight elastic forces acting between two spacecraft point masses is similar to that given in Reference 15.

Now consider a rotation matrix $[RN] \in \boldsymbol{SO}(3)$ that maps vectors from an inertial frame N into a new reference frame R. If we denote the vectors $\boldsymbol{R_1}$, $\boldsymbol{R_2}$, $\boldsymbol{\omega}$ in the reference frame R, then the conditions of relative equilibria given in Eqs. 2.20 are invariant under the transformation $\boldsymbol{R_1} = [RN]\,\boldsymbol{r_{1e}}$, $\boldsymbol{R_2} = [RN]\,\boldsymbol{r_{2e}}$ and $\boldsymbol{\omega} = [RN]\,\boldsymbol{\xi}$. In order to solve for relative equilibria, the new reference frame should be chosen such that the number of unknowns are at minimum in the equilibrium equations. As illustrated in Figure 2.4, a reference frame is chosen such that the x-axis is parallel to the line connecting the two crafts, with the z-axis perpendicular to both the vectors $\boldsymbol{r_{1e}}$ and $\boldsymbol{r_{2e}}$, and the y-axis completing the triad.

In the context of the new frame R, the position vectors are expressed as $\boldsymbol{R}_1 = (x_1, y_c, 0)^T$, $\boldsymbol{R}_2 = (x_2, y_c, 0)^T$, and $\boldsymbol{\omega} = (\omega_1, \omega_2, \omega_3)^T$. The equilibrium conditions (2.20a) and (2.20b)

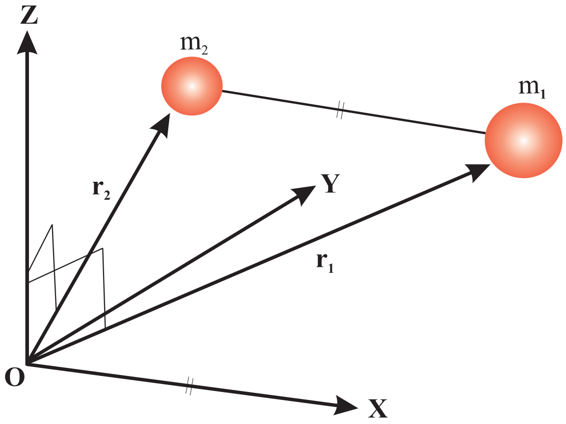

Figure 2.4: The Rotating Reference Frame (Restricted Two-body System)

expressed in scalar form are,

$$-\left(\omega_2^2+\omega_3^2\right)x_1+\omega_1\omega_2 y_c+\mu\frac{x_1}{R_1^3}=-\frac{V_t^{\prime}}{m_1} \tag{2.21}$$

$$\omega_1\omega_2 x_1-\left(\omega_1^2+\omega_3^2\right)y_c+\mu\frac{y_c}{R_1^3}=0 \tag{2.22}$$

$$\left(\omega_1 x_1+\omega_2 y_c\right)\omega_3=0 \tag{2.23}$$

$$-\left(\omega_2^2+\omega_3^2\right)x_2+\omega_1\omega_2 y_c+\mu\frac{x_2}{R_2^3}=\frac{V_t^{\prime}}{m_2} \tag{2.24}$$

$$\omega_1\omega_2 x_2-\left(\omega_1^2+\omega_3^2\right)y_c+\mu\frac{y_c}{R_2^3}=0 \tag{2.25}$$

$$\left(\omega_1 x_2+\omega_2 y_c\right)\omega_3=0 \tag{2.26}$$

where $R_1=\|\boldsymbol{R_1}\|$ and $R_2=\|\boldsymbol{R_2}\|$. It is also assumed that $x_1>x_2$ and $L=x_1-x_2>0$. Further, define $\boldsymbol{R}_c=(x_c,y_c,0)^T$ where $x_c=(m_1x_1+m_2x_2)/(m_1+m_2)$. Then the expressions for x_1, x_2 and y_c are

$$x_1=x_c+m_2L/\left(m_1+m_2\right) \tag{2.27a}$$

$$x_2=x_c-m_1L/\left(m_1+m_2\right) \tag{2.27b}$$

$$y_c=\left[R_c^2-\frac{L^2}{4}\left(\frac{m_1-m_2}{m_1+m_2}\right)^2\right]^{1/2} \tag{2.27c}$$

The relative equilibria of the two craft formation corresponds to solving the equations (2.21-2.26) for a given set of values for μ, m_1, m_2, L and $R_c = \|\boldsymbol{R_c}\|$. Reference 15 presents great-circle and nongreat-circle equilibrium solutions in the context of a spring force acting between two point masses. And these equilibrium results are applicable to any elastic force type such as a Coulomb force acting between the craft. Therefore, such results are utilized to investigate the relative equilibria of elastic tether formation for a range of spacecraft separation distances and semi-major axes. The great-circle and nongreat-circle equilibrium solutions are summarized here and Reference 15 provides the details of the derivations.

Case 1a. Setting $\omega_3 \neq 0$ in the equilibrium conditions and using $y_c \neq 0$ yields an *along-track* equilibrium solution (Figure 2.5(a))

$$\boldsymbol{R}_1 = \left(\tfrac{1}{2}L, y_c, 0\right)^T,\ \boldsymbol{R}_2 = \left(-\tfrac{1}{2}L, y_c, 0\right)^T,\ \boldsymbol{\omega} = (0, 0, \omega_3)^T$$
$$y_c = R_c,\ \omega_3^2 = \tfrac{\mu}{R^3} \text{ and } V_t^{'} = 0.$$

Case 1b. Setting $\omega_3 \neq 0$ and $y_c = 0$ gives a *radial* equilibrium solution (Figure 2.5(b))

$$\boldsymbol{R}_1 = (x_1, 0, 0)^T,\ \boldsymbol{R}_2 = (x_2, 0, 0)^T,\ \boldsymbol{\omega} = (0, 0, \omega_3)^T$$
$$\omega_3^2 = \tfrac{\mu}{(m_1+m_2)R_c}\left(\tfrac{m_1}{x_1^2} + \tfrac{m_2}{x_2^2}\right) \text{ and } V_t^{'} = \tfrac{\mu m_1 m_2\left(x_1^3 - x_2^3\right)}{(m_1+m_2)x_1^2 x_2^2 R_c} > 0.$$

Case 1c. Similarly, $\omega_3 = 0, y_c \neq 0$, and $R_1 = R_2$ yields *orbit normal* equilibrium (Figure 2.5(c))

$$\boldsymbol{R}_1 = \left(\tfrac{1}{2}L, y_c, 0\right)^T,\ \boldsymbol{R}_2 = \left(-\tfrac{1}{2}L, y_c, 0\right)^T,\ \boldsymbol{\omega} = (\omega_1, 0, 0)^T$$
$$m_1 = m_2,\ y_c = R_c,\ \omega_1^2 = \tfrac{\mu}{R^3},\ V_t^{'} = -\tfrac{\mu m_1 L}{2R^3} < 0$$

Case 2. Setting $\omega_3 = 0, y_c \neq 0, R_1 \neq R_2$ gives *nongreat-circle* equilibrium solution (Figure 2.5(d)) As in Reference 15, manipulating Eqs. (2.21-2.26) yields the condition $x_c\omega_1 + y_c\omega_2 \neq 0$, or equivalently, $\boldsymbol{R}_c \cdot \boldsymbol{\omega} \neq 0$. This analytically proves that for the given conditions in Case 2 there is no great-circle equilibria. Additionally, Reference 15 shows that nongreat-circle equilibria exist only if $m_1 \neq m_2$. For instance, Coulomb formations allow very lumpy distribution of masses and thus, these nongreat-circle equilibria conditions are of interest. Therefore, the nongreat-circle equilibrium conditions are

$$\boldsymbol{R}_1 = (x_1, y_c, 0)^T, \boldsymbol{R}_2 = (x_2, y_c, 0)^T, \boldsymbol{\omega} = (\omega_1, \omega_2, 0)^T \tag{2.28}$$

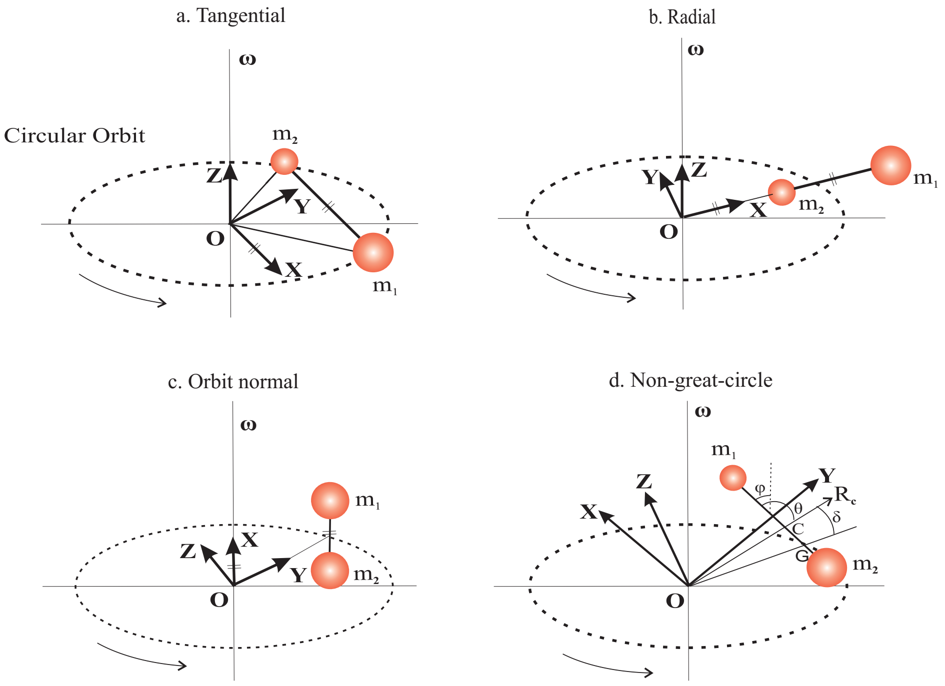

Figure 2.5: Relative Equilibrium Solutions

and

$$f = f_x f_1 + f_y f_2 = 0 \tag{2.29}$$

where

$$\begin{aligned}
f_x &= \frac{m_1 x_1}{R_1^3} + \frac{m_2 x_2}{R_2^3} \\
f_1 &= \frac{x_2}{R_1^3} - \frac{x_1}{R_2^3} \\
f_y &= \left(\frac{m_1}{R_1^3} + \frac{m_2}{R_2^3}\right) y_c \\
f_2 &= \left(\frac{1}{R_1^3} - \frac{1}{R_2^3}\right) y_c
\end{aligned}$$

Therefore, f written in terms of m_1, m_2, R_1, R_2, x_c, y_c and L is

$$f = \left(x_c^2 + y_c^2 - \frac{L^2 m_1 m_2}{(m_1+m_2)^2}\right)\left(\frac{m_1}{R_1^6} + \frac{m_2 - m_1}{R_1^3 R_2^3} - \frac{m_2}{R_2^6}\right) \tag{2.30}$$

$$+ \frac{x_c L}{m_1 + m_2}\left((m_2 - m_1)\left(\frac{m_1}{R_1^6} - \frac{m_2}{R_2^6}\right) - \frac{4 m_1 m_2}{R_1^3 R_2^3}\right) = 0 \tag{2.31}$$

The solutions of Eq. (2.30) provide the nongreat-circle equilibria. This formulation of the nongreat-circle equilibria is independent of tether force between the spacecraft and is thus useful for analyzing the equilibria for a range of spacecraft separation distances from LEO to GEO heights. In order to simplify the solution methodology, Eq. (2.30) is expressed in terms of one variable θ, the angle between $\boldsymbol{R}_c$ and the x-axis of the rotating frame as shown in Figure 2.5(d). Therefore, let $x_c = R_c \cos(\theta)$ and $y_c = R_c \sin(\theta)$. Plugging in these x_c and y_c values into Eq. (2.30) yields a function of θ for given values of μ, m_1, m_2, L and R_c. Since $f(\theta)$ is a continuous function for a tether formation on $[0, \pi]$, with $(R_c >> L)$ and $f(0) < 0$, $f(\pi) > 0$, there exists at least one solution for $f(\theta) = 0$. Furthermore, since $\frac{df(\theta)}{d\theta} > 0$ on $[0, \pi]$, this solution is unique. The actual deflection angle, φ, from the vertical is computed from the angle between x-axis and $\boldsymbol{\omega}$, while $\theta - \varphi$ is the angle between $\boldsymbol{\omega}$ and $\boldsymbol{R}_c$. The deflection angle φ and error δ are shown in Figure 2.5(d) where the error δ is defined to be $\theta - \varphi - 90°$.

Reference 15 discusses the existence of nongreat-circle equilibria for long tethers. For spacecraft that are separated by 350 km at LEO a deflection of about 1 degree from the vertical to the orbital plane is observed. For instance, Table 2.1 shows the results of $f(\theta) = 0$ for LEO where $R_c = 7000$ km and $L = 350$ km. The error $\delta \neq 0$ numerically proves the existence of nongreat-circle equilibria for long tethers. To gain further insights, the effect

Table 2.1: Non-great-circle Relative Equilibria at LEO[15]

m_1 (kg)	m_2 (kg)	θ (deg)	φ (deg)	δ (deg)
100	9900	91.052659	1.052684	−0.000026048

of nongreat-circle equilibria on a two-craft formation is studied as a function of spacecraft separation distance L and mass distribution ratio χ defined as

$$\chi = \frac{m_1}{m_1 + m_2} \tag{2.32}$$

The spacecraft separation distances range from 10 m to 1000 km and formation center of mass distances from LEO to GEO heights. The contour plots shown in Figure 2.6 indicate that increasing the semi-major axes R_c while holding L fixed leads to a decrease in deflection. However, fixing R_c and allowing L to increase leads to an increase in deflections. As the spacecraft formation becomes more asymmetric, the contour plots show that as spacecraft separation distances L reach 1000 km, deflections of up to the order of 10 degrees are observed. Therefore, large separation distances and mass asymmetry has an effect at LEO to GEO heights; however, for tether formation separation distances on the order of hundreds of meters, the deflection from normal is less than 10^{-6} degrees, and mass asymmetry also showed negligible effect on the attitude deflection. Even for a case where there is a 1:10,000 mass ratio, the nongreat-circle equilibria deflection from low earth orbits to geostationary orbits is less than 10^{-5} degrees. Evaluating Eq. (2.30) yields very small function values (on the order of 10^{-12}) and hence the solutions are limited to a lower bound of 10^{-6} degrees. This numerically unresolved region is shown as "noise" pattern in Figure 2.6. However, this degree of accuracy is sufficient to ignore the effect of orbit-attitude coupling for short tether formation separation distances. Specifically, for Coulomb formation separation distances on the order of dozens of meters at GEO, thus ignoring orbit-attitude coupling, the use of numerical search algorithms such as evolutionary search strategies is justified in the search for static Coulomb structures.

2.4 Relative Equilibria in the Restricted Three-body System

In a restricted three-body system for the Coulomb spacecraft formation with $\boldsymbol{SO}(3)$ symmetry, the relative equilibrium is one in a uniformly rotating frame. If the vector $\boldsymbol{\xi}$ denotes the angular velocity of the uniformly rotating frame located at barycenter O, the augmented

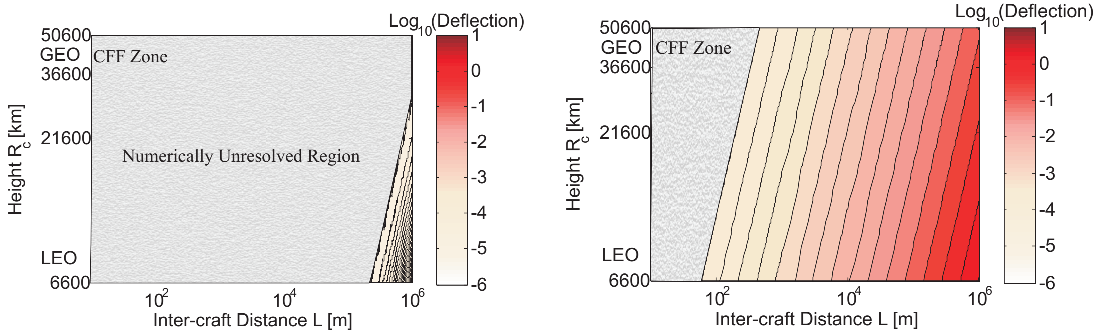

(a) χ=0.49975 (b) χ=0.35

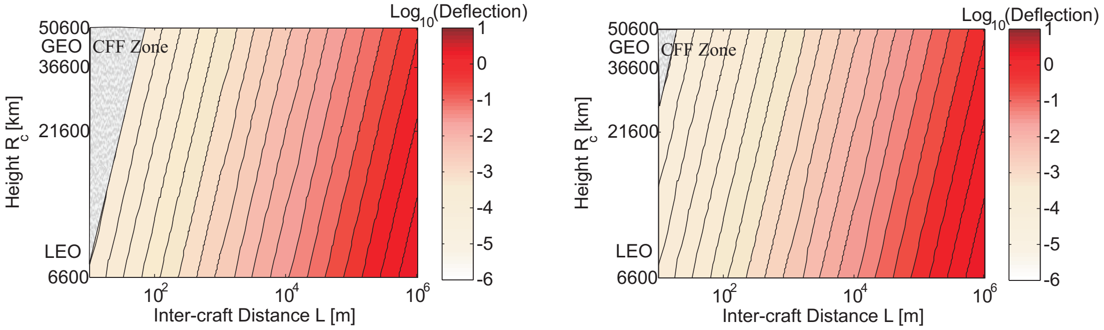

(c) χ=0.05 (d) χ=0.0001

Figure 2.6: Deflection for an Asymmetric Mass Distribution in Circular Earth Orbits [deg]

potential for the two spacecraft formation is

$$\begin{aligned} V_\xi\left(\boldsymbol{r_1},\boldsymbol{r_2}\right) = &-\mu_1\left(\frac{m_1}{\|\boldsymbol{r_1}-\boldsymbol{d}_1\|}+\frac{m_2}{\|\boldsymbol{r_2}-\boldsymbol{d}_1\|}\right)-\mu_2\left(\frac{m_1}{\|\boldsymbol{r_1}-\boldsymbol{d}_2\|}+\frac{m_2}{\|\boldsymbol{r_2}-\boldsymbol{d}_2\|}\right) \\ &+V_t\left(\|\boldsymbol{r_1}-\boldsymbol{r_2}\|\right)-\frac{m_1}{2}\left\langle\boldsymbol{\xi}\times\boldsymbol{r_1},\boldsymbol{\xi}\times\boldsymbol{r_1}\right\rangle-\frac{m_2}{2}\left\langle\boldsymbol{\xi}\times\boldsymbol{r_2},\boldsymbol{\xi}\times\boldsymbol{r_2}\right\rangle \end{aligned} \tag{2.33}$$

In this case, the relative equilibria of the system are characterized by the critical points of the augmented potential V_ξ. The first variation of V_ξ taken component wise with respect to

$\boldsymbol{q} = (\boldsymbol{r_1}, \boldsymbol{r_2})$ is

$$\begin{aligned}
\boldsymbol{D}V_\xi(\boldsymbol{r_1}, \boldsymbol{r_2}) \cdot (\delta\boldsymbol{r_1}, \delta\boldsymbol{r_2}) = {} & \mu_1 m_1 \frac{\boldsymbol{r_1} - \boldsymbol{d}_1}{\|\boldsymbol{r_1} - \boldsymbol{d}_1\|^3} \cdot \delta\boldsymbol{r_1} + \mu_1 m_2 \frac{\boldsymbol{r_2} - \boldsymbol{d}_1}{\|\boldsymbol{r_2} - \boldsymbol{d}_1\|^3} \cdot \delta\boldsymbol{r_2} \\
& + \mu_2 m_1 \frac{\boldsymbol{r_1} - \boldsymbol{d}_2}{\|\boldsymbol{r_1} - \boldsymbol{d}_2\|^3} \cdot \delta\boldsymbol{r_1} + \mu_2 m_2 \frac{\boldsymbol{r_2} - \boldsymbol{d}_2}{\|\boldsymbol{r_2} - \boldsymbol{d}_2\|^3} \cdot \delta\boldsymbol{r_2} \\
& + V_t^{'}(\|\boldsymbol{r_1} - \boldsymbol{r_2}\|) \frac{\boldsymbol{r_1} - \boldsymbol{r_2}}{\|\boldsymbol{r_1} - \boldsymbol{r_2}\|} \cdot (\delta\boldsymbol{r_1} - \delta\boldsymbol{r_2}) \\
& + m_1 \left(\hat{\boldsymbol{\xi}}\hat{\boldsymbol{\xi}}\boldsymbol{r_1}\right) \cdot \delta\boldsymbol{r_1} + m_2 \left(\hat{\boldsymbol{\xi}}\hat{\boldsymbol{\xi}}\boldsymbol{r_2}\right) \cdot \delta\boldsymbol{r_2}
\end{aligned} \tag{2.34}$$

If $V_t = V_c$, the Coulomb potential, then $V_c^{'}$ is given by Eq. (2.19). Setting $DV_\xi(\boldsymbol{r_{1e}}, \boldsymbol{r_{2e}}) = 0$ leads to the following relative equilibria conditions:

$$\mu_1 m_1 \frac{\boldsymbol{r_{1e}} - \boldsymbol{d}_1}{\|\boldsymbol{r_{1e}} - \boldsymbol{d}_1\|^3} + \mu_2 m_1 \frac{\boldsymbol{r_{1e}} - \boldsymbol{d}_2}{\|\boldsymbol{r_{1e}} - \boldsymbol{d}_2\|^3} + m_1 \hat{\boldsymbol{\xi}}\hat{\boldsymbol{\xi}}\boldsymbol{r_{1e}} + V_t^{'} \frac{\boldsymbol{r_{1e}} - \boldsymbol{r_{2e}}}{\|\boldsymbol{r_{1e}} - \boldsymbol{r_{2e}}\|} = 0 \tag{2.35a}$$

$$\mu_1 m_2 \frac{\boldsymbol{r_{2e}} - \boldsymbol{d}_1}{\|\boldsymbol{r_{2e}} - \boldsymbol{d}_1\|^3} + \mu_2 m_2 \frac{\boldsymbol{r_{2e}} - \boldsymbol{d}_2}{\|\boldsymbol{r_{2e}} - \boldsymbol{d}_2\|^3} + m_2 \hat{\boldsymbol{\xi}}\hat{\boldsymbol{\xi}}\boldsymbol{r_{2e}} - V_t^{'} \frac{\boldsymbol{r_{1e}} - \boldsymbol{r_{2e}}}{\|\boldsymbol{r_{1e}} - \boldsymbol{r_{2e}}\|} = 0 \tag{2.35b}$$

The vectors $\boldsymbol{R}_{11}$, $\boldsymbol{R}_{12}$, $\boldsymbol{R}_{21}$ and $\boldsymbol{R}_{22}$ shown in Figure 2.3 are represented in terms of $\boldsymbol{r_{1e}}$, $\boldsymbol{r_{2e}}$, $\boldsymbol{d}_1$, and $\boldsymbol{d}_2$ as

$$\begin{aligned}
\boldsymbol{R}_{11} &= \boldsymbol{r_{1e}} - \boldsymbol{d}_1, \qquad & \boldsymbol{R}_{12} &= \boldsymbol{r_{1e}} - \boldsymbol{d}_2 \\
\boldsymbol{R}_{21} &= \boldsymbol{r_{2e}} - \boldsymbol{d}_1, \qquad & \boldsymbol{R}_{22} &= \boldsymbol{r_{2e}} - \boldsymbol{d}_2
\end{aligned} \tag{2.36}$$

Therefore, Eqs. (2.35a) and (2.35b) become

$$\mu_1 m_1 \frac{\boldsymbol{r_{1e}} - \boldsymbol{d}_1}{R_{11}^3} + \mu_2 m_1 \frac{\boldsymbol{r_{1e}} - \boldsymbol{d}_2}{R_{12}^3} + m_1 \hat{\boldsymbol{\xi}}\hat{\boldsymbol{\xi}}\boldsymbol{r_{1e}} + V_t^{'} \frac{\boldsymbol{r_{1e}} - \boldsymbol{r_{2e}}}{\|\boldsymbol{r_{1e}} - \boldsymbol{r_{2e}}\|} = 0 \tag{2.37a}$$

$$\mu_1 m_2 \frac{\boldsymbol{r_{2e}} - \boldsymbol{d}_1}{R_{21}^3} + \mu_2 m_2 \frac{\boldsymbol{r_{2e}} - \boldsymbol{d}_2}{R_{22}^3} + m_2 \hat{\boldsymbol{\xi}}\hat{\boldsymbol{\xi}}\boldsymbol{r_{2e}} - V_t^{'} \frac{\boldsymbol{r_{1e}} - \boldsymbol{r_{2e}}}{\|\boldsymbol{r_{1e}} - \boldsymbol{r_{2e}}\|} = 0 \tag{2.37b}$$

where $R_{11} = \|\boldsymbol{R}_{11}\|$, $R_{12} = \|\boldsymbol{R}_{12}\|$, $R_{21} = \|\boldsymbol{R}_{21}\|$ and $R_{22} = \|\boldsymbol{R}_{22}\|$.

Now consider a rotation matrix $[FS] \in \boldsymbol{SO}(3)$ that maps vectors from a synodic frame S into a new reference frame F. If we denote the vectors $\boldsymbol{R_1}$, $\boldsymbol{R_2}$, $\boldsymbol{\omega}$ in the reference frame S, then the conditions of relative equilibria given in Eqs. 2.37 are invariant under the transformation $\boldsymbol{R_1} = [FS]\,\boldsymbol{r_{1e}}$, $\boldsymbol{R_2} = [FS]\,\boldsymbol{r_{2e}}$ and $\boldsymbol{\omega} = [FS]\,\boldsymbol{\xi}$. As illustrated in Figure

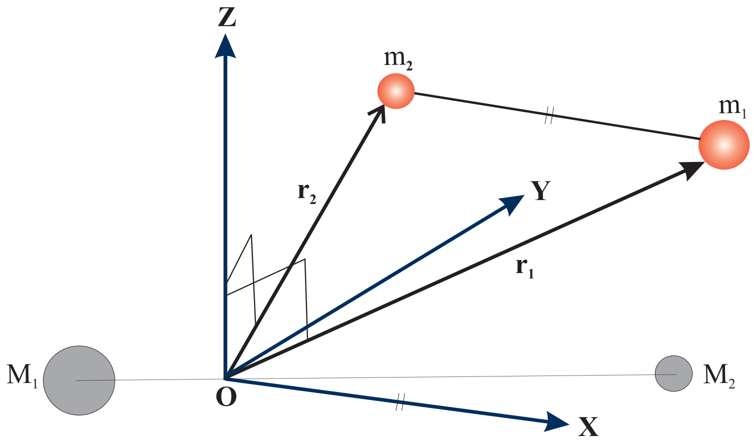

Figure 2.7: The Rotating Reference Frame (Restricted Three-body System)

2.7, a reference frame is chosen such that the x-axis is parallel to the line connecting the two crafts, the z-axis being perpendicular to both the vectors $\boldsymbol{r_{1e}}$ and $\boldsymbol{r_{2e}}$, and the y-axis completing the triad. Also, let γ be the angle in the orbit plane between the two frames S and F.

In the context of the new frame F, the position vectors are expressed as $\boldsymbol{R}_1 = (x_1, y_c, 0)^T$, $\boldsymbol{R}_2 = (x_2, y_c, 0)^T$, and $\boldsymbol{\omega} = (\omega_1, \omega_2, \omega_3)^T$. The vectors $\boldsymbol{d}_1$ and $\boldsymbol{d}_2$ in the F frame become $(-d_1 \cos\gamma, -d_1 \sin\gamma, 0)$ and $(d_2 \cos\gamma, d_2 \sin\gamma, 0)$. Now the equilibrium conditions (2.37a) and (2.37b) expressed in scalar form are given below. It is also assumed that $x_1 > x_2$ and let $L = x_1 - x_2 > 0$. Further, define $\boldsymbol{R}_c = (x_c, y_c, 0)^T$ where $x_c = (m_1 x_1 + m_2 x_2) / (m_1 + m_2)$. The expressions for x_1, x_2 and y_c are given in Eqs. 2.27.

$$-\left(\omega_2^2+\omega_3^2\right)x_1+\omega_1\omega_2 y_c+\mu_1\left(\frac{x_1+d_1\cos\gamma}{R_{11}^3}\right)+\mu_2\left(\frac{x_1-d_2\cos\gamma}{R_{12}^3}\right)=-\frac{V_t'}{m_1} \tag{2.38}$$

$$\omega_1\omega_2 x_1-\left(\omega_1^2+\omega_3^2\right)y_c+\mu_1\left(\frac{y_c+d_1\sin\gamma}{R_{11}^3}\right)+\mu_2\left(\frac{y_c-d_2\sin\gamma}{R_{12}^3}\right)=0 \tag{2.39}$$

$$\left(\omega_1 x_1+\omega_2 y_c\right)\omega_3=0 \tag{2.40}$$

$$-\left(\omega_2^2+\omega_3^2\right)x_2+\omega_1\omega_2 y_c+\mu_1\left(\frac{x_2+d_1\cos\gamma}{R_{21}^3}\right)+\mu_2\left(\frac{x_2-d_2\cos\gamma}{R_{22}^3}\right)=\frac{V_t'}{m_2} \tag{2.41}$$

$$\omega_1\omega_2 x_2-\left(\omega_1^2+\omega_3^2\right)y_c+\mu_1\left(\frac{y_c+d_1\sin\gamma}{R_{21}^3}\right)+\mu_2\left(\frac{y_c-d_2\sin\gamma}{R_{22}^3}\right)=0 \tag{2.42}$$

$$\left(\omega_1 x_2+\omega_2 y_c\right)\omega_3=0 \tag{2.43}$$

Determining the relative equilibria of the two craft formation corresponds to solving the equations (2.38-2.43) for a given set of values for μ_1, μ_2, m_1, m_2, L and $R_c = \|\boldsymbol{R_c}\|$. Since there are more unknowns than the number of equations, certain constraints are needed in order to find the relative equilibria. For libration point missions, the frame rotates at a constant angular velocity Ω given in Eq. 2.12. Let us consider angular velocity constraints $\omega_3 = \Omega \neq 0$ (Case 1) and $\omega_3 = 0$ (Case 2).

Case 1. As $\omega_3 \neq 0$ Eq. (2.40) implies $(\omega_1 x_1 + \omega_2 y_c) = 0$ and $x_1 \neq 0$ due to the adopted frame which indicates that $\omega_1 = 0$ and $\omega_2 y_c = 0$. Using the conditions $\omega_3 \neq 0$ and $\omega_1 = 0$ in equations (2.39) and (2.42) and subtracting one from the other gives rise to

$$\left[\mu_1\left(\frac{1}{R_{11}^3}-\frac{1}{R_{21}^3}\right)(y_c+d_1\sin\gamma)+\mu_2\left(\frac{1}{R_{12}^3}-\frac{1}{R_{22}^3}\right)(y_c-d_2\sin\gamma)\right]=0 \tag{2.44}$$

From Eq. (2.44), two more conditions arise, $y_c + d_1\sin\gamma \neq 0$ and $y_c - d_2\sin\gamma \neq 0$, or $y_c + d_1\sin\gamma = 0$ and $y_c - d_2\sin\gamma = 0$. Therefore, the conditions for relative equilibria are further expressed as Case 1a and Case 1b.

Case 1a. $\omega_1 = 0$, $\omega_3 \neq 0$, $\omega_2 y_c = 0$, $y_c + d_1\sin\gamma \neq 0$ and $y_c - d_2\sin\gamma \neq 0$.

Here, $y_c + d_1\sin\gamma \neq 0$ implies that $y_c \neq 0$ and $\gamma \neq 0$. This forces $\omega_2 = 0$ and Eq. (2.44) yields $R_{11} = R_{21}$ and $R_{12} = R_{22}$. Applying these conditions to Eqs. (2.38) and (2.41) and dividing by the other results in the conditions $(m_1 x_1 + m_2 x_2) = 0$ and $\gamma = 90$ degrees.

Therefore the *along-track* equilibrium solutions in the context of a restricted three-body system (circular orbits) are

$$\boldsymbol{R}_1 = \left(\tfrac{1}{2}L, y_c, 0\right)^T,\ \boldsymbol{R}_2 = \left(-\tfrac{1}{2}L, y_c, 0\right)^T,\ \boldsymbol{\omega} = (0, 0, \Omega)^T$$
$$y_c = R_c, \text{ and } V_t^{'} = -\tfrac{m_1 m_2 L}{(m_1+m_2)}\left(\left(\tfrac{\mu_1}{R_{11}^3} + \tfrac{\mu_2}{R_{12}^3}\right) - \Omega^2\right)$$

Since $\boldsymbol{R}_c \cdot \boldsymbol{\omega} = 0$, this is a great-circle relative equilibrium. However, in the context of a restricted three-body system, for any of the collinear libration points it can be shown that $\Omega^2 < \frac{\mu_1}{R_{11}^3} + \frac{\mu_2}{R_{12}^3}$, which implies that $V_t^{'} < 0$ (compressive elastic force). For any of the triangular libration points it can be shown that $\Omega^2 > \frac{\mu_1}{R_{11}^3} + \frac{\mu_2}{R_{12}^3}$, which implies that $V_t^{'} > 0$ (tensile elastic force). For example, Figure 2.8 shows the along-track equilibrium solutions at a collinear (L_2) and a triangular (L_4) libration point. In particular, for a Coulomb tether, Eq.(2.19) indicates that the two spacecraft masses must be charged with same polarity at the collinear libration points and must be charged with opposite polarity at the triangular libration points.

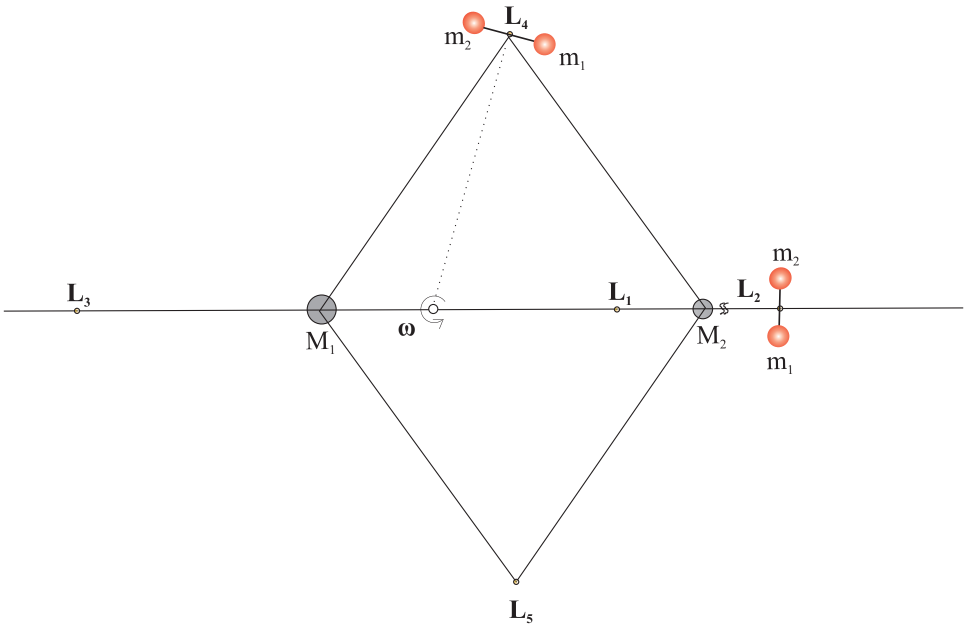

Figure 2.8: Along-track Relative Equilibrium at Libration Points

Case 1b. $\omega_1 = 0$, $\omega_3 = \Omega \neq 0$, $\omega_2 y_c = 0$, $y_c + d_1 \sin\gamma = 0$ and $y_c - d_2 \sin\gamma = 0$.

Assuming that $x_1 > x_2 > 0$ for a tether formation and since $\omega_3 \neq 0$ and $y_c + d_1 \sin\gamma = 0, y_c - d_2 \sin\gamma = 0$ implies that $y_c = 0$ and $\gamma = 0$ for collinear libration points. However, for Earth-Moon triangular libration points $y_c = 0$ and $\gamma = 60.31$ degrees, appropriate values of R_{11}, R_{12}, R_{21} and R_{22} should satisfy Eq. (2.44). Therefore, for any libration point, from Eq. (2.40) one can set $\omega_1 = 0$ and $\omega_2 = 0$. With these conditions, Eqs. (2.38) to (2.43) reduce to

$$\left(-\Omega^2 + \frac{\mu_1}{R_{11}^3} + \frac{\mu_2}{R_{12}^3}\right) x_1 + \frac{\mu_1 d_1}{R_{11}^3} - \frac{\mu_2 d_2}{R_{12}^3} = -\frac{V_t^{'}}{m_1} \tag{2.45a}$$

$$\left(-\Omega^2 + \frac{\mu_1}{R_{21}^3} + \frac{\mu_2}{R_{22}^3}\right) x_2 + \frac{\mu_1 d_1}{R_{21}^3} - \frac{\mu_2 d_2}{R_{22}^3} = \frac{V_t^{'}}{m_2} \tag{2.45b}$$

Solving these equations yields a *radial* relative equilibrium with the tether forces directed along the radial axis. The equilibrium solution configuration is

$$\boldsymbol{R}_1 = (x_1, 0, 0)^T,\ \boldsymbol{R}_2 = (x_2, 0, 0)^T,\ \boldsymbol{\omega} = (0, 0, \Omega)^T$$

$$V_t^{'} = \tfrac{m_1 m_2}{m_1 + m_2}\left(\Omega^2 L - \mu_1\left(\tfrac{1}{R_{11}^3} - \tfrac{1}{R_{21}^3}\right) - \mu_2\left(\tfrac{1}{R_{12}^3} - \tfrac{1}{R_{22}^3}\right)\right)$$

Since $x_1 > x_2$, from Eq. (2.36) it can be shown for a radial equilibrium that $R_{11} > R_{21}$ and $R_{12} > R_{22}$ for both the collinear and triangular libration points, indicating that $V_t^{'} > 0$. Again, $\boldsymbol{R}_c \cdot \boldsymbol{\omega} = 0$ is a great-circle relative equilibrium as shown in Figure 2.9. This implies that there is a tensile elastic force acting between the two masses along the radial direction when the formation is at any of the libration points. Hence, for a Coulomb tether, $V_t^{'} > 0$ indicates that the two spacecraft masses must be charged with opposite polarity.

Case 2. $\omega_3 = 0$. The relative equilibrium equations reduce to

$$-\omega_2^2 x_1 + \omega_1\omega_2 y_c + \mu_1\left(\frac{x_1 + d_1\cos\gamma}{R_{11}^3}\right) + \mu_2\left(\frac{x_1 - d_2\cos\gamma}{R_{12}^3}\right) = -\frac{V_t^{'}}{m_1} \tag{2.46a}$$

$$\omega_1\omega_2 x_1 - \omega_1^2 y_c + \mu_1\left(\frac{y_c + d_1\sin\gamma}{R_{11}^3}\right) + \mu_2\left(\frac{y_c - d_2\sin\gamma}{R_{12}^3}\right) = 0 \tag{2.46b}$$

$$-\omega_2^2 x_2 + \omega_1\omega_2 y_c + \mu_1\left(\frac{x_2 + d_1\cos\gamma}{R_{21}^3}\right) + \mu_2\left(\frac{x_2 - d_2\cos\gamma}{R_{22}^3}\right) = \frac{V_t^{'}}{m_2} \tag{2.46c}$$

$$\omega_1\omega_2 x_2 - \omega_1^2 y_c + \mu_1\left(\frac{y_c + d_1\sin\gamma}{R_{21}^3}\right) + \mu_2\left(\frac{y_c - d_2\sin\gamma}{R_{22}^3}\right) = 0 \tag{2.46d}$$

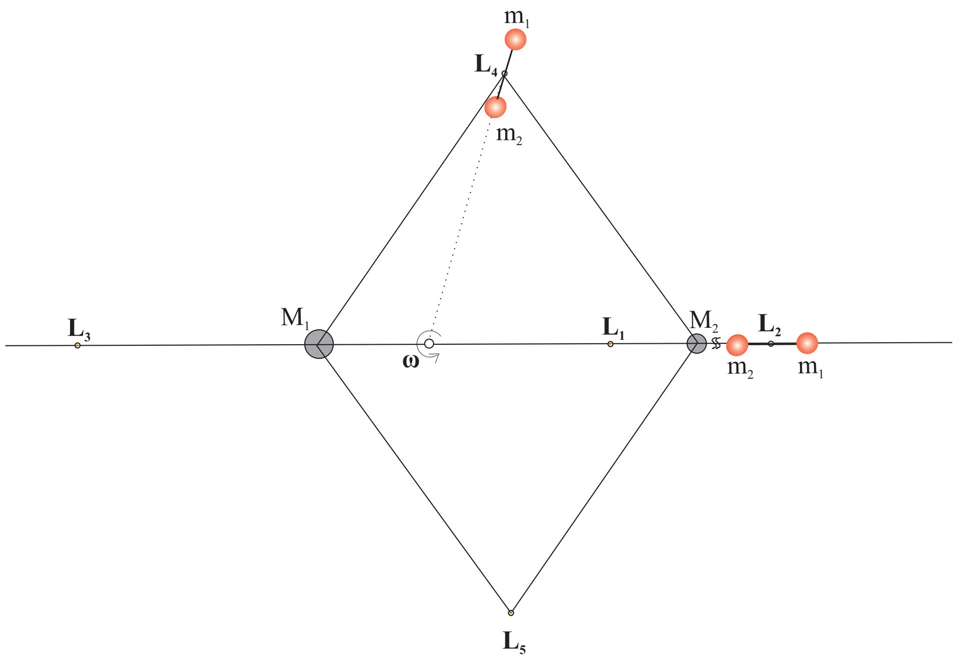

Figure 2.9: Radial Relative Equilibrium at Libration Points

Setting $y_c + d_1 \sin\gamma = 0$ and $y_c - d_2 \sin\gamma = 0$, the equilibrium conditions yield radial equilibrium solutions as seen in Case 1b, but with ω_3 replaced by ω_2. Therefore, we consider only the case where $y_c + d_1 \sin\gamma \neq 0$ and $y_c - d_2 \sin\gamma \neq 0$. Furthermore, it is assumed that $R_{11} = R_{21}$ and $R_{12} = R_{22}$ (Case 2a) as well as $R_{11} \neq R_{21}$ and $R_{12} \neq R_{22}$ (Case 2b).

Case 2a. $\omega_3 = 0$, $R_{11} = R_{21}$, $R_{12} = R_{22}$, $y_c + d_1 \sin\gamma \neq 0$ and $y_c - d_2 \sin\gamma \neq 0$.

Using $y_c + d_1 \sin\gamma \neq 0$ and $y_c - d_2 \sin\gamma \neq 0$ yields $R_{11} = R_{21}$ and $R_{12} = R_{22}$, giving the condition $x_1 = -x_2$. Eqs. (2.46b) and (2.46d) imply that $\omega_1 \neq 0$; additionally, set $\omega_1 = \Omega$ and $\omega_2 = 0$. Then, using $x_1 = -x_2$ and $\omega_2 = 0$ in Eqs. (2.46a) and (2.46c) yields $m_1 = m_2$ as the only possible condition. As a result, the equilibrium solutions obtained are

$$\boldsymbol{R}_1 = \left(\tfrac{1}{2}L, y_c, 0\right)^T,\ \boldsymbol{R}_2 = \left(-\tfrac{1}{2}L, y_c, 0\right)^T,\ \boldsymbol{\omega} = (\Omega, 0, 0)^T$$
$$m_1 = m_2,\ y_c = R_c,\ V_t' = -\tfrac{m_1 m_2 L}{(m_1+m_2)}\left(\tfrac{\mu_1}{R_{11}^3} + \tfrac{\mu_2}{R_{12}^3}\right) < 0$$

These *orbit normal* equilibrium solutions are applicable for both triangular and collinear libration points. Specifically, for triangular libration points $R_{11} = R_{21} = R_{12} = R_{22}$ holds true. Since $\boldsymbol{R}_c \cdot \boldsymbol{\omega} = 0$, once again this is a great-circle relative equilibrium. Since $V_t' < 0$, there is a compressive elastic force acting between the two masses perpendicular to the orbital plane and the two masses are equal and equidistant from the barycenter. Figure 2.10 specifically, illustrates this for a collinear (L_2) and a triangular (L_4) libration point. For a Coulomb formation, since $V_c' < 0$, the two spacecraft masses must be charged with the same polarity.

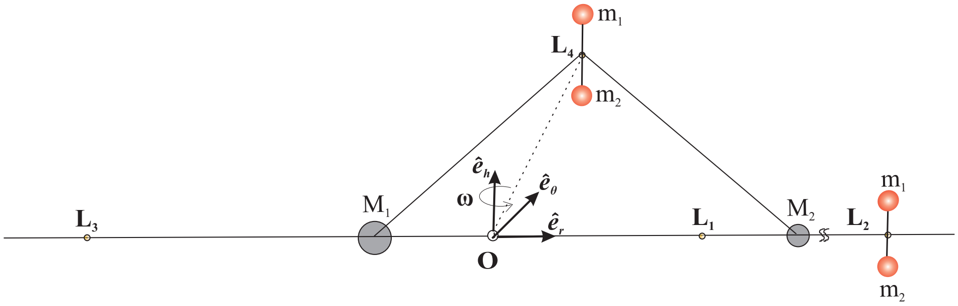

Figure 2.10: Orbit Normal Relative Equilibrium at Libration Points

Case 2b. $\omega_3 = 0$, $R_{11} \neq R_{21}$, $R_{12} \neq R_{22}$, $y_c + d_1 \sin\gamma \neq 0$ and $y_c - d_2 \sin\gamma \neq 0$.

Assuming that the F frame is aligned with the orbit normal configuration gives $\gamma = 90$ degrees. Solving Eqs. (2.46b) and (2.46d) yields

$$\begin{aligned} -\left(x_1 - x_2\right)\omega_1\omega_2 = y_c & \left(\left(\frac{\mu_1}{R_{11}^3} + \frac{\mu_2}{R_{12}^3}\right) - \left(\frac{\mu_1}{R_{21}^3} + \frac{\mu_2}{R_{22}^3}\right)\right) \\ & + \mu_1 d_1 \left(\frac{1}{R_{11}^3} - \frac{1}{R_{21}^3}\right) + \mu_2 d_2 \left(\frac{1}{R_{22}^3} - \frac{1}{R_{12}^3}\right) \neq 0 \end{aligned} \tag{2.47}$$

which implies that $\omega_1 \neq 0$ and $\omega_2 \neq 0$. Combining Eqs. (2.46a) and (2.46c)

$$\left(m_1 + m_2\right)\left(\omega_2 x_c - \omega_1 y_c\right)\omega_2 = m_1 x_1 \left(\frac{\mu_1}{R_{11}^3} + \frac{\mu_2}{R_{12}^3}\right) + m_2 x_2 \left(\frac{\mu_1}{R_{21}^3} + \frac{\mu_2}{R_{22}^3}\right) \neq 0 \tag{2.48}$$

Eq. (2.48) implies that $(\omega_2 x_c - \omega_1 y_c) \neq 0$. Multiplying Eq. (2.46b) by m_1 and (2.46d) by

m_2 and adding the resulting equations gives

$$\begin{aligned} -\left(m_1+m_2\right)\left(\omega_2 x_c-\omega_1 y_c\right)\omega_1 = &\left(m_1\left(\frac{\mu_1}{R_{11}^3}+\frac{\mu_2}{R_{12}^3}\right)+m_2\left(\frac{\mu_1}{R_{21}^3}+\frac{\mu_2}{R_{22}^3}\right)\right)y_c \\ &+m_1\left(\frac{\mu_1 d_1}{R_{11}^3}-\frac{\mu_2 d_2}{R_{12}^3}\right)+m_2\left(\frac{\mu_1 d_1}{R_{21}^3}-\frac{\mu_2 d_2}{R_{22}^3}\right)\neq 0 \end{aligned} \tag{2.49}$$

Defining f_x and f_y to be

$$f_x=\mu_1\left(\frac{m_1 x_1}{R_{11}^3}+\frac{m_2 x_2}{R_{21}^3}\right)+\mu_2\left(\frac{m_1 x_1}{R_{12}^3}+\frac{m_2 x_2}{R_{22}^3}\right)\neq 0 \tag{2.50}$$

$$\begin{aligned} f_y = &\left(\mu_1\left(\frac{m_1}{R_{11}^3}+\frac{m_2}{R_{21}^3}\right)+\mu_2\left(\frac{m_1}{R_{12}^3}+\frac{m_2}{R_{22}^3}\right)\right)y_c \\ &+m_1\left(\frac{\mu_1 d_1}{R_{11}^3}-\frac{\mu_2 d_2}{R_{12}^3}\right)+m_2\left(\frac{\mu_1 d_1}{R_{21}^3}-\frac{\mu_2 d_2}{R_{22}^3}\right)\neq 0 \end{aligned} \tag{2.51}$$

The ratio of Eqs. (2.48) and (2.49) becomes

$$\frac{\omega_2}{\omega_1}=-\frac{f_x}{f_y} \tag{2.52}$$

Eliminating ω_1 and ω_2 from Eqs. (2.47), (2.48) and (2.49) yields

$$f=f_x f_1+f_y f_2=0 \tag{2.53}$$

where

$$\begin{aligned} f_1 = &\, x_2\left(\frac{\mu_1}{R_{11}^3}+\frac{\mu_2}{R_{12}^3}\right)-x_1\left(\frac{\mu_1}{R_{21}^3}+\frac{\mu_2}{R_{22}^3}\right) \\ &+\left(x_2\left(\frac{\mu_1 d_1}{R_{11}^3}-\frac{\mu_2 d_2}{R_{12}^3}\right)+x_1\left(\frac{\mu_2 d_2}{R_{22}^3}-\frac{\mu_1 d_1}{R_{21}^3}\right)\right)\frac{1}{y_c} \end{aligned}$$

and

$$\begin{aligned} f_2 = &\left(\left(\frac{\mu_1}{R_{11}^3}+\frac{\mu_2}{R_{12}^3}\right)-\left(\frac{\mu_1}{R_{21}^3}+\frac{\mu_2}{R_{22}^3}\right)\right)y_c \\ &+\left(\frac{\mu_1 d_1}{R_{11}^3}-\frac{\mu_2 d_2}{R_{12}^3}\right)+\left(\frac{\mu_2 d_2}{R_{22}^3}-\frac{\mu_1 d_1}{R_{21}^3}\right) \end{aligned}$$

.

The solutions of Eq. (2.53) give the nongreat-circle equilibria and it can be shown that such nongreat-circle equilibria exist only if $m_1 \neq m_2$. The nongreat-circle equilibria formulation is independent of the tether force between the spacecraft and is thus useful for analyzing the equilibria for a range of spacecraft separation distances with the formation at the libration points. Similar to the solution procedure followed for a two-body system, Eq. (2.53) is expressed in terms of one variable θ, the angle between $\boldsymbol{R}_c$ and the x-axis of the rotating frame.

At the Earth-Moon collinear libration points, the effect of nongreat-circle equilibria on a two-craft formation is studied as a function of spacecraft separation distance L and mass distribution ratio χ defined in Eq. (2.32). The spacecraft separation distances range from 10 m to 5000 km with the formation center of mass distances fixed at the libration points L_1, L_2 and L_3. Figure 2.11 shows the numerical solutions for a range of spacecraft separation distances. For spacecraft separated by more than 5000 km at L_1 and L_2, a deflection of about 1 degree from the vertical to the orbital plane is observed. For such large separation distances, a deflection of about 10 degrees is observed at L_3. This is due to L_3 being close to Earth compared to that of L_1 and L_2. On the other hand, for short separation distances the deflection becomes negligible. For instance, Coulomb formations are feasible at the libration points with the spacecraft separation distances ranging from 10m to 30m due to the reduced range of the Debye length. As shown in Figure 2.11(a), for Coulomb formation distances at L_1, L_2 and L_3, the deflection from normal is less than 10^{-6} degrees. From Figure 2.11(b), mass asymmetry of the two craft also yielded negligible effect on the attitude deflection at such short separation distances. Consequently, at libration points, although the orbit-attitude coupling effects dominate for large spacecraft separation distances on the order of thousands of kilometers such effects can be ignored for short separation distances such as in Coulomb formations.

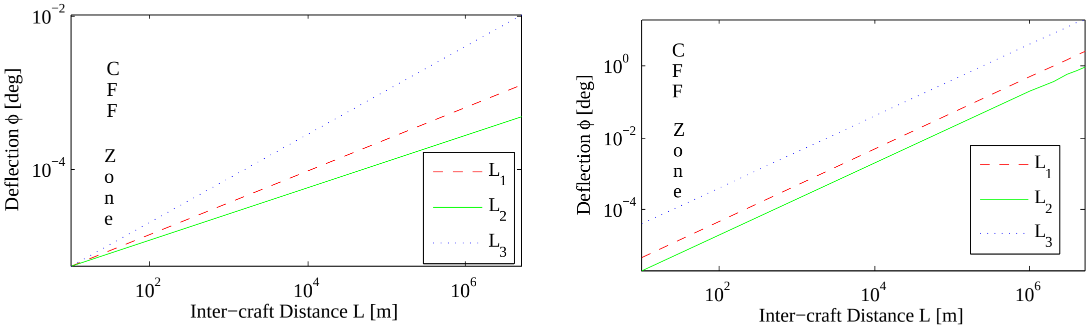

(a) χ=0.49975

(b) χ=0.0001

Figure 2.11: Deflection for an Asymmetric Mass Distribution at Libration Points [deg]

2.5 Summary

In this chapter, the relative equilibria of a two-craft formation moving in a two-body system and a three-body system are discussed. A general framework of two-craft connected by an elastic tether force is studied in this chapter with an emphasis on a virtual Coulomb tether as a special case. The orbit-attitude coupling effects should be considered for large spacecraft separation distances; for LEO, greater than tens of kilometers, for GEO, hundreds of kilometers, and at libration points, tens of thousands of kilometers. Such coupling effects can be ignored for shorter spacecraft separation distances. For example, previous Coulomb formation flying work used the simple principle axes condition. The negligible nongreat-circle effects shown in this chapter for smaller inter-craft separation distances validates this assumption for Coulomb tether applications. Consequently, for a charged two-craft formation, the principal axis condition is very good for genetic algorithms which seek approximate equilibrium answers. However, for full non-linear solutions, these effects can be taken into consideration. Moreover, this chapter presents the relative equilibria of a two-craft formation at all five libration points and also numerically shows that nongreat-circle effects exist at the Earth-Moon collinear libration points. Interestingly, in the restricted three-body system, a tether force is required for the along-track equilibrium, however, no tether force is necessary in the restricted two-body system. Furthermore, the results obtained in this chapter could be used to investigate the linearized dynamics and stability of a 2-craft Coulomb tether formation at libration points.

Chapter 3

ORBIT RADIAL DYNAMIC ANALYSIS OF A TWO-CRAFT COULOMB FORMATION AT LIBRATION POINTS

In this chapter, the linearized orbit-radial dynamics and stability analysis of a 2-craft virtual Coulomb structure at Earth-Moon libration points are investigated. Reference 45 presents three relative equilibria of the charged 2-craft problem at libration points (orbit-radial, along-track and orbit-normal). Figure 3.1 shows the orbit-radial equilibrium at Earth-Moon libration points.

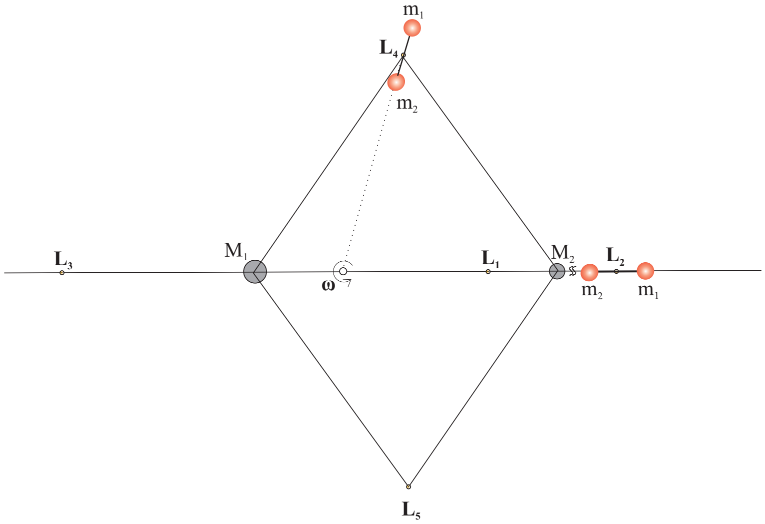

Figure 3.1: Radial Relative Equilibrium at Libration Points

The goal of this chapter is to study the orbit radial dynamics and stability conditions at the libration points and to investigate the presence of any cross-coupling effects that may not exist for circular orbits at GEO. The relative distance between the two satellites of the Coulomb tether is controlled using electrostatic Coulomb forces. In order to stabilize the formation shape at the libration points, a similar active charge feedback law, introduced in Reference 5 for the study of the linear dynamics of orbit radial 2-craft formations at GEO, is applied at the libration point scenario. First the nonlinear and linearized equations of motion are investigated. Of interest is how these compare to the earlier circular GEO orbit results, and if these can be generalized into a single mathematical framework. To stabilize the separation distance, a partial-state charge feedback control law (separation distance and separation rate only) is studied, followed by a linear stability analysis of coupled attitude and separation distance dynamics. Furthermore, an alternate linear, full-state feedback control law (in-plane attitude, separation distance, and their rates) is investigated for a radial equilibrium two-craft Coulomb tether formation at a collinear libration point. The linearized analytical results are then compared to nonlinear numerical simulations to validate the control performance results. In the presence of differential solar drag perturbations, a Lyapunov feedback controller is designed for stabilizing a radial equilibrium two-craft Coulomb formation at collinear libration points.

3.1 Linear Dynamics and Stability Analysis - Collinear Libration Points

3.1.1 Charged Relative Equations of Motion

The linearized equations of motion for a two spacecraft Coulomb formation at a collinear Earth-Moon libration point are briefly derived in this section. The characteristics of the frames involved in the analysis and the notation used are summarized.

Let M_1 and M_2 be the dominant masses of the two gravitational primaries, Earth and Moon. As shown in Figure 3.2, if O is the center of mass of both primaries, any non-rotating frame with origin at O is considered as an inertial frame. The circular relative motion of primaries occurs in a plane with angular rotation axis. The synodic frame $\mathcal{S} : \{\hat{\boldsymbol{e}}_r, \hat{\boldsymbol{e}}_\theta, \hat{\boldsymbol{e}}_h\}$ is rotating around the $O - z$ axis with the constant angular velocity Ω defined as

$$\Omega = \sqrt{\frac{G\left(M_1 + M_2\right)}{d^3}} \tag{3.1}$$

Here G is the gravity constant and d is the distance between the two primaries. The primaries are at rest in the synodic frame at positions $M_1(-d_1, 0, 0)$ and $M_2(d_2, 0, 0)$. If $\boldsymbol{r}_0 = [r_{x_0}, r_{y_0}, r_{z_0}]^T$ is the position vector in the synodic frame $\mathcal{S}$ of a collinear libration point with respect to the barycenter O, then the two distance vectors of a collinear libration point from the two primaries in the plane are

$$ {}^{\mathcal{S}}\boldsymbol{R}_1 = \begin{bmatrix} r_{x0} + d_1 \\ 0 \\ 0 \end{bmatrix} \quad \text{and} \quad {}^{\mathcal{S}}\boldsymbol{R}_2 = \begin{bmatrix} r_{x0} - d_2 \\ 0 \\ 0 \end{bmatrix} \tag{3.2} $$

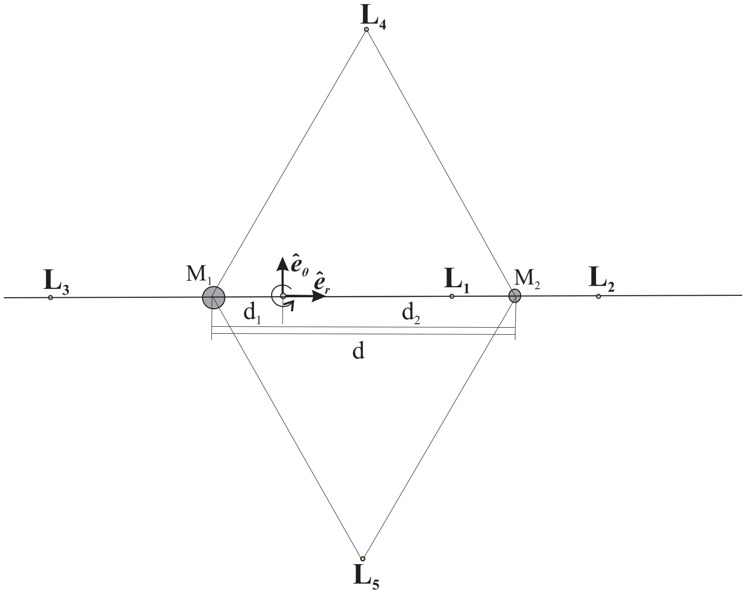

Figure 3.2: Stationary Libration points

In order to describe the relative motion of the satellite with respect to the formation center of mass, a rotating Hill orbit frame $\mathcal{O} : \{\hat{\boldsymbol{o}}_r, \hat{\boldsymbol{o}}_\theta, \hat{\boldsymbol{o}}_h\}$ whose origin coincides with L_2 libration point is chosen as shown in Figure 4.2. The formation center of mass is assumed to be at the origin of this rotating Cartesian coordinate system and the relative position vector of the i^{th} satellite is defined as $\boldsymbol{\rho}_i = (x_i, y_i, z_i)^T$; where the x_i component is in the $\hat{\boldsymbol{o}}_r$ direction (orbit radial), the y_i component is in the $\hat{\boldsymbol{o}}_\theta$ direction of orbital velocity (along-track), and the component z_i is in the $\hat{\boldsymbol{o}}_h$ direction (orbit normal). Since the orbit frame origin coincides with the formation center of mass, the center of mass condition is defined as

$$m_1\boldsymbol{\rho_1} + m_2\boldsymbol{\rho_2} = 0 \tag{3.3}$$

where m_i is the satellite mass. Also, for a collinear libration point, the orbit frame and the synodic frames coincide so that the position vectors $\boldsymbol{R}_1$ and $\boldsymbol{R}_2$ are equivalent in both frames.

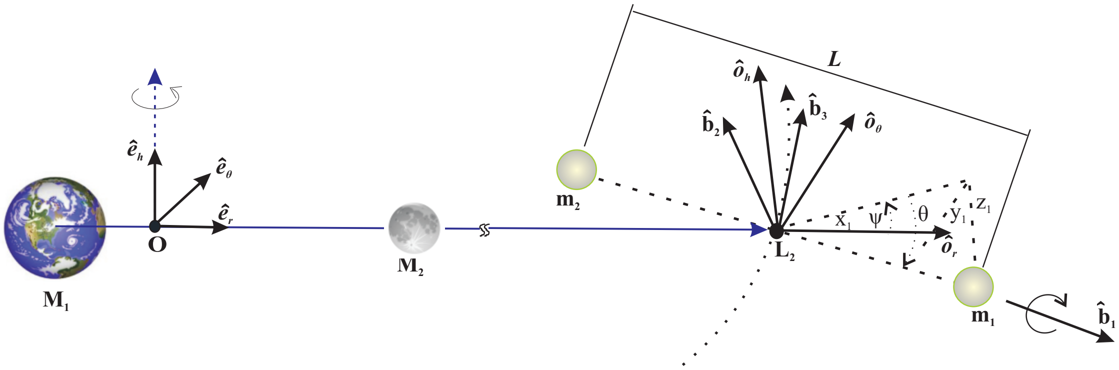

Figure 3.3: Euler Angles Representing the Attitude of Coulomb Tether with Respect to the Orbit Frame at L_2

If the two-craft formation is treated as a rigid body and aligned in the radial direction, then, for this orbit nadir aligned formation, consider a body-fixed coordinate frame $\mathcal{B}$: $\{\hat{\boldsymbol{b}}_1, \hat{\boldsymbol{b}}_2, \hat{\boldsymbol{b}}_3\}$ where $\hat{\boldsymbol{b}}_1$ is aligned with the relative position vector $\boldsymbol{\rho_1}$ of mass m_1. Therefore, in this configuration, the $\mathcal{O}$ and $\mathcal{B}$ frame orientation vectors are exactly aligned and $\boldsymbol{\rho_1}$ in a body-fixed frame is given by

$$\boldsymbol{\rho_1} = \frac{m_2}{m_1 + m_2} L\hat{\boldsymbol{b}}_1 + 0\hat{\boldsymbol{b}}_2 + 0\hat{\boldsymbol{b}}_3 \tag{3.4}$$

where L is the distance between the satellites 1 and 2. Let the 3-2-1 Euler angles (ψ, θ, ϕ) be the pitch, roll and yaw angles which represent the relative attitude between the $\mathcal{B}$ and $\mathcal{O}$ frames. From the point-mass assumption of the two-craft, the yaw rotation about $\hat{\boldsymbol{b}}_1$ (angle ϕ) can be ignored. Then the direction cosine matrix $[BO(\psi, \theta)]$ that relates the $\mathcal{O}$ frame to

$\mathcal{B}$ frame is given by

$$[BO] = \begin{bmatrix} \cos\theta\cos\psi & \cos\theta\,\sin\psi & -\sin\theta \\ -\sin\psi & \cos\psi & 0 \\ \sin\theta\,\cos\psi & \sin\theta\,\sin\psi & \cos\theta \end{bmatrix} \tag{3.5}$$

Consequently, the position vector of mass m_1 in the $\mathcal{O}$ frame is written as

$$^{\mathcal{O}}\boldsymbol{\rho_1} = \begin{pmatrix} x_1 \\ y_1 \\ z_1 \end{pmatrix} = [BO]^T \begin{pmatrix} \frac{m_2}{m_1+m_2}L \\ 0 \\ 0 \end{pmatrix} = \frac{m_2 L}{m_1 + m_2} \begin{bmatrix} \cos\theta\,\cos\psi \\ \cos\theta\,\sin\psi \\ -\sin\theta \end{bmatrix} \tag{3.6}$$

Using Eq. (3.3), the position vector of mass m_2 in the $\mathcal{O}$ frame becomes

$$^{\mathcal{O}}\boldsymbol{\rho_2} = \begin{pmatrix} x_2 \\ y_2 \\ z_2 \end{pmatrix} = \frac{m_1 L}{m_1 + m_2} \begin{bmatrix} -\cos\theta\,\cos\psi \\ -\cos\theta\,\sin\psi \\ \sin\theta \end{bmatrix} \tag{3.7}$$

Furthermore, using the transport theorem,[14] the inertial velocity of mass m_i expressed in the $\mathcal{O}$ frame components becomes

$$^{\mathcal{O}}\boldsymbol{v_i} = \begin{pmatrix} \dot{x}_i - \Omega y_i \\ \dot{y}_i + \Omega\,(x_i + r_c) \\ \dot{z}_i \end{pmatrix} \tag{3.8}$$

The center of mass position vector $\boldsymbol{r_c}$ is assumed to have a constant orbital rate of Ω. The kinetic energy of the system is given by

$$T = \frac{1}{2} m_1\, \boldsymbol{v_1} \cdot \boldsymbol{v_1} + \frac{1}{2} m_2\, \boldsymbol{v_2} \cdot \boldsymbol{v_2} \tag{3.9}$$

Using Eqs. (3.6) - (3.8), Eq. (3.9) is rewritten as

$$T = \frac{1}{2}\frac{m_1 m_2}{m_1 + m_2}\left[\dot{L}^2 + L^2(\dot{\theta}^2 + (\dot{\psi} + \Omega)^2 \cos^2\theta)\right] + \frac{1}{2}\left(m_1 + m_2\right)\Omega^2 r_c^2 \tag{3.10}$$

The gravitational potential energy of the two-craft formation due to the two planets is

$$V_g = -GM_1\left(\frac{m_1}{|\boldsymbol{R}_1 + \boldsymbol{\rho}_1|} + \frac{m_2}{|\boldsymbol{R}_1 + \boldsymbol{\rho}_2|}\right) - GM_2\left(\frac{m_1}{|\boldsymbol{R}_2 + \boldsymbol{\rho}_1|} + \frac{m_2}{|\boldsymbol{R}_2 + \boldsymbol{\rho}_2|}\right) \tag{3.11}$$

Substituting $\mu_1 = GM_1$, $\mu_2 = GM_2$, $\boldsymbol{\rho_1} = \frac{m_2}{m_1+m_2}L\boldsymbol{t_1}$, and $\boldsymbol{\rho_2} = \frac{m_1}{m_1+m_2}L\boldsymbol{t_2}$, the expression for $\frac{1}{|\boldsymbol{R}_1+\boldsymbol{\rho}_1|}$ expanded in a Taylor series about the equilibrium point, and retaining up to the second order terms of $\frac{L}{R_1}$, becomes

$$\frac{1}{|\boldsymbol{R}_1 + \boldsymbol{\rho}_1|} = \frac{1}{R_1}\left\{1 - \frac{m_2}{m_1 + m_2}\left(\frac{L}{R_1}\right)\boldsymbol{u}_1 \cdot \boldsymbol{t}_1 + \left(\frac{m_2}{m_1 + m_2}\right)\left(\frac{L}{R_1}\right)^2\left(3\left(\boldsymbol{u}_1 \cdot \boldsymbol{t}_1\right)^2 - 1\right)\right\} \tag{3.12}$$

where

$$\boldsymbol{t}_1 = \cos\theta\,\cos\psi\,\boldsymbol{\hat{o}}_r + \cos\theta\,\sin\psi\,\boldsymbol{\hat{o}}_\theta - \sin\theta\,\boldsymbol{\hat{o}}_h \tag{3.13}$$

$$\boldsymbol{t}_2 = -\cos\theta\,\cos\psi\,\boldsymbol{\hat{o}}_r - \cos\theta\,\sin\psi\,\boldsymbol{\hat{o}}_\theta + \sin\theta\,\boldsymbol{\hat{o}}_h \tag{3.14}$$

and $\boldsymbol{u}_1$, $\boldsymbol{u}_2$ are the unit vectors in the direction of $\boldsymbol{R}_1$ and $\boldsymbol{R}_2$.

After carrying out similar approximations for the other terms in Eq. (3.11), V_g finally becomes

$$\begin{aligned} V_g = &-\frac{\mu_1}{R_1}\left\{(m_1 + m_2) + \frac{1}{2}\frac{m_1 m_2}{(m_1 + m_2)}\left(\frac{L}{R_1}\right)^2\left(3\left(\boldsymbol{u}_1 \cdot \boldsymbol{t}_1\right)^2 - 1\right)\right\} \\ &-\frac{\mu_2}{R_2}\left\{(m_1 + m_2) + \frac{1}{2}\frac{m_1 m_2}{(m_1 + m_2)}\left(\frac{L}{R_2}\right)^2\left(3\left(\boldsymbol{u}_2 \cdot \boldsymbol{t}_2\right)^2 - 1\right)\right\} \end{aligned} \tag{3.15}$$

and the Coulomb potential for the two-craft formation is[1]

$$V_c = k_c \frac{q_1 q_2}{L} e^{-L/\lambda_d} \tag{3.16}$$

where q_i is the satellite charge and the parameter $k_c = 8.99 \times 10^9$ Nm^2/C^2 is Coulomb's constant. The exponential term in the Coulomb potential depends on the Debye length parameter λ_d which controls the electrostatic field strength of plasma shielding between the craft. At Geostationary Orbits (GEO) the Debye length varies between 80-1400 m, with a mean of about 180 m.[7] In the interplanetary space at Earth-moon libration points, the Debye length varies between 10-40 m.[1,48] Note that the simple point charge electrostatic field formulation in Eq. (3.16) assumes that the vehicle potential is small compared to the local plasma temperature. As discussed in Reference 42, this charge shielding formulation forms a conservative lower bound on the actual electrostatic force created between two charged bodies. For example, assuming an actual Debye length of 4 meters causes and 1 meter diameter spheres at 30 kV yields effective Debye lengths $\hat{\lambda}_d$ which are 3 times larger. As a result, because we are considering kilo-Volt levels of potential, the effective Debye lengths in deep space still yield charged relative motion dynamics that are primarily influenced through classical electrostatics.

The non-linear equations of motion are deduced from the Lagrangian $\mathcal{L} = T - (V_g + V_c)$ of the system in the following form

$$\begin{gathered} \frac{\mathrm{d}}{\mathrm{d}t}\frac{\partial \mathcal{L}}{\partial \dot{q}^i} - \frac{\partial \mathcal{L}}{\partial q^i} = \mathcal{Q}_i \\ q^i = (\theta, \psi, L) \quad (i = 1 \ldots 3) \end{gathered} \tag{3.17}$$

where $\mathcal{Q}_i$ is the generalized force in the q^ith degree of freedom excluding gravitational effects. For the circularly restricted three-body system, using Eqs. (3.10), (3.15) and (3.16) in Eq. (3.17), the nonlinear equations governing the roll angle θ out of the orbital plane, the pitch angle ψ in the orbital plane, and the separation distance L become

$$\ddot{\theta} + 2\dot{\theta}\frac{\dot{L}}{L} + \cos\theta\sin\theta((\dot{\psi}+\Omega)^2 + 3\Omega^2\sigma\cos^2\psi) = 0 \tag{3.18a}$$

$$\ddot{\psi} - (\dot{\psi}+\Omega)(2\dot{\theta}\tan\theta - 2\frac{\dot{L}}{L}) + 3\Omega^2\sigma\sin\psi\cos\psi = 0 \tag{3.18b}$$

$$\ddot{L} - L(\dot{\theta}^2 + (\dot{\psi}+\Omega)^2\cos^2\theta - \Omega^2\sigma(1-3\cos^2\theta\cos^2\psi)) + \frac{k_c}{m_1}Q\frac{1}{L^2}\frac{m_1+m_2}{m_2} = 0 \tag{3.18c}$$

where $Q = q_1q_2$, $\nu = \frac{M_2}{M_1+M_2}$, $1-\nu = \frac{M_1}{M_1+M_2}$ and

$$\sigma = \frac{1-\nu}{|\frac{r_{x0}}{d}+\nu|^3} + \frac{\nu}{|\frac{r_{x0}}{d}-1+\nu|^3} > 0 \tag{3.19}$$

is a positive constant that depends on the collinear Lagrangian point chosen. The equations of motion Eq. (3.18) are coupled non-linear ordinary differential equations that define the motion of a two-craft Coulomb formation at any of the three collinear Lagrangian points.

If the two-craft formation is aligned in the radial direction, the formation remains statically fixed relative to the rotating orbiting frame $\mathcal{O}$ provided the non-linear equations Eq. (3.18) satisfy the following radial equilibrium conditions

$$\theta = \dot{\theta} = \ddot{\theta} = \psi = \dot{\psi} = \ddot{\psi} = \dot{L} = \ddot{L} = 0 \qquad \text{and} \qquad L = L_{\text{ref}} \tag{3.20}$$

Eq. (3.18c) provides the nominal product of charges $Q_{\text{ref}} = q_1q_2$ needed to achieve this static Coulomb formation as

$$Q_{\text{ref}} = -(2\sigma+1)\,\Omega^2\frac{L^3}{k_c}\frac{m_1m_2}{m_1+m_2} \tag{3.21}$$

Thus, the satellites appear frozen with respect to the rotating frame when the charge product Q_{ref} satisfies Eq. (3.21). Since the charge product term is negative it implies that the spacecraft charges will have opposite charge signs and also, an infinite number of charge pairs can satisfy $Q_{\text{ref}} = q_1q_2$. Although unequal charges are possible between the two crafts, in this study, the charge magnitudes are set equal.

The linearized version of the nonlinear equations Eq. (3.18) are obtained by applying a

Taylor series expansion about the equilibrium states given in Eq. (3.20). Both the roll and pitch equations of motion are linearized about small roll and pitch angles respectively. The separation distance equations of motion are linearized about small variations in δL as well as about small variations in the product charge term δQ as follows

$$L = L_{\text{ref}} + \delta L \tag{3.22a}$$

$$Q = Q_{\text{ref}} + \delta Q \tag{3.22b}$$

where mission requirements determine the reference separation length L_{ref}, and Q_{ref} is determined through the constraint Eq. (3.21) for a particular choice of L_{ref}. Performing the necessary linearizations yields

$$\ddot{\theta} + (1 + 3\sigma)\Omega^2\theta = 0 \tag{3.23a}$$

$$\ddot{\psi} + \frac{2\Omega}{L_{\text{ref}}}\delta\dot{L} + 3\sigma\Omega^2\psi = 0 \tag{3.23b}$$

$$\delta\ddot{L} - 2\Omega L_{\text{ref}}\dot{\psi} - 3(2\sigma + 1)\Omega^2\delta L - \left(\frac{k_c}{m_1}\frac{1}{L_{\text{ref}}^2}\frac{m_1 + m_2}{m_2}\right)\delta Q = 0 \tag{3.23c}$$

Thus, Eqs. (3.23a) and (3.23b) are the linearized attitude dynamics of the Coulomb tether body frame $\mathcal{B}$ and Eq. (3.23c) is the linearized separation distance differential equation about the static nadir reference configuration at a collinear libration point.

Interestingly, for "$\sigma = 1$", the equations turn out to be the same equations that were found in Reference 5 for orbit radial 2-craft formation at GEO. Thus, the linearized equations of motion for small motions about orbit radial equilibria in Eqs. (3.23) form a general framework that covers both circular GEO and collinear libration point departure motion. By changing the constant σ either motion is described. Furthermore, in Eq. (3.23c) the stiffness term on δL is the only difference in the separation distance differential equation from Reference 5. Thus, the equations of motion are slightly different at a collinear libration point, but no significant changes in the stability behavior are expected. And, note that Eq. (3.23c) provides the necessary relationship between the change in relative separation of the satellites δL and the additional charge product δQ required.

It is inferred from these equations that the out-of-plane motion $\theta(t)$ is uncoupled from the in-plane motion ($\psi(t)$ and $\delta L(t)$) and is analogous to that of simple oscillatory motion because of the gravity gradient torques due to the two planets. Also, in this linearized analysis, the decoupling of the roll motion $\theta(t)$ from $\psi(t)$, $\delta L(t)$ and $\delta Q(t)$ prevents the control of roll motion using Coulomb charge. Moreover, in a special case where the satellites are at rest with no Coulomb force between them ($Q = \delta Q(t) = \dot{\psi} = 0$), Eq. (3.23c) simplifies to that of an unstable oscillator. Therefore, without any active Coulomb force, the two-craft formation cannot stay at the specified locations. Furthermore, $\delta L(t)$ is coupled to the body frame pitch rate $\dot{\psi}(t)$ and the pitch motion $\psi(t)$ is coupled with the $\delta L(t)$) motion which may make it possible to control the charge for asymptotic stabilization. This coupling effect is analytically proven in the next section using the controllability properties.

3.1.2 Feedback Control Development

Under the influence of external disturbances such as solar radiation pressure, the two-craft formation deviates from the desired radial equilibrium configuration. Because the deviations from the desired equilibrium configuration are small, linear control design techniques are used to stabilize the in-plane motion without exceeding the charge requirements. In this section, two control laws are designed and compared which are used to control the in-plane motion. First, the in-plane motion is controlled with Coulomb forces using a partial-state charge feedback control defining the small charge product variation with a proportional-derivative feedback control of small separation distances. The Coulomb force acts along the relative position vector due to the charges of each craft and thus, these Coulomb charges can be used to control the spacecraft separation distance. Second, using state space methods, a full-state feedback control is designed to control the combined attitude and separation distance. Full-state feedback control could be used for tighter mission requirements.

3.1.2.1 Charge Feedback Control

A proportional-derivative feedback control of δL is designed by defining[5]

$$\delta Q = \frac{m_1 m_2 L_{\text{ref}}^2}{(m_1 + m_2)\, k_c}(-C_1 \delta L - C_2 \delta \dot{L}) \tag{3.24}$$

Substituting this expression for δQ in Eq. (3.23c), the closed-loop separation distance dynamics become

$$\delta \ddot{L} + (C_1 - 3(2\sigma + 1)\Omega^2)\delta L + C_2 \delta \dot{L} - (2\Omega L_{\text{ref}})\dot{\psi} = 0 \tag{3.25}$$

Since the δL differential equation does not involve a $\delta \dot{L}$ damping term, the derivative feedback is essential for asymptotic convergence. This charge feedback control law is implemented by determining the charges q_1 and q_2. Since $Q = q_1 q_2$, using Eq. (3.22b), the spacecraft charges must satisfy

$$q_1 q_2 = Q_{\text{ref}} + \delta Q \tag{3.26}$$

where Q_{ref} value is evaluated from Eq. (3.21) while δQ value is given by the charge feedback law expression in Eq. (3.24). Due to the above constraint yielding an infinite number of solutions, the following implementation is used where equal charges in magnitude across the craft are chosen.

$$q_1 = \sqrt{|Q_{\text{ref}} + \delta Q|} \tag{3.27}$$

$$q_2 = -q_1 \tag{3.28}$$

Because $\delta Q \ll Q_{\text{ref}}$ and $Q_{\text{ref}} < 0$, note that here $Q_{\text{ref}} + \delta Q < 0$ which implies that $q_1 > 0$ and $q_2 < 0$.

In order to prevent numerical difficulties due to a small value of Ω, the linearized attitude dynamics Eqs. (3.23a) - (3.23b) and the closed loop separation distance dynamics given in

Eq. (3.25) are made independent of Ω by the following transformation

$$\mathrm{d}\tau = \Omega \mathrm{d}t \tag{3.29a}$$

$$(*)^{'} = \frac{\mathrm{d}(*)}{\mathrm{d}\tau} = \frac{1}{\Omega}\frac{\mathrm{d}(*)}{\mathrm{d}t} \tag{3.29b}$$

Thus, the orbit rate (Ω) independent linearized equations of motion for a two-craft Coulomb tether formation at any collinear libration point are given by

$$\theta^{''} + (1+3\sigma)\,\theta = 0 \tag{3.30a}$$

$$\psi^{''} + \frac{2}{L_{\text{ref}}}\delta L^{'} + 3\sigma\psi = 0 \tag{3.30b}$$

$$\delta L^{''} + \tilde{C}_2\delta L^{'} - (2L_{\text{ref}})\psi^{'} + (\tilde{C}_1 - 3(2\sigma+1))\delta L = 0 \tag{3.30c}$$

where $\tilde{C}_2 = \frac{C_2}{\Omega}$ and $\tilde{C}_1 = \frac{C_1}{\Omega^2}$ are non-dimensionalized feedback gains. Routh-Hurwitz stability criteria are used to fine tune these gain values that satisfy the stability requirements. The characteristic equation for the coupled δL and ψ equation is

$$\lambda^4 + \tilde{C}_2\lambda^3 + (\tilde{C}_1 + 1 - 3\sigma)\lambda^2 + 3\sigma\tilde{C}_2\lambda + 3\sigma(\tilde{C}_1 - 6\sigma - 3) = 0 \tag{3.31}$$

Roots of Eq. (3.31) should have negative real parts for asymptotic stability. For all roots to have negative real parts, a Routh table construction allows one to determine the following necessary constraints on the gains $\tilde{C}_1$ and $\tilde{C}_2$

$$\tilde{C}_1 > 6\sigma + 3 \tag{3.32a}$$

$$\tilde{C}_2 > \sqrt{n - 3(2\sigma+1)} \tag{3.32b}$$

To fix the gain values that satisfy the stability criteria in Eq. (3.32), near ideal damping conditions are assumed. Let the scaling factors n and β be positive and real such that the gains are rewritten as

$$\tilde{C}_1 = n > 6\sigma + 3 \tag{3.33a}$$

$$\tilde{C}_2 = \beta\sqrt{n - 3(2\sigma + 1)} \tag{3.33b}$$

The natural frequency of the ψ equation is $\sqrt{3\sigma}$ and is independent of the choice of $\tilde{C}_1$ and $\tilde{C}_2$, and the natural frequency for the δL equation is $\sqrt{n - 3(2\sigma + 1)}$. For the ψ' coupling term in the δL equation to serve as a defacto damping term, a value of $n = 9\sigma + 3$ will match these frequencies. Also, critical damping for the δL equation without the ψ' term is ensured for $\beta = 2$. Therefore, with the inclusion of the ψ' term for effective damping, one expects the value of n and β to be in the vicinity of $n = 9\sigma + 3$ and $\beta = 2$. At L_2 where $\sigma = 3.190432478$, the root locus plots for the coupled equations where the parameters are varied, $n = 26$ ensures good rates of convergence for all the modes and $\beta = 2.22$ satisfies effective damping for the modes. The optimal root locus plot is shown in Figure 3.4.

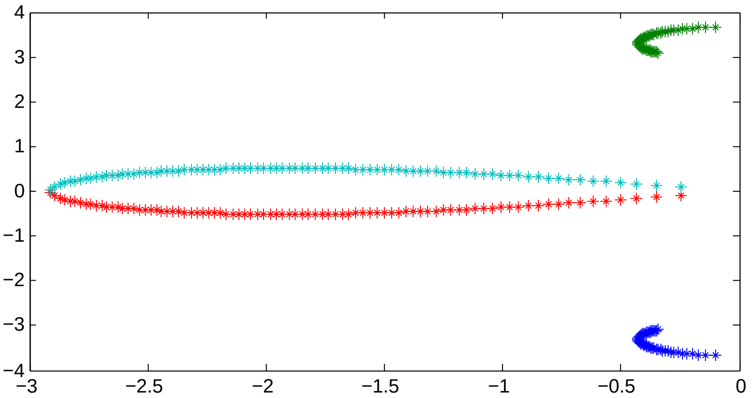

Figure 3.4: Root-Locus Plot of the Linearized Differential Equations at L_2 for gain $\beta = 2.22$

3.1.2.2 Application of LQR Design

In order to investigate the stability and control using the state feedback controller, a two-craft Coulomb tether formation at a collinear libration point must be represented in the following state space form

$$\dot{\boldsymbol{x}} = \boldsymbol{A}\boldsymbol{x} + \boldsymbol{B}\boldsymbol{u} \tag{3.34}$$

$$\boldsymbol{y} = \boldsymbol{C}\boldsymbol{x} \tag{3.35}$$

where the state $\boldsymbol{x}$ is

$$\boldsymbol{x} = \left[\theta, \dot{\theta}, \psi, \dot{\psi}, \delta L, \dot{\delta L}\right]^T \tag{3.36}$$

Using the Coulomb control as an actuator mechanism, the $\boldsymbol{A}$ and $\boldsymbol{B}$ matrices can be represented from Eqs. (3.23a) - (3.23c). As previously seen, the out-of-plane $\theta(t)$ motion is decoupled from the in-plane motion ($\psi(t)$ and $\delta L(t)$), which can be formally examined by checking the *controllability* of the system.[49] Since the rank of the controllability matrix is 4 and the number of state variables is 6, the tether formation is not completely controllable with charge only. When the out-of-plane $\theta(t)$ motion is not considered, then, with the reduced state space of four state variables $\boldsymbol{x} = \left[\psi, \dot{\psi}, \delta L, \dot{\delta L}\right]^T$, the rank of the controllability matrix is 4. Therefore, subsequent analysis uses the following reduced $\boldsymbol{A}$ and $\boldsymbol{B}$ matrices

$$\boldsymbol{A} = \begin{bmatrix} 0 & 1 & 0 & 0 \\ -3\sigma & 0 & 0 & -\frac{2}{L_{\text{ref}}} \\ 0 & 0 & 0 & 1 \\ 0 & 2L_{\text{ref}} & 3(2\sigma+1) & 0 \end{bmatrix} \tag{3.37}$$

$$\boldsymbol{B} = \begin{bmatrix} 0 & 0 & 0 & \frac{k_c}{m_1}\frac{1}{L_{\text{ref}}^2}\frac{m_1+m_2}{m_2} \end{bmatrix}^T \tag{3.38}$$

If only the length and length rate state variables are available from the measurements of an optical sensor, then the remaining two state variables (pitch and pitch rate) must be estimated from the output measurements. Therefore, the $\boldsymbol{C}$ matrix in the output equation becomes

$$\boldsymbol{C} = \begin{bmatrix} 0 & 0 & 1 & 0 \\ 0 & 0 & 0 & 1 \end{bmatrix} \tag{3.39}$$

However, the $\boldsymbol{C}$ matrix should satisfy the *observability* condition.[49] Because the rank of the observability matrix is 4, the values of the ψ and $\dot{\psi}$ states can be estimated from the measured outputs δL and $\dot{\delta L}$. Hence, the in-plane linear model of a two-craft Coulomb tether formation at a collinear libration point is both controllable and observable.

Assuming that the information about all four state variables is available either through direct measurement or by estimation, the following feedback control is used to control the system with the feedback gain matrix, $\boldsymbol{K}$, computed using either the pole placement method or the linear quadratic regulator (LQR) method.

$$\boldsymbol{u} = -\boldsymbol{K}\boldsymbol{x} \tag{3.40}$$

Here the LQR methodology is applied to determine the optimal control, $\boldsymbol{u}$, such that the gain vector $\boldsymbol{K}$ minimizes the performance index

$$J = \int_0^\infty (\boldsymbol{x}^T \boldsymbol{W_Q} \boldsymbol{x} + \boldsymbol{u}^T \boldsymbol{W_R} \boldsymbol{u}) dT \tag{3.41}$$

where $\boldsymbol{W_Q}$ and $\boldsymbol{W_R}$ are the weighting matrices that are used as design parameters. One can establish a faster response for in-plane control by selecting appropriate weighting matrices for which the settling time is less than one orbit.

3.1.3 Numerical Simulation

The performance and stability of a 25m Coulomb virtual tether formation is illustrated in the following numerical simulation. Table 3.1 lists the simulation parameters and the values used. The parameters n and β are selected based on root locus plot analysis where the gains $\tilde{C}_1$ and $\tilde{C}_2$ computed from Eq. (3.33) satisfy the stability criteria in Eq. (3.32) and also lead to effective damping. The two-craft Coulomb tether performance at the collinear libration point L_2 is simulated by integrating the linearized equations of motion in Eq. (3.30) and then compared with the results obtained from integrating the non-linear equations of motion in Eq. (3.18). During this simulation, the Debye length is assumed to be zero in order to investigate the effects of linearization on the relative motion.

Table 3.1: Input Parameters Used in the Simulation for L_2

Parameter	Value	Units
m_1	150	kg
m_2	150	kg
L_{ref}	25	m
k_c	8.99×10^9	$\frac{\text{Nm}^2}{\text{C}^2}$
Q_{ref}	-0.006816	μC^2
Ω	2.661699×10^{-6}	rad/sec
$\delta L(0)$	0.5	m
$\psi(0)$	0.1	rad
$\theta(0)$	0.1	rad
n	26	
β	2.22	
σ	3.190432478	

Figure 3.5(a) shows the Coulomb tether motion with the proportional-derivative charge feedback law in Eq. (3.24). Both the pitch motion ψ and the separation distance deviation δL converged to zero. Therefore, stabilizing the separation distance to zero also stabilized the in-plane rotation angle after about 1.3 orbits; and the uncoupled roll motion θ is a stable sinusoidal motion as expected. Furthermore, Figure 3.5(a) shows that the non-linear simulation shown as dashed lines closely follows the linearized simulation. Whereas, the δL states asymptotically converge to zero in the linearized simulation, they reach steady state oscillations in the non-linear simulation. This notable difference is observed in the two-body system as well.[5] Using the same reference charge product Q_{ref} computed from Eq. (3.24) for both simulations resulted in this inconsistent behaviour. This charge yields a static formation in the linearized formulation; however, in the non-linear formulation, this charge will not yield a static formation. This is due to the charge feedback control not operating about a steady state charge in the non-linear problem. Although the δL and ψ errors converge

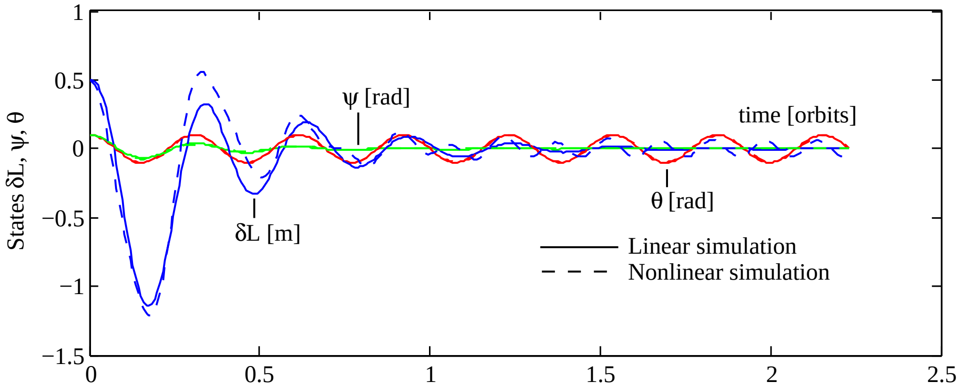

(a) Time Histories of Length Variations δL, In-plane Pitch Angle ψ, and Out-of-plane Roll Angle θ

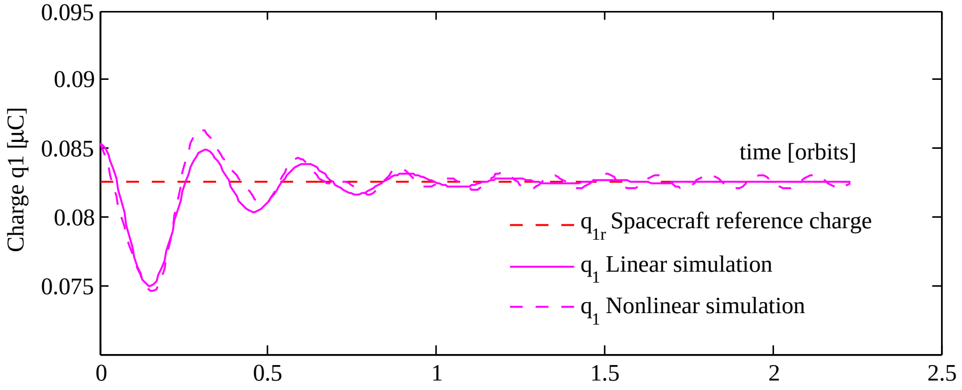

(b) Spacecraft Charge Time Histories

Figure 3.5: Simulation Results from Integrating the Linearized and Nonlinear Equations of Motion at L_2

to zero in the non-linear simulation, the discrepancies in charge computation between the linear and non-linear simulations cause the orbital dynamics to perturb the system.[5] This makes the states grow again, resulting in these steady state oscillations. Therefore, for the non-linear problem, a control strategy could be implemented wherein the Q_{ref} value could be numerically recomputed. Despite this deviation, the non-linear and linear simulation results compare very well, thus validating the performance prediction of the linearized analysis.

Figure 3.5(b) shows the spacecraft control charge q_1 usage for both the linear and non-linear simulation formulations. The charge results for both converge to the static equilibrium reference value q_{1r}. For orbit-radial equilibrium, the control charge q_1 is the negative of q_2. Since the control charges are on the order of micro-Coulombs, they can easily be implemented in practice using charge emission devices.

A numerical simulation using an optimal regulator results in a settling time of less than one orbit, a maximum overshoot of less than ±2.5 m in separation distance and ±.1 rad in pitch angle variation. A faster response for in-plane control than that of a charge feedback control law can be obtained by selecting appropriate $\boldsymbol{W_Q}$ and $\boldsymbol{W_R}$ weighting matrices. The following $\boldsymbol{W_Q}$ and $\boldsymbol{W_R}$ matrices allow the settling time to be less than one orbit

$$\boldsymbol{W_Q} = \begin{bmatrix} 75 & 0 & 0 & 0 \\ 0 & 0.0001 & 0 & 0 \\ 0 & 0 & 0.1 & 0 \\ 0 & 0 & 0 & 0.000001 \end{bmatrix} \quad \text{and} \quad \boldsymbol{W_R} = 10000 \tag{3.42}$$

Figure 3.6 shows the state response of the system for the LQR method. The results indicate that with the acceptable limits for separation distance and attitude variations, the settling time is around one orbit. However, the maximum overshoot increases the charge requirements as compared to using the charge feedback law in Eq.(3.24). For subsequent analysis, we use the charge control law because of the minimal number of control variables used in it.

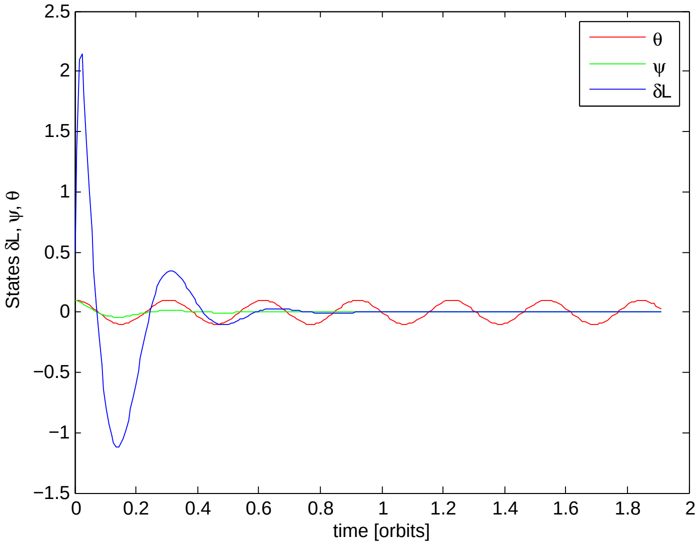

Figure 3.6: LQR Time Histories of Length Variations δL, pitch angle ψ and roll angle θ

3.2 Linear Dynamics and Stability Analysis - Triangular Libration Points

3.2.1 Charged Relative Equations of Motion

This section derives the equations of motion of a two-craft Coulomb tether whose center of mass is at the triangular equilibrium point L_4 as shown in Figure 3.7 and nominally aligned in the orbit-radial direction of the orbit frame. This derivation closely resembles the derivation of the equations of motion for a two-craft Coulomb tether at any collinear libration point given in section 3.1 The two distance vectors $\boldsymbol{R}_1$ and $\boldsymbol{R}_2$ of L_4 in the synodic frame from the two primaries in the plane are given by

$$^{\mathcal{S}}\boldsymbol{R}_1 = \begin{bmatrix} r_{x_0} + d_1 \\ r_{y_0} \\ 0 \end{bmatrix} \quad \text{and} \quad ^{\mathcal{S}}\boldsymbol{R}_2 = \begin{bmatrix} r_{x_0} - d_2 \\ r_{y_0} \\ 0 \end{bmatrix} \tag{3.43}$$

The expressions for the kinetic energy in Eq. (3.10) and Coulomb potential in Eq. (3.16) remain the same. However, the gravitational potential in Eq. (3.15) involves adding the two position vectors $\boldsymbol{R}_i + \boldsymbol{\rho}_i$, where $\boldsymbol{R}_i$ is in the synodic frame $\mathcal{S}$ and $\boldsymbol{\rho}_i$ is in the orbiting frame $\mathcal{O}$. Therefore, the vectors $\boldsymbol{R}_i$ are expressed in its orbiting frame components using the transformation $^{\mathcal{O}}\boldsymbol{R}_i = [OS]^{\mathcal{S}}\boldsymbol{R}_i$ with the transformation matrix $[OS]$ given by

$$[OS] = \begin{bmatrix} \cos\alpha & \sin\alpha & 0 \\ -\sin\alpha & \cos\alpha & 0 \\ 0 & 0 & 1 \end{bmatrix} \tag{3.44}$$

where α is the angle between the synodic frame at the barycenter O and the orbiting frame at L_4 as shown in Figure 3.7. For Earth-moon system, the value of α is 60.31 degrees.[16]

Using the Lagrangian formulation in Eq. (3.17), the nonlinear equations governing the roll angle θ out of the orbital plane, the pitch angle ψ in the orbital plane, and the separation

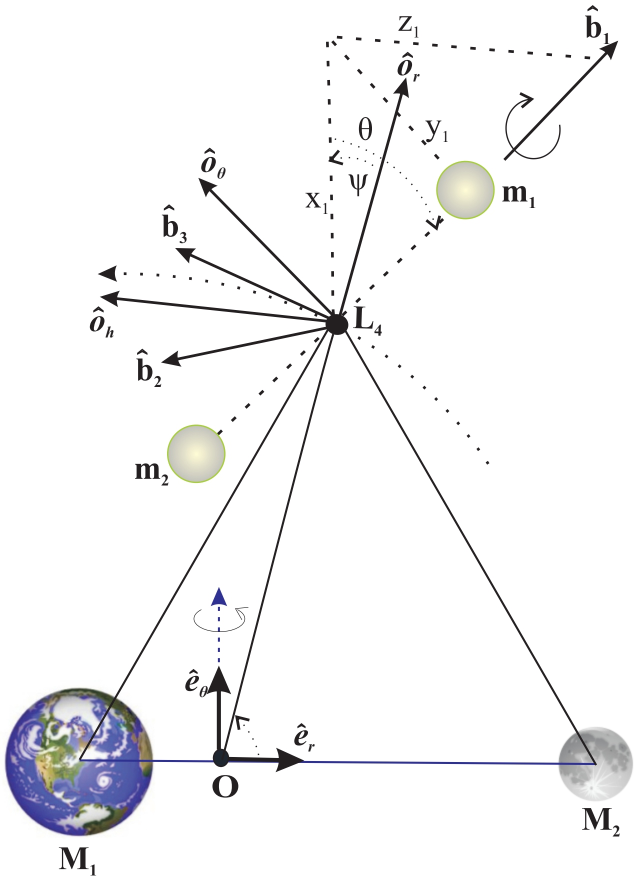

Figure 3.7: Euler Angles Representing the Attitude of Coulomb Tether with Respect to the Orbit Frame at L_4

distance L thus obtained are

$$\begin{aligned}
&\ddot{\theta}+\frac{2\dot{L}}{L}\dot{\theta}+\cos\theta\,\sin\theta((\dot{\psi}+\Omega)^2\\
&\quad+\frac{3\Omega^2}{4}((1-\nu)(A_\alpha\,\cos\psi+B_\alpha\,\sin\psi)^2+\nu(C_\alpha\,\cos\psi+D_\alpha\,\sin\psi)^2))=0 \qquad (3.45a)\\
&\ddot{\psi}-2\dot{\theta}\tan\theta(\dot{\psi}+\Omega)+\frac{2\dot{L}}{L}(\dot{\psi}+\Omega)-\frac{3}{4}\Omega^2((1-\nu)(A_\alpha B_\alpha\,\cos 2\psi+\frac{B_\alpha^2-A_\alpha^2}{2}\sin 2\psi)\\
&\quad+\nu(C_\alpha D_\alpha\,\cos 2\psi+\frac{D_\alpha^2-C_\alpha^2}{2}\sin 2\psi))=0 \qquad (3.45b)\\
&\ddot{L}-L(\dot{\theta}^2+(\dot{\psi}+\Omega)^2\cos^2\theta-\Omega^2)\\
&\quad+\frac{3}{4}L\Omega^2\cos^2\theta((1-\nu)(A_\alpha\,\cos\psi+B_\alpha\,\sin\psi)^2+\nu(C_\alpha\,\cos\psi+D_\alpha\,\sin\psi)^2)\\
&\quad-k_c\frac{m_1+m_2}{m_1m_2}q_1q_2e^{-L/\lambda d}\left(\frac{L+\lambda_d}{L^2\lambda_d}\right)=0 \qquad (3.45c)
\end{aligned}$$

where

$$A_\alpha = \cos\alpha + \sqrt{3}\sin\alpha \tag{3.46a}$$

$$B_\alpha = -\sin\alpha + \sqrt{3}\cos\alpha \tag{3.46b}$$

$$C_\alpha = -\cos\alpha + \sqrt{3}\sin\alpha \tag{3.46c}$$

$$D_\alpha = \sin\alpha + \sqrt{3}\cos\alpha \tag{3.46d}$$

The linearized version of the nonlinear equations in Eq. (3.45) comes from expanding in a Taylor series about the equilibrium states given in Eq. (3.20). Both the roll and pitch equations of motion are linearized about small roll and pitch angles respectively. The separation distance equations of motion are linearized about small variations in δL as well as small variations in the product charge term δQ defined as in Eq. (3.22). Mission requirements determine the reference separation length L_{ref}, and, Q_{ref} is determined from the following constraint on a particular choice of L_{ref}

$$Q_{\text{ref}} = -\frac{3}{4}\sigma_{EQRE1}\Omega^2 \frac{L_{\text{ref}}^3}{k_c}\frac{m_1 m_2}{m_1+m_2} \tag{3.47}$$

where

$$\sigma_{EQRE1} = 1 + 2\sin^2\alpha + \sqrt{3}\sin 2\alpha\,(1-2\nu) \tag{3.48}$$

Performing the necessary linearizations yields

$$\ddot{\theta} + (1 + \frac{3}{4}\sigma_{EQRE1})\Omega^2\theta = 0 \tag{3.49a}$$

$$\ddot{\psi} + \frac{2\Omega}{L_{\text{ref}}}\delta\dot{L} - \frac{3}{2}\sigma_{EQRE3}\Omega^2\,\psi = 0 \tag{3.49b}$$

$$\delta\ddot{L} - 2\Omega L_{\text{ref}}\dot{\psi} - \frac{9}{4}\sigma_{EQRE1}\Omega^2\delta L - \frac{3}{2}L_{\text{ref}}\,\sigma_{EQRE2}\Omega^2\,\psi - (\frac{k_c}{m_1}\frac{1}{L_{\text{ref}}^2}\frac{m_1+m_2}{m_2})\delta Q = 0 \tag{3.49c}$$

with

$$\sigma_{EQRE2} = \sqrt{3}\cos 2\alpha\,(1-2\nu) + \sin 2\alpha \tag{3.50}$$

$$\sigma_{EQRE3} = \sqrt{3}\sin 2\alpha\,(2\nu-1) + \cos 2\alpha \tag{3.51}$$

Thus, Eqs. (3.49a) and (3.49b) represent the linearized attitude dynamics of the Coulomb tether body frame $\mathcal{B}$ and Eq. (3.49c) represents the linearized separation distance differential equation about the static nadir reference configuration at a triangular libration point. As opposed to the collinear solution, the ψ term here is a new component; however, due to the quite small value of $\sigma_{EQRE2} = -2.0405 \times 10^{-4}$ at L_4, its effect is negligible on the separation distance differential equation. Furthermore, since $\sigma_{EQRE1} = 3.963662$ and $\sigma_{EQRE3} = -1.963662$, the dynamics at L_4 become very similar to those found in Reference 5 for an orbit radial 2-craft formation at GEO. Hence, the stability behaviour should be approximately the same as that observed in Reference 5.

3.2.2 Charge Feedback Control

Using the proportional-derivative feedback control of δL from Eq.(3.24), the orbit rate Ω independent linearized equations of motion for a two-craft Coulomb tether formation at the triangular libration point L_4 are given by

$$\theta'' + (1 + \frac{3}{4}\sigma_{EQRE1})\theta = 0 \tag{3.52a}$$

$$\psi'' + \frac{2}{L_{\text{ref}}}\delta L' - \frac{3}{2}\sigma_{EQRE3}\,\psi = 0 \tag{3.52b}$$

$$\delta L'' + \tilde{C}_2\,\delta L' - (2L_{\text{ref}})\psi' - (\frac{3}{2}L_{\text{ref}}\,\sigma_{EQRE2}\,)\psi - (\frac{9}{4}\sigma_{EQRE1} - \tilde{C}_1)\delta L = 0 \tag{3.52c}$$

where $\tilde{C}_2 = \frac{C_2}{\Omega}$ and $\tilde{C}_1 = \frac{C_1}{\Omega^2}$ are non-dimensionalized feedback gains. Routh-Hurwitz stability criteria can be used to fine tune these gain values that satisfy the stability requirements.

The characteristic equation for the coupled δL and ψ equation is

$$\begin{aligned}\lambda^4 + \tilde{C}_2\lambda^3 + (\tilde{C}_1 + 4 - \frac{3}{2}\sigma_{EQRE3} - \frac{9}{4}\sigma_{EQRE1})\lambda^2 + (3\sigma_{EQRE2} - \frac{3}{2}\sigma_{EQRE3}\tilde{C}_2)\lambda \\ + \frac{3}{2}\sigma_{EQRE3}(\frac{9}{4}\sigma_{EQRE1} - \tilde{C}_1) = 0\end{aligned} \tag{3.53}$$

Roots of this equation should have negative real parts for asymptotic stability. A Routh table allows one to determine the following necessary constraints on the gains $\tilde{C}_1$ and $\tilde{C}_2$ that ensures all roots have negative real parts

$$\tilde{C}_1 > \frac{9}{4}\sigma_{EQRE1} \tag{3.54a}$$

$$\tilde{C}_2 > 0 \tag{3.54b}$$

To fix the gain values that satisfy the stability criteria in Eq. (3.54), near ideal damping conditions are assumed. Let the scaling factors n and β be positive and real, allowing the gains to be rewritten as

$$\tilde{C}_1 = n > \frac{9}{4}\sigma_{EQRE1} \tag{3.55a}$$

$$\tilde{C}_2 = \beta\sqrt{n - \frac{9}{4}\sigma_{EQRE1}} \tag{3.55b}$$

Following the same line of reasoning discussed for collinear libration points earlier and studying the root locus plots for the coupled equations where the n and β parameters are varied, $n = 11.71$ ensures good rates of convergence for all the modes and $\beta = 2.22$ provides effective damping for the modes. The optimal root locus plot is shown in Figure 3.8.

3.2.3 Numerical Simulation

Except for the parameters listed in Table 3.2, the remaining simulation parameter values used are shown in Table 3.1. The parameter $n = 11.71$ for L_4 is obtained from the root locus plot analysis. The gains $\tilde{C}_1$ and $\tilde{C}_2$ computed from Eq. (3.55) satisfy the stability criteria in Eq. (3.54) and also yield effective damping. Integrating the linearized equations of motion in Eq. (3.52) simulates the two-craft Coulomb tether performance at L_4. This is then compared

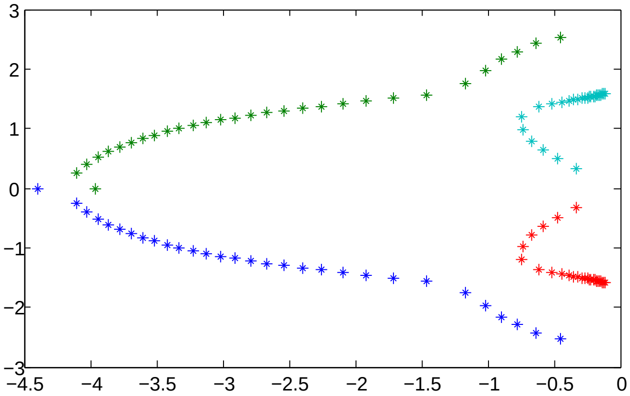

Figure 3.8: Root-Locus Plot of the Linearized Differential Equations at L_4 for gain $\beta = 2.22$

Table 3.2: Input Parameters Used in the Simulation for L_4

Parameter	Value	Units
Q_{ref}	-0.002745	μC^2
n	11.71	
β	2.22	
σ_{EQRE1}	3.963662	
σ_{EQRE2}	-2.0405×10^{-4}	
σ_{EQRE3}	-1.963662	

with the results obtained from integrating the non-linear equations of motion in Eq. (3.45). Figure 3.9(a) illustrates the Coulomb tether motion with the proportional-derivative charge feedback law. Both the yaw motion ψ and the separation distance deviation δL converge to zero. Therefore, stabilizing the separation distance to zero also stabilized the in-plane rotation angle after about 1 orbit; and the uncoupled roll motion θ is a stable sinusoid as expected. Furthermore, Figure 3.9(a) shows that the non-linear simulation plotted as dashed lines closely follows the linearized simulation; whereas the δL states asymptotically converge to zero in the linearized simulation, they reach steady state oscillations in the non-linear simulation. The reasons for this notable difference are already explained in numerical simulation part of section 3.1 Despite this difference, the non-linear and linear simulation results compare very well, thus justifying the linearization assumptions used. Figure 3.9(b) shows

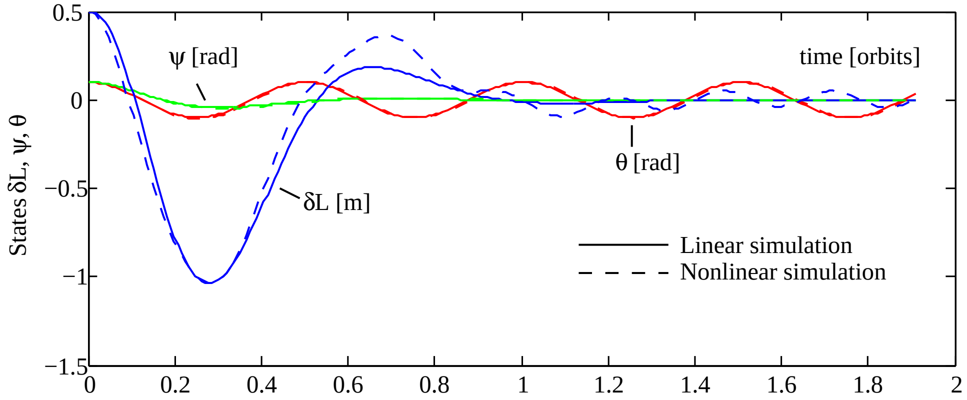

(a) Time Histories of Length Variations δL, In-plane Pitch Angle ψ, and Out-of-plane Roll Angle θ

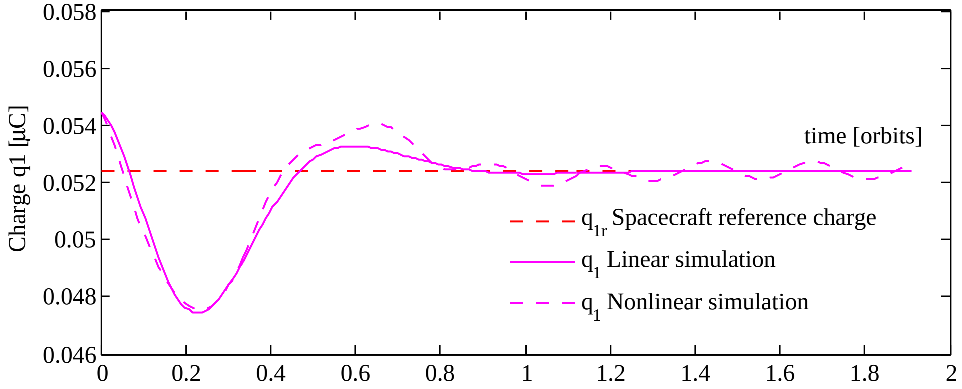

(b) Spacecraft Charge Time Histories

Figure 3.9: Simulation Results from Integrating the Linearized and Nonlinear Equations of Motion at L_4

the spacecraft control charge q_1 usage for both linear and non-linear simulation formulations. The charge results for both converge to the static equilibrium reference value q_{1r}. The control charges required for L_4 are less than those of L_2, which are on the order of micro-Coulombs and can easily be implemented in practice using charge emission devices.

3.3 Differential Solar Perturbation

Differential solar drag is the largest disturbance acting on a tether formation at GEO and at libration points (Sun-Earth or Earth-Moon).[7,48] For example, on a typical micro-craft in Earth orbit the maximum solar torque magnitude of about 10^{-5} Nm is essentially constant with orbit altitude.[51] The gravity gradient torque is inversely proportional to the orbit radius cubed, but in low orbits has a maximum magnitude on the order of solar torque, and above an altitude of about 20,000 kilometers it becomes relatively insignificant (less than 1%).[51] Therefore, at libration point distances, in the presence of a differential solar drag on the formation, the gravity gradient torques may no longer be sufficient to stabilize the in-plane motion of a 2-craft virtual Coulomb structure in the radial equilibrium position. Moreover, in the presence of differential solar drag on a two craft Coulomb formation in circular orbits, Reference 5 shows that the states are bounded with the charge feedback law. These limitations motivate to study the nonlinear dynamics and stability analysis of an orbit-radial two-craft Coulomb formation about circular orbits and at Earth-Moon libration points.

References 54 and 55 use a Lyapunov approach for tether deployment and retrieval in circular orbits. In their study, tether mass and flexibility, solar radiation pressure as well as aerodynamic effects are neglected. The Lyapunov feedback control method use a Lyapunov function based on a first integral of motion of the dynamical system. The control laws are simple and utilize tether tension control as well as out-of-plane thrusting. In this section, a similar approach is taken to stabilize the formation shape and size in circular orbits and at the libration points in the presence of differential solar radiation pressure affects. The goal is to design a generic Lyapunov feedback controller that can withstand differential solar perturbation effects and to asymptotically stabilize an orbit radial 2-craft Coulomb structure about circular orbits and collinear libration points. The environmental torques due to gravity gradient forces and solar radiation pressure affects at GEO and at Earth-Moon libration points are discussed. Of interest is to study if the gravity gradient forces on a radial equilibrium two-craft Coulomb tether formation are sufficient to withstand the differential solar drag affects. Numerical results show the gravity gradient and differential solar drag force magnitudes on the formation. Finally, a generic controller is designed that can withstand differential solar perturbation effects in orbit radial configuration about circular orbits and at Earth-Moon collinear libration points. Numerical simulations validate the Lyapunov controller performance.

3.3.1 Environmental Torques - GEO and Libration Points

This section discusses environmental torques due to gravity gradient and solar radiation pressure effects on a two-craft formation. The gravity gradient torque expressions and solar radiation pressure models at GEO and at Earth-Moon libration points are presented. To study whether the gravity gradient forces on a radial equilibrium two-craft Coulomb tether formation are sufficient to withstand the solar drag affects, the magnitudes of gravity gradient forces at GEO heights and libration point distances are compared against the differential solar drag forces on the formation. Numerical results show the gravity gradient and differential solar drag force magnitudes on the formation at GEO and at Earth-Moon libration points.

3.3.1.1 Gravity Gradient Torques

The gravity gradient torque expression at GEO is obtained from[14]

$$ {}^{\mathcal{B}}\boldsymbol{L}_G = \begin{bmatrix} L_{G_1} \\ L_{G_2} \\ L_{G_3} \end{bmatrix} = \frac{3GM_e}{r_c^5} \begin{bmatrix} r_{c2}r_{c3}(I_{33}-I_{22}) \\ r_{c1}r_{c3}(I_{11}-I_{33}) \\ r_{c1}r_{c2}(I_{22}-I_{11}) \end{bmatrix} \tag{3.56} $$

where r_{c1}, r_{c2} and r_{c3} are the $\mathcal{B}$ frame components of a two-craft formation center of mass position vector $\boldsymbol{r}_c$ in GEO. G is the gravity constant and M_e is the mass of the planet Earth. The body frame inertia matrix of a two-craft formation in radial equilibrium is[5]

$$ {}^{\mathcal{B}}[I] = \begin{bmatrix} 0 & 0 & 0 \\ 0 & I & 0 \\ 0 & 0 & I \end{bmatrix} \tag{3.57} $$

where $I = \frac{m_1 m_2}{m_1+m_2}L^2$ and m_1, m_2 are the masses of the two spacecraft.

Using Eq. (3.56), the gravity gradient torque of a radial equilibrium two-craft Coulomb tether formation at GEO becomes

$$^{\mathcal{B}}\boldsymbol{L}_G = 3\Omega^2 \begin{bmatrix} 0 \\ -I\cos\theta\sin\theta\cos^2\psi \\ -I\cos\theta\cos\psi\sin\psi \end{bmatrix} \tag{3.58}$$

where $\Omega^2 = \frac{\mu}{r_c^3}$ with $\mu = GM_e$.

Similarly, the gravity gradient torque expression at libration points is

$$^{\mathcal{B}}\boldsymbol{L}_G = \begin{bmatrix} L_{G_1} \\ L_{G_2} \\ L_{G_3} \end{bmatrix} = \frac{3GM_1}{r_c^5} \begin{bmatrix} r_{c2}r_{c3}(I_{33} - I_{22}) \\ r_{c1}r_{c3}(I_{11} - I_{33}) \\ r_{c1}r_{c2}(I_{22} - I_{11}) \end{bmatrix} + \frac{3GM_2}{r_c^{'5}} \begin{bmatrix} r'_{c2}r'_{c3}(I_{33} - I_{22}) \\ r'_{c1}r'_{c3}(I_{11} - I_{33}) \\ r'_{c1}r'_{c2}(I_{22} - I_{11}) \end{bmatrix} \tag{3.59}$$

where r_{c1}, r_{c2}, r_{c3} and r'_{c1}, r'_{c2} and r'_{c3} are the $\mathcal{B}$ frame components of a two-craft formation center of mass position vectors $\boldsymbol{r}_c$ and $\boldsymbol{r}'_c$ at a collinear libration point from the two primaries in the plane.

Using Eq. (3.59), the gravity gradient torque of a radial equilibrium two-craft Coulomb tether formation at a collinear libration point becomes

$$^{\mathcal{B}}\boldsymbol{L}_G = 3(\Omega_1^2 + \Omega_2^2) \begin{bmatrix} 0 \\ -I\cos\theta\sin\theta\cos^2\psi \\ -I\cos\theta\cos\psi\sin\psi \end{bmatrix} \tag{3.60}$$

where $\Omega_1^2 = \frac{\mu_1}{r_c^3}$ and $\Omega_1^2 = \frac{\mu_2}{r_c^{'3}}$ with $\mu_1 = GM_1$ and $\mu_2 = GM_2$.

3.3.1.2 Solar Radiation Pressure (SRP)

At GEO, the inertial acceleration vector $\boldsymbol{a}_{\text{SRP}}$ in m/s^2 due to the effects of solar radiation pressure (SRP) is given as[5,50]

$$\boldsymbol{a}_{\text{SRP}} = -\frac{C_r A F}{mc}\frac{\boldsymbol{r}}{\|\boldsymbol{r}\|^3} \tag{3.61}$$

where $\boldsymbol{a}_{\text{SRP}}$ is the inertial position vector from the sun to the orbiting planet in AU, m is the mass of the spacecraft in kg, and A is the cross-sectional area of the spacecraft that is facing the sun in m^2. The constant $F = 1372.5398$ Watts/m^2 is the solar radiation flux, $c = 299792458$ m/s is the speed of light, and $C_r = 1.3$ is the radiation pressure coefficient. To compare the results at GEO from Reference 5, as shown in Figure 3.10, the craft are modeled as cylinders of radius 0.5 m, height of 1 m and mass of 150 kg. For craft 1, the cylindrical surface with a square cross-sectional area of 1 m^2 is constantly facing the sun, whereas for craft 2, it is the top of the cylinder with circular cross-sectional of 0.25π m^2 that is facing the sun.

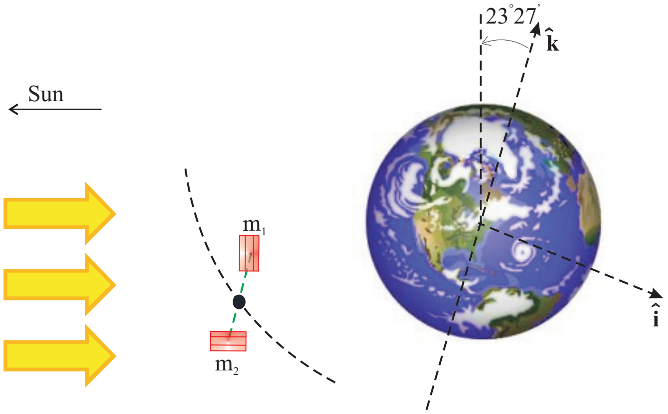

Figure 3.10: Sun's Position and the Orientation of the Cylindrical Craft

In the Earth-Moon system, the solar radiation pressure model is much different from that of the GEO environment. In the vicinity of the collinear libration points, the sun lines are treated as parallel lines. In order to describe the relative motion of the satellite with respect to the formation center of mass, a rotating Hill orbit frame $\mathcal{O} : \{\hat{\boldsymbol{o}}_r, \hat{\boldsymbol{o}}_\theta, \hat{\boldsymbol{o}}_h\}$ whose origin coincides with the L_2 libration point is chosen as shown in Figure 3.11. This rotating coordinate system orbits the Earth-Moon barycenter O with constant orbital angular velocity Ω. In addition, the Earth-Moon system orbits the Sun with an angular velocity of Ω_B. Consequently, the incident Sun line rotates in the orbit frame with a net angular velocity of $\omega_s = \Omega - \Omega_B$. A notable difference in the Earth-Moon system is that the direction of the incident sun line $\boldsymbol{s}$ will vary continuously with respect to the $\mathcal{O}$ frame as

$$\boldsymbol{s} = [\cos(\omega_s t), -\sin(\omega_s t), 0] \tag{3.62}$$

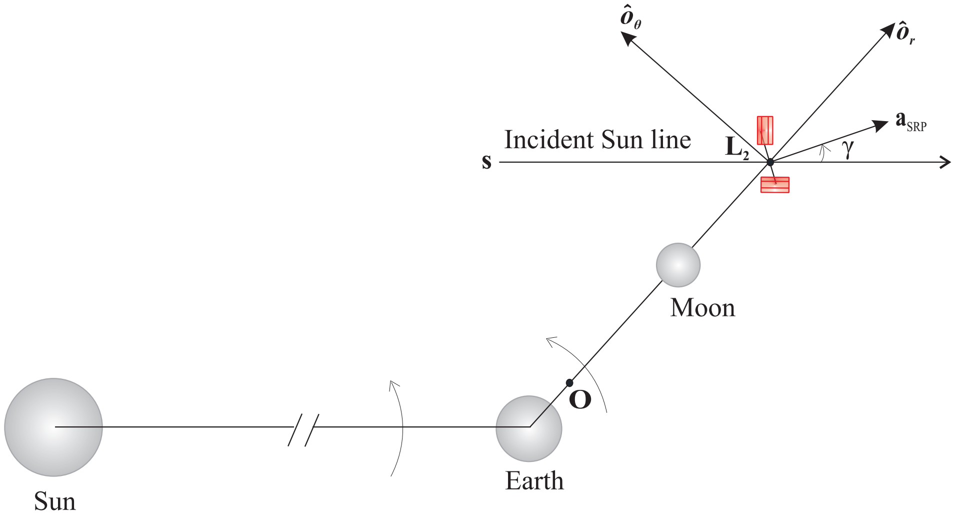

Figure 3.11: Solar Radiation Pressure in the Vicinity of L_2

The solar torque on each craft depends on the orientation of the craft-normal relative to the orbit frame. The orientation of each craft with respect to the orbit frame is defined in terms of a cone angle δ and a clock angle γ, as shown in Figure 3.12.[50, 52] For this study, the cone and clock angles (δ, γ) for each craft are fixed.

Therefore, the components of $\boldsymbol{a}_{\mathrm{SRP}}$ for a craft in the Earth-Moon orbit frame are given by[50, 52]

$$a_{\mathrm{SRPre}} = a_{\mathrm{SRPmax}} \cos^2\gamma \cos(\omega_s t - \gamma) \tag{3.63a}$$

$$a_{\mathrm{SRPat}} = -a_{\mathrm{SRPmax}} \cos^2\gamma \sin(\omega_s t - \gamma) \sin\delta \tag{3.63b}$$

$$a_{\mathrm{SRPon}} = a_{\mathrm{SRPmax}} \cos^2\gamma \sin(\omega_s t - \gamma) \cos\delta \tag{3.63c}$$

where $a_{\mathrm{SRPmax}} = |\boldsymbol{a}_{\mathrm{SRP}}|$, a_{SRPre} is the component in orbit radial direction, a_{SRPat} is in the direction of orbital velocity (along-track), and the component a_{SRPon} is in the orbit normal

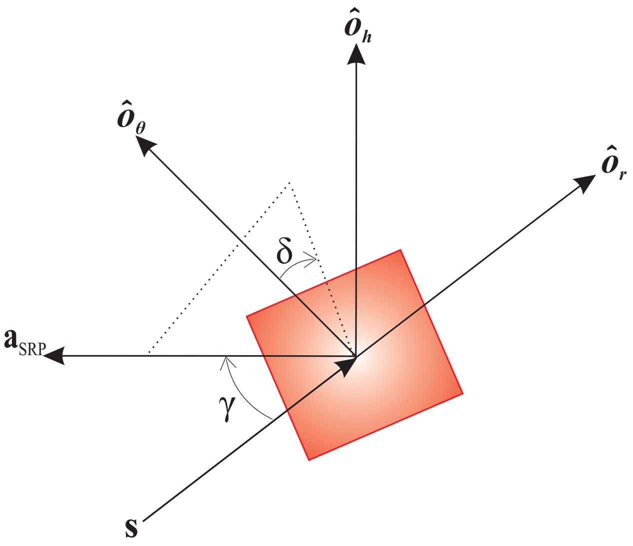

Figure 3.12: Cone and Clock Angles of the Craft-normal relative to the Orbit Frame

direction. Eqs. (3.63) show that the SRP acceleration in the Earth-Moon system is periodic and time varying.

3.3.1.3 Numerical Simulation

The solar drag and gravity gradient force magnitudes for nominal conditions are illustrated in the following numerical simulation. The simulation parameters and the values used are listed in Table 3.1.

Figure 3.13(a) shows the time histories of gravity gradient forces and differential solar drag on a two-craft formation in the GEO environment. For the nominal separation distance, the gravity gradient force is computed from the torque expression in Eq. (3.56) and the differential solar drag force is computed using Eq. (3.61). For craft 1, a square cross-sectional area of 1 m^2 is constantly facing the sun, and, for craft 2, the circular cross-sectional of area of 0.25π m^2 is facing the sun. It clearly shows that the gravity gradient forces are sufficient to withstand the solar drag in the GEO environment. The results in Figure 3.13(b) are obtained by fixing the craft 1 cross-sectional area and varying the craft 2 cross-sectional area from 1 m^2 to 2 m^2. These results indicate that even after increasing the solar drag, the combination of the maximum gravity gradient force and the reference Coulomb force magnitude obtained from Eq. (3.21) are sufficient to stabilize the formation.

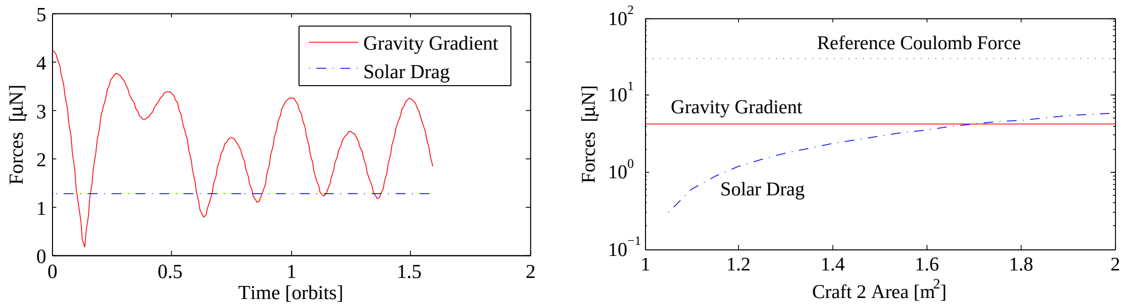

(a) Time Histories of Gravity Gradient and Solar Drag Forces
(b) Force Magnitudes as a Function of Craft Area Ratio

Figure 3.13: Radial Equilibrium Simulation Results at GEO for Nominal Initial Conditions

Figure 3.14(a) shows the time histories of gravity gradient forces and differential solar drag for a two-craft formation at the Earth-Moon L_2 libration point environment. It clearly shows that the gravity gradient forces are very weak, and thus cannot withstand the solar drag at L_2. The results in Figure 3.14(b) also indicate that the maximum gravity gradient force magnitude and the reference Coulomb force magnitude on each craft are not sufficient for stabilizing the formation. Therefore, unless equal sunlit surface areas of the two-craft are assumed such that the differential solar drag is zero, the charged feedback control law used in Reference 46 will not be able to stabilize the two-craft formation at the libration points. Consequently, for unequal sunlit surface areas of the two-craft a full state feedback control is required that uses larger Coulomb forces in the longitudinal direction and electric propulsion thrusters for transverse control.

3.3.2 Lyapunov Feedback Control

A generic controller is designed in this section that can withstand differential solar perturbation for orbit radial configuration about circular orbits and at Earth-Moon collinear libration points. Numerical simulations are shown to validate the controller performance.

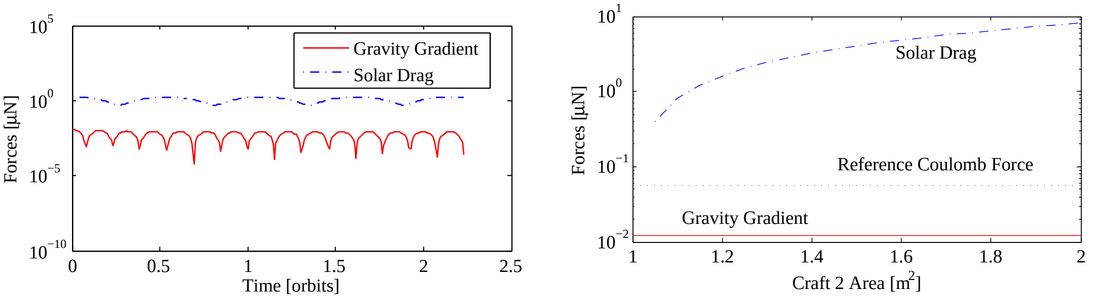

(a) Time Histories of Gravity Gradient and Solar Drag Forces

(b) Force Magnitudes as a Function of Craft Area Ratio

Figure 3.14: Radial Equilibrium Simulation Results at Earth-Moon L_2 for Nominal Initial Conditions

3.3.2.1 Feedback Control Development

Lyapunov's second method is used to develop a feedback control law for stabilizing a radial equilibrium two-craft Coulomb tether formation in the presence of time varying solar radiation pressure disturbances. Because the kinetic energy in Eqs. (3.8) and (3.9) is not just a quadratic function of the velocities, the Hamiltonian takes the form[53]

$$\hat{\mathcal{H}} = T_2 - T_0 + V_g \tag{3.64}$$

where

$$T_2 = \frac{1}{2}m_1(\dot{x}_1^2 + \dot{y}_1^2 + \dot{z}_1^2) + \frac{1}{2}m_2(\dot{x}_2^2 + \dot{y}_2^2 + \dot{z}_2^2) \tag{3.65a}$$

$$T_0 = \frac{\Omega^2}{2}[m_1(y_1^2 + (x_1 + r_c)^2) + m_2(y_2^2 + (x_2 + r_c)^2)] \tag{3.65b}$$

and V_g is given by the Eq. (3.11).

Since the Lagrangian does not contain time explicitly, it follows that the Hamiltonian is constant. Therefore, the two-craft Coulomb tether formation possesses a *Jacobi integral* in place of the energy integral as a constant of motion. The nondimensional $\hat{\mathcal{H}}$ in body coordinates is written as

$$\hat{\mathcal{H}} = \frac{1}{2}(l^{'2} + l^2(\psi^{'2}\cos^2\theta + 3\sigma\cos^2\theta\,\sin^2\psi + \theta^{'2} + (1+3\sigma)\sin^2\theta - (1+2\sigma)) \tag{3.66}$$

where σ is a positive constant that depends on the collinear Lagrangian point chosen. For "$\sigma = 1$", the equation turns out to be the same equation that was found in Reference 54 for circular Earth orbits. References 54 and 55 use the Hamiltonian as a Lyapunov function for stability analysis. Before the Hamiltonian is used as a Lyapunov function at libration points, its positive definiteness must be ascertained. Based on the constant of motion in Eq. (3.66), a Lyapunov function V_{lyp} is defined as

$$\begin{aligned} V_{\text{lyp}} = \frac{1}{2}(l^{'2} + \tilde{K}_1(l-l_f)^2 + (\tilde{K}_2 + l^2)(\psi^{'2}\cos^2\theta + 3\sigma\cos^2\theta\,\sin^2\psi \\ + \theta^{'2} + (1+3\sigma)\sin^2\theta)) \end{aligned} \tag{3.67}$$

where $l_f > 0$ is the desired final value of l, $\tilde{K}_1$ is a positive constant and $\tilde{K}_2$ can either be positive or zero. V_{lyp} is clearly positive definite, and $V_{\text{lyp}} = 0$ at the local radial equilibrium conditions in Eq. (3.20). Assuming f_{dl}, $f_{d\psi}$ and $f_{d\theta}$ to be the non-dimensional differential solar perturbations, the time derivative of V_{lyp} is

$$\begin{aligned} V_{\text{lyp}}^{'} = l^{'}((1+2\sigma)l - u_l - f_{dl} + \tilde{K}_1(l-l_f)) - 2\frac{\tilde{K}_2}{l}(\psi^{'}(1+\psi^{'})\cos^2\theta + \theta^{'2}) \\ + \theta^{'}(\tilde{K}_2 + l^2)(\frac{u_\theta}{l} + \frac{f_{d\theta}}{l}) + \psi^{'}(\tilde{K}_2 + l^2)(\frac{u_\psi}{l} + \frac{f_{d\psi}}{l}) \end{aligned} \tag{3.68}$$

where u_l, u_ψ and u_θ are the non-dimensional control variables. The control variable u_l is associated with Coulomb propulsion acting in the longitudinal direction, and u_ψ and u_θ act in the transverse directions. Moreover, u_ψ and u_θ could utilize electric propulsion for inertial thrusting along these directions.

The following control laws for u_l, u_ψ and u_θ can be selected

$$u_l = (1+2\sigma)l + \tilde{K}_1(l-l_f) - 2\frac{\tilde{K}_2}{l}(\psi^{'}(1+\psi^{'})\cos^2\theta + \theta^{'2}) + \tilde{K}_3 l^{'} - f_{dl} \tag{3.69a}$$

$$u_\psi = -\tilde{K}_5 l\psi^{'} - f_{d\psi} \tag{3.69b}$$

$$u_\theta = -\tilde{K}_4 l\theta^{'} - f_{d\theta} \tag{3.69c}$$

where $\tilde{K}_3$, $\tilde{K}_4$ and $\tilde{K}_5$ are positive constants.

Using these control laws, Eq. (3.68) leads to

$$V_{\text{lyp}}^{'} = -\tilde{K}_3 l^{'2} - (\tilde{K}_2 + l^2)(\tilde{K}_4\theta^{'2} + \tilde{K}_5\psi^{'2}) \tag{3.70}$$

Proper choice of the gains guarantees the stability of the closed-loop system.

Substituting the control laws from Eq. (3.69) into the dynamics (Eqs. 3.17, 3.18), the closed-loop system of equations thus obtained are

$$\theta^{''} + 2\frac{l^{'}}{l}\theta^{'} + \cos\theta\,\sin\theta((1+\psi^{'})^2 + 3\,\sigma\cos^2\psi\,) + \tilde{K}_4\theta^{'} = 0 \tag{3.71a}$$

$$\psi^{''}\cos^2\theta + 2\cos\theta(\frac{l^{'}}{l}\cos\theta - \theta^{'}\sin\theta)(1+\psi^{'}) + 3\sigma\cos^2\theta\,\cos\psi\,\sin\psi\, + \tilde{K}_5\,\psi^{'} = 0 \tag{3.71b}$$

$$\begin{aligned} &l^{''} - l(\theta^{'2} + (1+\psi^{'})^2\cos^2\theta - \sigma(1-3\cos^2\theta\,\cos^2\psi)) + (1+2\sigma)l + \tilde{K}_1(l-l_f) \\ &- \frac{2\tilde{K}_2}{l}(\psi^{'}(1+\psi^{'})\cos^2\theta + \theta^{'2}) + \tilde{K}_3 l^{'} = 0 \end{aligned} \tag{3.71c}$$

These closed-loop system of equations can be used for three dimensional control of a 2-craft virtual Coulomb structure about circular orbits and at Earth-Moon libration points. Furthermore, they can be used either for station-keeping or for 2-craft expansion and contraction reconfigurations.

3.3.2.2 Numerical Simulation

Based on Lyapunov feedback control design, the performance and stability of a 25m Coulomb virtual tether formation at the Earth-Moon L_2 is illustrated in the following numerical simulation. The same spacecraft parameters and nominal separation distance are used as in

Table 3.1. Figure 3.15(a) shows the Coulomb tether motion with the Lyapunov feedback law in Eq. (3.69) for gain settings $\tilde{K}_1 = 2$, $\tilde{K}_2 = 0$, $\tilde{K}_3 = 4$, $\tilde{K}_4 = 2$ and $\tilde{K}_5 = 2$. The in-plane pitch motion ψ, out-of-plane motion θ, and the separation distance deviation δL converged to zero. The attitude motion converged in less than 0.5 orbits, whereas, the separation distance converged in about 1.3 orbits.

Figure 3.15(b) illustrates the spacecraft control charge q_1 usage for the non-linear simulation. Because the solar drag perturbations on the two-craft formation exhibit cyclic behaviour as shown in Figure 3.15(c), the charge results depicted in Figure 3.15(b) also exhibit the cyclic nature and do not converge to the static equilibrium reference value q_{1r}. Furthermore, the micro-Coulomb charge requirements are easily realizable in practice. Figure 3.15(d) illustrates the Coulomb force utilization for longitudinal control and inertial thrusters usage for in-plane and out-of-plane control. Therefore, Coulomb control and transverse control (micro-thrusters) forces are on the order of micro-Newtons. Transverse control can be implemented either using Colloid or PPT micro-thrusters.

3.4 Summary

The feasibility of a two-craft Coulomb tether concept is studied at libration points for orbit-radial equilibrium. The new two-craft dynamics at the libration points is provided as a general framework in which circular Earth orbit dynamics form a special case. The general equations of motion for collinear libration points has a σ parameter which varies for each collinear libration point. Interestingly, setting "$\sigma = 1$" yields the same equations of motion for orbit-radial equilibrium in Earth circular orbits. For the triangular libration points, there is an additional ψ term in equations of motion; however, the coefficient of this ψ term is very small. Although the orbit-radial dynamics at libration points are slightly different than those found in Reference 5 for an orbit radial 2-craft formation at GEO, the stability conditions are similar. At libration points, the out-of-plane motion is marginally stable and decoupled from the in-plane motion. The in-plane motion is stabilized using only separation distance measurements (computing rates). A linearized charge feedback law stabilizes the separation distance using Coulomb force and exploits the gravity gradient torque due to the

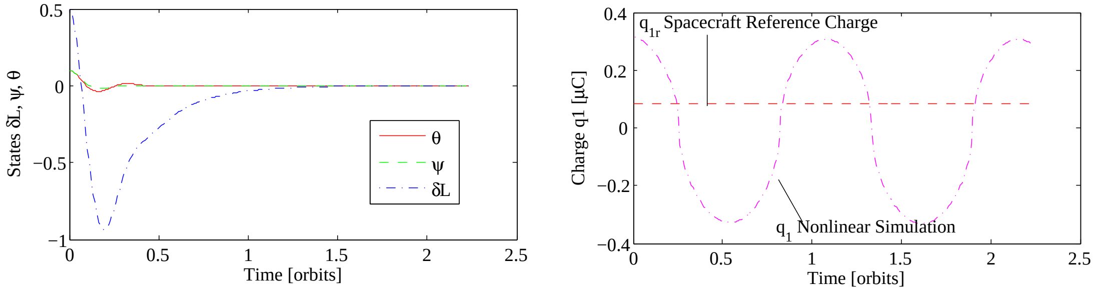

(a) Time Histories of Length Variations δL, In-plane Pitch Angle ψ, and Out-of-plane Roll Angle θ

(b) Spacecraft Charge Time Histories

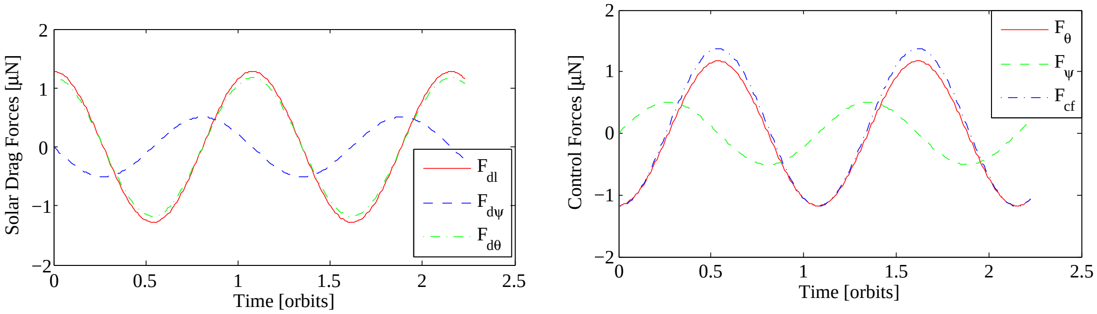

(c) Solar Drag Perturbation Time Histories

(d) Control Time Histories

Figure 3.15: Radial Equilibrium Nonlinear Control Simulation Results at L_2

two primaries for stabilizing the in-plane attitude motion. Also, a full-state feedback linear quadratic regulator meets variable mission requirements (i.e stabilizing the formation within a given time). Numerical simulations at L_2 and L_4 with the charge feedback law show that the formation stabilized faster at L_4 (within 1 orbit) than at L_2 (1.3 orbits). This is perhaps due to the unstable nature of the collinear libration point causing a slow stabilization of the formation. Also, due to the large distances from the Earth-Moon barycenter to the libration points and due to the smaller rotation rate of the barycenter, the micro-Coulomb charge requirements at the libration points is at least an order of magnitude smaller compared to that of a two-body system in Reference 5.

However, the charge feedback law assumes that the two-craft areas exposed to sunlight are equal such that the differential solar radiation pressure is zero. If the two craft sunlit areas are not equal, the assumption is that the two craft are oriented independently to keep the differential SRP to zero. Consequently, when the differential solar drag on the two-craft formation is not zero and in the presence of time varying SRP disturbances, a Lyapunov feedback control method is presented for feedback stabilization of a radial equilibrium two-craft Coulomb tether formation about circular orbits and at libration points. The method uses a Lyapunov function based on a first integral of motion of the two-craft Coulomb formation. The controller designed using this method works very well and the control law utilizes a three-dimensional control (separation distance, in-plane and out-of-plane motion). The Lyapunov feedback control law obtained has a σ parameter which varies for each collinear libration point. Interestingly, setting "$\sigma = 1$" yields a control law for orbit-radial equilibrium in Earth circular orbits. Therefore, the Lyapunov control law at the libration points is provided as a generic control law in which circular Earth orbit control forms a special case. At the Earth-Moon L_2 simulations, it is recommended that the control gains be chosen such that the pitch and roll angles do not exceed 90 degrees. This will ensure that undesirable equilibrium points are not reached. Depending on the desired final separation distance between the craft, the gains for the Coulomb propulsion control law should be appropriately adjusted.

Chapter 4

HYBRID CONTROL OF ALONG-TRACK AND ORBIT NORMAL TWO-CRAFT COULOMB FORMATION AT LIBRATION POINTS

The previous chapter investigates the linearized orbit radial dynamics and stability analysis of a 2-craft virtual Coulomb structure at Earth-Moon libration points. A charge feedback law is used to stabilize a charged spacecraft cluster to a specific shape and orientation. Such an active charge feedback control is developed utilizing the differential gravity field effect due to Earth-Moon on a Coulomb tethered two-spacecraft system. The stability characteristics of such a formation are similar to that of an orbital rigid body motion moving in the presence of two celestial objects. With this control, the spacecraft separation distance is maintained at a fixed value, while the coupled gravity gradient torques on the formation due to the two celestial objects are exploited to stabilize the tether attitude about the orbit radial direction. For the Coulomb tether regulation problem in the previous chapter, the charge feedback law assumes that the two-craft sunlit areas are equal such that the differential solar radiation pressure is zero. With this assumption, the feedback control law guarantees asymptotic stability for separation distance and in-plane angle. This asymptotic stability is achieved by exploiting the charged relative motion of the spacecraft and varying the 2-craft separation distance. Controlling the separation distance stabilizes the in-plane rotation angle; however, the spacecraft charge control law does not affect the out-of-plane rotational motion. Also, the new two-craft dynamics at the libration points provide a general framework in which circular Earth orbit dynamics form a special case. If the two-craft sunlit areas are not equal, and in the presence of time varying SRP disturbances, a Lyapunov feedback control method is presented for stabilizing a radial equilibrium two-craft Coulomb formation at L_2.

Apart from the orbit-radial equilibrium, Reference 45 presents two other relative equilibria of the charged 2-craft problem at libration points. These equilibria are in the along-track direction and in the orbit normal direction as shown in Figure 4.1. Interestingly, in the restricted three-body system, a tether force is required for the along-track equilibrium, however, no force is necessary in the restricted two-body system. Therefore, at libration points, nonzero tension is required between the two crafts in the along-track direction to maintain the static unperturbed formation. On the other hand, repulsive forces are required for maintaining the cluster along the orbit normal direction at libration points.

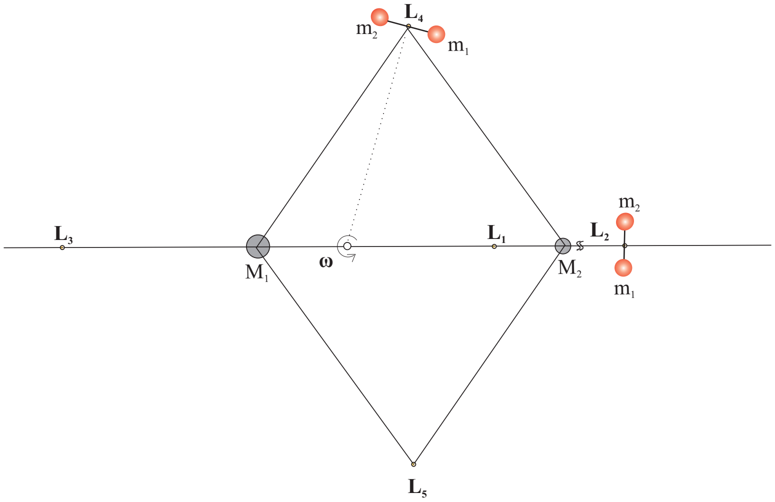

(a) Along-track Relative Equilibrium

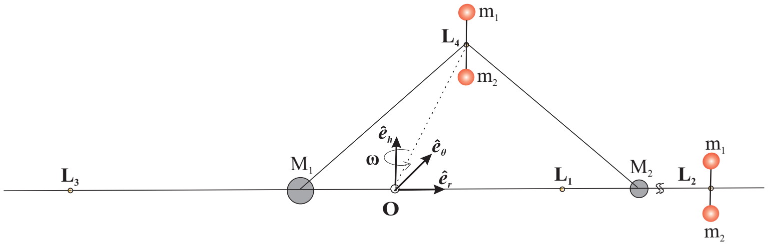

(b) Orbit Normal Relative Equilibrium

Figure 4.1: Along-track and Orbit Normal Relative Equilibria at Libration Points

This chapter studies the stability of a two-craft formation about along-track and orbit normal relative equilibrium configurations at Earth-Moon libration points. The assumption is that the two craft sunlit areas are equal such that the differential solar radiation pressure on the formation is zero. Along the orbit radial direction, while the charged two-craft formation could stabilize the cluster using only Coulomb forces, this chapter studies a hybrid feedback control strategy in which both conventional inertial thrusters and Coulomb forces are used. The methodology is similar to that introduced in Reference 5 for circular Earth GEO orbits. The goal is to use the electric propulsion thrusters as little as possible while maximizing the Coulomb force usage. The control strategy is designed such that the thruster is never directed at the 2nd craft such that the thruster exhaust plume impingement issues on the neighboring craft are avoided. The formation is studied at libration points where the Debye lengths are reasonable enough to consider Coulomb spacecraft missions. Numerical simulations using a charge feedback law are presented at both a collinear and a triangular libration point. If the two-craft sunlit areas are not equal, the assumption is that the two craft are oriented independently to keep the differential SRP to zero.

4.1 Linear Dynamics and Stability Analysis - Collinear Libration Points

4.1.1 Charged Relative Equations of Motion

4.1.1.1 Along-Track Configuration

This section derives the equations of motion of a 2-craft Coulomb tether that is nominally aligned with the along-track direction $\hat{\boldsymbol{o}}_\theta$ of a rotating Hill orbit frame $\mathcal{O} : \{\hat{\boldsymbol{o}}_r, \hat{\boldsymbol{o}}_\theta, \hat{\boldsymbol{o}}_h\}$ whose origin coincides with L_2 libration point as shown in Figure 4.2. This derivation closely follows the derivation of the equations of motion for craft aligned along the orbit radial direction, which is given in detail in Reference 46.

Figure 4.3 illustrates a static two-craft formation in the orbit velocity direction with a separation distance of L_{ref}.

The non-linear equations of motion are deduced from the Lagrangian $\mathcal{L} = T - (V_g + V_c)$ of the system in the following form

$$\begin{aligned} &\frac{\mathrm{d}}{\mathrm{d}t}\frac{\partial \mathcal{L}}{\partial \dot{q}^i} - \frac{\partial \mathcal{L}}{\partial q^i} = \mathcal{Q}_i \\ &q^i = (\phi, \psi, L) \quad (i = 1 \dots 3) \end{aligned} \tag{4.1}$$

where $\mathcal{Q}_i$ is the generalized force in the q^ith degree of freedom excluding gravitational effects. For the circularly restricted three-body system, the nonlinear equations governing the yaw

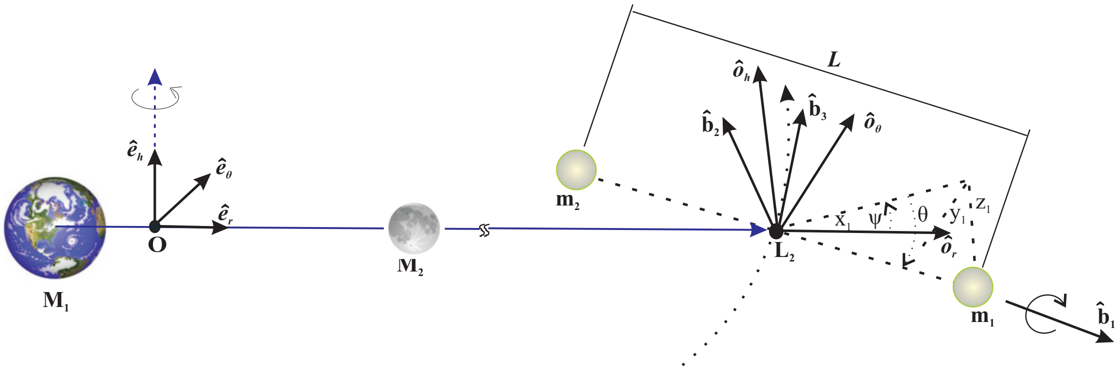

Figure 4.2: Euler Angles Representing the Attitude of Coulomb Tether with Respect to the Orbit Frame at L_2

angle ϕ out of the orbital plane, the pitch angle ψ in the orbital plane, and the separation distance L become

$$\ddot{\phi} + 2\dot{\phi}\frac{\dot{L}}{L} + \cos\phi\sin\phi((\dot{\psi}+\Omega)^2 + 3\Omega^2\sigma\sin^2\psi) = 0 \tag{4.2a}$$

$$\ddot{\psi} - 2(\dot{\psi}+\Omega)(\dot{\phi}\tan\phi - \frac{\dot{L}}{L}) - 3\Omega^2\sigma\sin\psi\cos\psi = 0 \tag{4.2b}$$

$$\ddot{L} - L(\dot{\phi}^2 + (\dot{\psi}+\Omega)^2\cos^2\phi + \Omega^2\sigma(3\cos^2\phi\cos^2\psi - 1)) + \frac{k_c}{m_1}Q\frac{1}{L^2}\frac{m_1+m_2}{m_2} = 0 \tag{4.2c}$$

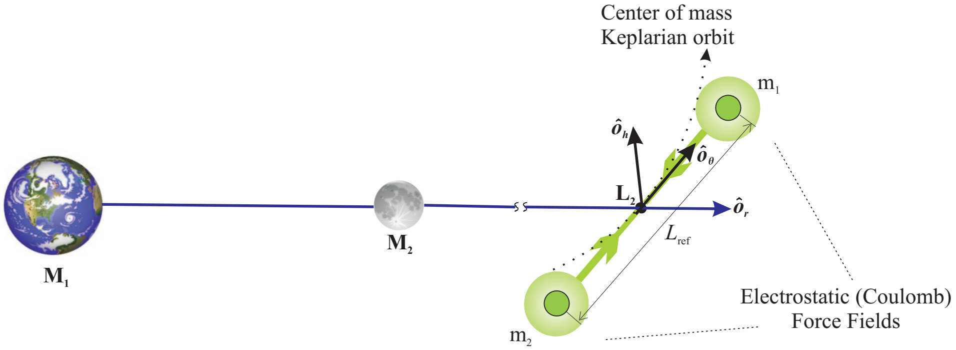

Figure 4.3: Two-Craft Formation in Along-track Direction at L_2

where $Q = q_1q_2$, $\nu = \frac{M_2}{M_1+M_2}$, $1-\nu = \frac{M_1}{M_1+M_2}$ and

$$\sigma = \frac{1-\nu}{|\frac{r_{x0}}{d}+\nu|^3} + \frac{\nu}{|\frac{r_{x0}}{d}-1+\nu|^3} > 0 \tag{4.3}$$

is a positive constant that depends on the collinear Lagrangian point chosen. The equations of motion in Eq. (4.2) are coupled non-linear ordinary differential equations that define the motion of a two-craft Coulomb formation in along-track direction at any of the three collinear Lagrangian points.

If the two-craft formation is aligned in the along-track direction, the formation remains statically fixed relative to the rotating orbiting frame $\mathcal{O}$ provided the non-linear equations Eq. (4.2) satisfy the following along-track equilibrium conditions

$$\phi = \dot{\phi} = \ddot{\phi} = \psi = \dot{\psi} = \ddot{\psi} = \dot{L} = \ddot{L} = 0 \qquad \text{and} \qquad L = L_{\text{ref}} \tag{4.4}$$

Eq. (4.2c) provides the nominal product of charges $Q_{\text{ref}} = q_1q_2$ needed to achieve this static Coulomb formation as

$$Q_{\text{ref}} = (\sigma - 1)\,\Omega^2 \frac{L^3}{k_c}\frac{m_1m_2}{m_1+m_2} \tag{4.5}$$

Thus, the satellites appear frozen with respect to the rotating frame when the charge product Q_{ref} satisfies Eq. (4.5). Since the charge product term is positive it implies that the spacecraft charges will have same charge signs and also, an infinite number of charge pairs can satisfy $Q_{\text{ref}} = q_1q_2$. In this study, the charge magnitudes are set equal.

The linearized version of the nonlinear equations Eq. (4.2) are obtained by applying a Taylor series expansion about the equilibrium states given in Eq. (4.4). Both the yaw and pitch equations of motion are linearized about small yaw and pitch angles respectively. The separation distance equations of motion are linearized about small variations in δL as well as about small variations in the product charge term δQ as follows

$$L = L_{\text{ref}} + \delta L \tag{4.6a}$$

$$Q = Q_{\text{ref}} + \delta Q \tag{4.6b}$$

where mission requirements determine the reference separation length L_{ref}, and Q_{ref} is determined through the constraint Eq. (4.5) for a particular choice of L_{ref}. Performing the necessary linearizations yields

$$\ddot{\phi} + \Omega^2 \phi = 0 \tag{4.7a}$$

$$\ddot{\psi} + \frac{2\Omega}{L_{\text{ref}}} \delta \dot{L} - 3\Omega^2 \sigma \psi = 0 \tag{4.7b}$$

$$\delta \ddot{L} - 2\Omega L_{\text{ref}} \dot{\psi} - 3\Omega^2 (1 - \sigma) \delta L - \left(\frac{k_c}{m_1} \frac{1}{L_{\text{ref}}^2} \frac{m_1 + m_2}{m_2} \right) \delta Q = 0 \tag{4.7c}$$

Thus, Eqs. (4.7a) and (4.7b) are the linearized attitude dynamics of the Coulomb tether body frame $\mathcal{B}$ and Eq. (4.7c) is the linearized separation distance differential equation about the along-track reference configuration at a collinear libration point. It is inferred from these equations that the out-of-plane motion $\phi(t)$ is uncoupled from the in-plane motion ($\psi(t)$ and $\delta L(t)$) and is analogous to that of a marginally stable linear oscillator because of the gravity gradient torques due to the two planets.

4.1.1.2 Orbit Normal Configuration

The derivation of the equations of motion for a two-craft Coulomb tether along orbit normal direction follow the same steps as those of the along-track equilibrium. The nonlinear equations governing the yaw angle ϕ and the roll angle θ out of the orbital plane and the separation distance L become

$$\begin{aligned}
&\ddot{\phi} + 2\frac{\dot{L}}{L}(\dot{\phi} - \Omega\sin\theta) - \frac{1}{4}((\Omega^2\cos 2\theta + \Omega^2 - 2\dot{\theta}^2 - 6\Omega^2\sigma\sin^2\theta)\sin 2\phi \\
&\quad + 4\Omega\dot{\theta}\cos\theta\cos 2\phi + 4\Omega\dot{\theta}\cos\theta) = 0 \qquad \text{(4.8a)} \\
&\ddot{\theta} + 2\frac{\dot{L}}{L}(\dot{\theta} + \Omega\cos\theta\tan\phi) - \frac{1}{2}\Omega^2\sin 2\theta + \Omega\dot{\phi}\cos\theta\sec^2\phi - \frac{3}{2}\Omega^2\sigma\sin 2\theta \\
&\quad - 2\dot{\theta}\dot{\phi}\tan\phi + \Omega\dot{\phi}\cos\theta\cos 2\phi\sec^2\phi = 0 \qquad \text{(4.8b)} \\
&\ddot{L} - \frac{L}{4}(3\Omega^2 + 2\dot{\theta}^2 + 4\dot{\phi}^2 - 2\Omega^2\cos 2\theta\cos^2\phi - (\Omega^2 - 2\dot{\theta}^2)\cos 2\phi - 8\Omega\dot{\phi}\sin\theta \\
&\quad + 4\Omega\dot{\theta}\cos\theta\sin 2\phi - 4\Omega^2\sigma(1 - 3\cos^2\phi\sin^2\theta)) + \frac{k_c}{m_1}Q\frac{1}{L^2}\frac{m_1 + m_2}{m_2} = 0 \qquad \text{(4.8c)}
\end{aligned}$$

where $Q = q_1 q_2$ and σ is a positive constant as defined in Eq. (4.3) that depends on the collinear Lagrangian point chosen. The equations of motion in Eq. (4.8) are coupled nonlinear ordinary differential equations that define the motion of a two-craft Coulomb formation along orbit normal direction at any of the three collinear Lagrangian points.

If the two-craft formation is aligned in orbit normal direction, the formation remains statically fixed relative to the rotating orbiting frame $\mathcal{O}$ provided the non-linear equations Eq. (4.8) satisfy the following orbit normal equilibrium conditions

$$\phi = \dot{\phi} = \ddot{\phi} = \theta = \dot{\theta} = \ddot{\theta} = \dot{L} = \ddot{L} = 0 \qquad \text{and} \qquad L = L_{\text{ref}} \tag{4.9}$$

Eq. (4.8c) provides the nominal product of charges $Q_{\text{ref}} = q_1 q_2$ needed to achieve this static Coulomb formation as

$$Q_{\text{ref}} = \sigma\Omega^2\frac{L^3}{k_c}\frac{m_1 m_2}{m_1 + m_2} \tag{4.10}$$

Thus, the satellites appear frozen with respect to the rotating frame when the charge product Q_{ref} satisfies Eq. (4.10). Since the charge product term is positive it implies that the spacecraft charges will have same charge signs and also, an infinite number of charge pairs can satisfy $Q_{\text{ref}} = q_1 q_2$. In this study, the charge magnitudes are set equal.

Mission requirements determine the reference separation length L_{ref}, and Q_{ref} is determined through the constraint Eq. (4.10) for a particular choice of L_{ref}. Performing the necessary linearizations yields

$$\ddot{\phi} - \Omega^2\phi - 2\Omega\dot{\theta} = 0 \tag{4.11a}$$

$$\ddot{\theta} - (1 + 3\sigma)\Omega^2\theta + 2\Omega\dot{\phi} = 0 \tag{4.11b}$$

$$\delta\ddot{L} + 3\sigma\Omega^2\delta L - \Big(\frac{k_c}{m_1}\frac{1}{L_{\text{ref}}^2}\frac{m_1 + m_2}{m_2}\Big)\delta Q = 0 \tag{4.11c}$$

Thus, Eqs. (4.11a) and (4.11b) are the linearized attitude dynamics of the Coulomb tether body frame $\mathcal{B}$ and Eq. (4.11c) is the linearized separation distance differential equation about the orbit normal reference configuration at a collinear libration point. Note both the out-of-plane angles $\phi(t)$ and $\theta(t)$ are coupled, while the charged separation distance error dynamics is uncoupled in this linearized formulation. Also, one can observe from Eq. (4.11c) that the separation distance error ($\delta L(t)$) is already marginally stable even without any feedback control through the charge product error term ($\delta Q(t)$).

Interestingly, for along-track and orbit normal reference configurations, for "$\sigma = 1$", the Eqs. (4.7) and (4.11) turn out to be the same equations that were found in Reference 5 at GEO. Thus, the linearized equations of motion for small motions about along-track equilibria in Eqs. (4.7) and about orbit normal equilibria in Eqs. (4.11) form a general framework that covers both circular GEO and collinear libration point departure motion. By changing the constant σ either motion is described. Furthermore, in Eq. (4.7c) the stiffness term on δL is the only difference in the separation distance differential equation from Reference 5. Thus, the equations of motion are slightly different at a collinear libration point, but no significant changes in the stability behavior are expected. And, note that Eq. (4.7c) for along-track and Eq. (4.11c) for orbit normal reference configurations provide the necessary relationship between the change in relative separation of the satellites δL and the additional charge product δQ required.

4.1.2 Hybrid Feedback Control Development

Under the influence of external disturbances, the two-craft formation deviates from the desired equilibrium configuration. Because the deviations from the desired equilibrium configuration are small, linear control design techniques are used to stabilize the motion without exceeding the charge requirements.

4.1.2.1 Along-Track Configuration

In this section, the stability of the linearized along-track equations of motion given by Eq. (4.7) is investigated and a hybrid feedback control law that stabilizes the system is developed. It is clear from Eq. (4.7) that the out-of-plane angle ϕ is decoupled from the in-plane angle ψ and separation distance error δL. On the other hand, Eqs. (4.7b) and (4.7c) are the coupled in-plane angle ψ and separation distance error δL equations of motion. Therefore the in-plane motion can be controlled with Coulomb forces using a partial-state charge feedback control defining the small charge product variation with a proportional-derivative feedback control of small separation distances. The Coulomb force acts along the relative position vector due to the charges of each craft and thus, these Coulomb charges can be used to control the spacecraft separation distance. A proportional-derivative feedback control of δL is designed by defining[5]

$$\delta Q = \frac{m_1 m_2 L_{\text{ref}}^2}{(m_1 + m_2)\, k_c}(-C_1 \delta L - C_2 \delta \dot{L}) \tag{4.12}$$

Substituting this expression for δQ in Eq. (4.7c), the closed-loop separation distance dynamics become

$$\delta \ddot{L} + (C_1 - 3(1-\sigma)\Omega^2)\delta L + C_2 \delta \dot{L} - (2\Omega L_{\text{ref}})\dot{\psi} = 0 \tag{4.13}$$

Since the δL differential equation does not involve a $\delta \dot{L}$ damping term, the derivative feedback is essential for asymptotic convergence. A procedure similar to that used in Reference 5 at GEO, the Routh-Hurwitz stability criterion is used to select the gains C_1 and C_2 to asymptotically stabilize both δL and ψ. And, there are no real values for gain C_1 and

C_2 that will stabilize the coupled system with only the Coulomb forces.[5] In addition to the Coulomb forces, some thrust forces are required acting on both satellites along the $\hat{b}_1$ axis that stabilize the in-plane angle ψ. As shown in the Figure 4.4 these thrust forces can be modeled as equal and opposite forces with magnitude F_1. The thrust force magnitude is the second control variable with in-plane angle ψ feedback and it is defined as[5]

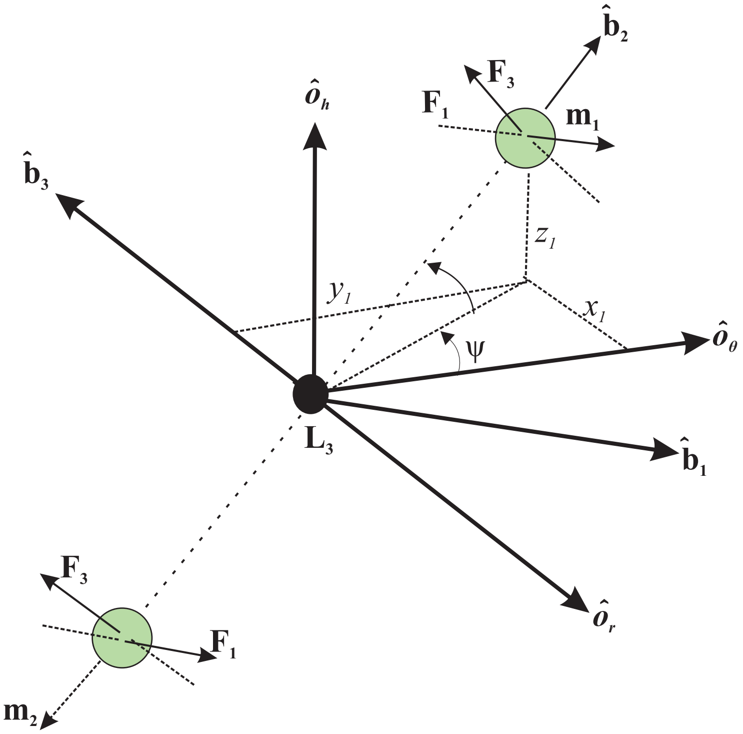

Figure 4.4: Thrust Force Directions for Along-track Configuration

$$F_1 = \frac{m_1 m_2}{m_1 + m_2} L_{\text{ref}}(K_1 \psi) \tag{4.14}$$

where K_1 is the in-plane angle feedback gain. These forces introduce a net torque in the ψ equation and the modified coupled equations of motion are written as

$$\ddot{\psi} + \frac{2\Omega}{L_{\text{ref}}}\delta\dot{L} - (3\sigma\Omega^2 - K_1)\psi = 0 \tag{4.15a}$$

$$\delta\ddot{L} + (C_1 - 3(1-\sigma)\Omega^2)\delta L + C_2\delta\dot{L} - (2\Omega L_{\text{ref}})\dot{\psi} = 0 \tag{4.15b}$$

The charge feedback control law is implemented by determining the charges q_1 and q_2. Since $Q = q_1 q_2$, using Eq. (4.6b), the spacecraft charges must satisfy

$$q_1 q_2 = Q_{\text{ref}} + \delta Q \tag{4.16}$$

where Q_{ref} value is evaluated from Eq. (4.5) while δQ value is given by the charge feedback law expression in Eq. (4.12). Due to the above constraint yielding an infinite number of solutions, the following implementation is used where equal charges in magnitude across the craft are chosen.

$$q_1 = \sqrt{|Q_{\text{ref}} + \delta Q|} \tag{4.17}$$

$$q_2 = q_1 \tag{4.18}$$

Because $\delta Q \ll Q_{\text{ref}}$ and $Q_{\text{ref}} > 0$, note that here $Q_{\text{ref}} + \delta Q > 0$ which implies that $q_1 > 0$ and $q_2 > 0$.

In order to prevent numerical difficulties due to a small value of Ω, the linearized attitude dynamics Eqs. (4.7a) - (4.7b) and the closed loop separation distance dynamics given in Eq. (4.13) are made independent of Ω by the following transformation

$$\mathrm{d}\tau = \Omega \mathrm{d}t \tag{4.19a}$$

$$(*)^{'} = \frac{\mathrm{d}(*)}{\mathrm{d}\tau} = \frac{1}{\Omega}\frac{\mathrm{d}(*)}{\mathrm{d}t} \tag{4.19b}$$

Thus, the orbit rate (Ω) independent linearized equations of motion for a two-craft Coulomb tether formation at any collinear libration point are given by

$$\phi^{''} + \phi = 0 \tag{4.20a}$$

$$\psi^{''} + \frac{2}{L_{\text{ref}}}\delta L^{'} - (3\sigma - \tilde{K}_1)\psi = 0 \tag{4.20b}$$

$$\delta L^{''} + \tilde{C}_2 \delta L^{'} - 2L_{\text{ref}}\psi^{'} + (\tilde{C}_1 - 3(1-\sigma))\delta L = 0 \tag{4.20c}$$

where $\tilde{C}_2 = \frac{C_2}{\Omega}$, $\tilde{C}_1 = \frac{C_1}{\Omega^2}$ and $\tilde{K}_1 = \frac{K_1}{\Omega^2}$ are non-dimensionalized feedback gains. Routh-Hurwitz stability criteria are used to fine tune these gain values that satisfy the stability requirements. The characteristic equation for the coupled δL and ψ equation is

$$\begin{aligned}\lambda^4 + \tilde{C}_2\lambda^3 + (1 + \tilde{C}_1 + \tilde{K}_1)\lambda^2 + \tilde{C}_2(\tilde{K}_1 - 3\sigma)\lambda + \tilde{C}_1\tilde{K}_1 - 3\tilde{K}_1 \\ + 9\sigma - 3\tilde{C}_1\sigma + 3\tilde{K}_1\sigma - 9\sigma^2 = 0 \end{aligned} \tag{4.21}$$

Roots of Eq. (4.21) should have negative real parts for asymptotic stability. For all roots to have negative real parts, a Routh table construction allows one to determine the following necessary constraints on the gains $\tilde{C}_1$, $\tilde{C}_2$ and $\tilde{K}_1$

$$\tilde{C}_1 > 3(1 - \sigma) \tag{4.22a}$$

$$\tilde{C}_2 > 0 \tag{4.22b}$$

$$\tilde{K}_1 > 3\sigma \tag{4.22c}$$

To fix the gain values that satisfy the stability criteria in Eq. (4.22), near ideal damping conditions are assumed. Let the scaling factors n_1, n_2 and β be positive and real such that the gains are rewritten as

$$\tilde{C}_1 = n_1 > 3(1 - \sigma) \tag{4.23a}$$

$$\tilde{C}_2 = \beta\sqrt{n_1} \tag{4.23b}$$

$$\tilde{K}_1 = n_2 > 3\sigma \tag{4.23c}$$

The natural frequency of the ψ equation is $\sqrt{n_2 - 3\sigma}$ and is independent of the choice of $\tilde{C}_1$ and $\tilde{C}_2$, and the natural frequency for the δL equation is $\sqrt{n_1 - 3(1 - \sigma)}$. For the ψ' coupling term in the δL equation to serve as a defacto damping term, n_1 and n_2 are chosen in such a way that these frequencies match. The value of n_2 is chosen as 6σ and for this fixed n_2 value, the root locus for the coupled δL and ψ equations is studied for a range of β values in the vicinity of $\beta = 2$, with n_1 varying from 0.1 to 20. The root locus plot analysis yield the optimal scaling factors to be $\beta = 2.3$ and $n_1 = 2.96$.

The out-of-plane angle ϕ can be asymptotically stabilized by using an equal and opposite thrust force on both the satellites along the $\hat{b}_3$ axis. The thrust force magnitude F_3 is the third control variable with $\dot{\phi}$ feedback and it is defined as[5]

$$F_3 = \frac{m_1 m_2}{m_1 + m_2} L_{\text{ref}}(K_2 \dot{\phi}) \tag{4.24}$$

where K_2 is the out-of-plane angle feedback gain. These forces introduce a net torque in the ϕ equation and the modified equation of motion is written as

$$\phi^{''} + \tilde{K}_2 \phi^{'} + \phi = 0 \tag{4.25}$$

where $\tilde{K}_2 = \frac{K_2}{\Omega}$ and $\tilde{K}_2 = 2$ yields critical damping.

Figure 4.4 illustrates the thrusters in action along the $\hat{b}_1$ and $\hat{b}_3$ axes for the along-track configuration.[5] For the satellite 1, the thrusting force F_1 acts along the positive $\hat{b}_1$ direction and the force F_3 is acting along the negative F_3 direction. For the satellite 2, the direction of these forces are in reverse. To avoid any potential plume exhaust impingement issues, all thruster forces are directed in orthogonal directions to the cluster line of sight vector ($\hat{b}_3$).

4.1.2.2 Orbit Normal Configuration

In the orbit normal configuration, the equation of motion of the separation distance error δL is decoupled from the angles. Instead, equations of motion of the two out-of-plane angles ϕ and θ are coupled. Consequently, the separation distance can only be stabilized using the linearized Coulomb forces and some thrust force is needed to stabilize the angles. In order to control the natural frequency as well as to make δL equation of motion asymptotically stable, a separation distance error and error rate (δL,$\delta \dot{L}$) feedback through the control variable δQ is sufficient. The feedback control law is defined as[5]

$$\delta Q = \frac{m_1 m_2 L_{\text{ref}}^2}{(m_1 + m_2)\, k_c}(-C_1 \delta L - C_2 \delta \dot{L}) \tag{4.26}$$

where $C_1 > -3\sigma\Omega^2$ and $C_2 > 0$ are the position and velocity feedback gain, respectively.

The closed loop separation distance error equation is expressed as

$$\delta\ddot{L} + (C_1 + 3\sigma\Omega^2)\delta L + C_2\delta\dot{L} = 0 \tag{4.27}$$

The separation distance equation is critically damped by fixing $C_2 > 2\sqrt{3\sigma\Omega^2 + C_1}$.

Thrust forces on both the satellites can be used to stabilize the coupled out-of-plane angles.[5] The thrusting force F_1 is acting along the positive $\hat{b}_1$ direction and the force F_2 is acting along the positive $\hat{b}_2$ direction for the satellite 1. The direction of these forces are in reverse for the satellite 2. Note all thruster forces are directed in orthogonal directions to the cluster line of sight vector ($\hat{b}_3$) and thereby avoid any potential plume exhaust impingement issues. The feedback control laws for the thrust force magnitudes are defined as[5]

$$F_1 = \frac{m_1 m_2}{m_1 + m_2} L_{\text{ref}}(K_2\theta) \tag{4.28}$$

$$F_2 = \frac{m_1 m_2}{m_1 + m_2} L_{\text{ref}}(K_1\phi + K_3\dot{\phi}) \tag{4.29}$$

where K_1 and K_3 are the ϕ angle and angle rate gains, and K_2 is the θ angle gain. These forces introduce torque into the angular equations of motion. Therefore the nondimensional closed loop equations are

$$\phi^{''} - 2\theta^{'} + (\tilde{K}_1 - 1)\phi + \tilde{K}_3\phi^{'} = 0 \tag{4.30a}$$

$$\theta^{''} + (\tilde{K}_2 - (1 + 3\sigma))\theta + 2\phi^{'} = 0 \tag{4.30b}$$

$$\delta L^{''} + (\tilde{C}_1 + 3\sigma)\delta L + \tilde{C}_2\delta L^{'} = 0 \tag{4.30c}$$

The characteristic equation of the coupled equations of motion given in Eqs. (4.30a) and (4.30b) is

$$\begin{aligned}\lambda^4 + \tilde{K}_3\lambda^3 + (2 + \tilde{K}_1 + \tilde{K}_2 - 3\sigma)\lambda^2 + (-\tilde{K}_3 + \tilde{K}_2\tilde{K}_3 - 3\tilde{K}_3\sigma)\lambda \\ + 1 - \tilde{K}_1 - \tilde{K}_2 + \tilde{K}_1\tilde{K}_2 + 3\sigma - 3\tilde{K}_1\sigma = 0\end{aligned} \tag{4.31}$$

where $\tilde{C}_2 = \frac{C_2}{\Omega}$, $\tilde{C}_1 = \frac{C_1}{\Omega^2}$, $\tilde{K}_1 = \frac{K_1}{\Omega^2}$, $\tilde{K}_2 = \frac{K_1}{\Omega^2}$ and $\tilde{K}_3 = \frac{K_1}{\Omega}$ are non-dimensionalized feedback gains. The Routh-Hurwitz criterion establishes the following constraints on the gains

$$\tilde{K}_1 > 1 \tag{4.32a}$$

$$\tilde{K}_2 > 1 + 3\sigma \tag{4.32b}$$

$$\tilde{K}_3 > 0 \tag{4.32c}$$

To fix the gain values that satisfy the stability criteria in Eq. (4.32), near ideal damping conditions are assumed. Let the scaling factors n and β be positive and real such that the gains $\tilde{K}_1$ and $\tilde{K}_3$ are rewritten as

$$\tilde{K}_1 = n > 1 \tag{4.33a}$$

$$\tilde{K}_3 = \beta\sqrt{n-1} \tag{4.33b}$$

In the equation of motion for ϕ, ignoring the $\dot{\theta}$ term guarantees critical damping. Fixing values of $\tilde{K}_2 > 1 + 3\sigma$, the root locus is analyzed for the coupled ϕ and θ equations for a range of β values in the vicinity of β= 2 with n varying from 1.1 to 10. For $\tilde{K}_2 = 2 + 3\sigma$, root locus analysis yields the optimal scaling factors to be β= 2.5 and $n = 2.7$.

4.1.3 Numerical Simulation

The performance and stability of a 25 m along-track and orbit normal Coulomb formation is illustrated in the following numerical simulations at Earth-Moon L_2 libration point. The hybrid feedback control strategy is illustrated and the Coulomb tether performance is simulated for both the linear and non-linear formulations.

4.1.3.1 Along-Track Configuration

Table 4.1 lists the simulation parameters and the values used for the along-track Coulomb tether configuration with a separation distance of 25 meter. The parameters n_1 and β are selected based on root locus plot analysis where the gains $\tilde{C}_1$, $\tilde{C}_2$ and $\tilde{K}_1$ computed from

Eq. (4.23) satisfy the stability criteria in Eq. (4.22) and that lead to effective damping. The two-craft Coulomb tether performance at the collinear libration point L_2 is simulated by integrating the linearized equations of motion in Eqs. (4.20b), (4.20c) and (4.25) and then compared with the results obtained from integrating the non-linear equations of motion in Eq. (4.2). During this simulation, the Debye length is assumed to be zero in order to investigate the effects of linearization on the relative motion.

Table 4.1: Input Parameters Used in Along-track Simulation for L_2

Parameter	Value	Units
m_1	150	kg
m_2	150	kg
L_{ref}	25	m
k_c	8.99×10^9	$\frac{\text{Nm}^2}{\text{C}^2}$
Q_{ref}	0.002023	μC^2
Ω	2.661699×10^{-6}	rad/sec
$\delta L(0)$	0.5	m
$\psi(0)$	0.1	rad
$\phi(0)$	0.1	rad
n_1	2.96	
β	2.3	
σ	3.190432478	
$\tilde{C}_1$	2.96	
$\tilde{C}_2$	3.95706	
$\tilde{K}_1$	6σ	
$\tilde{K}_2$	2	

Figure 4.5(a) shows the Coulomb tether motion with the charge feedback law augmented with the thrust forces generated using conventional thrusters. The pitch motion ψ, yaw motion ϕ and the separation distance deviation δL converged to zero justifying the linearization assumptions. Also, stabilizing the separation distance to zero also stabilized the in-plane rotation angle after about 1.1 orbits. Figure 4.5(b) shows the spacecraft control charge q_1 usage for both the linear and non-linear simulation formulations. The charge results for both converge to the static equilibrium reference value q_{1r}. Unlike zero charge required for along-track equilibrium configuration at GEO, non-zero charge is required at L_2. For along-track

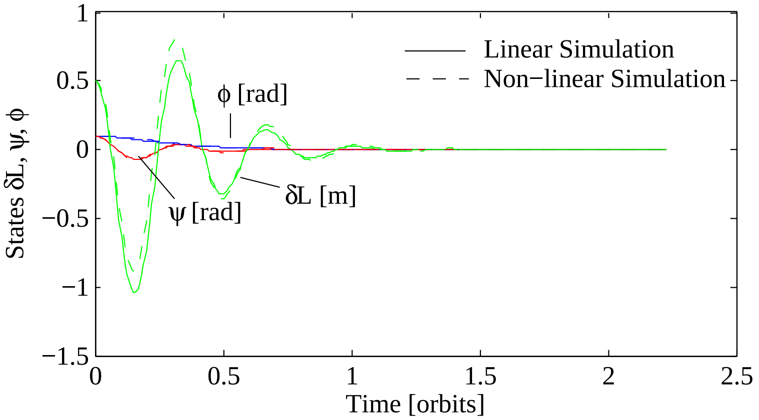

(a) Time Histories of Length Variations δL, In-plane Pitch Angle ψ, and Out-of-plane Yaw Angle ϕ

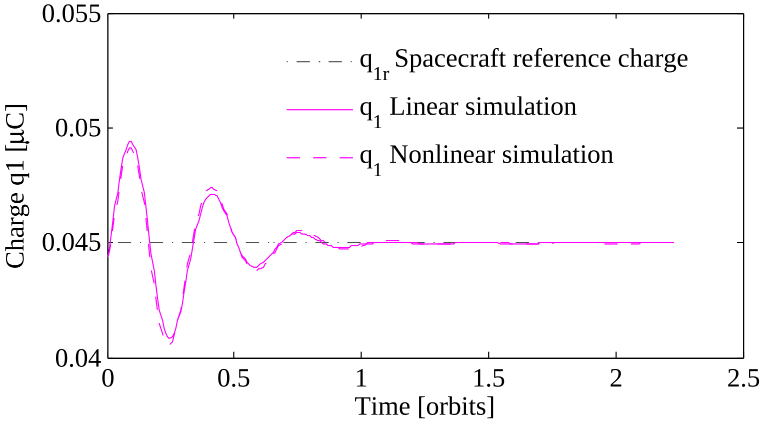

(b) Spacecraft Charge Time Histories

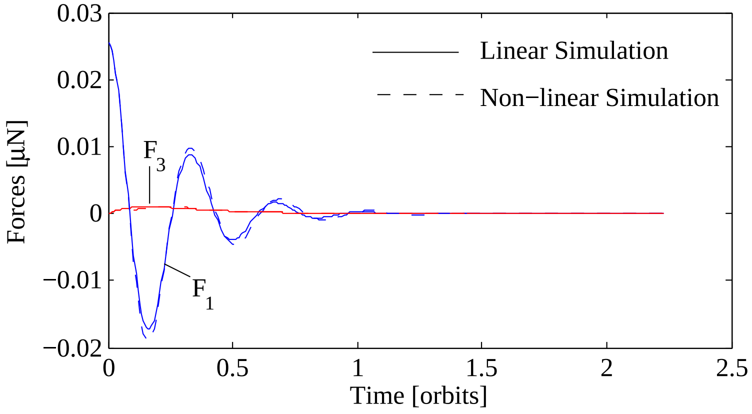

(c) Spacecraft Force Time Histories

Figure 4.5: Simulation Results at L_2 for Two-Craft in the Along-track Direction with a Separation distance of 25 m

equilibrium, the control charges q_1 and q_2 are both positive. Since the control charges are less than that of micro-Coulombs, they can easily be implemented in practice using charge emission devices. Figure 4.5(c) shows the thrusting force that is required to stabilize the angles which is less than micro-Newtons. To avoid plume impingement issues, the thrusting always takes place in the $\tilde{b}_1$ and $\tilde{b}_3$ directions perpendicular to the craft orientation which is along the $\tilde{b}_2$ axis. Furthermore, Figure 4.5 show that the non-linear simulations shown as dashed lines closely follow the linearized simulations shown as continuous lines.

4.1.3.2 Orbit Normal Configuration

Table 4.2 lists the simulation parameters and the values used for the orbit normal Coulomb tether configuration with a separation distance of 25 meter. The same spacecraft parameters and nominal separation distance are used as in Table 4.1. Table 4.2 lists the reference charge, n and β parameters, and the gains. The parameters n and β are selected based on root locus plot analysis. The gains $\tilde{C}_1$, $\tilde{C}_2$, $\tilde{K}_1$, $\tilde{K}_2$ and $\tilde{K}_3$ computed from Eq. (4.33) satisfy the stability criteria in Eq. (4.32) and also lead to effective damping. The two-craft Coulomb tether performance at the collinear libration point L_2 is simulated by integrating the linearized equations of motion in Eq. (4.30) and then compared with the results obtained from integrating the non-linear equations of motion in Eq. (4.8). In this simulation, in order to investigate the effects of linearization on the relative motion the Debye length is assumed to be zero.

Table 4.2: Input Parameters Used in Orbit Normal Simulation for L_2

Parameter	Value	Units
Q_{ref}	0.002946	μC^2
n	2.7	
β	2.5	
$\tilde{C}_1$	0	
$\tilde{C}_2$	$2\sqrt{3\sigma}$	
$\tilde{K}_1$	2.7	
$\tilde{K}_2$	$2+3\sigma$	
$\tilde{K}_3$	3.2596	

Figure 4.6(a) shows the Coulomb tether motion with the charge feedback law augmented with the thrust forces generated using conventional thrusters. The roll motion θ, yaw motion ϕ and the separation distance deviation δL asymptotically go to zero. Also, the separation distance error is critically damped and the motion stabilized after about 1.4 orbits. Figure 4.6(b) shows the spacecraft control charge q_1 usage for both the linear and non-linear simulation formulations. The charge results for both converge to the static equilibrium reference value q_{1r}. For orbit normal equilibrium, the control charges q_1 and q_2 are both positive. Since the control charges are less than that of micro-Coulombs, they can easily be implemented in practice using charge emission devices. Figure 4.6(c) gives the thrusting force that is required to stabilize the angles which is less than micro-Newton level. To avoid plume impingement issues, thrust force F_1 acts in the $\tilde{b}_1$ direction and thrust force F_2 acts in the $\tilde{b}_2$ direction both perpendicular to the craft orientation which is along the $\tilde{b}_3$ axis. Furthermore, Figure 4.6 show that the non-linear simulations closely match the linearized simulations justifying the linearization assumptions.

4.2 Linear Dynamics and Stability Analysis - Triangular Libration Points

4.2.1 Charged Relative Equations of Motion

4.2.1.1 Along-Track Configuration

This section derives the equations of motion of a two-craft Coulomb tether whose center of mass is at the triangular equilibrium point L_4 as shown in Figure 4.7 and nominally aligned in the along-track direction of the orbit frame. This derivation closely resembles the derivation of the equations of motion for a two-craft Coulomb tether at any collinear libration point given in section 4.1 The two distance vectors $\boldsymbol{R}_1$ and $\boldsymbol{R}_2$ of L_4 in the synodic frame from the two primaries in the plane are given by

$$ {}^{\mathcal{S}}\boldsymbol{R}_1 = \begin{bmatrix} r_{x_0} + d_1 \\ r_{y_0} \\ 0 \end{bmatrix} \quad \text{and} \quad {}^{\mathcal{S}}\boldsymbol{R}_2 = \begin{bmatrix} r_{x_0} - d_2 \\ r_{y_0} \\ 0 \end{bmatrix} \tag{4.34} $$

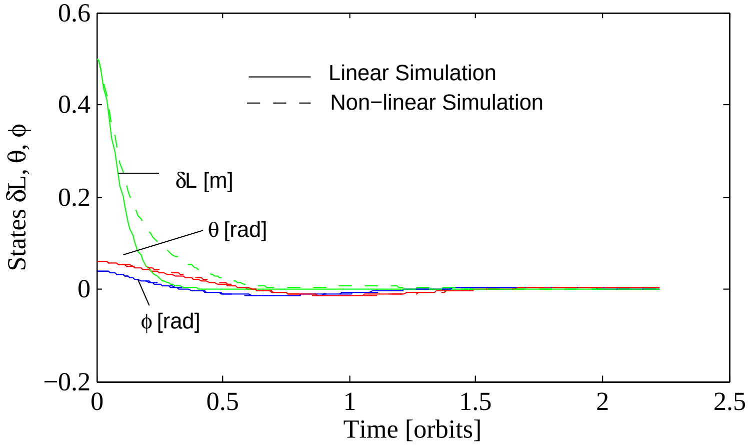

(a) Time Histories of Length Variations δL, Out-of-plane Yaw and Roll Angles ϕ and θ

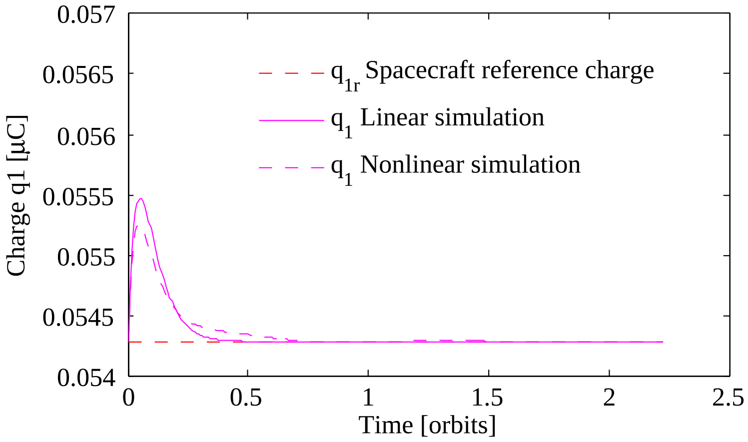

(b) Spacecraft Charge Time Histories

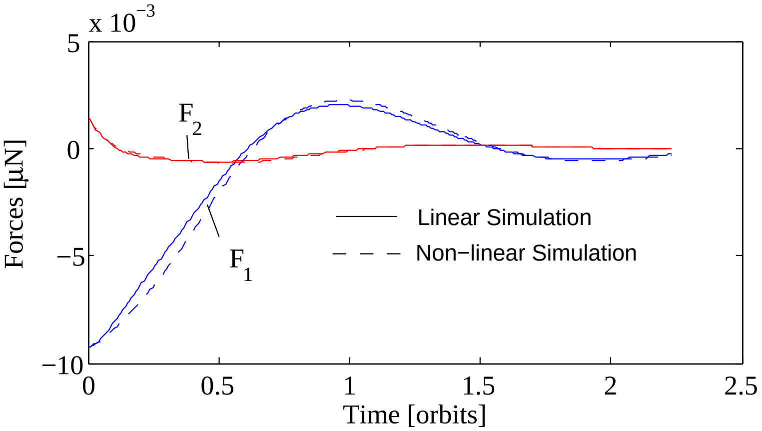

(c) Spacecraft Force Time Histories

Figure 4.6: Simulation Results at L_2 for Two-Craft in the Orbit Normal Direction with a Separation distance of 25 m

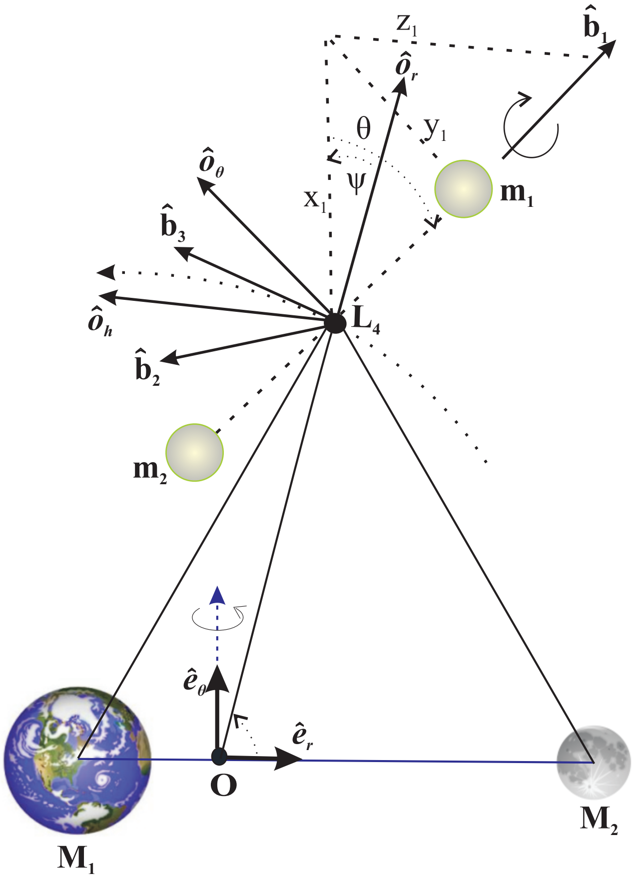

Figure 4.7: Euler Angles Representing the Attitude of Coulomb Tether with Respect to the Orbit Frame at L_4

where α is the angle between the synodic frame at the barycenter O and the orbiting frame at L_4 as shown in Figure 3.7. For Earth-moon system, the value of α is 60.31 degrees.[16]

Assuming the following definitions for the circularly restricted three-body system

$$A_\alpha = \cos\alpha + \sqrt{3}\sin\alpha \tag{4.35a}$$

$$B_\alpha = \sin\alpha - \sqrt{3}\cos\alpha \tag{4.35b}$$

$$C_\alpha = \cos\alpha - \sqrt{3}\sin\alpha \tag{4.35c}$$

$$D_\alpha = \sin\alpha + \sqrt{3}\cos\alpha \tag{4.35d}$$

and from the Lagrangian formulation the nonlinear equations governing the yaw angle ϕ out of the orbital plane, the pitch angle ψ in the orbital plane, and the separation distance L become

$$\begin{aligned}
&\ddot{\phi} + \frac{2\dot{L}}{L}\dot{\phi} + \cos\phi\,\sin\phi((\dot{\psi}+\Omega)^2 \\
&\quad + \frac{3}{4}\Omega^2((1-\nu)(A_\alpha\,\sin\psi + B_\alpha\,\cos\psi)^2 + \nu(C_\alpha\,\sin\psi + D_\alpha\,\cos\psi)^2)) = 0 && (4.36a)\\
&\ddot{\psi} - 2(\dot{\psi}+\Omega)(\dot{\phi}\tan\phi - \frac{\dot{L}}{L}) - \frac{3}{4}\Omega^2((1-\nu)(A_\alpha\,\sin\psi + B_\alpha\,\cos\psi)(A_\alpha\,\sin\psi - B_\alpha\,\cos\psi) \\
&\quad + \nu(C_\alpha\,\sin\psi + D_\alpha\,\cos\psi)(C_\alpha\,\cos\psi - D_\alpha\,\sin\psi) = 0 && (4.36b)\\
&\ddot{L} - L(\dot{\phi}^2 + (\dot{\psi}+\Omega)^2\cos^2\phi - \Omega^2 \\
&\quad + \frac{3}{4}\cos^2\phi((1-\nu)(A_\alpha\,\sin\psi + B_\alpha\,\cos\psi)^2 + \nu(C_\alpha\,\sin\psi + D_\alpha\,\cos\psi)^2) \\
&\quad + \frac{k_c}{m_1}Q\frac{1}{L^2}\frac{m_1+m_2}{m_2} = 0 && (4.36c)
\end{aligned}$$

The linearized version of the nonlinear equations in Eq. (4.36) comes from expanding in a Taylor series about the equilibrium states given in Eq. (4.9). Both the roll and pitch equations of motion are linearized about small roll and pitch angles respectively. The separation distance equations of motion are linearized about small variations in δL as well as small variations in the product charge term δQ defined as in Eq. (4.6).

Mission requirements determine the reference separation length L_{ref}, and, Q_{ref} is determined from the following constraint on a particular choice of L_{ref}

$$Q_{\text{ref}} = -\frac{3}{4}\sigma_{EQAT1}\Omega^2\frac{L_{\text{ref}}^3}{k_c}\frac{m_1 m_2}{m_1+m_2} \tag{4.37}$$

where

$$\sigma_{EQAT1} = 1 + 2\cos^2\alpha + \sqrt{3}\sin 2\alpha\,(2\nu - 1) \tag{4.38}$$

Performing the necessary linearizations yields

$$\ddot{\phi} + (1 + \frac{3}{4}\sigma_{EQAT1})\Omega^2\phi = 0 \tag{4.39a}$$

$$\ddot{\psi} + \frac{2\Omega}{L_{\text{ref}}}\delta\dot{L} - \frac{3}{2}\sigma_{EQAT3}\Omega^2\,\psi = 0 \tag{4.39b}$$

$$\delta\ddot{L} - 2\Omega L_{\text{ref}}\dot{\psi} - \frac{9}{4}\sigma_{EQAT1}\Omega^2\delta L - \frac{3}{2}\,\sigma_{EQAT2}\Omega^2 L_{\text{ref}}\,\psi - (\frac{k_c}{m_1}\frac{1}{L_{\text{ref}}^2}\frac{m_1+m_2}{m_2})\delta Q = 0 \tag{4.39c}$$

with

$$\sigma_{EQAT2} = \sqrt{3}\cos 2\alpha\,(2\nu - 1) - \sin 2\alpha \tag{4.40}$$

$$\sigma_{EQAT3} = \sqrt{3}\sin 2\alpha\,(1 - 2\nu) \tag{4.41}$$

Thus, Eqs. (4.39a) and (4.39b) represent the linearized attitude dynamics of the Coulomb tether body frame $\mathcal{B}$ and Eq. (4.39c) represents the linearized separation distance differential equation about the static along-track reference configuration at a triangular libration point. As opposed to the collinear solution, the ψ and δL terms here are the new components; however, due to the quite small values of $\sigma_{EQAT1} = 0.03633$ and $\sigma_{EQAT2} = 2.04056 \times 10^{-4}$ at L_4, its effect is negligible on the separation distance differential equation. Furthermore, since $\sigma_{EQAT3} = 1.45432$, the dynamics at L_4 become similar to those found in Reference 5 for along-track 2-craft formation at GEO. Hence, the stability behaviour should be approximately the same as that observed in Reference 5.

4.2.1.2 Orbit Normal Configuration

This section derives the equations of motion of a two-craft Coulomb tether whose center of mass is at the triangular equilibrium point L_4 as shown in Figure 3.7 and nominally aligned in the orbit-normal direction of the orbit frame. This derivation closely resembles the derivation of the equations of motion for a two-craft Coulomb tether at any collinear libration point given in section 4.1. The synodic frame setup is already explained in section 4.1. Using the Lagrangian formulation, The nonlinear equations governing the yaw angle ϕ

and the roll angle θ out of the orbital plane, and the separation distance L become

$$\begin{aligned}
&\ddot{\phi} + \frac{2\dot{L}}{L}(\dot{\phi} - \Omega\sin\theta) - \Omega\dot{\theta}\cos\theta - \frac{1}{4}((\Omega^2\cos 2\theta + \Omega^2 - 2\dot{\theta}^2)\sin 2\phi + 4\Omega\dot{\theta}\cos\theta\cos 2\phi) \\
&\quad - \frac{3\Omega^2}{4}((1-\nu)(A_\alpha\cos\phi\sin\theta + B_\alpha\sin\phi)(-A_\alpha\sin\phi\sin\theta + B_\alpha\cos\phi) \\
&\quad + \nu(C_\alpha\cos\phi\sin\theta + D_\alpha\sin\phi)(-C_\alpha\sin\phi\sin\theta + D_\alpha\cos\phi)) = 0
\end{aligned} \tag{4.42a}$$

$$\begin{aligned}
&\ddot{\theta} + 2\frac{\dot{L}}{L}(\dot{\theta} + \Omega\cos\theta\tan\phi) - \frac{1}{2}\Omega^2\sin 2\theta + \Omega\dot{\phi}\cos\theta\sec^2\phi \\
&\quad - 2\dot{\theta}\dot{\phi}\tan\phi + \Omega\dot{\phi}\cos\theta\cos 2\phi\sec^2\phi \\
&\quad - \frac{3}{4}\Omega^2((1-\nu)((A_\alpha^2\sin\theta + A_\alpha B_\alpha\tan\phi) + \nu(C_\alpha^2\sin\theta + C_\alpha D_\alpha\tan\phi)) = 0
\end{aligned} \tag{4.42b}$$

$$\begin{aligned}
&\ddot{L} - \frac{L}{4}(3\Omega^2 + 2\dot{\theta}^2 + 4\dot{\phi}^2 - 2\Omega^2\cos 2\theta\cos^2\phi - (\Omega^2 - 2\dot{\theta}^2)\cos 2\phi \\
&\quad - 8\Omega\dot{\phi}\sin\theta + 4\Omega\dot{\theta}\cos\theta\sin 2\phi) + \Omega^2 L \\
&\quad - \frac{3}{4}\Omega^2 L((1-\nu)(A_\alpha\cos\phi\sin\theta + B_\alpha\sin\phi)^2 + \nu(C_\alpha\cos\phi\sin\theta + D_\alpha\sin\phi)^2) \\
&\quad + \frac{k_c}{m_1}Q\frac{1}{L^2}\frac{m_1 + m_2}{m_2} = 0
\end{aligned} \tag{4.42c}$$

where

$$A_\alpha = \cos\alpha + \sqrt{3}\sin\alpha \tag{4.43a}$$

$$B_\alpha = \sin\alpha - \sqrt{3}\cos\alpha \tag{4.43b}$$

$$C_\alpha = -\cos\alpha + \sqrt{3}\sin\alpha \tag{4.43c}$$

$$D_\alpha = -(\sin\alpha + \sqrt{3}\cos\alpha) \tag{4.43d}$$

The linearized version of the nonlinear equations in Eq. (4.42) comes from expanding in a Taylor series about the equilibrium states given in Eq. (4.9). Both the yaw and roll equations of motion are linearized about small yaw and roll angles respectively. The separation distance equations of motion are linearized about small variations in δL as well as small variations in the product charge term δQ defined as in Eq. (4.6).

Mission requirements determine the reference separation length L_{ref}, and, Q_{ref} is determined from the following constraint on a particular choice of L_{ref}

$$Q_{\text{ref}} = \Omega^2 \frac{L_{\text{ref}}^3}{k_c} \frac{m_1 m_2}{m_1 + m_2} \tag{4.44}$$

where

$$\sigma_{EQON1} = 1 + 2\cos^2\alpha + \sqrt{3}\sin 2\alpha\,(2\nu - 1) \tag{4.45}$$

Performing the necessary linearizations yields

$$\ddot{\phi} - (1 + \frac{3}{4}\sigma_{EQON1})\Omega^2\phi - \frac{3}{4}\sigma_{EQON2}\Omega^2\theta - 2\Omega\dot{\theta} = 0 \tag{4.46a}$$

$$\ddot{\theta} - (1 + \frac{3}{4}\sigma_{EQON3})\Omega^2\theta - \frac{3}{4}\sigma_{EQON2}\Omega^2\phi + 2\Omega\dot{\phi} = 0 \tag{4.46b}$$

$$\delta\ddot{L} + 3\Omega^2\delta L - (\frac{k_c}{m_1}\frac{1}{L_{\text{ref}}^2}\frac{m_1 + m_2}{m_2})\delta Q = 0 \tag{4.46c}$$

with

$$\sigma_{EQON2} = \sqrt{3}\cos 2\alpha\,(2\nu - 1) - \sin 2\alpha \tag{4.47}$$

$$\sigma_{EQON3} = 1 + 2\sin^2\alpha + \sqrt{3}\sin 2\alpha\,(1 - 2\nu) \tag{4.48}$$

Thus, Eqs. (4.46a) and (4.46b) represent the linearized attitude dynamics of the Coulomb tether body frame $\mathcal{B}$ and Eq. (4.46c) represents the linearized separation distance differential equation about the static orbit-normal reference configuration at a triangular libration point. As opposed to the collinear solution, the θ term in Eq. (4.46a) and the ψ term in Eq. (4.46b) are the new components; however, due to the quite small value of $\sigma_{EQRE2} = 2.04055 \times 10^{-4}$ at L_4, its effect is negligible on the coupled attitude differential equations. The separation distance differential equation is exactly the same to that found in Reference 5 for orbit-normal 2-craft formation at GEO. Furthermore, since $\sigma_{EQRE1} = 0.03633$ and $\sigma_{EQRE3} = 3.9636$, the dynamics at L_4 become very similar to those found in Reference 5. Hence, the stability behaviour should be approximately the same as that observed in Reference 5.

4.2.2 Hybrid Feedback Control Development

4.2.2.1 Along-Track Configuration

Using the out-of-plane angle $\dot{\phi}$ feedback from Eq.(4.14) for ϕ differential equation, in-plane angle ψ feedback from Eq.(4.22) for ψ equation, and proportional-derivative feedback control of δL from Eq.(4.12), the orbit rate Ω independent linearized equations of motion for a two-craft Coulomb tether formation at the triangular libration point L_4 are given by

$$\phi'' + \tilde{K}_2\phi' + (1 + \frac{3}{4}\sigma_{EQAT1})\phi = 0 \tag{4.49a}$$

$$\psi'' + \frac{2}{L_{\text{ref}}}\delta L' - (\frac{3}{2}\sigma_{EQAT3} - \tilde{K}_1)\psi = 0 \tag{4.49b}$$

$$\delta L'' + \tilde{C}_2\delta L' - 2L_{\text{ref}}\psi' + (\tilde{C}_1 - \frac{9}{4}\sigma_{EQAT1})\delta L - \frac{3}{2}\sigma_{EQAT2}L_{\text{ref}}\,\psi = 0 \tag{4.49c}$$

where $\tilde{C}_1 = \frac{C_1}{\Omega^2}$, $\tilde{C}_2 = \frac{C_2}{\Omega}$, $\tilde{K}_1 = \frac{K_1}{\Omega^2}$ and $\tilde{K}_2 = \frac{K_2}{\Omega}$ are non-dimensionalized feedback gains. Routh-Hurwitz stability criteria can be used to fine tune these gain values that satisfy the stability requirements. The characteristic equation for the coupled δL and ψ equation is

$$\begin{aligned}\lambda^4 + \tilde{C}_2\lambda^3 + (4 + \tilde{C}_1 - \frac{9}{4}\sigma_{EQAT1} - \frac{3}{2}\sigma_{EQAT3})\lambda^2 + \ (\tilde{C}_2\tilde{K}_1 + 3\sigma_{EQAT2} - \frac{3}{2}\tilde{C}_2\sigma_{EQAT3})\\ + (\tilde{C}_1\tilde{K}_1 - \frac{9}{4}\tilde{K}_1\sigma_{EQAT1} - \frac{3}{2}\tilde{C}_1\sigma_{EQAT3} + \frac{27}{8}\sigma_{EQAT1}\sigma_{EQAT3}) = 0\end{aligned} \tag{4.50}$$

Roots of this equation should have negative real parts for asymptotic stability. A Routh table allows one to determine the following necessary constraints on the gains $\tilde{C}_1$, $\tilde{C}_2$ and $\tilde{K}_1$ that ensures all roots have negative real parts

$$\tilde{C}_1 > \frac{9}{4}\sigma_{EQAT1} \tag{4.51a}$$

$$\tilde{C}_2 > \frac{3}{4}\sigma_{EQAT2} \tag{4.51b}$$

$$\tilde{K}_1 > \frac{3}{2}\sigma_{EQAT3} \tag{4.51c}$$

To fix the gain values that satisfy the stability criteria in Eq. (4.51), near ideal damping conditions are assumed. Let the scaling factors n_1, n_2 and β be positive and real such that the gains are rewritten as

$$\tilde{C}_1 = n_1 > \frac{9}{4}\sigma_{EQAT1} \tag{4.52a}$$

$$\tilde{C}_2 = \beta\sqrt{n_1} \tag{4.52b}$$

$$\tilde{K}_1 = n_2 > \frac{3}{2}\sigma_{EQAT3} \tag{4.52c}$$

The natural frequency of the ψ equation is $\sqrt{n_2 - \frac{3}{2}\sigma_{EQAT3}}$ and the natural frequency for the δL equation is $\sqrt{n_1 - \frac{9}{4}\sigma_{EQAT1}}$. For the ψ' coupling term in the δL equation to serve as a defacto damping term, n_1 and n_2 are chosen in such a way that these frequencies match. The value of n_2 is chosen as $4\sigma_{EQAT3}$ and for this fixed n_2 value, the root locus for the coupled δL and ψ equations is studied for a range of β values in the vicinity of $\beta = 2$, with n_1 varying from 0.1 to 5. The root locus plot analysis yield the scaling factors to be $\beta = 2.0$ and $n_1 = 2.2$. The out-of-plane angle ϕ can be asymptotically stabilized by using an equal and opposite thrust force F_3 on both the satellites along the $\hat{b}_3$ axis. The out-of-plane angle feedback gain $\tilde{K}_2 = 2$ yields critical damping.

4.2.2.2 Orbit Normal Configuration

For orbit normal configuration at the triangular libration point, the same line of reasoning discussed for collinear libration points is followed here. Using the out-of-plane angle and angle rate $\phi, \dot{\phi}$ feedback from Eq.(4.29) for ϕ differential equation, out-of-plane angle θ feedback from Eq.(4.28) for θ equation, and proportional-derivative feedback control of δL from Eq.(4.26), the orbit rate Ω independent linearized equations of motion for a two-craft Coulomb tether formation at the triangular libration point L_4 are given by

$$\phi'' - 2\theta' + (\tilde{K}_1 - 1 - \frac{3}{4}\sigma_{EQON1})\phi - \frac{3}{4}\sigma_{EQON2}\theta + \tilde{K}_3\phi' = 0 \tag{4.53a}$$

$$\theta'' + (\tilde{K}_2 - 1 - \frac{3}{4}\sigma_{EQON3})\theta - \frac{3}{4}\sigma_{EQON2}\phi + 2\phi' = 0 \tag{4.53b}$$

$$\delta L'' + (\tilde{C}_1 + 3)\delta L + \tilde{C}_2\delta L' = 0 \tag{4.53c}$$

where $\tilde{C}_1 = \frac{C_1}{\Omega^2}$, $\tilde{C}_2 = \frac{C_2}{\Omega}$, $\tilde{K}_1 = \frac{K_1}{\Omega^2}$, $\tilde{K}_2 = \frac{K_2}{\Omega^2}$ and $\tilde{K}_3 = \frac{K_3}{\Omega}$ are non-dimensionalized feedback gains. Routh-Hurwitz stability criteria can be used to fine tune these gain values that satisfy the stability requirements. The characteristic equation for the coupled ϕ and θ equations is

$$\begin{aligned}
&\lambda^4 + \tilde{K}_3\lambda^3 + (2 + \tilde{K}_1 + \tilde{K}_2 - \frac{3}{4}(\sigma_{EQON1} + \sigma_{EQON3}))\lambda^2 \\
&\quad + \tilde{K}_3(\tilde{K}_2 - 1 - \frac{3}{4}\sigma_{EQON3})\lambda + 1 - \tilde{K}_1 - \tilde{K}_2 + \tilde{K}_1\tilde{K}_2 + \frac{3}{4}\sigma_{EQON1} - \frac{3}{4}\sigma_{EQON1} \\
&\quad - \frac{9}{16}\sigma^2_{EQON2} + \frac{3}{4}\sigma_{EQON3} - \frac{3}{4}\tilde{K}_1\sigma_{EQON3} + \frac{9}{16}\sigma_{EQON1}\sigma_{EQON3} = 0 \qquad (4.54)
\end{aligned}$$

Roots of this equation should have negative real parts for asymptotic stability. A Routh table allows one to determine the following necessary constraints on the gains

$$\tilde{K}_1 > \frac{3}{4}\sigma_{EQON1} - 3 \qquad (4.55a)$$

$$\tilde{K}_2 > 1 + \frac{3}{4}\sigma_{EQON3} - \frac{9}{64}\sigma^2_{EQON2} \qquad (4.55b)$$

$$\tilde{K}_3 > 0 \qquad (4.55c)$$

To fix the gain values that satisfy the stability criteria in Eq. (4.55), near ideal damping conditions are assumed. Let the scaling factors n and β be positive and real such that the gains $\tilde{K}_1$ and $\tilde{K}_3$ are rewritten as

$$\tilde{K}_1 = n > \frac{3}{4}\sigma_{EQON1} - 3 \qquad (4.56a)$$

$$\tilde{K}_3 = \beta\sqrt{n-1} \qquad (4.56b)$$

In the equation of motion for ϕ, ignoring the $\dot{\theta}$ term guarantees critical damping. Fixing values of $\tilde{K}_2 > 1 + \frac{3}{4}\sigma_{EQON3} - \frac{9}{64}\sigma^2_{EQON2}$, the root locus is analyzed for the coupled ϕ and θ equations for a range of β values in the vicinity of β= 2 with n varying from 1.1 to 10. For $\tilde{K}_2 = 2 + \frac{3}{4}\sigma_{EQON3} - \frac{9}{64}\sigma^2_{EQON2}$, root locus analysis yields the optimal scaling factors to be β= 2.5 and $n = 2.7$.

Table 4.3: Input Parameters Used in Along-track Simulation for L_4

Parameter	Value	Units
Q_{ref}	-2.51682×10^{-5}	μC^2
n_1	2.2	
β	2.0	
σ_{EQAT1}	0.036337	
σ_{EQAT2}	2.04056×10^{-4}	
σ_{EQAT3}	1.45432	
$\tilde{C}_1$	2.2	
$\tilde{C}_2$	2.91083	
$\tilde{K}_1$	5.81728	
$\tilde{K}_2$	2	

4.2.3 Numerical Simulation

4.2.3.1 Along-Track Configuration

The along-track Coulomb tether with a separation distance of 25 meter is simulated at L_4. The same spacecraft parameters and nominal separation distance are used as in Table 4.1. Table 4.3 lists the reference charge, parameters, and the gains. The parameters n_1 and β are selected based on root locus plot analysis. The gains $\tilde{C}_1$, $\tilde{C}_2$ and $\tilde{K}_1$ computed from Eq. (4.52) satisfy the stability criteria in Eq. (4.51) and lead to effective damping. The two-craft Coulomb tether performance at the triangular libration point L_4 is simulated by integrating the linearized equations of motion in Eqs. (4.49) and then compared with the results obtained from integrating the non-linear equations of motion in Eq. (4.36). During this simulation, the Debye length is assumed to be zero in order to investigate the effects of linearization on the relative motion. Figure 4.8(a) shows the Coulomb tether motion with the charge feedback law augmented with the thrust forces generated using conventional thrusters. The pitch motion ψ, yaw motion ϕ and the separation distance deviation δL converged to zero. Also, stabilizing the separation distance to zero also stabilized the in-plane rotation angle after about 1.4 orbits. Figure 4.8(b) shows the spacecraft control charge q_1 usage for both the linear and non-linear simulation formulations. The charge results for

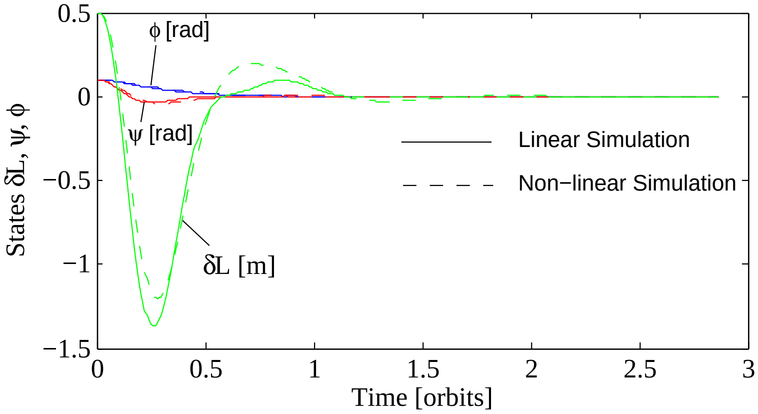

(a) Time Histories of Length Variations δL, In-plane Pitch Angle ψ, and Out-of-plane Yaw Angle ϕ

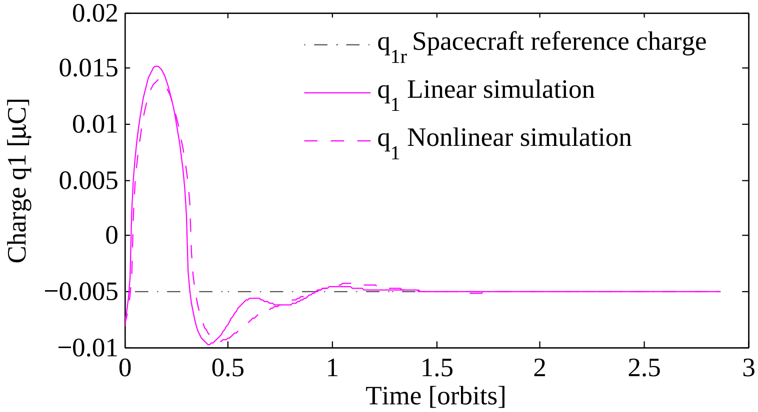

(b) Spacecraft Charge Time Histories

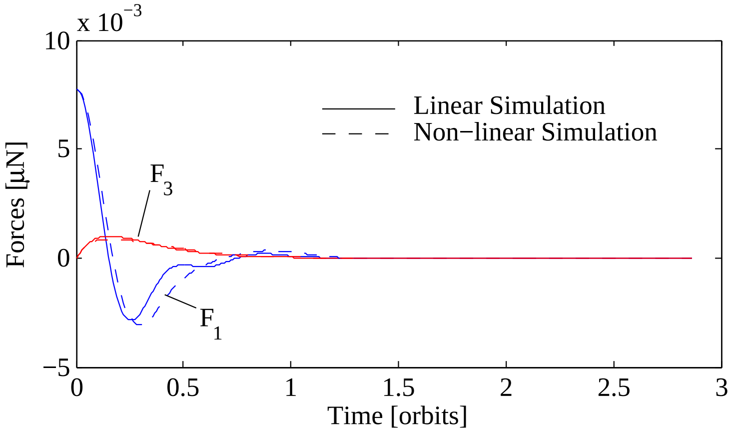

(c) Spacecraft Force Time Histories

Figure 4.8: Simulation Results at L_4 for Two-Craft in the Along-Track Direction with a Separation distance of 25 m

both converge to the static equilibrium reference value q_{1r}. Unlike zero charge required for along-track equilibrium configuration at GEO, non-zero charge is required at L_4. However, the non-zero reference charge (-2.51682$\times 10^{-5}\mu$C^2) is very small compared to that of at L_2 (0.002946 μC^2). For along-track equilibrium at L_4, the control charge q_1 is the negative of q_2. Since the control charges are less than that of micro-Coulombs, they can easily be implemented in practice using charge emission devices. Figure 4.8(c) gives the micro-Newton level thrusting force that is required to stabilize the angles. To avoid plume impingement issues, the thrusting always takes place in the $\tilde{b}_1$ and $\tilde{b}_3$ directions perpendicular to the craft orientation which is along the $\tilde{b}_2$ axis. Furthermore, Figure 4.8 show that the non-linear simulations shown as dashed lines closely follow the linearized simulation shown as continuous lines.

4.2.3.2 Orbit Normal Configuration

The orbit normal Coulomb tether with a separation distance of 25 meter is simulated at L_4. The same spacecraft parameters and nominal separation distance are used as in Table 4.2. Table 4.4 lists the reference charge, parameters, and the gains. The parameters n and β are selected based on root locus plot analysis. The gains $\tilde{C}_1$, $\tilde{C}_2$ and $\tilde{K}_1$ computed from Eq. (4.56) satisfy the stability criteria in Eq. (4.55) and lead to effective damping. The two-craft Coulomb tether performance at the triangular libration point L_4 is simulated by integrating the linearized equations of motion in Eqs. (4.53) and then compared with the results obtained from integrating the non-linear equations of motion in Eq. (4.42). During this simulation, the Debye length is assumed to be zero.

Figure 4.9(a) shows the tether motion, charge on a single craft and thrust forces, respectively. Similar to the results at L_2, the Coulomb tether motion at L_4 uses the charge feedback law augmented with the thrust forces. The roll motion θ, yaw motion ϕ and the separation distance deviation δL asymptotically go to zero and the motion is stabilized after about 1.3 orbits. Figure 4.9(b) shows that the charge results for both both the linear and non-linear simulation formulations converge to the static equilibrium reference value q_{1r}. For orbit normal equilibrium at L_4, the control charges q_1 and q_2 are both positive. To avoid plume

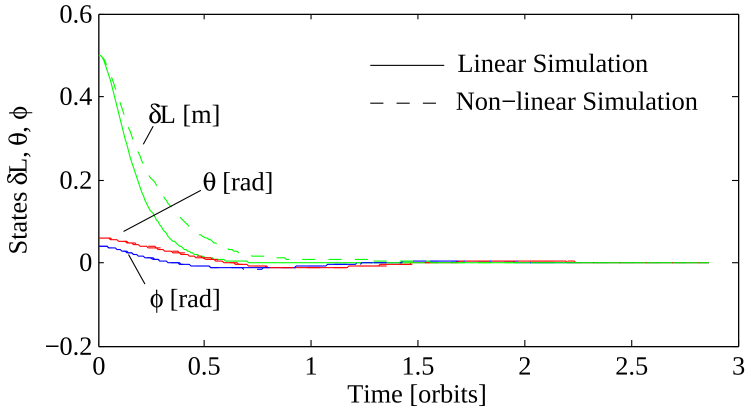

(a) Time Histories of Length Variations δL, Out-of-plane Yaw and Roll Angles ϕ and θ

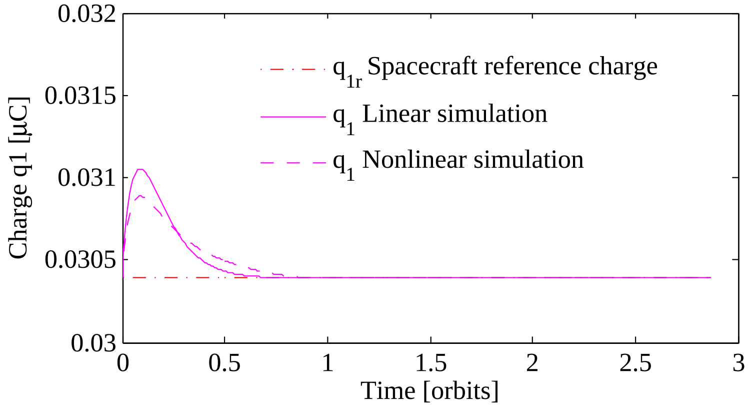

(b) Spacecraft Charge Time Histories

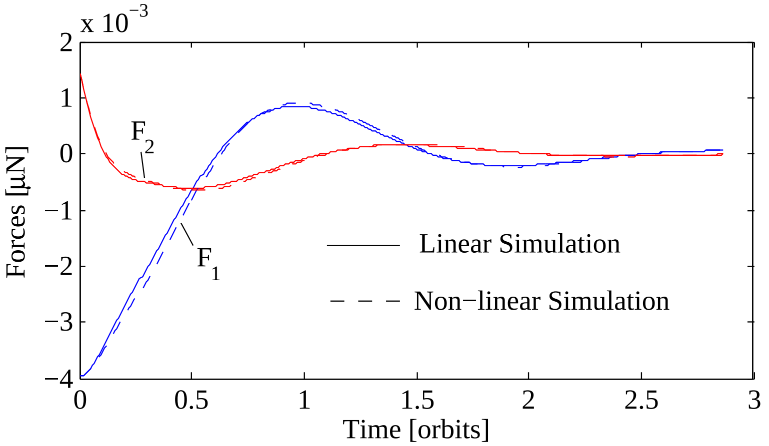

(c) Spacecraft Force Time Histories

Figure 4.9: Simulation Results at L_4 for Two-Craft in the Orbit Normal Direction with a Separation distance of 25 m

Table 4.4: Input Parameters Used in Orbit Normal Simulation for L_4

Parameter	Value	Units
Q_{ref}	9.23505×10^{-4}	μC^2
n	2.7	
β	2.5	
σ_{EQON1}	0.036337	
σ_{EQON2}	2.04056×10^{-4}	
σ_{EQON3}	3.96366	
$\tilde{C}_1$	0	
$\tilde{C}_2$	3.4641	
$\tilde{K}_1$	2.7	
$\tilde{K}_2$	4.97274	
$\tilde{K}_3$	3.25960	

impingement issues, thrust force F_1 acts in the $\tilde{b}_1$ direction and thrust force F_2 acts in the $\tilde{b}_2$ direction both perpendicular to the craft orientation which is along the $\tilde{b}_3$ axis. Furthermore, Figure 4.9 show that the non-linear simulations depicted as dashed lines closely follow the linearized simulations depicted as continuous lines justifying the linearization assumptions.

4.3 Summary

The feasibility of a two-craft Coulomb formation concept is studied at libration points for along-track and orbit normal equilibria. The assumption is that the sunlit areas of the two-craft are equal such that the differential solar radiation pressure on the formation is zero. The new two-craft dynamics at the libration points provide a general framework in which circular Earth orbit dynamics form a special case. The general equations of motion for collinear libration points have a σ parameter which varies for each collinear libration point. Interestingly, setting "$\sigma = 1$" yields the same equations of motion for along-track and orbit normal equilibrium configurations in circular Earth orbits.[5] Though there are additional terms in the equations of motion for along-track and orbit normal equilibrium configurations at the triangular libration points, the effect of these additional terms on the dynamics is small. Therefore, the dynamics and the stability conditions are similar to those found in

Reference 5 for along-track and orbit normal equilibrium 2-craft formation at GEO. Both virtual Coulomb tether configurations are stabilized with a hybrid control of Coulomb forces and conventional thrusters that stabilize the separation distance and orientation respectively. The control charges needed are very small, on an order much less than micro-Coulombs and thus, realizable in practice. The thrusting forces required are less than micro-Newtons in magnitude and are applied in orthogonal directions. Numerical simulations illustrating the linearized performance predictions are compared against nonlinear system responses.

Chapter 5

OPTIMAL RECONFIGURATIONS OF TWO-CRAFT COULOMB FORMATION IN CIRCULAR ORBITS

The second part of the thesis investigates optimal reconfigurations of a two-craft Coulomb formation in circular Earth orbits by applying nonlinear optimal control techniques. The objective of these reconfigurations is to maneuver the two-craft formation between two charged equilibria configurations. The four optimality criteria considered are minimum reconfiguration time, minimum acceleration of the separation distance, minimum Coulomb and electric propulsion fuel usage, and minimum electrical power consumption. The goal is to determine optimal reconfigurations maximizing the use of Coulomb propulsion while minimizing the electric propulsion usage.

In this chapter, the basic optimal control problem for the general nonlinear system is discussed with state-control constraints such that a performance measure is minimized.[27,28,33] The application of the Pontryagin's Minimum Principle yields the necessary conditions for optimal control. Then, for a two spacecraft Coulomb formation in circular Earth orbits, the nondimensionalized nonlinear equations of motion are derived. The optimal control problem formulations for a two-craft formation are discussed with the choices of the cost function, control variables and constraints, and, for the problem formulations at hand, the Pontryagin's necessary conditions are presented. Three solution methods for discretizing the optimal control problem are explored: the indirect multiple shooting method,[26] the direct penalty function method,[29] and the pseudospectral method.[30] To solve the optimal control problems in this chapter, the pseudospectral method is eventually chosen over multiple shooting and direct penalty function methods.

Numerical simulations consider different optimal reconfigurations of a two-craft Coulomb virtual tether formation in circular GEO orbits: radial, along-track and orbit normal spacecraft separation distance expansion and contraction maneuvers, radial to along-track and radial to orbit-normal maneuvers, and a family of radial to along-track maneuvers. The reconfiguration between equilibra is considered by varying the desired separation distance. In a radial relative equilibrium configuration, only the Coulomb force is required for controlling the in-plane motion and for steering the satellites from their initial to their final radial position. In this reconfiguration maneuver, the gravity gradient torque stabilizes the in-plane motion. For along-track and orbit normal equilibrium locations, the reconfiguration maneuver requires hybrid controls. Here the Coulomb force is varied to control the separation distance and inertial micro-thrusters are activated for transverse control. In-plane radial to along-track maneuvers and out-of-plane radial to orbit-normal maneuvers with constant separation distance at the initial and final positions are investigated. Additionally, a family of radial to along-track maneuvers with fixed separation distance in the radial direction but varying final separation distance in the along-track equilibrium are investigated as well. Pseudo-spectral methods are used to numerically solve the two-point boundary value problem. Pontryagin's Minimum Principle verifies the open loop solutions' optimality.

5.1 The Optimal Control Problem

The general family of optimal control problems considered in this thesis can be stated as follows:[33] determine the state-control function pair, $\boldsymbol{x}(t), \boldsymbol{u}(t)$ over $[t_0, t_f]$ that minimize the cost functional,

$$J[\boldsymbol{x}(t), \boldsymbol{u}(t)] = E(\boldsymbol{x}(t_f), t_f) + \int_{t_0}^{t_f} F(\boldsymbol{x}(t), \boldsymbol{u}(t))dt \tag{5.1}$$

subject to

$$\text{equations of motion} \qquad \boldsymbol{f}(\boldsymbol{x}(t), \boldsymbol{u}(t)) - \dot{\boldsymbol{x}}(t) = 0 \tag{5.2}$$

$$\text{boundary constraints} \qquad \boldsymbol{r}(\boldsymbol{x}(t_0), \boldsymbol{x}(t_f)) = 0 \tag{5.3}$$

$$\text{path constraints} \qquad \boldsymbol{h}(\boldsymbol{x}(t), \boldsymbol{u}(t)) \leq 0 \tag{5.4}$$

where the functions E and F are called the *endpoint cost* and *running cost* respectively. The calculus of variations method can be used in solving the optimal control problem (OCP) subject to the conditions imposed at the initial and final time. Using this method, the cost functional takes a second form in terms of the adjoint variables. So, to conveniently formulate the problem and solve it as a two point boundary problem a control (or Pontryagin's) Hamiltonian is defined as

$$\mathcal{H}(\boldsymbol{x}(t), \boldsymbol{u}(t), \boldsymbol{\lambda}(t)) = F(\boldsymbol{x}(t), \boldsymbol{u}(t)) + \boldsymbol{\lambda}^T(t)\boldsymbol{f}(\boldsymbol{x}(t), \boldsymbol{u}(t)) \tag{5.5}$$

where $\boldsymbol{\lambda}(t)$ are the adjoint variables. The vanishing of the gradient of the Hamiltonian $\mathcal{H}$ provides the Pontryagin's necessary conditions for optimal control. According to the minimum principle, at each instant of time, $t \in [t_0^*, t_f^*]$, select an optimal control value, $\boldsymbol{u}^*$, which globally minimizes the Hamiltonian function with $\mathcal{H}$ considered as a function of $\boldsymbol{u}$ only. Therefore, $\boldsymbol{u}^*$ must satisfy the Hamiltonian minimization condition (HMC),

$$(HMC) \begin{cases} \underset{\boldsymbol{u}}{\text{Minimize}} & \mathcal{H}(\boldsymbol{x}(t), \boldsymbol{u}(t), \boldsymbol{\lambda}(t)) \\ \text{subject to} & \boldsymbol{h}^L \leq \boldsymbol{h}(\boldsymbol{x}(t), \boldsymbol{u}(t)) \leq \boldsymbol{h}^U \\ & \boldsymbol{u}^L \leq \boldsymbol{u}(t) \leq \boldsymbol{u}^U \end{cases} \tag{5.6}$$

which generates a control function, $(\boldsymbol{x}(t), \boldsymbol{\lambda}(t)) \longmapsto \boldsymbol{u}^*(t)$, which is a candidate for minimizing the cost. Also, the control space is state dependent as well. Considering the bounded state-control constraints a constrained calculus of variations problem can be reformulated as an unconstrained one by applying the Karush−Kuhn−Tucker (KKT) conditions to the HMC problem. The KKT conditions for a nonlinear programming problem provide the *gradient normality condition* and the *complementarity conditions.* The KKT conditions can be obtained by forming the Lagrangian of the Hamiltonian, $\bar{\mathcal{H}}$,

$$\bar{\mathcal{H}}(\boldsymbol{x}(t), \boldsymbol{u}(t), \boldsymbol{\lambda}(t)) = \mathcal{H}(\boldsymbol{x}(t), \boldsymbol{u}(t), \boldsymbol{\lambda}(t)) + \boldsymbol{\mu}_h^T \boldsymbol{h}(\boldsymbol{x}(t), \boldsymbol{u}(t)) + \boldsymbol{\mu}_x^T \boldsymbol{x}(t) + \boldsymbol{\mu}_u^T \boldsymbol{u}(t) \tag{5.7}$$

where $\boldsymbol{\mu}_h(t)$, $\boldsymbol{\mu}_x(t)$ and $\boldsymbol{\mu}_u(t)$ are the KKT (Lagrange) multipliers associated with the path constraints, state-variable and control-variable box constraints respectively. The vanishing of the gradient of the Lagrangian of the Hamiltonian, $\frac{\partial \bar{\mathcal{H}}}{\partial \boldsymbol{u}}$, provides the gradient normality condition. And the complementarity conditions are given by

$$\mu_{h,i} \begin{cases} \leq 0 & \text{if } h_i(\boldsymbol{x}(t), \boldsymbol{u}(t)) = h_i^L \\ \geq 0 & \text{if } h_i(\boldsymbol{x}(t), \boldsymbol{u}(t)) = h_i^U \\ = 0 & \text{if } h_i^L < h_i(\boldsymbol{x}, \boldsymbol{u}) < h_i^U \end{cases} \tag{5.8}$$

$$\mu_{x,i} \begin{cases} \leq 0 & \text{if } x_i = x_i^L \\ \geq 0 & \text{if } x_i = x_i^U \\ = 0 & \text{if } x_i^L < x_i < x_i^U \end{cases} \tag{5.9}$$

$$\mu_{u,i} \begin{cases} \leq 0 & \text{if } u_i = u_i^L \\ \geq 0 & \text{if } u_i = u_i^U \\ = 0 & \text{if } u_i^L < u_i < u_i^U \end{cases} \tag{5.10}$$

The complementarity conditions associated in minimizing the control Hamiltonian provide the switching structure.

Collecting all the necessary conditions for the optimal control problem yields the state, adjoint, transversality and HMC conditions for all $t \in [t_0^*, t_f^*]$ given below. Therefore, an optimal solution must satisfy the below necessary conditions. Furthermore, since the cost and the dynamics do not explicitly depend on time then at an optimal solution where the cost functional is at a minimum leads to $\frac{\partial \mathcal{H}}{\partial t} = 0$. This condition along with the transversality condition in Eq. (5.11c) gives the Hamiltonian function value at the optimal state-control function pair which can be later used to check the optimality of the numerical results.

$$\dot{\boldsymbol{x}}^*(t) = \frac{\partial \mathcal{H}}{\partial \boldsymbol{\lambda}}(\boldsymbol{x}^*(t), \boldsymbol{u}^*(t), \boldsymbol{\lambda}^*(t)) \tag{5.11a}$$

$$\dot{\boldsymbol{\lambda}}^*(t) = -\frac{\partial \mathcal{H}}{\partial \boldsymbol{x}}(\boldsymbol{x}^*(t), \boldsymbol{u}^*(t), \boldsymbol{\lambda}^*(t)) \tag{5.11b}$$

$$\left[\frac{\partial E}{\partial \boldsymbol{x}}(\boldsymbol{x}^*(t_f), t_f) - \boldsymbol{\lambda}^*(t_f)\right]^T \delta \boldsymbol{x}_f + \left[\mathcal{H}(\boldsymbol{x}^*(t_f), \boldsymbol{u}^*(t_f), \boldsymbol{\lambda}^*(t_f)) + \frac{\partial E}{\partial t}(\boldsymbol{x}^*(t_f), t_f)\right] \delta t_f = 0 \tag{5.11c}$$

$$\frac{\partial \bar{\mathcal{H}}(\boldsymbol{x}^*(t), \boldsymbol{u}^*(t), \boldsymbol{\lambda}^*(t), \boldsymbol{\mu}^*(t))}{\partial \boldsymbol{u}} = 0 \tag{5.11d}$$

5.2 Two-Craft Nonlinear Equations of Motion

The equations of motion for a two spacecraft Coulomb formation with hybrid thrusting (both electrostatic and inertial thrusting) are briefly derived in this section. The notation is similar to that used in Reference 5. In order to describe the relative motion of the satellite with respect to the formation center of mass a rotating Hill orbit frame $\mathcal{O} : \{\hat{\boldsymbol{o}}_r, \hat{\boldsymbol{o}}_\theta, \hat{\boldsymbol{o}}_h\}$ as shown in Figure 5.1 is chosen.[5]

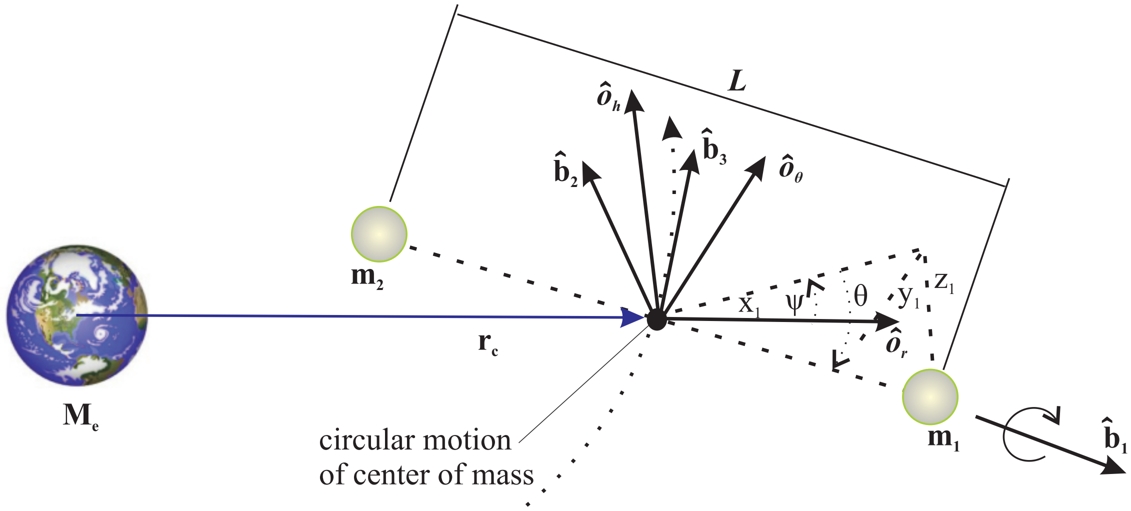

Figure 5.1: Euler Angles Representing the Attitude of Coulomb Tether with Respect to the Orbit Frame

The formation center of mass is assumed to be the origin of this rotating Cartesian coordinate system and the relative position vector of the i^{th} satellite is defined as $\boldsymbol{\rho_i} = (x_i, y_i, z_i)^T$; where the x_i component is in the $\hat{\boldsymbol{o}}_r$ direction (orbit radial), the y_i is component in the $\hat{\boldsymbol{o}}_\theta$ direction of orbital velocity (along-track), and the component z_i is in the $\hat{\boldsymbol{o}}_h$ direction (orbit normal). The orbit frame origin coincides with the formation center of mass, and the center of mass position vector $\boldsymbol{r_c}$ is assumed to have a constant orbital rate of $\Omega = \sqrt{G\,M_e/r_c^3}$, where G is the gravity constant and M_e is the Earth's mass.

Assume that the two-craft formation is treated as a rigid body and aligned in the radial direction. For this orbit nadir aligned formation, consider a body fixed coordinate frame $\mathcal{B} : \{\hat{\boldsymbol{b}}_1, \hat{\boldsymbol{b}}_2, \hat{\boldsymbol{b}}_3\}$ where $\hat{\boldsymbol{b}}_1$ is aligned with the relative position vector $\boldsymbol{\rho_1}$ of mass m_1. In this configuration, the $\mathcal{O}$ and $\mathcal{B}$ frame orientation vectors are exactly aligned. Furthermore, the relative attitude between the $\mathcal{B}$ and $\mathcal{O}$ frames is represented using the 3-2-1 Euler angle notation $(\psi - \text{pitch}, \theta - \text{roll}, \phi - \text{yaw})$.

Using the direction cosine matrix expression given in Reference 5 to relate the $\mathcal{O}$ frame to $\mathcal{B}$ frame, the position vectors of mass m_1 and m_2 in the $\mathcal{O}$ frame are expressed as

$$ {}^{\mathcal{O}}\boldsymbol{\rho_1} = \begin{pmatrix} x_1 \\ y_1 \\ z_1 \end{pmatrix} = \frac{m_2 L}{m_1 + m_2} \begin{bmatrix} \cos\theta\,\cos\psi \\ \cos\theta\,\sin\psi \\ -\sin\theta \end{bmatrix} \tag{5.12a} $$

$$ {}^{\mathcal{O}}\boldsymbol{\rho_2} = \begin{pmatrix} x_2 \\ y_2 \\ z_2 \end{pmatrix} = \frac{m_1 L}{m_1 + m_2} \begin{bmatrix} -\cos\theta\,\cos\psi \\ -\cos\theta\,\sin\psi \\ \sin\theta \end{bmatrix} \tag{5.12b} $$

Furthermore, using the transport theorem,[14] the inertial velocity of mass m_i expressed in the $\mathcal{O}$ frame components becomes

$$ {}^{\mathcal{O}}\boldsymbol{v_i} = \begin{pmatrix} \dot{x}_i - \Omega y_i \\ \dot{y}_i + \Omega\,(x_i + r_c) \\ \dot{z}_i \end{pmatrix} \tag{5.13} $$

Using Eqs. (5.12) and (5.13), the kinetic energy of the system is given by

$$T = \frac{1}{2}\frac{m_1 m_2}{m_1 + m_2}\left[\dot{L}^2 + L^2(\dot{\theta}^2 + (\dot{\psi} + \Omega)^2 \cos^2\theta)\right] + \frac{1}{2}\left(m_1 + m_2\right)\Omega^2 r_c^2 \tag{5.14}$$

The gravitational potential energy retaining up to the second order terms is given by

$$V_g = -\frac{\mu}{r_c}(m_1 + m_2) + \frac{1}{2}\frac{\mu}{r_c^3}\frac{m_1 m_2}{m_1 + m_2}L^2(1 - 3\,\cos^2\theta\,\cos^2\psi) \tag{5.15}$$

and the associated Coulomb potential for the two-craft formation is[1]

$$V_c = k_c \frac{q_1 q_2}{L}\exp(-L/\lambda_d) \tag{5.16}$$

where q_i is the satellite charge and the parameter $k_c = 8.99 \times 10^9$ Nm^2/C^2 is Coulomb's constant. The exponential term in the expression depends on the Debye length parameter λ_d which controls the lower bound on the electrostatic field strength of plasma shielding between the craft. At Geostationary Orbits (GEO) the Debye length vary between 80-1400 m, with a mean of about 180 m.[7] The Coulomb spacecraft formation studied in this chapter is assumed to be orbiting on high Earth orbits.

The nonlinear equations of motion are deduced from the Lagrangian $\mathcal{L} = T - (V_g + V_c)$ of the system in the following form

$$\begin{gathered}\frac{\mathrm{d}}{\mathrm{d}t}\frac{\partial \mathcal{L}}{\partial \dot{q}^i} - \frac{\partial \mathcal{L}}{\partial q^i} = \mathcal{Q}_i \\ q^i = (L, \psi, \theta) \quad (i = 1\ldots 3)\end{gathered} \tag{5.17}$$

where $\mathcal{Q}_i$ is the generalized force in the q^ith-degree of freedom excluding gravitational effects. For the circular orbit case, the nonlinear equations governing the separation distance L, the pitch angle ψ in the orbital plane, and roll angle θ out-of-the orbital plane are

$$\ddot{L} - L(\dot{\theta}^2 + (\Omega + \dot{\psi})^2 \cos^2\theta - \Omega^2(1 - 3\cos^2\theta\, \cos^2\psi)) = \frac{\mathcal{Q}_L}{m} \tag{5.18a}$$

$$\ddot{\psi}\cos^2\theta - 2\dot{\theta}\sin\theta\, \cos\theta(\Omega + \dot{\psi}) + 2\frac{\dot{L}}{L}\cos^2\theta(\Omega + \dot{\psi}) + 3\Omega^2\, \cos^2\theta\, \cos\psi\, \sin\psi = \frac{\mathcal{Q}_\psi}{mL^2} \tag{5.18b}$$

$$\ddot{\theta} + 2\frac{\dot{L}}{L}\dot{\theta} + \cos\theta\, \sin\theta((\Omega + \dot{\psi})^2 + 3\Omega^2\, \cos^2\psi\,) = \frac{\mathcal{Q}_\theta}{mL^2} \tag{5.18c}$$

where $m = \frac{m_1 m_2}{m_1 + m_2}$, and $\mathcal{Q}_L$, $\mathcal{Q}_\psi$, $\mathcal{Q}_\theta$ are the generalized forces associated with L, ψ and θ, respectively. For a two spacecraft Coulomb formation, with F_{cf} being the Coulomb force acting between the two crafts, $\mathcal{Q}_L = -F_{\text{cf}}$, and is expressed as

$$F_{\text{cf}} = -k_c \frac{q_1 q_2}{L^2} \exp(-L/\lambda_d)\Big(1 + \frac{L}{\lambda_d}\Big) \tag{5.19}$$

And $\mathcal{Q}_\psi = F_\psi L$ and $\mathcal{Q}_\theta = F_\theta L$ where F_ψ and F_θ are the electric propulsion (EP) thrusting forces that introduce net formation torques in the ψ and θ directions. Note that to avoid any potential plume exhaust impingement issues both the EP thruster forces are directed in orthogonal directions to the formation line of sight vector.

Further, to prevent numerical difficulties with very small numbers, Eqs. (5.18a) - (5.18c) are rescaled by defining the following nondimensional variables:

$$\tau = \Omega t, \quad l = \frac{L}{L_{\text{ref}}}, \quad u_l = \frac{F_{\text{cf}}}{m\Omega^2 L_{\text{ref}}}, \quad u_\psi = \frac{F_\psi}{m\Omega^2 L_{\text{ref}}}, \quad u_\theta = \frac{F_\theta}{m\Omega^2 L_{\text{ref}}} \tag{5.20}$$

where L_{ref} is the reference tether length. Therefore the radial equilibrium non-dimensional equations of motion become

$$l'' - l({\theta'}^2 + (1 + \psi')^2 \cos^2\theta - (1 - 3\cos^2\theta\, \cos^2\psi)) = -u_l \tag{5.21a}$$

$$\psi''\cos^2\theta + 2\cos\theta(\frac{l'}{l}\cos\theta - \theta'\sin\theta)(1 + \psi') + 3\cos^2\theta\, \cos\psi\, \sin\psi = \frac{u_\psi}{l} \tag{5.21b}$$

$$\theta'' + 2\frac{l'}{l}\theta' + \cos\theta\, \sin\theta((1 + \psi')^2 + 3\, \cos^2\psi\,) = \frac{u_\theta}{l} \tag{5.21c}$$

where the prime denotes the derivative with respect to non-dimensional time. And u_l, u_ψ and u_θ are the non-dimensional control variables. The control variable u_l is associated with Coulomb propulsion, and u_ψ and u_θ are related to electric propulsion. The equations of motion are coupled nonlinear ordinary differential equations.

Similarly, assuming that the two-craft formation is aligned in the along-track and orbit normal directions, the equations of motion in the respective directions are obtained. Therefore the along-track equilibrium nondimensional equations of motion are

$$l'' - l({\phi'}^2 + (1+\psi')^2 \cos^2\phi - (1 - 3\cos^2\phi\sin^2\psi)) = -u_l \tag{5.22a}$$

$$\psi''\cos^2\phi + 2\,\cos\phi(\frac{l'}{l}\cos\phi - \phi'\sin\phi)(1+\psi') - 3\cos^2\phi\,\cos\psi\,\sin\psi = \frac{u_\psi}{l} \tag{5.22b}$$

$$\phi'' + 2\frac{l'}{l}\phi' + \cos\phi\,\sin\phi((1+\psi')^2 + 3\,\sin^2\psi\,) = \frac{u_\phi}{l} \tag{5.22c}$$

and the orbit normal nondimensional equations of motion are

$$\begin{aligned} l'' &- \frac{l}{4}(3 + 2{\theta'}^2 + 4{\phi'}^2 - 2\cos 2\theta\cos^2\phi - (1 - 2{\theta'}^2)\cos 2\phi - 8\phi'\sin\theta \\ &+ 4\,\theta'\cos\theta\sin 2\phi - 4(1 - 3\,\cos^2\phi\,\sin^2\theta)) = -u_l \end{aligned} \tag{5.23a}$$

$$\phi''\cos^2\theta + 2cos\theta(\frac{l'}{l}\cos\theta - \theta'\sin\theta)(1+\psi') + 3\cos^2\theta\,\cos\psi\,\sin\psi = \frac{u_\psi}{l} \tag{5.23b}$$

$$\theta'' + 2\frac{l'}{l}\theta' + \cos\theta\,\sin\theta((1+\psi')^2 + 3\,\cos^2\psi\,) = \frac{u_\theta}{l} \tag{5.23c}$$

Further, if the two-craft formation is treated as a rigid body and is aligned in one of the three equilibrium configurations (radial, along-track or orbitnormal directions), the ideal product of charges needed to achieve such static Coulomb formations are obtained from Eqs. (5.21) as

$$(q_1q_2)_{\text{radial}} = -3\Omega^2\frac{L^3}{k_c}m\left(\frac{\lambda_d}{L+\lambda_d}\right)\exp(L/\lambda_d) \tag{5.24a}$$

$$(q_1q_2)_{\text{along-track}} = 0 \tag{5.24b}$$

$$(q_1q_2)_{\text{orbitnormal}} = \Omega^2\frac{L^3}{k_c}m\left(\frac{\lambda_d}{L+\lambda_d}\right)\exp(L/\lambda_d) \tag{5.24c}$$

Reference 5 obtained Eqs. (5.24) using the linearized dynamical models. Because the above constraints yield an infinite number of charge solutions, equal charges in magnitude across the craft are chosen. For instance, for a radial equilibrium configuration assuming equal charges in magnitude and using Eqs. (5.19) and (5.24a) yields

$$q_1 = \sqrt{|(q_1 q_2)_{\text{radial}}|} \tag{5.25}$$

$$q_2 = -q_1 \tag{5.26}$$

5.3 Reconfiguration Maneuvers

The formulation of any optimal control problem involves equations describing the dynamics of the system, the cost to be minimized, and any constraints which must be met to consider a solution valid. This section discusses the optimal control problem formulation for optimal two-craft formation reconfigurations, the four performance criteria used (minimum time, minimum acceleration, minimum propulsion fuel, and minimum power consumption), and the Pontryagin's necessary conditions that any candidate optimal solution must satisfy.

5.3.1 Problem Statement

An optimum reconfiguration maneuver drives the two craft formation from its initial position given by $\boldsymbol{x}(\tau_0) = \boldsymbol{x}_0$ at nondimensional initial time τ_0 to its final position given by $\boldsymbol{x}(\tau_f) = \boldsymbol{x}_f$ at final time τ_f, while minimizing a cost function, subject to dynamical constraints. The state vector $\boldsymbol{x}$ is defined as

$$\boldsymbol{x} = (\psi, \psi^{'}, l, l^{'}, \theta, \theta^{'})^T \tag{5.27}$$

The four cost functions are defined below, and the dynamical constraints are presented in Eqs. (5.21). If $u_{\psi\max}$ and $u_{\theta\max}$ are the maximum thrust forces due to electric propulsion and $u_{l\max}$ is the maximum thrust force due to Coulomb propulsion, then the control constraints are given by

$$-u_{\psi\max} \leq u_\psi \leq u_{\psi\max} \tag{5.28a}$$

$$-u_{l\max} \leq u_l \leq u_{l\max} \tag{5.28b}$$

$$-u_{\theta\max} \leq u_\theta \leq u_{\theta\max} \tag{5.28c}$$

If the unconstrained control appears non-linearly in either the state dynamics or the performance criterion (final time can be either fixed or free), the resulting optimal control solution results in continuous control. However, if the constrained control appears linearly, then the resulting optimal control solution results in bang-bang type controller.[27,28]

5.3.2 Measures of Optimality

Four measures of optimality are defined here that minimize a performance criterion (cost function) subject to dynamical constraints. The optimality criteria are minimum time, minimum acceleration of the separation distance between the two craft, minimum Coulomb and electric propulsion fuel consumption (modeled as the L^1-norm of the control acceleration) and minimum power consumption.

- *Minimum Time*

  Minimum time cost function belong to an important class of solutions for reconfiguration maneuvers. They set the lower bound on achievable time and the optimal control to obtain minimum-time response is maximum effort throughout the interval of operation.[28] The cost function to minimize is

  $$J = \int_{\tau_0}^{\tau_f} d\tau \tag{5.29}$$

  Generally time-optimal control solutions are of a bang-bang type.

- *Minimum Length Acceleration*

  For a 2-craft virtual Coulomb structure, it is desirable to keep the deployment/retrieval dynamics as smooth as possible for reconfigurations, so that the Coriolis forces balance the gravity gradient forces. Hence, minimizing the length acceleration is convenient performance measure to study. The cost function for a 2-craft Coulomb structure is

$$J = \int_{\tau_o}^{\tau_f} (l'')^2 d\tau \tag{5.30}$$

which minimizes the total length acceleration, l'', appearing as a quadratic function.

- *Minimum Propulsion Fuel*

This optimization criterion seeks to minimize the Coulomb and electric propulsion thrust magnitudes; the Coulomb thrust acts in the longitudinal direction and the electric propulsion thrusts are orthogonal to the formation line of sight vector in the ψ and θ directions of the rotating body frame. A thrust magnitude is directly related to the propulsion mass and the control acceleration. The minimum fuel cost function is expressed as

$$J = \int_{\tau_0}^{\tau_f} (W_{\text{cp}} |u_l| + W_{\text{ep}} |u_\psi| + W_{\text{ep}} |u_\theta|) d\tau \tag{5.31}$$

where W_{cp} and W_{ep} are the weights associated with Coulomb propulsion and electric propulsion satisfying the condition $W_{\text{cp}} + W_{\text{ep}} = 1$. Since the cost associated with Coulomb propulsion is negligible compared to the electric propulsion (I_{sp} values of 10^8–10^{13} seconds versus 10^3–10^4 seconds), the weight associated with Coulomb propulsion is set to $W_{\text{cp}} = 0$, and accordingly $W_{\text{ep}} = 1$. However, for a radial equilibrium-to-equilibrium expansion or contraction reconfiguration there is no electric propulsion usage as such maneuvers require no inertial thrusting. Hence the minimum propulsion fuel cost function is not modeled for the radial-to-radial equilibrium reconfiguration cases. For other equilibrium-to-equilibrium reconfiguration maneuvers, the cost function becomes the fuel usage of the EP propulsion system:

$$J = \int_{\tau_0}^{\tau_f} (|u_\psi| + |u_\theta|) d\tau \tag{5.32}$$

The cost function used here is the L^1 norm of the control instead of the quadratic cost function (L^2 norm squared), because L^1 measures fuel use and is thus the correct cost function for minimum fuel control. A quadratic cost-optimal controller takes more fuel.[24] Furthermore, quadratic cost controllers are continuous controllers which create new system engineering problems such as inducing undesirable effects on precision pointing payloads.[24] Therefore, the choice for the cost function formulation is the l^1 based L^1 norm ($\|\boldsymbol{u}(\tau)\|_{L^1} = \int \|\boldsymbol{u}(\tau)\|_{l^1} d\tau = \int (|u_1(\tau)| + \ldots + |u_n(\tau)|)d\tau$).

Furthermore, the derivative of the l^1 based L^1 norm is discontinuous at zero, but the introduction of more control variables resolves this issue.[38] For example, in the ψ direction, the control vector is represented with two positive variables, a positive and negative measure of the control acceleration directed along the orthogonal directions to the formation line of sight vector. Both positive components have a lower bound of zero and an upper bound $u_{\psi\max}$. As a consequence, the augmented control variables' derivatives are continuous and make the problem a smooth, nonlinear programming problem to solve. Also, only the negative or positive part of the control in one direction is nonzero at any given point in time.

- *Minimum Propulsion Power* The objective of this performance measure is to minimize total electric power required to engage the Coulomb and electric propulsion methods. The cost function is

$$J = \int_{\tau_0}^{\tau_f} (P_{\text{cp}}^2 + P_{\text{ep}}^2) d\tau \tag{5.33}$$

Assuming that the radii of the two-craft are the same, the Coulomb propulsion power P_{cp} required to maintain the spacecraft at some steady-state potential V_{sc} is[1]

$$P_{\text{cp}} = |V_{\text{sc}} I_{\text{e}}| \tag{5.34}$$

where the spacecraft potential $V_{\rm sc}$ and the current emitted $I_{\rm e}$ are given by

$$V_{\rm sc} = \sqrt{\left|-k_c u_l m\Omega^2 \exp(L/\lambda_d)\frac{L^2}{r_{\rm sc}^2}\left(\frac{\lambda_d}{L+\lambda_d}\right)\right|} \tag{5.35}$$

$$I_{\rm e} = 4\pi r_{\rm sc}^2 J_{\rm p} \tag{5.36}$$

where $r_{\rm sc}$ is the spacecraft radius in m, and $J_{\rm p}$ is the plasma current density in A/m^2. In the presence of the photoelectric effect, $J_{\rm p}$ as a function of the spacecraft potential is[1]

$$J_{\rm p} = \begin{cases} J_{\rm e0}\exp(\frac{-e|V_{\rm sc}|}{kT_{\rm e}}) - J_{\rm i0}\,(1+\frac{e|V_{\rm sc}|}{kT_{\rm i}}) - J_{\rm pe0} & \text{for } V_{\rm sc} < 0 \\ J_{\rm e0}\,(1+\frac{eV_{\rm sc}}{kT_{\rm e}}) - J_{\rm i0}\exp(\frac{-eV_{\rm sc}}{kT_{\rm i}}) - J_{\rm pe0}\exp(\frac{-eV_{\rm sc}}{kT_{\rm pe}})(1+\frac{eV_{\rm sc}}{kT_{\rm pe}}) & \text{for } V_{\rm sc} > 0 \end{cases} \tag{5.37}$$

with the electron, ion and photoelectron saturation currents given by $J_{\rm e0} = en_{\rm e}\sqrt{\frac{kT_{\rm e}}{2\pi m_{\rm e}}}$, $J_{\rm i0} = -en_{\rm i}\sqrt{\frac{kT_{\rm i}}{2\pi m_{\rm i}}}$ and $J_{\rm pe0}$. The various plasma constants in Eq. (5.37) are the electron charge e in C, ion(electron) density $n_{\rm i(e)}$ in m^{-3}, Boltzmann constant k in J/K, ion(electron) temperature $T_{\rm i(e)}$ in K, $T_{\rm pe}$ is temperature of photoelectrons in K and the ion(electron) density $m_{\rm i(e)}$ in kg. The experimental values of these plasma parameters during average GEO environment conditions are given in Reference 1.

The electric propulsion (EP) power $P_{\rm ep}$ is dependent on the control acceleration magnitude ($|u_\psi|+|u_\theta|$), thruster efficiency η, and specific impulse $I_{\rm sp}$. Thus, $P_{\rm ep}$ is modeled as[41]

$$P_{\rm ep} = m\Omega^2 L_{\rm ref}\frac{(|u_\psi|+|u_\theta|)v_{\rm e}}{2\eta} \tag{5.38}$$

where $v_{\rm e} = gI_{\rm sp}$ is the engine exhaust velocity. Xenon is assumed to be the propellant utilized for the EP system and the thruster efficiency η is determined by the relation

$$\eta = \frac{bv_{\rm e}^2}{v_{\rm e}^2 + d^2} \tag{5.39}$$

where $b = 0.81$ and $d = 13.5$km/s are propellant-dependant coefficients derived from theoretical and experimental data.[41] For EP systems using xenon, the typical specific impulse limits are 1000s $\leq I_{\text{sp}} \leq$ 7000s.[41] I_{sp} is assumed to be constant over the entire maneuver which implies a fixed engine operating with no throttling. For this optimization criteria, the Coulomb and electric propulsion power levels are assumed to be of the same order (between 1 to 10 Watts).

5.3.3 Pontryagin's Necessary Conditions

Since the cost functions and the dynamical constraints do not explicitly depend on time, a necessary condition at an optimal solution where the cost functional is at a minimum is $\frac{\partial \mathcal{H}}{\partial t} = 0$. This condition along with the transversality condition in Eq. (5.11c) provides the Hamiltonian function value at the optimal state-control function pair. At an optimal state-control function pair, for minimum time cost function the Hamiltonian function value is -1, and for minimum acceleration, minimum fuel, and minimum power cost functions the Hamiltonian function value is 0. These constant Hamiltonian function values for different performance criteria are later used to check the optimality of the numerical results.

5.4 Solving the Optimal Control Problem

Optimal control problems can rarely be solved analytically, and numerical methods are needed in such cases to solve them.[26] The first step is to discretize the problem, which is to define the system at discrete points which results in a finite number of variables because the system variables are only defined at the discrete points. The number of variables for the optimal control problem is then the number of variables in the system times the number of discretization points. The consequence of discretizing the optimal control problems explored here are nonlinearly unconstrained and constrained optimization problems. The unstable dynamics of the two-craft Coulomb formation require a more accurate representation of the maneuver to solve the problem. There are many ways to discretize the optimal control problem. The choice of a discretization method may lead to different sizes of discrete problem with different theoretical and numerical properties. Solution techniques to the OCP can be broadly classified as either indirect or direct methods. This section discusses three methods explored for discretizing the optimal control problem presented in this thesis: indirect multiple shooting method, direct penalty function method and pseudospectral method. To combine the pros and cons of both direct and indirect approaches, the pseudospectral method was eventually chosen over multiple shooting and direct penalty function methods.

5.4.1 Indirect Method

Indirect methods based on the calculus of variation utilizes the first-order necessary conditions for optimality given by the Pontryagin's minimum principle (PMP). The aim is to find an approximate solution to these necessary conditions by solving a two-point boundary value problem. Indirect methods are based on finding the state, costate and control variables that solve these boundary value problems. Out of wide variety of techniques available to solve BVP, perhaps multiple-shooting method is the most accurate and reliable technique for solving BVP involving differential equations. However, the convergence characteristics heavily depend on a good initial guess for both the state and costate equations. Further, the switching structure of the constraints has to be known a priori. Direct and indirect variants of shooting, multiple shooting, transcription/collocation methods are available and for a detailed review of these solution techniques refer to Betts.[26] Further, for implementation details on indirect methods refer Reference 29.

This section presents the multiple shooting technique explored to solve an unconstrained optimal control problem in this thesis.[29] If $\boldsymbol{x}(t) \in \mathbb{R}^n$ represents the state vector and $\boldsymbol{\lambda}(t) \in \mathbb{R}^n$ denotes the costate variables then find the control $\boldsymbol{u}(t) \in \mathbb{R}^m$ that minimizes the cost functional given in Eq. (5.1). From Eq. (5.11), the first order necessary conditions for the extremum for an unconstrained optimal control problem become

$$\dot{\boldsymbol{x}} = \frac{\partial \mathcal{H}}{\partial \boldsymbol{\lambda}} \tag{5.40a}$$

$$\dot{\boldsymbol{\lambda}} = -\frac{\partial \mathcal{H}}{\partial \boldsymbol{x}} \tag{5.40b}$$

$$\frac{\partial \mathcal{H}}{\partial \boldsymbol{u}} = 0 \tag{5.40c}$$

$$\frac{\partial E}{\partial \boldsymbol{x}}(\boldsymbol{x}(t_f)) - \boldsymbol{\lambda}(t_f) = 0 \tag{5.40d}$$

$$\boldsymbol{x}_0 = \boldsymbol{x}(t_0), \boldsymbol{x}_f = \boldsymbol{x}(t_f) \tag{5.40e}$$

Assuming that you can express the control variables in terms of the state and co-state variables the two point boundary value problem becomes

$$\dot{\boldsymbol{y}} = \boldsymbol{p}(\boldsymbol{y}) \tag{5.41a}$$

$$\boldsymbol{r}(\boldsymbol{y}(t_0), \boldsymbol{y}(t_f)) = 0 \tag{5.41b}$$

where $\boldsymbol{y} = [\boldsymbol{x}, \boldsymbol{\lambda}]^T$, $\boldsymbol{p}(\boldsymbol{y}) = [\frac{\partial \mathcal{H}}{\partial \boldsymbol{\lambda}}, -\frac{\partial \mathcal{H}}{\partial \boldsymbol{x}}]^T$ and $\boldsymbol{r}(\boldsymbol{y}(t_0), \boldsymbol{y}(t_f))$ are the boundary conditions obtained from Eqs. (5.40d)-(5.40e). To apply the multiple shooting technique to the boundary-value problem in Eq. (5.41), the time span $[0, t_f]$ is divided into M intervals such that $0 = t_0 < t_1 < \ldots < t_M = t_f$. In each interval, let $\boldsymbol{y}(t; \boldsymbol{s}_i^y)$ denote the solution to the initial-value problem

$$\dot{\boldsymbol{y}} = \boldsymbol{p}(t, \boldsymbol{y}), \quad t \in (t_i, t_{i+1}) \tag{5.42a}$$

$$\boldsymbol{y}(t_i) = \boldsymbol{s}_i^y,\ i = 0, 1, \ldots, M-1 \tag{5.42b}$$

where $\boldsymbol{s}_i^y$ represents the solution to the boundary-value problem in Eq. (5.41) at the nodes $t_i, i = 0, 1, 2, \ldots, M$. An additional requirement is that the solution at each node be continuous, i.e.,

$$\boldsymbol{y}(t_{i+1}; \boldsymbol{s}_i^y) - \boldsymbol{s}_{i+1}^y = 0,\ i = 0, 1, 2, \ldots, M-1 \tag{5.43}$$

where $\boldsymbol{y}(t_{i+1}; \boldsymbol{s}_i^y)$ is the solution to the ordinary differential equation Eq. (5.42a) at time $t = t_{i+1}$ using the initial condition $\boldsymbol{y}(t_i) = \boldsymbol{s}_i^y$. Further, the boundary conditions are satisfied such that

$$\boldsymbol{r}(\boldsymbol{s}_0^y, \boldsymbol{s}_M^y) = 0 \tag{5.44}$$

The conditions (5.43) and (5.44) provide $2n(M+1)$ non-linear equations in $2n(M+1)$ unknowns which can be solved in an iterative manner using Newton's method. The multiple shooting algorithm is summarized as follows:

Given $M, t_0, t_1, \ldots, t_{M-1}, \boldsymbol{s}^0$, and a small number $\epsilon > 0$,

1. Compute $F(\boldsymbol{s}^0)$, where

$$F(\boldsymbol{s}) = \begin{bmatrix} \boldsymbol{y}(t_1; \boldsymbol{s}_0^y) - \boldsymbol{s}_1^y \\ \vdots \\ \boldsymbol{y}(t_M; \boldsymbol{s}_{M-1}^y) - \boldsymbol{s}_M^y \\ \boldsymbol{r}(\boldsymbol{s}_0^y, \boldsymbol{s}_M^y) \end{bmatrix} = 0;\ \boldsymbol{s} = \begin{bmatrix} \boldsymbol{s}_0^y \\ \vdots \\ \boldsymbol{s}_M^y \end{bmatrix} \tag{5.45}$$

2. If $\|F(\boldsymbol{s}^0)\| \le \epsilon, \boldsymbol{s}^0$ is the desired solution.

3. Compute $\Delta \boldsymbol{s} = -J^{-1}(\boldsymbol{s}^0)F(\boldsymbol{s}^0)$

   If $\|\Delta \boldsymbol{s}\| \le \epsilon, \boldsymbol{s}^0$ is the desired solution. Here $J(\boldsymbol{s})$ is the Jacobian matrix of the form

$$J(\boldsymbol{s}) = \begin{bmatrix} A_0 & C_0 & & & \\ 0 & A_1 & C_1 & & \\ \vdots & & \ddots & \ddots & \\ 0 & & & A_{M-1} & C_{M-1} \\ B_0 & & & 0 & B_M \end{bmatrix} \tag{5.46}$$

with (5.47)

$$A_i = \left[\frac{\partial \boldsymbol{y}}{\partial \boldsymbol{s}_i^y}\right]; C_i = -I,\ i = 0, 1, \ldots, M-1 \tag{5.48}$$

$$B_0 = \left[\frac{\partial \boldsymbol{r}}{\partial \boldsymbol{s}_0^y}\right]; B_M = \left[\frac{\partial \boldsymbol{r}}{\partial \boldsymbol{s}_M^y}\right] \tag{5.49}$$

4. Find an $\alpha^* > 0$ such that $F(\boldsymbol{s}^0 + \alpha^* \Delta \boldsymbol{s}) < F(\boldsymbol{s}^0)$.

5. Set $\boldsymbol{s}^0 = \boldsymbol{s}^0 + \alpha^* \Delta \boldsymbol{s}$.

   Set $F(\boldsymbol{s}^0) = F(\boldsymbol{s}^0 + \alpha^* \Delta \boldsymbol{s})$

   Go to step 2.

5.4.2 Direct Method

Direct methods directly solve for the unknown control variables; direct methods transform the continuous OCP into a discrete nonlinear programming (NLP) which is solved either by the penalty function method or augmented Lagrangian function method. In the direct method, the state and control variables are parameterized using piecewise polynomial approximations between the node points. A result of such approximations for the cost functional, state dynamics equations, state-control constraints and boundary conditions transforms the dynamic optimization problem to a unconstrained static optimization problem. To improve the solution accuracy, higher-order polynomial approximations can be used; however, using more sophisticated discretization techniques significantly increase numerical difficulties.

The major advantage of the direct method is that approximate optimal solutions are achieved with a poor initial guess; however, the disadvantage is that the resulting static optimization problem has a large number of unknown variables, and may be plagued with multiple minima as a result of the discretization process. Thus, computing the actual global minimum may be difficult, and as a result direct methods tend to give inaccurate solutions. Though it is simpler and easier computationally to discretize the OCP using direct algorithms, the method is not as accurate as indirect methods. Furthermore, many direct methods do not provide the costate information. The direct algorithm[29] explored for discretizing the optimal control problem presented in this thesis is given here.

If $\boldsymbol{x}(t) \in \mathbb{R}^n$ represents the state vector and $\boldsymbol{\lambda}(t) \in \mathbb{R}^n$ denotes the costate variables then find the control $\boldsymbol{u}(t) \in \mathbb{R}^m$ that minimizes the cost functional given in Eq. (5.1) subject to the constraints in Eq. (5.2) and the specified initial conditions $\boldsymbol{x}_0 = \boldsymbol{x}(t_0)$. Using the Hamiltonian definition in Eq. (5.5), the dynamic constraints in Eq. (5.2) can be adjoined to the cost functional in Eq. (5.1) via the Lagrange multipliers to get

$$J[\boldsymbol{x}(t), \boldsymbol{u}(t)] = E(\boldsymbol{x}(t_f), t_f) + \int_{t_0}^{t_f} (\mathcal{H} - \boldsymbol{\lambda}^T \dot{\boldsymbol{x}}) dt \tag{5.50}$$

From an initial guess, $\boldsymbol{u}^0(t)$, an improved control input $\boldsymbol{u}^1(t)$ is to be found, that will decrease the value of the cost functional. Let $\boldsymbol{u}^1(t) = \boldsymbol{u}^0(t) + \boldsymbol{h}_u(t)$, where $\boldsymbol{h}_u(t)$ represents an increment to the initial guess. Also let $\boldsymbol{x}^1(t) = \boldsymbol{x}^0(t) + \boldsymbol{h}_x(t)$, be the state trajectory that corresponds to the control input $\boldsymbol{u}^1(t)$. Choosing $\dot{\boldsymbol{\lambda}} = -\frac{\partial \mathcal{H}}{\partial \boldsymbol{x}}$ and $\boldsymbol{\lambda}(t_f) = \frac{\partial E}{\partial \boldsymbol{x}}(\boldsymbol{x}(t_f))$, and neglecting higher order terms the change in the cost functional becomes

$$\Delta J[\boldsymbol{x}(t), \boldsymbol{u}(t)] = \delta J = \int_{t_0}^{t_f} \frac{\partial \mathcal{H}}{\partial \boldsymbol{u}} \boldsymbol{h}_u(t) dt \tag{5.51}$$

A numerical approximation to the integral can be obtained by using the trapezoidal rule. Therefore, to consider the control input at discrete points, divide the time span $t \in [t_0, t_f]$ into $N-1$ equally spaced intervals such that $\Delta t = t_f/(N-1), t_i = i\Delta t, i = 0, 1, \ldots, N-1, t_0 = 0, t_{N-1} = t_f$. Treating $\boldsymbol{u}(t_i)$ as a set of n unknown parameters, the point-wise approximation for the control input becomes

$$\delta J = \sum_{i=0}^{N-1} \frac{\partial J}{\partial \boldsymbol{u}(t_i)} \boldsymbol{h}_u(t_i) \tag{5.52}$$

Then the gradient of the cost functional with respect to the control input becomes

$$\frac{\partial J}{\partial \boldsymbol{u}(t_i)} = \begin{cases} \frac{\partial \mathcal{H}}{\partial \boldsymbol{u}(t_i)} \Delta t & \text{for } i = 1, 2, \ldots, N-2 \\ \frac{1}{2} \frac{\partial \mathcal{H}}{\partial \boldsymbol{u}(t_i)} \Delta t & \text{for } i = 0, \text{and}, i = N-1 \end{cases} \tag{5.53}$$

As a result of these approximations, the unconstrained static optimization problem becomes:

Find $\boldsymbol{u}(t_0), \boldsymbol{u}(t_1), \ldots, \boldsymbol{u}(t_{N-1})$ that minimizes the cost function

$$J(\boldsymbol{u}(t_0), \boldsymbol{u}(t_1), \ldots, \boldsymbol{u}(t_{N-1})) \tag{5.54}$$

And this problem can be solved using Quasi-Newton method.

Defining $\tilde{\boldsymbol{u}}$, ΔJ and $\tilde{\boldsymbol{h}}_u$ as

$$\tilde{\boldsymbol{u}} = [\boldsymbol{u}(t_0)^T, \boldsymbol{u}(t_1)^T, \ldots, \boldsymbol{u}(t_{N-1})^T]^T \tag{5.55}$$

$$\Delta J = [(\frac{\partial J}{\partial \boldsymbol{u}(t_0)})^T, (\frac{\partial J}{\partial \boldsymbol{u}(t_1)})^T, \ldots, (\frac{\partial J}{\partial \boldsymbol{u}(t_{N-1})})^T]^T \tag{5.56}$$

$$\tilde{\boldsymbol{h}}_u = [\boldsymbol{h}_u(t_0), \boldsymbol{h}_u(t_1), \ldots, \boldsymbol{h}_u(t_{N-1})]^T \tag{5.57}$$

the direct algorithm that uses the Quasi-Newton method is summarized as follows.

Given $N, t_f, \tilde{\boldsymbol{u}}^0, K_{mu}^0 = I$, and a small number $\epsilon > 0$,

1. Compute the gradient $\nabla J(\tilde{\boldsymbol{u}}^0)$ using Eq. (5.53).

2. If $\|\nabla J(\tilde{\boldsymbol{u}}^0)\| \leq \epsilon, \tilde{\boldsymbol{u}}$ is the desired solution.

3. Compute $\tilde{\boldsymbol{h}}_u = -K_{mu}^0 \nabla J(\tilde{\boldsymbol{u}}^0)$.

4. If $\left\|\tilde{\boldsymbol{h}}_u\right\| \leq \epsilon$, stop, as no further improvement is possible.

5. Find an $\alpha^* > 0$ such that $J(\tilde{\boldsymbol{u}}^0 + \alpha^* \tilde{\boldsymbol{h}}_u) < J(\tilde{\boldsymbol{u}}^0)$.

6. Compute $\boldsymbol{\gamma} = \nabla J(\tilde{\boldsymbol{u}}^0 + \alpha^* \tilde{\boldsymbol{h}}_u) - \nabla J(\tilde{\boldsymbol{u}}^0)$.
   $\boldsymbol{d} = \tilde{\boldsymbol{u}}^0 + \alpha^* \tilde{\boldsymbol{h}}_u - \tilde{\boldsymbol{u}}^0 = \alpha^* \tilde{\boldsymbol{h}}_u$.
   $K_{mu}^0 = K_{mu}^0 + \left(1 + \frac{\boldsymbol{\gamma}^T K_{mu}^0 \boldsymbol{\gamma}}{\boldsymbol{d}^T \boldsymbol{\gamma}}\right) \frac{\boldsymbol{d}\boldsymbol{d}^T}{\boldsymbol{d}^T \boldsymbol{\gamma}} - \left(\frac{\boldsymbol{d}\boldsymbol{\gamma}^T K_{mu}^0 + K_{mu}^0 \boldsymbol{\gamma} \boldsymbol{d}^T}{\boldsymbol{d}^T \boldsymbol{\gamma}}\right)$.

7. Set $\tilde{\boldsymbol{u}}^0 = \tilde{\boldsymbol{u}}^0 + \alpha^* \tilde{\boldsymbol{h}}_u$.
   Set $\nabla J(\tilde{\boldsymbol{u}}^0) = \nabla J(\tilde{\boldsymbol{u}}^0 + \alpha^* \tilde{\boldsymbol{h}}_u)$.
   Go to step 2.

For instance, an educated guess is used for $\boldsymbol{u}^0(t)$ on first iteration to find the state $\boldsymbol{x}(t_i)$ forward in time $t = 0$ to $t = t_f$. Then, use $\boldsymbol{u}(t_0)$ and $\boldsymbol{x}(t_i)$ from previous step to find the Lagrange multiplier $\boldsymbol{\lambda}(t_i)$ backward in time $t = t_f$ to $t = 0$. Finally, using $\boldsymbol{u}(t_0)$, $\boldsymbol{x}(t_i)$, and $\boldsymbol{\lambda}(t_i)$ from previous steps the Quasi-Newton method summarized above is implemented to adjust the control history. Both the function and gradient evaluations require higher order polynomial approximations to improve the accuracy of the numerical solution.

5.4.3 Pseudospectral Method

Over the last decade, due to major enhancements in approximation theory and optimization techniques, functionally smooth nonlinear optimal control problems where the functions involved in the problem formulation are differentiable can be solved with relative ease.[34,35,38]

This approach of solving optimal control problems is encapsulated as the Covector Mapping Principle (CMP), and Figure 5.2 effectively depicts the CMP.[30] Problem B represents a given trajectory optimization problem. Application of Pontryagin's Minimum Principle (PMP) yields a ”two-point” boundary value problem. Call this Problem B^{λ}. Problem B^{λ} is twice the dimension of Problem B as a result of the costates, whose dimension is exactly equal to that of the states. Since Problem B^{λ} is typically unsolvable in closed-form, ”approximate” solutions to it are sought by ”approximation methods”. Problem $B^{\lambda N}$ represents the approximate solution to the problem where N denotes the number of discrete points used, for example, the number of points used in the Runge-Kutta method. Well-known discretization methods (such as a class of Runge-Kutta methods) fail for optimal control problems because dualization and discretization are non-commutative operations indicated by the commutation gap shown in Figure 5.2.[39, 40]

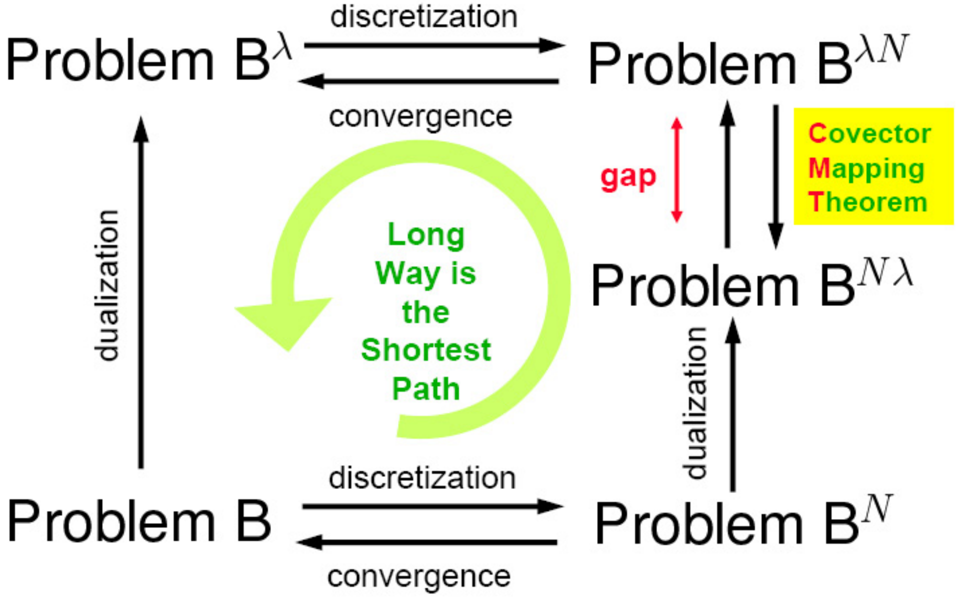

Figure 5.2: The Covector Mapping Principle[30]

The bottom of Figure 5.2 represents the discretization of Problem B to Problem B^N using the classical direct methods. If convergence can be proved, then passing to the limit, $N \rightarrow \infty$, solves the original continuous problem in the limit. A convergence theorem ensures that solutions are obtained to an arbitrary precision. But for the simplest problems, convergence can be shown to be generally invalid in the context of the Minimum Principle. When Problem B is a modern optimal control problem, Problem B^N is a non-linear programming problem. Hence $B^{N\lambda}$ refers to the set of necessary conditions obtained by applying the Karush-Kuhn-Tucker (KKT) theorem. Furthermore, Problems $B^{\lambda N}$ and $B^{N\lambda}$ do not necessarily generate the same solution. This means dualization and discretization are not commutative operations. However, it is proved that a covector mapping theorem for the Legendre pseudospectral method provides an order-preserving map between the duals. In addition, the Legendre pseudospectral method proves to be convergent with remarkably small grids.[30, 39, 40]

Consequently, the solutions can be obtained readily by implementing the CMP where the mapping between the states and costates is preserved.[30] The extremality of the computed solutions can be thoroughly verified by examining the necessary conditions. It is important to emphasize that such verifications can be performed without having to solve the two-point boundary value problem. For approximating the unknown functions over multiple nodes, the CMP utilizes the Legendre pseudospectral method (LPM), which in turn uses Lagrange interpolating polynomials to approximate the states and controls. For optimal node placement in time, a specific set of points are chosen for the interpolating nodes where the discrete variables are defined. As an example, the LGL (Legendre-Gauss-Lobatto) pseudospectral method uses nodes that correspond to the extrema of N^{th} order Legendre polynomials. Therefore, with fewer terms of a series in the approximation, spectral methods for approximating functions have exponential convergence property. Furthermore, it has been shown that the Legendre pseudospectral method (albeit a direct method) has the property that the solution satisfies the necessary optimality conditions and solves the OCP without using a good estimate of an optimal solution as a guess.[30, 33] Also, this eliminates traditional difficulties in solving for the costates in the OCP.[39]

In the Legendre PS methods, the states and controls are approximated using Nth order Lagrange polynomials which interpolate the functions at optimally chosen nodes. The node points are optimally chosen by the Legendre-Gauss-Lobatto (LGL) quadrature. The LGL node points are the extrema of the Nth order Legendre polynomials which give the least interpolation error in the L^2 sense. The LGL nodes are chosen over other quadrature nodes(like Chebyshev nodes) as they are more versatile and can also be used in the discretization of integrals by Gaussian quadrature. More precisely, the LGL node points t_l, $l = 0, \ldots, N$, spaced on the interval $[-1, 1]$ are defined as

$$t_0 = -1, \qquad t_N = 1$$

and for $1 \leq l \leq N-1$, t_l are the zeros of $\dot{L}_N(t)$, the derivative of the Legendre polynomial $L_N(t)$. The roots of the Legendre polynomials are distinct, lie in the interval $[-1, 1]$, have a symmetry with respect to the origin. The Legendre polynomials are orthogonal polynomials with properties:

1. For each N, $L_N(t)$ is a polynomial of degree N.
2. $\int_{-1}^{1} L_M(t)L_N(t)dt = \delta_{MN}\frac{2}{2n+1}$ where $L_M(t)$ and $L_N(t)$ are the polynomials and δ_{MN} is the Kronecker delta, which is 0 when $M \neq N$ and 1 when $M = N$.

The discretization process begins by approximating the continuous state and control variables using the Lagrange interpolating polynomials, $\phi_l(t)$, of order N as:

$$\boldsymbol{x}(t) \approx \boldsymbol{x}^N(t) = \sum_{l=0}^{N} \boldsymbol{x}_l \phi_l(t) \tag{5.58}$$

$$\boldsymbol{u}(t) \approx \boldsymbol{u}^N(t) = \sum_{l=0}^{N} \boldsymbol{u}_l \phi_l(t) \tag{5.59}$$

where $\phi_l(t)$ is related to the Legendre polynomials through

$$\phi_l(t) = \frac{1}{N(N+1)L_N(t_l)} \frac{(t^2-1)\dot{L}_N(t)}{t-t_l} \tag{5.60}$$

It can be verified that

$$\phi_l(t_k) = \delta_{lk} = \begin{cases} 1 & \text{if } l = k \\ 0 & \text{if } l \neq k \end{cases} \tag{5.61}$$

Hence, it follows that $\boldsymbol{x}_l = \boldsymbol{x}^N(t_l), \boldsymbol{u}_l = \boldsymbol{u}^N(t_l)$. The derivative terms are approximated from Eq. (5.58) by differentiating the approximation

$$\dot{\boldsymbol{x}}(t) \approx \dot{\boldsymbol{x}}^N(t) = \sum_{t=0}^{N} \boldsymbol{x}_l \dot{\phi}_l(t) \tag{5.62}$$

and then evaluating the expression at the LGL nodes. This process gives rise to the $(N+1) \times (N+1)$ differentiation matrix $\boldsymbol{D}_1$ with entries $D_{1,kl} = \dot{\phi}_l(t_k)$ or

$$\boldsymbol{D}_1 := [D_{1,kl}] := \begin{cases} \frac{L_N(t_k)}{L_N(t_l)} \cdot \frac{1}{t_k - t_l} & \text{if } k \neq l \\ -\frac{N(N+1)}{4} & \text{if } k = l = 0 \\ \frac{N(N+1)}{4} & \text{if } k = l = N \\ 0 & \text{otherwise} \end{cases} \tag{5.63}$$

which operates over each component of the discretization, $\boldsymbol{X} = (\boldsymbol{x}_0; \boldsymbol{x}_1; ...; \boldsymbol{x}_N)$, to generate a discrete derivative $\dot{\boldsymbol{X}} = \boldsymbol{D}_1 * \boldsymbol{X} = (\dot{\boldsymbol{x}}_0; \dot{\boldsymbol{x}}_1; ...; \dot{\boldsymbol{x}}_N)$. The dynamical constraints are discretized by imposing these constraints at the LGL nodes. Thus, the functions are replaced by vector of their values at the nodes, and the derivative operators are replaced by differentiation matrices. Further, the derivatives of the functions at these nodes are obtained by applying the differentiation matrices on the functions at the same nodes. Therefore, discretization of the Eq. (5.62) can be written as

$$\dot{\boldsymbol{x}}(\tau_i) \approx \dot{\boldsymbol{x}}^N(\tau_i) = \sum_{j=0}^{N} D_{1,ij} \boldsymbol{x}_j \in \frac{\tau_f - \tau_0}{2} F(\boldsymbol{x}_i, \tau_i) \qquad i = 0, 1, ..., N \tag{5.64}$$

where τ_i are the shifted LGL nodes and the factor $\frac{\tau_f - \tau_0}{2}$ comes from an affine transformation of the time domain given as

$$t \in [t_0, t_N] \to [-1, 1] : \tau = \frac{(\tau_f - \tau_0) + (\tau_f + \tau_0)}{2} \tag{5.65}$$

Similarly, the state-space constraint

$$\dot{\boldsymbol{x}}(\tau) = \boldsymbol{f}(\boldsymbol{x}(\tau), \boldsymbol{u}(\tau), \tau) \tag{5.66}$$

is approximated by

$$\dot{\boldsymbol{x}}^N(t_k) = \sum_{t=0}^{N} \boldsymbol{x}_l \dot{\phi}_l(t_k) = \sum_{t=0}^{N} D_{kl}\boldsymbol{x}_l = \frac{\tau_f - \tau_0}{2}\boldsymbol{f}(\boldsymbol{x}_k, \boldsymbol{u}_k, \tau_k) \tag{5.67}$$

Discretizing the generalized cost function in Eq. (5.1), the Gauss-Lobatto integration rule yields

$$J^N\left[\boldsymbol{X}, \boldsymbol{U}, \tau_0, \tau_f\right] = \frac{\tau_f - \tau_0}{2} \sum_{k=0}^{N} F\left(\boldsymbol{x}_k, \sum_{j=0}^{N} D_{1,kj}\boldsymbol{x}_j, \boldsymbol{u}_k, \tau_k\right) w_k + E(\boldsymbol{x}_0, \boldsymbol{x}_N, \tau_0, \tau_f) \tag{5.68}$$

where w_k are the LGL weights given by

$$w_k := \frac{2}{N(N+1)} \frac{1}{[L_N(t_k)]^2} \qquad k = 0, 1, ..., N. \tag{5.69}$$

The formulation is now been transformed to a nonlinear programming problem (NLP). The NLP problem obtained through pseudospectral methods preserves the structure of the original optimal control problem which is of significant consequence to the dualization of the problem and convergence of the discretization.[39,40] Also Reference 40 proves that smoother the optimal solution is, the faster the convergence of the pseudospectral solution.

The optimal control problems in this thesis are solved by the Legendre pseudo-spectral method.[30,31,33] Each optimal control problem in this thesis is solved using the commercial software package DIDO. The covector mapping theorem for the pseudo-spectral method is implemented in this powerful computational tool. DIDO discretizes an optimization problem by using the Legendre pseudo-spectral method and solves it using NLP solver SNOPT, a sequential quadratic programming solver.[33] DIDO generates spectrally accurate solutions whose extremality can be verified using Pontryagin's Minimum Principle. Moreover, this tool can solve non-smooth problems that have state/control discontinuities where these discontinuities can be seen in bang-bang controls.

5.5 Numerical Simulation

This section presents numerical simulations illustrating different optimal reconfigurations of a 2-craft Coulomb virtual tether formation in circular GEO orbits: radial, along-track and orbit normal spacecraft separation distance expansion and contraction maneuvers, radial to along-track and radial to orbit-normal maneuvers with constant separation distance at the initial and final positions, and a family of radial to along-track maneuvers. For each reconfiguration maneuver, four different performance criteria are considered for which optimal control solutions, associated state trajectories, and spacecraft charge time histories are presented. Eqs. (5.21) provide the equations of motion (state constraints) for these reconfiguration maneuvers. Table 5.1 provides the simulation parameters and their values. For each equilibrium-to-equilibrium reconfiguration, for bang-bang controls (minimum-time, minimum-fuel), the Coulomb propulsion thruster limit is fixed at a maximum equilibrium value of the maneuver. Therefore, the Coulomb thruster limit could vary depending on the maneuver under consideration, and from Eqs. (5.19) and (5.24), this limit is computed directly from the maximum equilibrium charge that can be produced. For example, for a radial-to-radial expansion, where the radial spacecraft separation distance is expanded from 25m to 35m, the charges vary from 1.45μC at 25m to 2.41μC at 35m which correspond to Coulomb forces of 29.91μN and 41.87μN respectively. Consequently, for this expansion, the Coulomb thruster limit is fixed at 41.87μN. For a similar expansion from 75m to 100m, the charges vary from 7.75μC to 12.21μC with Coulomb forces of 89.72μN and 119.62μN, and hence the limit is fixed at 119.62μN. For electric propulsion, a Colloid micro-thruster is used with a fixed limit of 30μN. Both the Coulomb and electric propulsion thruster limits can clearly go higher but such choices yield controls dominated by the respective thrusters. Furthermore, the perturbation forces due to the J_2 gravitational attraction and the solar radiation pressure at GEO are not considered in this simulation.

Table 5.1: Simulation Parameters Used for Reconfiguration Maneuvers

Parameter	Value	Units
m_1	150	kg
m_2	150	kg
L_{initial}	25	m
$u_{\psi\text{max}}$	30	μN
$u_{\theta\text{max}}$	30	μN
$I_{\text{sp}}(\text{EP})$	2000	sec
k_c	8.99×10^9	$\frac{\text{Nm}^2}{\text{C}^2}$
Ω	7.2915×10^{-5}	rad/sec

5.5.1 Radial Spacecraft Separation Distance Expansion and Contraction Maneuvers

This example illustrates how to optimally reconfigure a 2-craft Coulomb virtual tether formation to move the craft apart or closer using the Coulomb force and exploiting the gravity gradient to stabilize the formation. Numerical simulations are performed for two sets of maneuvers, expanding the radial Coulomb formation from an initial 25m to a final 35m and contracting the formation from a separation distance of 25m to 15m. The initial and final attitude values as well as the initial and final rates are set to zero through

$$\psi_i = \psi_f = \theta_i = \theta_f = \dot{\psi}_i = \dot{\psi}_f = \dot{\theta}_i = \dot{\theta}_f = \dot{L}_i = \dot{L}_f = 0 \tag{5.70}$$

For minimum-time, minimum-acceleration and minimum-power performance criteria, for an expansion maneuver in which the inter-craft distance increases from 25m to 35m, Figure 5.3 show the candidate in-plane trajectories, state histories, control solutions and Figure 5.4 shows the spacecraft charge time histories. The solutions are obtained for a choice of 100 nodes. Since the variations in the out-of-plane rotation angles (not shown) are negligible (on the order of 10^{-13} rad), only the in-plane trajectories are shown in Figure 5.3(a). The state histories in Figure 5.3(b) show that the boundary conditions are satisfied with viable variations of the in-plane rotation angles and the separation distances. The candidate control solutions in Figure 5.3(c) for minimum-time criteria display bang-bang characteristics, whereas, the minimum-acceleration and minimum-power criterion yields a continuous control solution. An end of a maneuver is denoted by a square box for the respective performance criterion. The charge on craft 2 will be equal and opposite to that of craft 1. Figure 5.4 shows the spacecraft charge time histories for one of the crafts. Since the magnitude of the control charges is on the order of micro-Coulombs, charge emission devices can be used in practice for implementation.

To verify that the control solution for each performance measure indeed drives the system from its known initial to the desired end state, the initial conditions and control solutions are used as input to the ode45 Matlab subroutine and the results are propagated. The propagated results (not shown) closely matched the pseudospectral approximations of the states, confirming the feasibility and convergence of the original solutions. Given the feasibility of the optimized solutions, the necessary conditions for optimality are examined. As previously stated, one such test is the approximate constancy of the Hamiltonian, whose theoretical constant value depends on the performance criterion. For the three performance measures, Table 5.2 shows that this necessary condition is indeed met. Table 5.2 also shows the optimal time required to complete the maneuver, maximum separation distance acceleration, and mean (root-mean-square - RMS) Coulomb propulsion thrust and power required. With the minimum-time criterion, the expansion is finished in 0.6584 orbits. Also, as an improvement over such a radial-expansion reconfiguration result of 1.8 days in Reference 5, which uses linearized time-varying dynamical models, the time taken using optimal control techniques is 0.65 days. Furthermore, optimal control techniques use variable separation distance rates as opposed to the constant rates used in Reference 5. The mean CP thrust and power required for the minimum-time criterion are high, and are low for the minimum-power maneuver. For the minimum-power and minimum-acceleration criteria, the maximum Coulomb thrust needed at the end of the maneuver is greater than the radial equilibrium value of 41.8682μN at 35m. This discrepancy is necessary to overcome the formation's rotational dynamics, and at the end of the maneuver, the controls should explicitly drop down to the equilibrium value. Moreover, the maximum power requirements on the order of 10 Watts can be met by the Coulomb propulsion devices.

Figure 5.5 shows the state trajectories, state time histories, control solutions and Figure

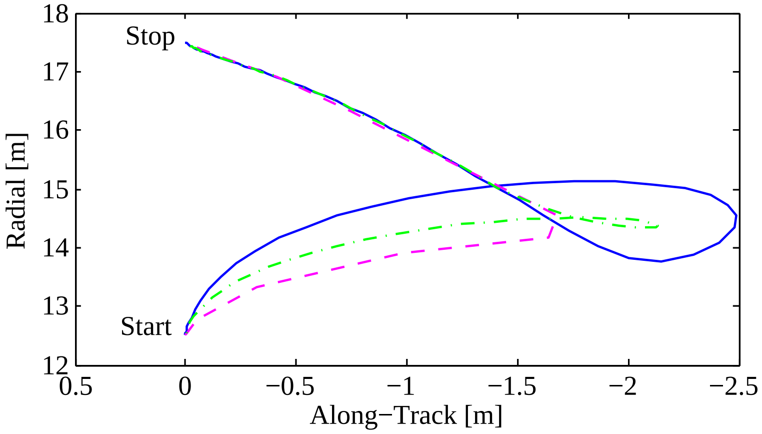

(a) In-plane Trajectories

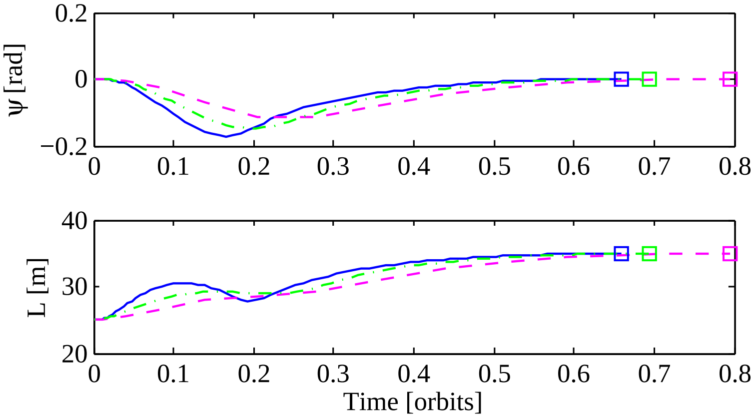

(b) In-plane Rotation Angle (ψ) and Two-Craft Separation Distance (L) Time Histories

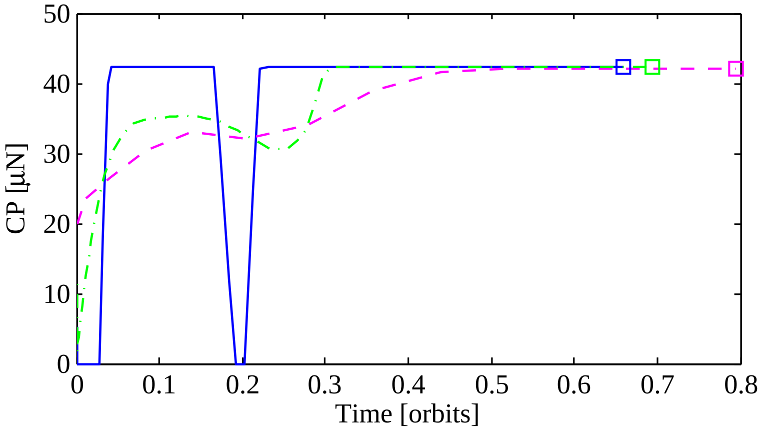

(c) Coulomb Propulsion (CP) Control Solutions

Figure 5.3: Simulation Results for Expanding the Radial Spacecraft Separation Distance from 25m to 35m. (— Min Time, − − Min Acceleration, − · − · Min Power)

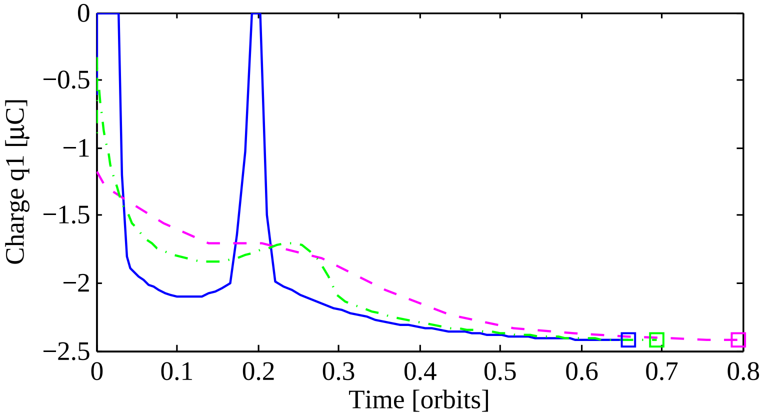

Figure 5.4: Spacecraft Charge Time Histories for Expanding the Radial Spacecraft Separation Distance from 25m to 35m. (— Min Time, − − Min Acceleration, − · − · Min Power)

Table 5.2: Results for Expanding the Radial Spacecraft Separation Distance from 25m to 35m.

Cost	Time t_f orbits	Max L'' $\frac{\text{m}}{\text{s}^2}$	CP Thrust [RMS] μN	CP Power [RMS] W	Hamiltonian [Mean]
Min Time	0.6584	5.0053×10^{-7}	39.9401	10.1978	-1.0079
Min Acceleration	0.7958	0.1342×10^{-7}	38.4081	9.8661	-0.1983
Min Power	0.6934	3.7761×10^{-7}	38.3876	9.7835	0.0002

5.6 shows the spacecraft charge time histories for a contraction maneuver in which the intercraft distance decreases from 25m to 15m. The optimal solutions are symmetric to those of the expansion maneuver solutions. From the results of Table 5.3, the contraction maneuver for the minimum-time criterion finished in 0.7106 orbits. Also, as an improvement over such radial-contraction reconfiguration results from Reference 5 which take 1.8 days, the time taken using optimal control techniques is 0.71 days. However, the contraction took 1.27 days to complete for the minimum-acceleration cost function. Similar to the expansion maneuver, the mean CP thrust and power required are highest for minimum-time criterion and are lowest for the minimum-power criterion. For the minimum-time and minimum-power criteria, the maximum Coulomb thrust at the beginning of the maneuver is greater than the radial equilibrium value of 29.9059μN at 25m. This extra thrust is required at the beginning of the contraction to overcome the angular momentum which causes the in-plane motion to destabilize. At the end of the maneuver at 15m, the controls should explicitly drop down to the equilibrium value of 17.9435μN. Since the separation distances in the contraction maneuver are less than those of the expansion maneuver, the maximum power requirements are about 4 Watts.

Table 5.3: Results for Contracting the Radial Spacecraft Separation Distance from 25m to 15m.

Cost	Time t_f orbits	Max L'' $\frac{\text{m}}{\text{s}^2}$	CP Thrust [RMS] μN	CP Power [RMS] W	Hamiltonian [Mean]
Min Time	0.7106	3.4690×10^{-7}	27.8732	3.8127	-0.9951
Min Acceleration	1.2732	0.4384×10^{-7}	26.7043	3.8335	-0.0959
Min Power	0.7625	2.2591×10^{-7}	26.2355	3.5994	0.0001

5.5.2 Along-track Spacecraft Separation Distance Expansion and Contraction Maneuvers

This example illustrates how to optimally reconfigure a 2-craft Coulomb virtual tether formation to move the craft apart or closer in along-track equilibrium configuration. This reconfiguration maneuver requires hybrid control of Coulomb forces and conventional thrusters

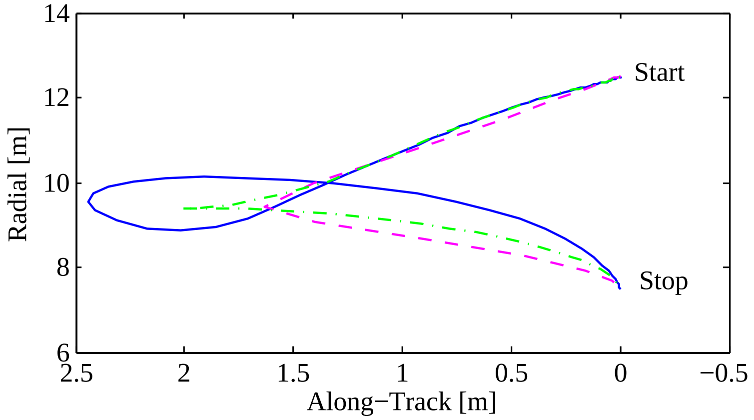

(a) In-plane Trajectories

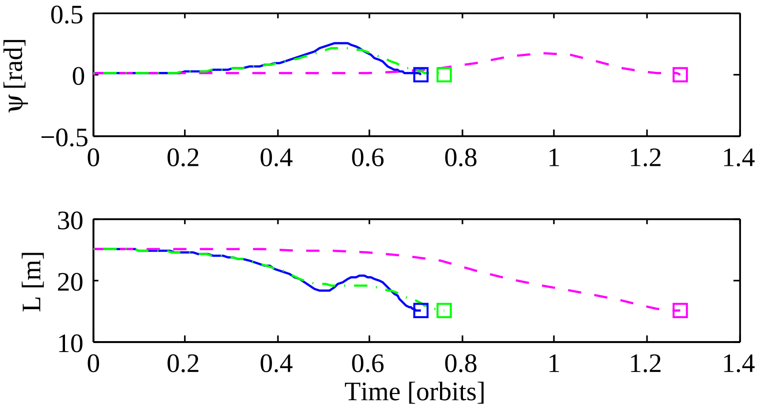

(b) In-plane Rotation Angle (ψ) and Two-Craft Separation Distance (L) Time Histories

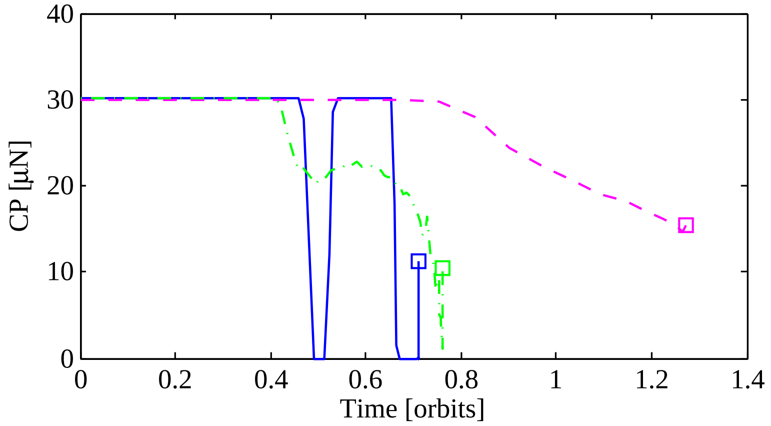

(c) Coulomb Propulsion (CP) Control Solutions

Figure 5.5: Simulation Results for Contracting the Radial Spacecraft Separation Distance from 25m to 15m. (— Min Time, – – Min Acceleration, – · – · Min Power)

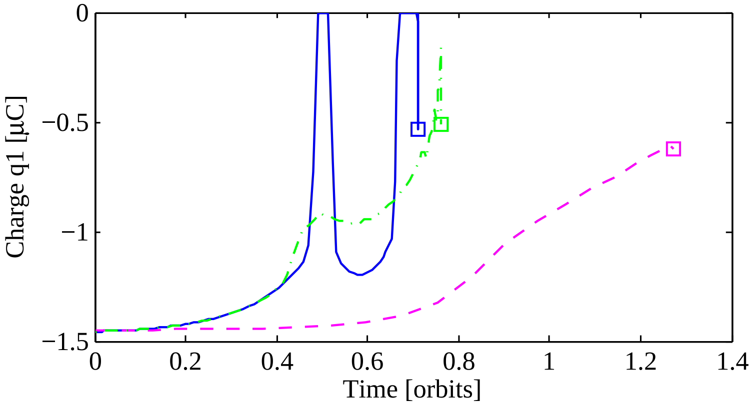

Figure 5.6: Spacecraft Charge Time Histories for Contracting the Radial Spacecraft Separation Distance from 25m to 15m. (— Min Time, – – Min Acceleration, – · – · Min Power)

that stabilize the separation distance and orientation respectively. Numerical simulations are performed for two sets of maneuvers, expanding the along-track Coulomb formation from an initial 25m to a final 35m and contracting the formation from a separation distance of 25m to 15m. The initial and final attitude values as well as the initial and final rates are set to zero through

$$\psi_i = \psi_f = \phi_i = \phi_f = \dot{\psi}_i = \dot{\psi}_f = \dot{\phi}_i = \dot{\phi}_f = \dot{L}_i = \dot{L}_f = 0 \tag{5.71}$$

For minimum-time, minimum-acceleration, minimum-fuel and minimum-power performance criteria, for an expansion maneuver in which the inter-craft distance increases from 25m to 35m, Figures 5.7 and 5.8 show the candidate in-plane trajectories, state histories, control solutions and the spacecraft charge time histories. The solutions are obtained for a choice of 25 nodes. Since the variations in the out-of-plane rotation angles (not shown) are negligible (on the order of 10^{-13} rad), only the in-plane trajectories are shown in Figure 5.7(a). The state histories in Figure 5.7(b) show that the boundary conditions are satisfied with viable variations of the in-plane rotation angles and the separation distances. The candidate control solutions in Figure 5.7(c) for minimum-time and minimum-fuel criteria display bang-bang characteristics, whereas, the minimum-power and minimum-acceleration criteria yields a continuous control solution. An end of a maneuver is denoted by a square box for the respective performance criterion. At the end of the maneuver, the controls should explicitly drop down to the equilibrium value. The charge on both craft will be zero at the end of the maneuver. Figure 5.8 shows the spacecraft charge time histories for one of the crafts. Since the magnitude of the control charges is on the order of micro-Coulombs, charge emission devices can be used in practice for implementation.

The propagated results (not shown) closely matched the pseudospectral approximations of the states, confirming the feasibility and convergence of the original solutions. Given the feasibility of the optimized solutions, the necessary conditions for optimality are examined. For the four performance measures, Table 5.4 shows that the approximate constancy of the Hamiltonian necessary condition is met. Table 5.4 also shows the optimal time required to complete the maneuver, maximum separation distance acceleration, and the RMS Coulomb and propulsion power required. With the minimum-time criterion, the expansion is finished in 0.1074 orbits. The mean Coulomb propulsion (CP) and electric propulsion (EP) power required for the minimum-time criterion are high, and are low for the minimum-power maneuver.

Table 5.4: Results for Expanding the Along-track Spacecraft Separation Distance from 25m to 35m.

Cost	Time t_f orbits	Max L'' $\frac{\text{m}}{\text{s}^2}$	CP Power [RMS] W	EP Power [RMS] W	Hamiltonian [Mean]
Min Time	0.1074	5.4894×10^{-7}	5.9631	0.5145	-0.9995
Min Acceleration	0.7958	1.2642×10^{-8}	0.7150	0.1327	-0.0046
Min Fuel	0.3239	5.594×10^{-7}	6.1763	0	0
Min Power	0.3386	7.0323×10^{-8}	0.1118	0.1075	0

Figures 5.9 and 5.10 shows the state trajectories, state time histories, control solutions and the spacecraft charge time histories for a contraction maneuver in which the inter-craft distance decreases from 25m to 15m. From the results of Table 5.5, the contraction maneuver for the minimum-time criterion finished in 0.1074 orbits. The contraction took 0.79 days to complete for the minimum-acceleration cost function. Similar to the expansion maneuver,

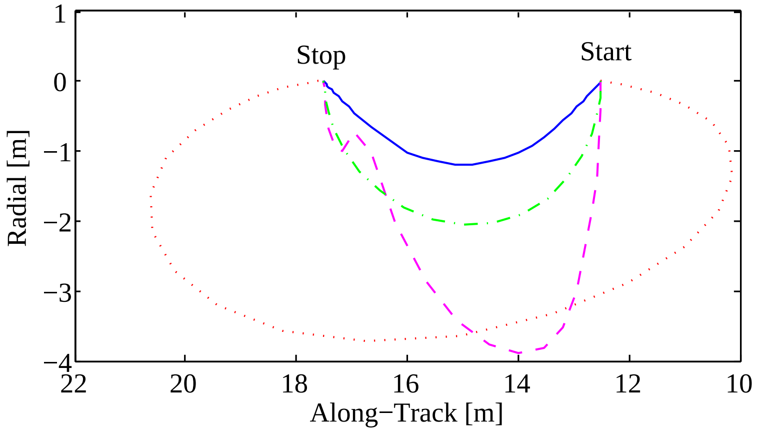

(a) In-plane Trajectories

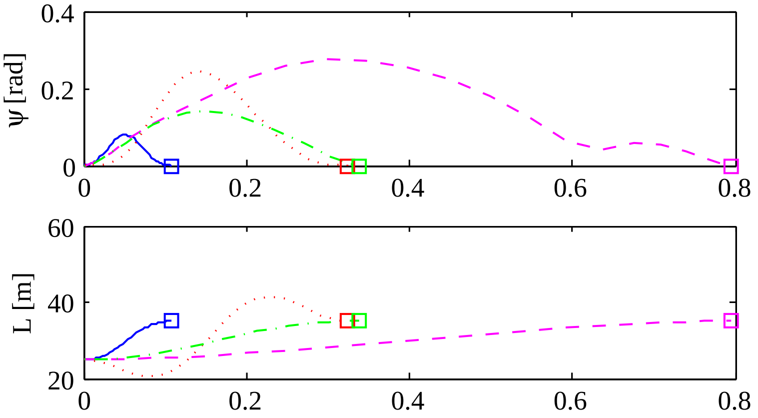

(b) In-plane Rotation Angle (ψ) and Two-Craft Separation Distance (L) Time Histories

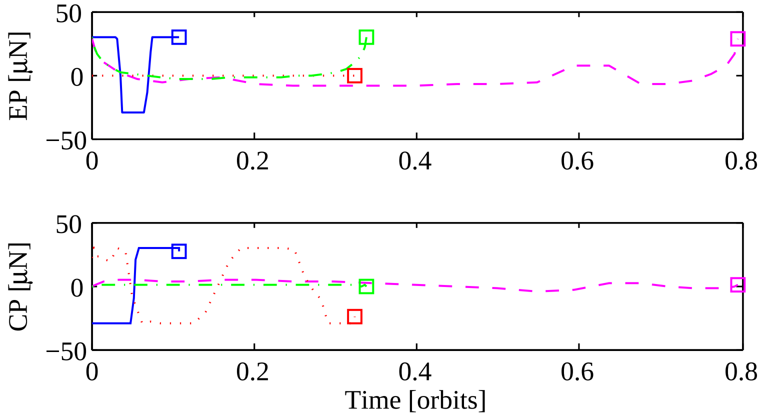

(c) Electric Propulsion (EP) and Coulomb Propulsion (CP) Controls

Figure 5.7: Simulation Results for Expanding the Along-track Spacecraft Separation Distance from 25m to 35m. (— Min Time, – – Min Acceleration, · · · Min Fuel, – · – · Min Power)

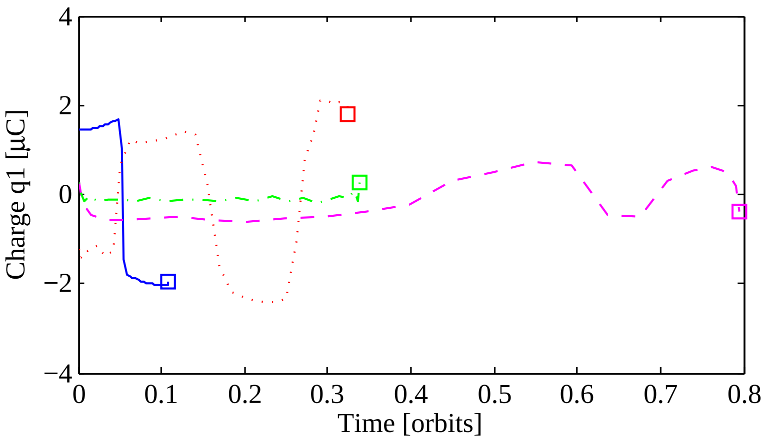

Figure 5.8: Spacecraft Charge Time Histories for Expanding the Along-track Spacecraft Separation Distance from 25m to 35m. (— Min Time, – – Min Acceleration, · · · Min Fuel, – · – · Min Power)

the mean Coulomb propulsion (CP) and electric propulsion (EP) power required for the minimum-time criterion are high, and are low for the minimum-power maneuver. With minimum-fuel cost function, it is observed that the contraction maneuver uses Coulomb propulsion with no electric propulsion thrust required.

Table 5.5: Results for Contracting the Along-track Spacecraft Separation Distance from 25m to 15m.

Cost	Time t_f orbits	Max L'' $\frac{\text{m}}{\text{s}^2}$	CP Power [RMS] W	EP Power [RMS] W	Hamiltonian [Mean]
Min Time	0.1074	5.5694×10^{-7}	3.0493	0.5127	-0.9997
Min Acceleration	0.7958	1.2484×10^{-8}	0.4341	0.1065	-0.0092
Min Fuel	0.3175	5.4186×10^{-7}	3.6399	0	0
Min Power	0.2763	1.0401×10^{-7}	0.2139	0.1581	-0.0001

5.5.3 Orbit-normal Spacecraft Separation Distance Expansion and Contraction Maneuvers

This example illustrates how to optimally reconfigure a 2-craft Coulomb virtual tether formation to move the craft apart or closer in orbit-normal equilibrium configuration. Similar

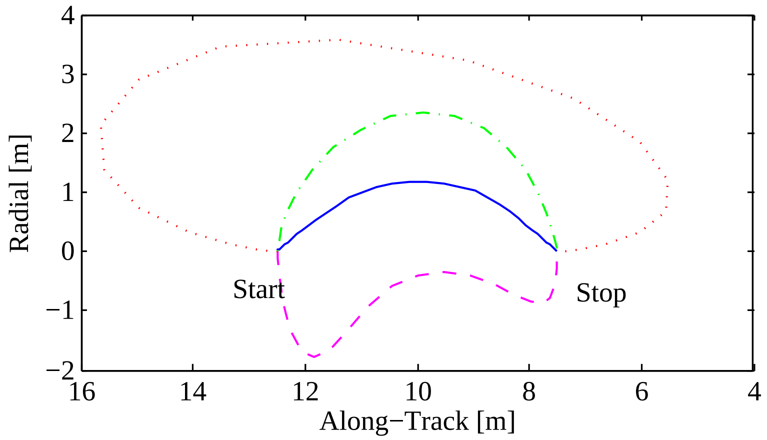

(a) In-plane Trajectories

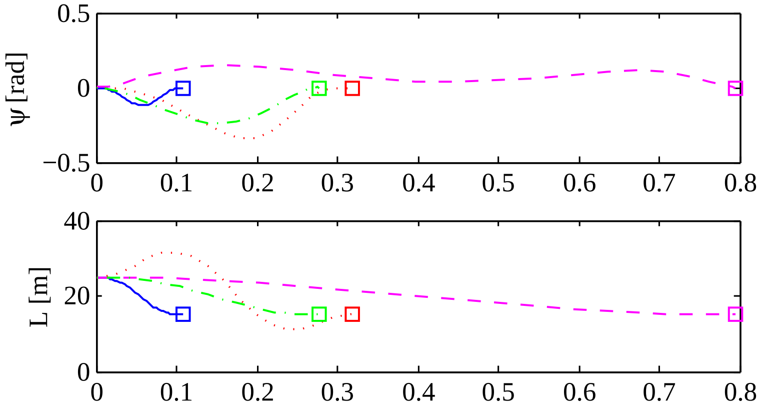

(b) In-plane Rotation Angle (ψ) and Two-Craft Separation Distance (L) Time Histories

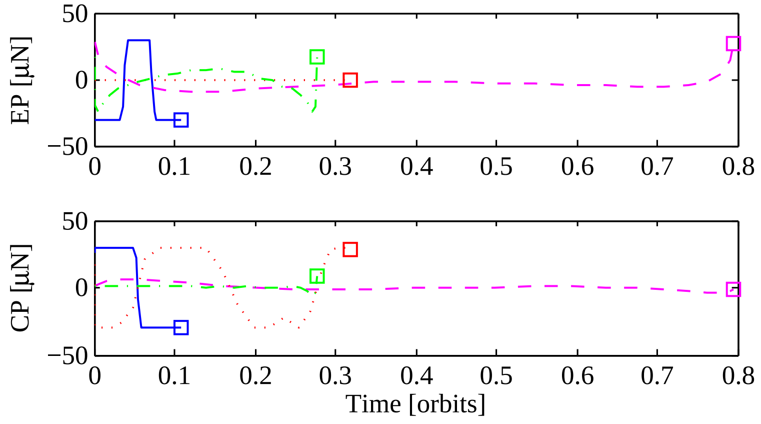

(c) Electric Propulsion (EP) and Coulomb Propulsion (CP) Controls

Figure 5.9: Simulation Results for Contracting the Along-track Spacecraft Separation Distance from 25m to 15m. (— Min Time, − − Min Acceleration, · · · Min Fuel, − · − · Min Power)

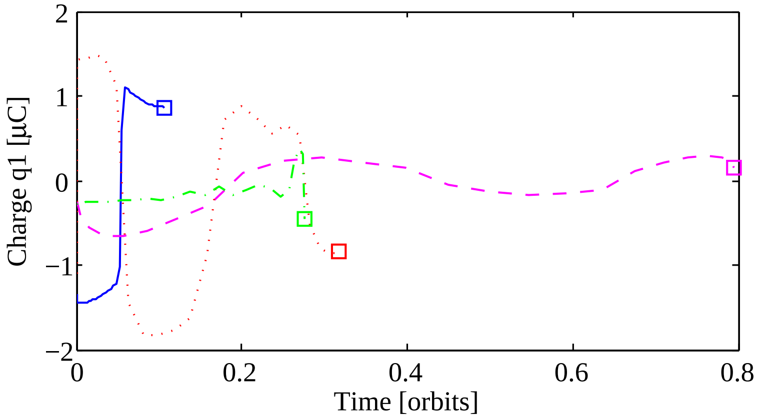

Figure 5.10: Spacecraft Charge Time Histories for Contracting the Along-track Spacecraft Separation Distance from 25m to 15m. (— Min Time, – – Min Acceleration, · · · Min Fuel, – · – · Min Power)

to the along-track maneuver, this reconfiguration requires hybrid control of Coulomb forces and conventional thrusters that stabilize the separation distance and orientation. Numerical simulations are performed for two sets of maneuvers, expanding the orbit-normal Coulomb formation from an initial 25m to a final 35m and contracting the formation from a separation distance of 25m to 15m. The initial and final attitude values as well as the initial and final rates are set to zero through

$$\phi_i = \phi_f = \theta_i = \theta_f = \dot{\phi}_i = \dot{\phi}_f = \dot{\theta}_i = \dot{\theta}_f = \dot{L}_i = \dot{L}_f = 0 \tag{5.72}$$

Figures 5.11 and 5.12 show the candidate solutions for an expansion maneuver in which the inter-craft distance increases from 25m to 35m. The solutions are obtained for a choice of 36 nodes. Figure 5.11(a) show the three-dimensional trajectories. The minimum-fuel trajectory indicates that the maneuver uses Coulomb propulsion with no electric propulsion thrust. The state histories in Figure 5.11(b) show that the boundary conditions are satisfied with viable variations of the rotation angles and the separation distances. The control solutions in Figure 5.11(c) for minimum-time and minimum-fuel criteria display bang-bang characteristics, whereas, the minimum-power and minimum-acceleration criteria yields a continuous control solution. The charge on craft 2 will be equal to that of craft 1. Figure

5.12 shows the spacecraft charge time histories for one of the crafts.

For the four performance measures, Table 5.6 shows that the approximate constancy of the Hamiltonian necessary condition is met. Table 5.6 also shows the optimal time required to complete the maneuver, maximum separation distance acceleration, and the RMS Coulomb and propulsion power required. With the minimum-time criterion, the expansion is finished in 0.1903 orbits. With minimum-fuel cost function, it is observed that the expansion maneuver uses Coulomb propulsion with no electric propulsion thrust required. The remaining analysis is similar to that of along-track configuration.

Table 5.6: Results for Expanding the Orbit-normal Spacecraft Separation Distance from 25m to 35m.

Cost	Time t_f orbits	Max $L^{''}$ $\frac{\text{m}}{\text{s}^2}$	CP Power [RMS] W	EP Power [RMS] W	Hamiltonian [Mean]
Min Time	0.1903	1.6535×10^{-7}	2.2345	1.0097	−0.9997
Min Acceleration	0.7958	1.2863×10^{-8}	1.2052	0.2573	−0.0046
Min Fuel	0.2721	5.0072×10^{-8}	4.7126	0	0
Min Power	0.2347	9.0036×10^{-8}	1.0247	0.4057	0.0001

Figures 5.13 and 5.14 show the candidate solutions for a contraction maneuver in which the inter-craft distance decreases from 25m to 15m. From the results of Table 5.7, the contraction maneuver for the minimum-time criterion finished in 0.1888 orbits and for the minimum-acceleration criterion it took the maximum of 0.7958 orbits. Similar to the expansion maneuver, the mean Coulomb propulsion (CP) and electric propulsion (EP) power required for the minimum-time criterion are high, and are low for the minimum-power maneuver. With minimum-fuel cost function, it is observed that the contraction maneuver uses Coulomb propulsion with no electric propulsion thrust required. The remaining analysis is similar to that of the expansion maneuver.

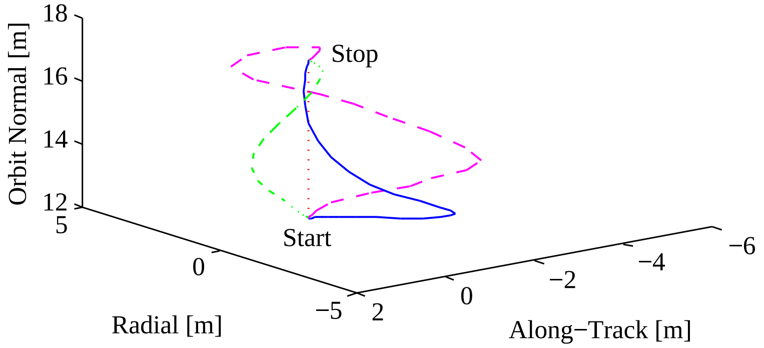

(a) 3D Trajectories

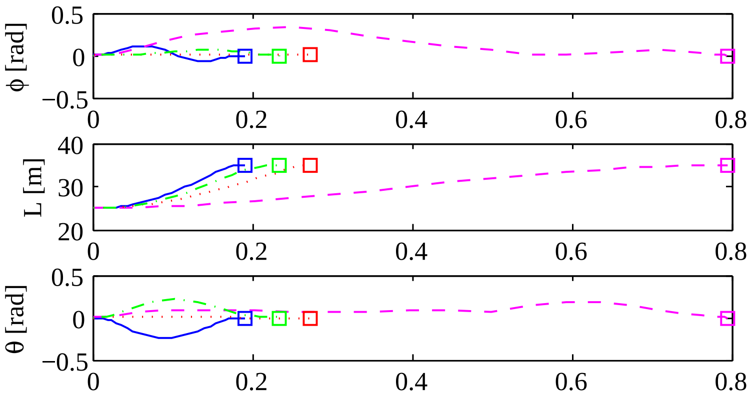

(b) Rotation Angles (ϕ, θ) and Two-Craft Separation Distance (L) Time Histories

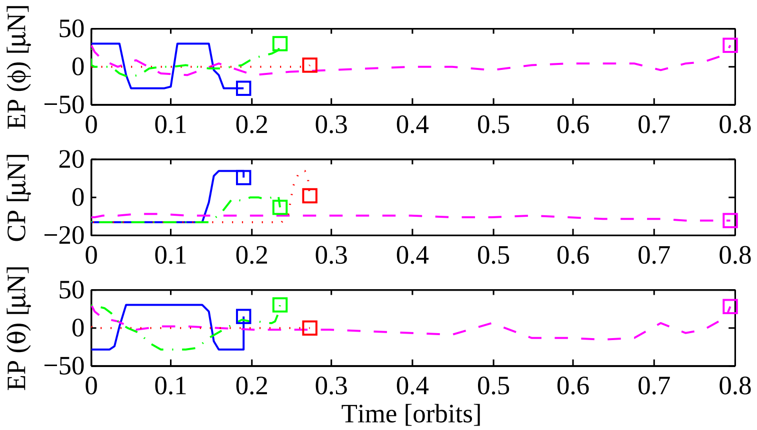

(c) Electric Propulsion (EP) and Coulomb Propulsion (CP) Controls

Figure 5.11: Simulation Results for Expanding the Orbit-normal Spacecraft Separation Distance from 25m to 35m. (— Min Time, – – Min Acceleration, · · · Min Fuel, – · – · Min Power)

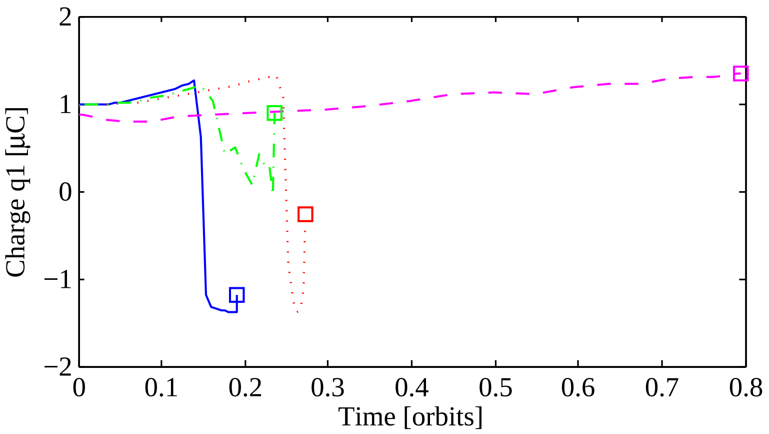

Figure 5.12: Spacecraft Charge Time Histories for Expanding the Orbit-normal Spacecraft Separation Distance from 25m to 35m. (— Min Time, – – Min Acceleration, · · · Min Fuel, – · – · Min Power)

Table 5.7: Results for Contracting the Orbit-normal Spacecraft Separation Distance from 25m to 15m.

Cost	Time t_f orbits	Max L'' $\frac{\text{m}}{\text{s}^2}$	CP Power [RMS] W	EP Power [RMS] W	Hamiltonian [Mean]
Min Time	0.1888	1.8416×10^{-7}	0.9585	0.8938	-1.0446
Min Acceleration	0.7958	1.272×10^{-8}	0.5536	0.2497	-0.0089
Min Fuel	0.2823	5.1993×10^{-8}	0.6742	0	0
Min Power	0.2574	6.5698×10^{-8}	0.5928	0.1034	0

5.5.4 Radial to Along-track Maneuver

The next example illustrates an optimal radial to along-track maneuver with the following boundary conditions

$$L_i = L_f = 25\,\text{m}, \psi_i = 0\,\text{rad}, \psi_f = -\pi/2\,\text{rad} \tag{5.73a}$$

$$\theta_i = \theta_f = \dot{\psi}_i = \dot{\psi}_f = \dot{\theta}_i = \dot{\theta}_f = \dot{L}_i = \dot{L}_f = 0 \tag{5.73b}$$

To utilize the rotational formation dynamics, the final in-plane attitude angle ψ_f is set to $-\pi/2\,\text{rad}$. Figures 5.15 and 5.16 show the simulation results for a radial to along-track

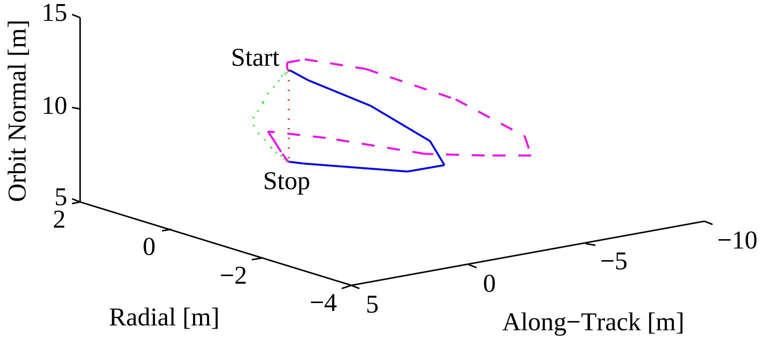

(a) 3D Trajectories

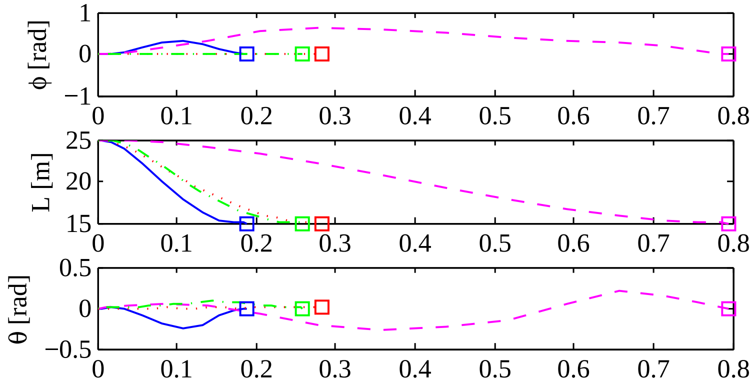

(b) Rotation Angles (ϕ, θ) and Two-Craft Separation Distance (L) Time Histories

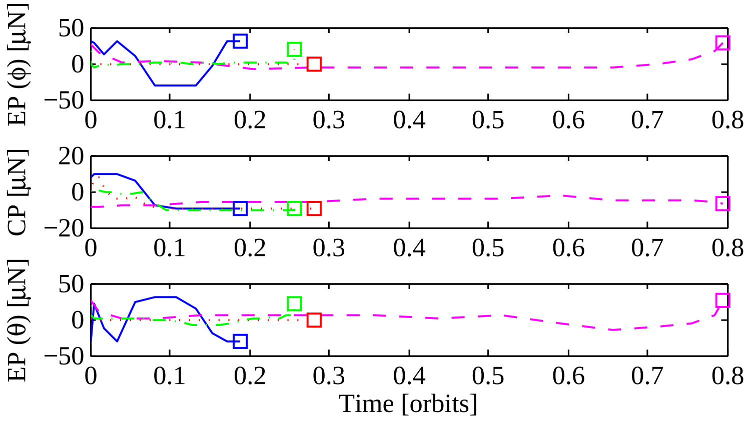

(c) Electric Propulsion (EP) and Coulomb Propulsion (CP) Controls

Figure 5.13: Simulation Results for Contracting the Orbit-normal Spacecraft Separation Distance from 25m to 15m. (— Min Time, − − Min Acceleration, · · · Min Fuel, − · − Min Power)

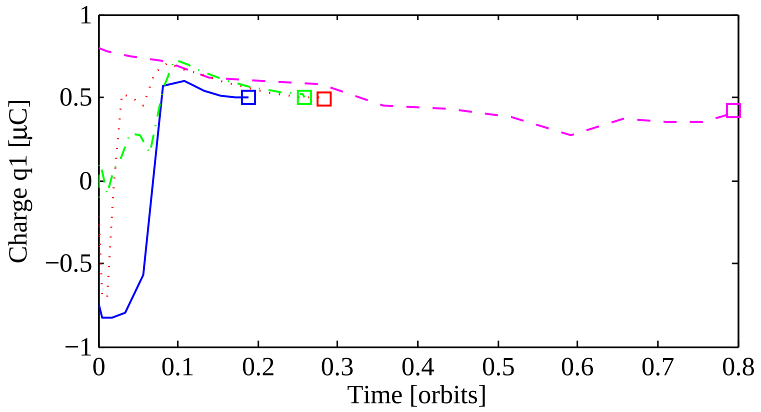

Figure 5.14: Spacecraft Charge Time Histories for Contracting the Orbit-normal Spacecraft Separation Distance from 25m to 15m. (— Min Time, – – Min Acceleration, · · · Min Fuel, – · – · Min Power)

reconfiguration with a fixed separation distance of 25m at the initial and final equilibrium positions. The results for all four cost functions are obtained for a choice of 75 nodes. Figure 5.15(a) illustrates the in-plane trajectories for this maneuver. It is interesting to note that the minimum-fuel trajectory differs significantly from the others. The in-plane state histories in Figure 5.15(b) indicate that the boundary conditions are met. Figure 5.15(c) shows that the minimum-fuel maneuver uses maximum Coulomb thrusting, thus minimizing the EP thrusting usage. The charge histories in Figure 5.16 not only show the easily controllable charge magnitudes but also show the charge sign switching during the reconfiguration.

The propagated results (not shown) using ode45 closely matched the pseudospectral approximation of the states, thus verifying the feasibility and convergence of the solution. Moreover, as shown in Table 5.8, the constancy of the Hamiltonian value is satisfied for each performance measure. The final time required to complete the maneuver is a minimum of 0.22 days for the minimum-time criterion and is a maximum of 0.54 days for the minimum-acceleration criterion. The RMS power consumption shown in Table 5.8 indicates that more Coulomb propulsion is used over electric propulsion. For the maneuver, a maximum of about 4 Watts for Coulomb thrusting and a maximum of about 0.5 Watt for EP thrusting are utilized, easily meeting the power requirements of charge emission devices and Colloid thrusters. At the end of the maneuver at 25m at the along-track equilibrium position, the minimum-time, minimum-fuel and minimum-power Coulomb controls should explicitly drop down to the equilibrium value of 0μN. The minimum-acceleration continuous Coulomb control dropped down to the equilibrium value at the final time.

Table 5.8: Results of a Radial to Along-track Maneuver with 25m Separation Distance at the Initial and Final Positions.

Cost	Time t_f orbits	Max L'' $\frac{\text{m}}{\text{s}^2}$	CP Power [RMS] W	EP Power [RMS] W	Hamiltonian [Mean]
Min Time	0.2259	5.8934×10^{-7}	3.2953	0.5225	-0.9996
Min Acceleration	0.5440	6.0722×10^{-9}	2.1579	0.2246	0
Min Fuel	0.4419	2.5784×10^{-7}	1.5135	0.3772	0.0448
Min Power	0.3970	3.9874×10^{-7}	1.5770	0.2121	0.0005

Figure 5.17 shows the trajectories and controls for the same radial to along-track reconfiguration, but with the boundary conditions not utilizing the rotational formation dynamics. This implies that the final in-plane attitude angle ψ_f is set to $\pi/2$ rad. The solutions are shown for all four cost functions and the in-plane trajectories are not very different to those of the solutions obtained utilizing the rotational formation dynamics. However, the control effort required for minimum-time exhibits sharp fluctuations which remained irrespective of the number of nodes chosen. Also, the reconfiguration times are longer compared to that of the reconfigurations with the boundary conditions utilizing the rotational formation dynamics. Furthermore, the numerical simulation times between the two boundary conditions varied greatly, which are presented in detail in the next section.

5.5.5 Family of Radial to Along-track Maneuvers

In this example, a family of optimal maneuvers from radial to along-track equilibrium positions are illustrated. Figure 5.18 displays the Coulomb and electric propulsion controls (RMS) as a function of varying separation distances for each of the four cost functions. Each maneuver is performed with a fixed separation distance of 25m at the initial radial position, and varying final separation distances. Furthermore, the boundary conditions take advantage

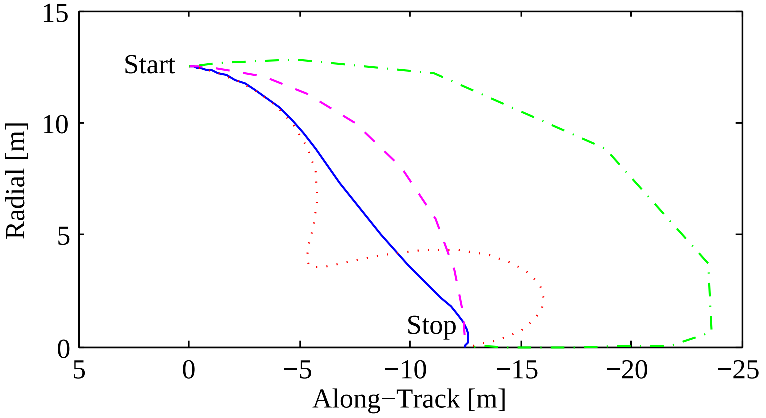

(a) In-plane Trajectories

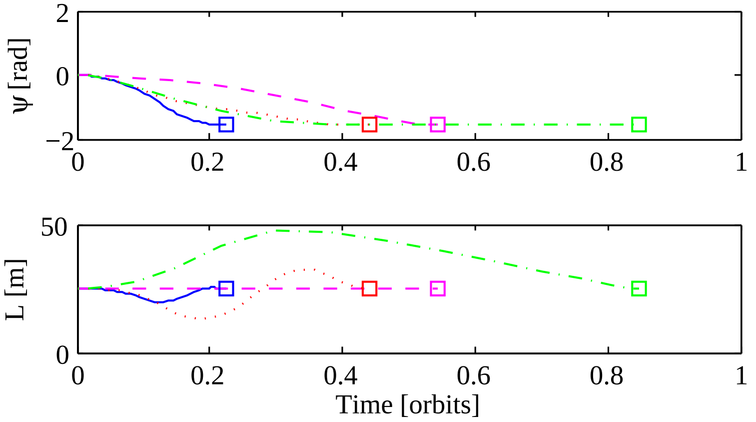

(b) In-plane Rotation Angle (ψ) and Two-Craft Separation Distance (L) Time Histories

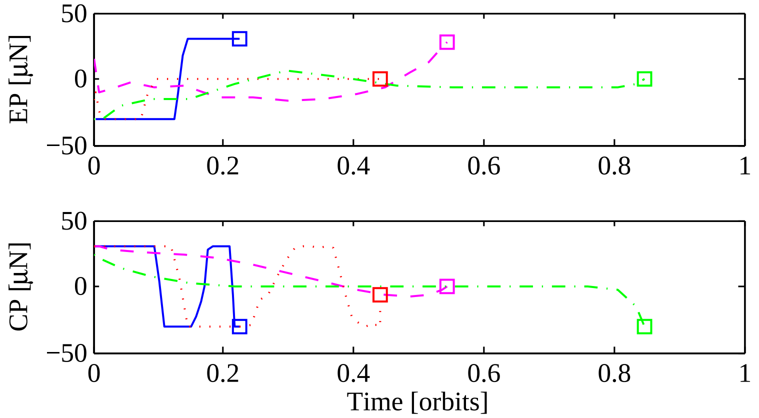

(c) Electric Propulsion (EP) and Coulomb Propulsion (CP) Controls

Figure 5.15: Simulation Results of a Radial to Along-track Maneuver with 25m Separation Distance at the Initial and Final Positions. (— Min Time, − − Min Acceleration, · · · Min Fuel, − · − · Min Power)

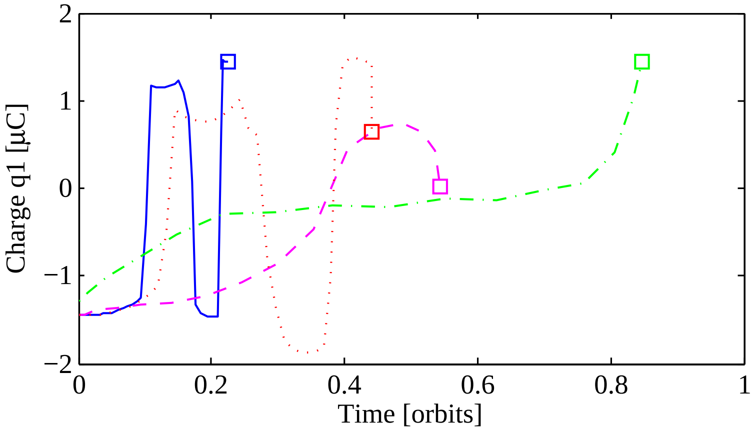

Figure 5.16: Spacecraft Charge Time Histories of a Radial to Along-track Maneuver with 25m Separation Distance at the Initial and Final Positions. (— Min Time, – – Min Acceleration, · · · Min Fuel, – · – · Min Power)

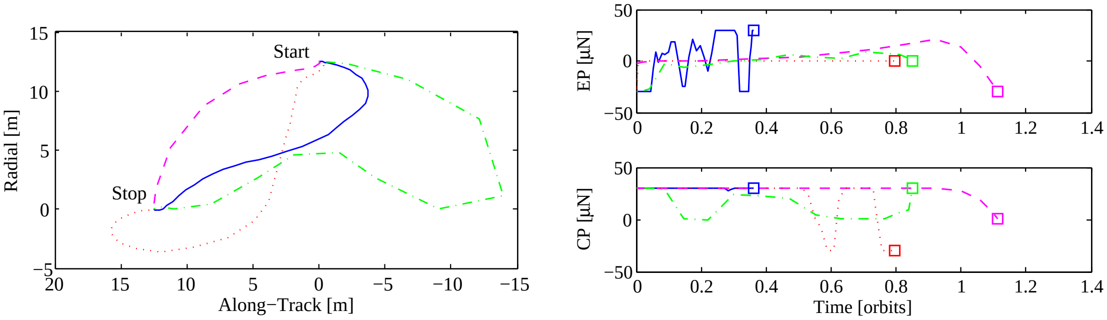

(a) In-plane Trajectories

(b) Electric Propulsion (EP) and Coulomb Propulsion (CP) Controls

Figure 5.17: Simulation Results of a Radial to Along-track Maneuver with 25m Separation Distance at the Initial and Final Positions with Boundary Conditions Not utilizing the Rotational Dynamics. (— Min Time, – – Min Acceleration, · · · Min Fuel, – · – · Min Power)

of the rotational formation dynamics of the two-craft system. The minimum-time performance measure consistently utilized more Coulomb and electric propulsion compared to the other measures. Whereas, for the minimum-power cost function, the Coulomb thrust used for two-craft separation distances between 90m and 125m is negligible (on the order of $10^{-5}\mu$N), and the EP thrust observed over the same distances is significantly higher. Another observation from Figures 5.18(a) and 5.18(b) is that minimum electric propulsion thrust is required for minimum-fuel cost function. The maneuver is able to use more Coulomb propulsion due to the exploitation of the rotational formation dynamics.

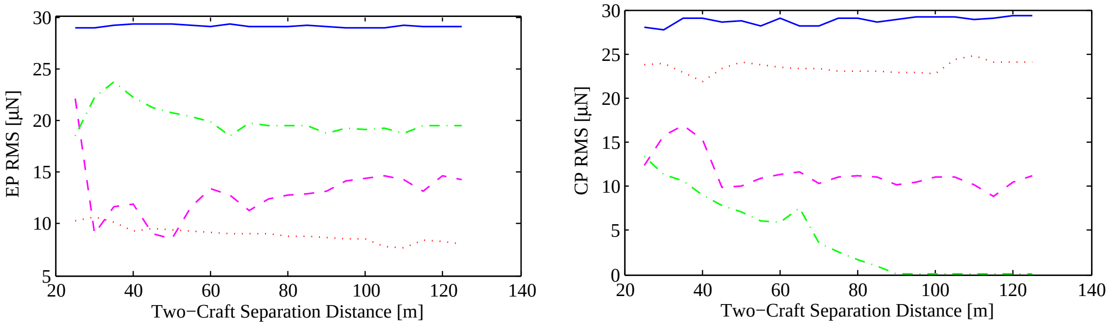

(a) EP Controls

(b) CP Controls

Figure 5.18: In-plane Control Solutions for Family of Maneuvers from Radial to Along-track Equilibrium Position with Initial Separation Distance of 25m. (— Min Time, – – Min Acceleration, · · · Min Fuel, – · – · Min Power)

Figure 5.19 show results for two sets of maneuvers for the minimum-time performance measure. One set of maneuvers is generated with the boundary conditions taking advantage of the rotational formation dynamics (natural boundary conditions) and the other set is generated without taking advantage of the rotational formation dynamics (non-natural boundary conditions). Figure 5.19(a) shows the minimum-time trajectories with an initial separation distance of 25m between the craft and a final separation distance varying between 25m and 125m. Figure 5.19(a) also shows the closed-form natural solution using the Hill's equations[14] in which one craft is placed in the radial equilibrium position and allowed to drift in the absence of any Coulomb interaction with the second craft. Although the two sets of trajectories appear symmetric, collisions may occur with the other craft with non-natural boundary conditions. The control solutions (not shown) exhibit sharp fluctuations for each maneuver with non-natural boundary conditions. Also, the reconfiguration times (not shown) are longer compared to that of the reconfigurations with natural boundary conditions. Moreover, Figure 5.19(b) shows the numerical simulation times for each set of maneuvers which are much lower with the natural boundary conditions. For instance, in a worst-case scenario, with a separation distance of 125m, the simulation times for the non-natural boundary conditions are almost two orders of magnitude greater than those of obtained using the natural boundary conditions. Therefore, utilizing the natural formation dynamics yields clean bang-bang controls, collisionless trajectories and much lower simulation times.

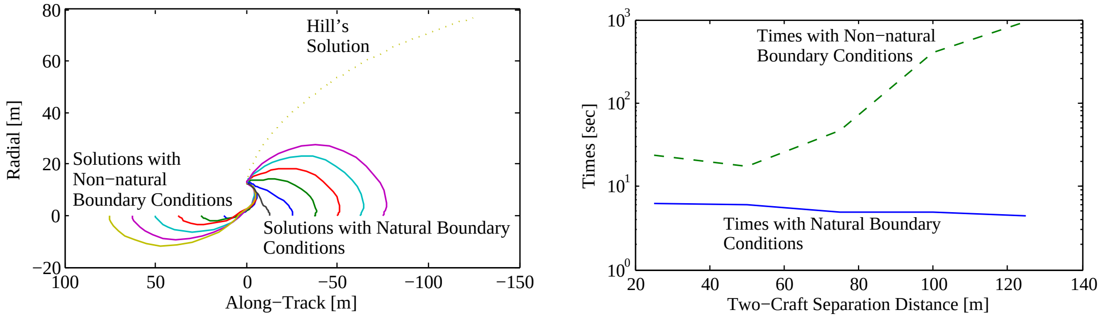

(a) Spacecraft Trajectories (b) Simulation Times

Figure 5.19: Minimum-Time Family of Maneuvers from Radial to Along-track Equilibrium Position with Initial Separation Distance of 25m.

5.5.6 Radial to Orbit-normal Maneuver

The final example illustrates an optimal radial to orbit-normal maneuver with the following boundary conditions

$$L_i = L_f = 25\,\text{m}, \phi_i = 0\,\text{rad}, \phi_f = 0\,\text{rad} \tag{5.74a}$$

$$\theta_i = \theta_f = \dot{\phi}_i = \dot{\phi}_f = \dot{\theta}_i = \dot{\theta}_f = \dot{L}_i = \dot{L}_f = 0 \tag{5.74b}$$

Figures 5.20 and 5.21 show the simulation results for a radial to orbit-normal reconfiguration with a fixed separation distance of 25m at the initial and final equilibrium positions. The results for all four cost functions are obtained for a choice of 25 nodes. Figure 5.20(a) illustrates the three-dimensional trajectories for this maneuver. It is interesting to note that the minimum-fuel trajectory differs significantly from the others. More importantly, the separation distance becomes close to zero as in Figure 5.20(b) indicating that the maneuver could lead to a collision with the second craft. The in-plane state histories in Figure 5.20(b) indicate that the boundary conditions are met. Figure 5.20(c) shows that the minimum-fuel maneuver uses maximum Coulomb thrusting, thus minimizing the EP thrusting usage. The charge histories in Figure 5.21 not only show the easily controllable charge magnitudes but also show the charge sign switching during the reconfiguration.

As shown in Table 5.9, the constancy of the Hamiltonian value is satisfied for each performance measure. The final time required to complete the maneuver is a minimum of 0.21 days for the minimum-time criterion and is a maximum of 0.79 days for the minimum-power criterion. The RMS power consumption shown in Table 5.9 indicates that more Coulomb propulsion is used over electric propulsion for minimum-time, minimum-acceleration and minimum-fuel criteria. However, for the minimum-power criterion, more electric propulsion is used over Coulomb propulsion. Note that overall power consumption is minimum for minimum-power criterion satisfying the cost function. For the maneuver, a maximum of about 4.3 Watts for Coulomb thrusting and a maximum of about 0.95 Watt for EP thrusting are utilized, easily meeting the power requirements of charge emission devices and Colloid thrusters. At the end of the maneuver at 25m in the orbit-normal equilibrium position, the minimum-time, minimum-fuel and minimum-power Coulomb controls should explicitly drop down to the equilibrium value of 9.88μN. The minimum-acceleration continuous Coulomb control dropped down to the equilibrium value at the final time.

5.6 Summary

This chapter presents an optimal-control framework for the reconfiguration of two-craft formations in circular orbits. Several reconfiguration problems are discussed, with each problem discretized using a Legendre pseudo-spectral method, and the resulting non-linear optimal

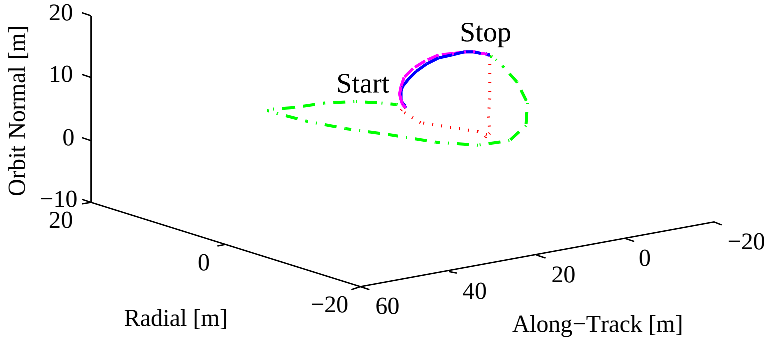

(a) 3D Trajectories

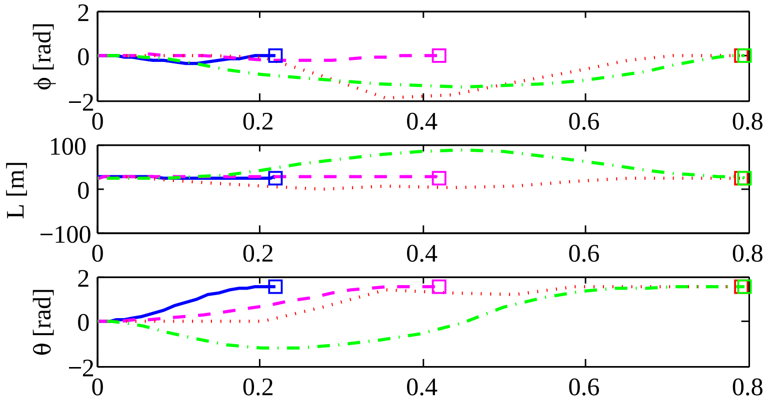

(b) Rotation Angles (ϕ, θ) and Two-Craft Separation Distance (L) Time Histories

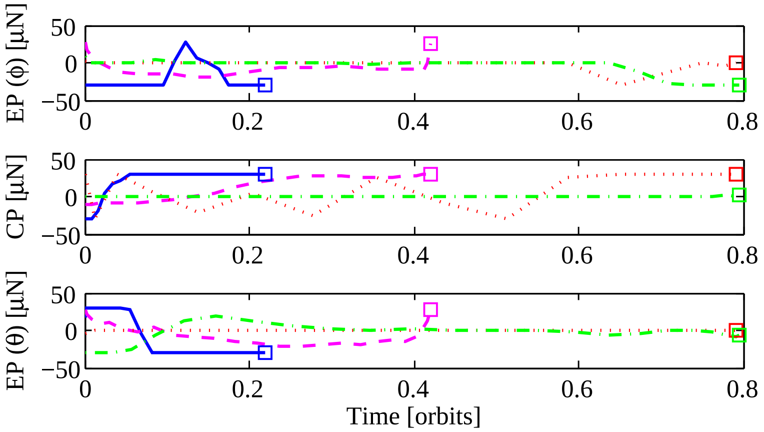

(c) Electric Propulsion (EP) and Coulomb Propulsion (CP) Controls

Figure 5.20: Simulation Results of a Radial to Orbit-normal Maneuver with 25m Separation Distance at the Initial and Final Positions. (— Min Time, – – Min Acceleration, · · · Min Fuel, – · – · Min Power)

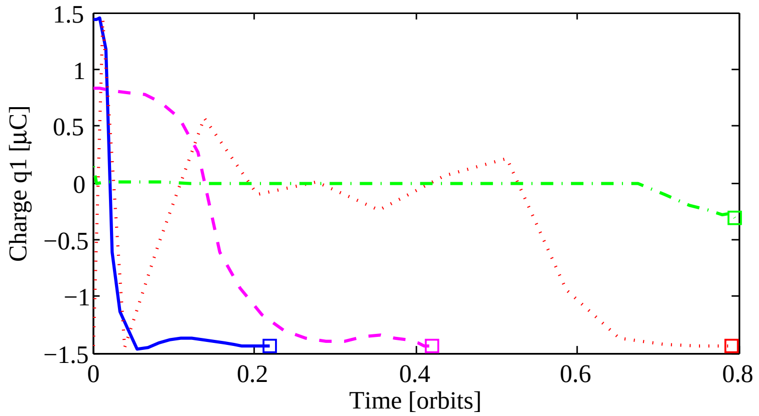

Figure 5.21: Spacecraft Charge Time Histories of a Radial to Orbit-normal Maneuver with 25m Separation Distance at the Initial and Final Positions. (— Min Time, – – Min Acceleration, · · · Min Fuel, – · – · Min Power)

Table 5.9: Results of a Radial to Orbit-normal Maneuver with 25m Separation Distance at the Initial and Final Positions.

Cost	Time t_f orbits	Max L'' $\frac{\text{m}}{\text{s}^2}$	CP Power [RMS] W	EP Power [RMS] W	Hamiltonian [Mean]
Min Time	0.2187	2.6986×10^{-7}	4.2630	0.9520	-0.9971
Min Acceleration	0.4198	8.3519×10^{-9}	3.2739	0.4295	0.0001
Min Fuel	0.6085	3.8721×10^{-7}	2.5488	0.1698	0.0319
Min Power	0.7958	3.9053×10^{-7}	0.0909	0.2930	-0.0005

control problems solved using the software package DIDO. Pontryagin's Minimum Principle verifies the feasibility and optimality of the open-loop numerical solutions. Four measures of optimality are discussed: minimum reconfiguration time, minimum acceleration of the separation distance, minimum electric propulsion fuel usage and minimum power consumption. Results for these cost functions are illustrated for each reconfiguration problem with the goal of maximizing Coulomb propulsion usage while utilizing minimum electric propulsion. Because no linearizations are involved with nonlinear optimal control techniques, boundary conditions in the nonlinear regime hold. Previous Coulomb formation flying work used linearized time-varying dynamical models. Compared to previous work, the expansion and contraction reconfigurations in the radial, along-track and orbit normal directions are achieved in shorter times. Successful in-plane radial to along-track optimal reconfigurations for each performance measure are shown along with a family of minimum-time optimal maneuvers. The results highlight the advantage of using natural formation dynamics in the selection of boundary conditions for such maneuvers. Then, a final numerical simulation illustrates an out-of-plane radial to orbit-normal maneuver.

Chapter 6

CONCLUSIONS

Techniques from geometric mechanics, linear and non-linear feedback control systems, and optimal control theory have been applied to investigate the dynamics and control of a two-craft Coulomb tether formation in circular orbits and at libration points. This chapter discusses the work accomplished that meets the objectives of the dissertation. It also describes avenues for future research beyond the scope of this dissertation.

6.1 Main Results in this Dissertation

6.1.1 Two-Craft Tether Formation Relative Equilibria about Circular Orbits and Libration Points

The relative equilibria of a two-craft formation moving in a restricted two-body system and a restricted three-body system are presented using the exact gravitational and Coulomb potentials. A general framework of two-craft connected by an elastic tether force is studied with an emphasis on a virtual Coulomb tether as a special case. The orbit-attitude coupling effects should be considered for large spacecraft separation distances; for LEO, greater than tens of kilometers, for GEO, hundreds of kilometers, and at libration points, tens of thousands of kilometers. Such coupling effects can be ignored for shorter spacecraft separation distances. The negligible non-great circle effects shown validate the simple principle axes condition to find equilibrium solutions in GEO circular orbits for Coulomb tether applications. Consequently, for a charged two-craft formation, the principal axis condition is very good for genetic algorithms which seek approximate equilibrium answers. However, for full non-linear solutions, these effects can be taken into consideration. Moreover, the three great-circle relative equilibria (radial, along-track and orbit normal) of a two-craft formation at all five libration points are presented. Also, the nongreat-circle effects are numerically shown to exist at the Earth-Moon collinear libration points. Interestingly, in the restricted three-body system, a tether force is required for the along-track equilibrium, however, no tether force is necessary in the restricted two-body system. For two-craft Coulomb tether separation distances in a restricted three-body system, the negligible non-great circle effects at collinear libration points indicate that the simple principle axes condition should suffice in the development of equations of motion. Furthermore, the results obtained here are used to investigate the dynamics and stability of a 2-craft Coulomb tether formation at libration points. One conference paper has been presented from this work[45] and a journal paper is under review.

6.1.2 Dynamic Analysis of Two-Craft Coulomb Formation at Libration Points

The feasibility of a two-craft Coulomb formation concept is studied at libration points for orbit-radial, along-track and orbit-normal equilibria. The new two-craft dynamics at the libration points is provided as a general framework in which circular Earth orbit dynamics form a special case. The general equations of motion for collinear libration points has a σ term which varies for each collinear libration point. Interestingly, setting "$\sigma = 1$" yields the same equations of motion for all three equilibrium configurations in circular Earth orbits. At the triangular libration points, although there are additional terms in equations of motion for the three equilibria, the effect of these additional terms on the dynamics is small. Therefore, the dynamics and the stability conditions are similar to those found in Reference 5 for a 2-craft formation at GEO. For orbit-radial equilibrium, a linearized charge feedback law is used wherein Coulomb force stabilizes the separation distance, while exploiting the gravity gradient torque due to the two primaries for stabilizing the in-plane attitude motion. For both along-track and orbit-normal configurations, a hybrid control of Coulomb forces and conventional thrusters is required for stabilizing the separation distance and orientation respectively. Also, due to the large distances from the Earth-moon barycenter to the libration points and due to the smaller rotation rate of the barycenter, the micro-Coulomb charge requirements at the libration points is at least an order of magnitude smaller then that of a two-body system in Reference 5. The thrusting forces required are less than micro-Newtons in magnitude and are applied in orthogonal directions. One conference paper has been presented from this work[46] and a journal paper is under preparation.

In the linearized study, the assumption is that the differential solar radiation pressure on the formation is zero. When the differential solar drag on the two-craft formation is not zero and in the presence of time varying SRP disturbances, a Lyapunov feedback control method is presented for feedback stabilization of a radial equilibrium two-craft Coulomb tether formation at any collinear libration point. The method uses a Lyapunov function based on a first integral of motion of the two-craft Coulomb formation. The controller designed by this method works very well and the control law utilizes a three-dimensional control (separation distance, in-plane and out-of-plane motion). Both the control charges needed in the order of micro-Coulombs and the transverse control forces in the order of micro-Newtons are realizable in practice. A conference paper is under preparation which focuses the application of Lyapunov feedback control method.

6.1.3 Optimal Reconfigurations of Two-Craft Coulomb Formation in Circular Orbits

An optimal-control framework for the reconfiguration of two-craft formations in circular orbits is presented. Several in-plane and out-of-plane reconfiguration problems are discussed, with each problem discretized using a Legendre pseudo-spectral method, and the resulting non-linear optimal control problems are solved using the software package DIDO. The feasibility and optimality of the open-loop numerical solutions are verified with Pontryagin's Minimum Principle. Four measures of optimality are discussed: minimum reconfiguration time, minimum acceleration of the separation distance, minimum electric propulsion fuel usage, and minimum electrical power consumption. Results for these cost functions are illustrated for each reconfiguration problem with the goal of maximizing Coulomb propulsion usage while utilizing minimum electric propulsion. The various two-craft reconfigurations considered are: radial, along-track and orbit normal spacecraft separation distance expansion and contraction maneuvers, radial to along-track and radial to orbit-normal maneuvers with constant separation distance at the initial and final positions, and a family of radial to along-track maneuvers. Because no linearizations are involved with nonlinear optimal control techniques, boundary conditions in the nonlinear regime hold. Previous Coulomb formation flying work used linearized time-varying dynamical models. Compared to previous work, the expansion and contraction reconfigurations in the radial, along-track and orbit normal directions are achieved in shorter times. Successful in-plane radial to along-track optimal reconfigurations for each performance measure are shown along with a family of minimum-time optimal maneuvers. For such maneuvers, the advantage of using natural formation dynamics in the selection of boundary conditions is highlighted. The orbit-normal spacecraft separation distance expansion and contraction maneuvers as well as radial to orbit-normal maneuvers involve three-dimensional reconfigurations which are illustrated considering the coupled in-plane and the out-of-plane motions. Not only are useful optimal reconfigurations for various problems found but interesting insights are given for respective cost functions. For instance, for a radial to orbit-normal maneuver with a minimum-fuel cost function, extra path constraints are necessary to avoid collisions between the craft. One conference paper has been presented from this work[47] and a journal paper is under preparation.

6.2 Future Work

There are many future research avenues for exploration beyond the work presented in this thesis. A few of them are given here.

In the presence of time varying SRP disturbances at libration points, similar to the nonlinear feedback control strategy presented for orbit-radial configuration, a Lyapunov feedback control method can be developed for stabilization of orbit normal or along-track two-craft Coulomb tether formations.

For the reconfiguration of two-craft formations in circular orbits, solar radiation pressure effects can be incorporated in the GEO environment. Also, optimal maneuvers of a two spacecraft Coulomb formation at libration points can be studied. Furthermore, the optimal-control framework presented here can be extended to determine optimal three-craft reconfigurations between two charged equilibria configurations. Such three-spacecraft Coulomb formations can be investigated by adding charge constraints to the problem formulation.

For satellite orbit problems, if the optimal control open-loop solutions can be generated fast enough, closed-loop feedback trajectories can be generated. In recent years, the notion of Carathodory$-\pi$ solutions are introduced that stem from the equivalence between closed-loop and feedback trajectories.[31] These ideas lead to a new set of foundations for achieving feedback wherein optimality principles are interwoven to achieve stability and system performance. Therefore, closed loop solutions can be investigated for optimal maneuvers of spacecraft Coulomb formations. By way of pseudospectral methods, optimal feedback control based on the Carathodory$-\pi$ trajectory concept is capable of solving real-time applications because these techniques can generate solutions at a sufficiently fast sampling rate.

BIBLIOGRAPHY

[1] King, L. B., Parker, G. G., Deshmukh, S., and Chong, J.-H., "Spacecraft Formation-Flying using Inter-Vehicle Coulomb Forces," Tech. rep., NASA/NIAC,January 2002, http://www.niac.usra.edu.

[2] King, L. B., Parker, G. G., Deshmukh, S., and Chong, J.-H., "Study of Interspacecraft Coulomb Forces and Implications for Formation Flying," *AIAA Journal of Propulsion and Power*, Vol. 19, No. 3, MayJune 2003, pp. 497-505.

[3] Cover, J. H., Knauer, W., and Maurer H. A., Lightweight Reflecting Structures Utilizing Electrostatic Inflation, US Patent 3,546,706, October 1966.

[4] Mullen, E. G., Gussenhoven, M. S., and Hardy, D. A., "SCATHA Survey of High-Voltage Spacecraft Charging in Sunlight," *Journal of the Geophysical Sciences*, Vol. 91, 1986, pp. 1074-1090.

[5] Natarajan, A., "A Study of Dynamics and Stability of Two-Craft Coulomb Tether Formations, *Ph.D. Dissertation*, Aerospace and Ocean Engineering Department, Virginia Polytechnic Institute and State University, Blacksburg, VA, May 2007.

[6] Schaub, H., Parker, G. G., and King, L. B., "Challenges and Prospect of Coulomb Formations," *AAS John L. Junkins Astrodynamics Symposium, College Station*, TX, May 23-24 2003, Paper No. AAS-03-278.

[7] Romanelli, C. C., Natarajan, A., Schaub, H., Parker, G. G., and King, L. B., "Coulomb Spacecraft Voltage Study Due to Differential Orbital Perturbations," *AAS/AIAA Space Flight Mechanics Meeting*, Tampa Florida, January 2226, 2006. Paper No. AAS 06-123.

[8] Berryman, J., and Schaub, H. "Static Equilibrium Configurations in GEO Coulomb Spacecraft Formations," *AAS/AIAA Space Flight Mechanics Meeting*, Copper Mountain, CO, Jan. 23-27, 2005. Paper No. 05-104.

[9] Berryman, J., and Schaub, H., "Analytical Charge Analysis for 2- and 3-Craft Coulomb Formations," *AIAA Journal of Guidance, Control and Dynamics*, Vol. 30, No. 6, Nov.-Dec. 2007, pp. 1701-1710.

[10] Vasavada, H., and Schaub, H., "Analytic Solutions for Equal Mass 4-Craft Static Coulomb Formation," *Journal of Astronautical Sciences*, Vol. 56, No. 1, January-March 2008, pp. 7-40.

[11] Schaub, H., Hall, C. D., and Berryman, J., "Necessary Conditions for Circularly-Restricted Static Coulomb Formations," *AAS Journal of Astronautical Sciences*, Vol 54, No. 3-4, July-Dec 2006, pp. 525-541.

[12] Beck, J.A., "Relative Equilibria of a Rigid Satellite in a Central Gravitational Field, *Ph.D. thesis, Air Force Institute of Technology*, Wright-Patterson AFB, OH, Sept. 1997, aFIT/DS/ENY/97-6.

[13] Wang, L. S., Maddocks, J.H., and Krishnaprasad, P.S., "Steady Rigid-Body Motions in a Central Gravitational Field," *Journal of the Astronautical Sciences*, Vol.40, No.4, 1992, pp. 449-478.

[14] Schaub, H., and Junkins, J. L., "Analytical Mechanics of Space Systems," *AIAA Education Series*, Reston, VA, 2003.

[15] Cheng, S. F, and Li-Sheng Wang, L. S, "Relative equilibria and stabilities of spring-connected bodies in a central gravitational field," *Celestial Mechanics and Dynamical Astronomy*, Volume 63, Numbers 3-4, September 1995, pp. 289-312.

[16] Misra, A. K., Bellerose, J., and Modi, V. J., "Dynamics of a Tethered System near the Earth-Moon Lagrangian Points," *Proceedings of the 2001 AAS/AIAA Astrodynamics Specialist Conference*, Quebec City, Canada, Vol. 109 of Advances in the Astronautical Sciences, 2002, pp. 415-435.

[17] Wong, B., Patil, R., and Misra, A., "Attitude Dynamics of a Rigid Body around the Lagrangian Points," AIAA 2006-6653.

[18] Pettazzi, L., Krger, H., Theil, S., and Izzo, D., "Electrostatic Forces for Satellite Swarm Navigation and Reconfiguration," *Technical Report*, ESA, Doc.No.: ARI-SS-FP-ZAR-001, 2006.

[19] Parker, G. G., Passerello, C. E., and Schaub, H., "Static Formation Control using Interspacecraft Coulomb Forces," *2nd International Symposium on Formation Flying Missions and Technologies*, Washington D.C., Sept. 14-16, 2004.

[20] Pettazzi, L., and Izzo, D., "Self-Assembly of Large Structures in Space Using Intersatellite Coulomb Forces," *56th International Astronautical Congress*, Fukuoka, Japan, Oct.17-21 2005. Paper IAC-06-C3.4/D3.4.07.

[21] Steindl, A., and Troger, H., "Optimal control of deployment of a tethered subsatellite," *Nonlinear dynamics* Vol. 31, No. 3, 2003, pp. 257–274.

[22] Steindl, A., Steiner, W., and Troger, H., "Optimal control of retrieval of a tethered subsatellite," *Solid Mech. Appl.* 122, 2005, pp. 441–450.

[23] Williams, P., and Trivailo., ”On the optimal deployment and retrieval of tethered satellites,” *The 41st AIAA/ASME/SAE/ASEE Joint Propulsion Conference and Exhibit* Tucson, 1013 July 2005.

[24] Ross, I. M., ”How to Find Minimum-Fuel Controllers,” *Proceedings of AIAA Guidance, Navigation, and Control Conference*, AIAA 2004-5346, Providence, Rhode Island, Aug. 16-19, 2004.

[25] Fleming, A., Sekhavat, P., and Ross, I. M., ”Minimum-Time Reorientation of an Asymmetric Rigid Body,” *AIAA Guidance, Navigation and Control Conference and Exhibit*, AIAA-2008-7012, Honolulu, Hawaii, 2008.

[26] Betts, J. T., ”Survey of Numerical Methods for Trajectory Optimization,” *Journal of Guidance, Control, and Dynamics*, Vol. 21, No. 2, 1998, pp. 193-207.

[27] Bryson, D.E., *Dynamic Optimization*, Addison-Wesley Longman, Inc., 1999.

[28] Kirk, D.E., *Optimal Control Theory: An Introduction*, Prentice-Hall, Inc., Englewood Cliffs, NJ, 1970.

[29] Agrawal, S. K., and Fabien, B. C., *Optimization of Dynamic Systems*, Kluwer Academic Publishers, 1999.

[30] Ross, I. M., ”A Roadmap for Optimal Control: The Right Way to Commute,” *Annals of the New York Academy of Sciences*, Vol. 1065, pp. 210-231, 2006.

[31] Ross, I. M., Sekhavat, P., Fleming, A., and Gong, Q., ”Optimal feedback control: foundations, examples, and experimental results for a new approach,” *Journal of Guidance, Control, and Dynamics*, Vol. 31, No. 2, 2008, pp. 307-321.

[32] Fahroo, F., and Ross, I. M., ”Costate Estimation by a Legendre Pseudospectral Method,” *Proceedings of AIAA Guidance, Navigation, and Control Conference*, AIAA-98-4222, Monterey, CA 93943, 1998.

[33] Ross, I. M., ”A Beginners Guide to DIDO: A MATLAB Application Package for Solving Optimal Control Problems,” *Elissar Technical Report TR-711*, http://www.elissar.biz, 2007.

[34] Ross, I. M., Gong, Q., and Sekhavat, P., ”Low-Thrust, High-Accuracy Trajectory Optimization,” *Journal of Guidance, Control, and Dynamics*, Vol. 30, No. 4, 2007, pp. 921-933.

[35] Infeld, S. I., Josselyn, S. B., Murray, W., and Ross, I. M., ”Design and Control of Libration Point Spacecraft Formations,” *Journal of Guidance, Control, and Dynamics*, Vol. 30, No. 4, 2007, pp. 899-909.

[36] Williams, P., Blanksby, C., and Trivailo, P., ”Receding Horizon Control of Tether System Using Quasilinearization and Chebyshev Pseudospectral Approximations,” *American Astronautical Society*, AAS Paper No. 03-535, Aug. 2003.

[37] Parker, G. G., King, L. B., and Schaub, H., ”Steered Spacecraft Deployment Using Interspacecraft Coulomb Forces,” *American Control Conference*, Minneapolis, Minnesota, June 14-16 2006. Paper No. WeC10.5.

[38] Ross, I. M., ”Space Trajectory Optimization and L^1-Optimal Control Problems,” *Modern Astrodynamics*, pp. 155-188, Elsevier Astrodynamics Series, 2006.

[39] Ross, I. M., and Fahroo, F., ”Legendre Pseudospectral Approximations of Optimal Control Problems,” *Lecture Notes in Control and Information Sciences*, Vol.295, Springer-Verlag, New York, 2003.

[40] Gong, Q., Ross, I. M., Kang, W., and Fahroo, F., ”Convergence of Pseudospectral Methods for Constrained Nonlinear Optimal Control Problems,” *The IASTED International Conference on Intelligence Systems and Control*, Honolulu, HI, August 2004.

[41] Kluever, C. A., ”Heliospheric Boundary Exploration Using Ion Propulsion Spacecraft,” *Journal of Spacecraft and Rockets*, Vol. 34, No. 3, May-June 1997, pp. 365-371.

[42] Murdoch, N., Izzo, D., Bombardelli, C., Carnelli, I., Hilgers, A., and Rodgers, D., The Electrostatic Tractor for Asteroid Deflection, *58th International Astronautical Congress*, 2008, Paper IAC-08-A3.I.5.

[43] Goldstein, H., *Classical Mechanics*, 2nd edition, AddisonWesley, Reading, 1980.

[44] Marsden, J.E. and Ratiu, T.S., *An Introduction to Mechanics and Symmetry, A Basic Exposition of Classical Mechanical Systems*, Springer-Verlag, New York, Heidelberg, Berlin, 1994.

[45] Inampudi, R., and Schaub, H., ”Two-Craft Coulomb Formation Relative Equilibria about Circular Orbits and Libration Points,” *AAS/AIAA Space Flight Mechanics Meeting*, San Diego, CA, February 15-17, 2010, AAS Paper No. 10-163.

[46] Inampudi, R., and Schaub, H., ”Orbit Radial Dynamic Analysis of Two-Craft Coulomb Formation at Libration Points,” *AAS/AIAA Astrodynamics Specialist Conference*, Toronto, Canada, Aug. 25, 2010. Paper No. AIAA 2010–7965.

[47] Inampudi, R., and Schaub, H., ”Optimal Reconfigurations of Two-Craft Coulomb Formation in Circular Orbits,” *AAS/AIAA Astrodynamics Specialist Conference*, Toronto, Canada, Aug. 25, 2010. Paper No. AIAA 2010–7953.

[48] Hastings, D., and Garrett, H., "Spacecraft-Environment Interactions," *Cambridge University Press*, 2004.

[49] Brogan, W. L., "Modern Control Theory," *Prentice Hall, 3 edition*, 1990.

[50] McInnes, C. R., "Solar Sailing: Technology, Dynamics and Mission Applications," *Springer-Praxis*, Chichester, UK, 1999.

[51] Lawrence, D. A., and Whorton, M. S., "Solar Sail Dynamics and Coning Control in Circular Orbits," *Journal of Guidance, Control, and Dynamics*, Vol. 32, No. 3, MayJune 2009, pp. 974-985.

[52] Li, H., "Application of Solar Radiation Pressure to Formation Control near Libration Points," *Ph.D. Dissertation*, Department of Aerospace Engineering and Mechanical Engineering, University of Cincinnati, Ohio, Feb. 2008.

[53] Meirovitch, L., "Methods of Analytical Dynamics," *Dover Publications, Inc*, Mineola, New York, 2003.

[54] Vadali, S. R., and Kim, E. S., "Feedback control of tethered satellites using Lyapunov stability theory," *Journal of Guidance, Control, and Dynamics*, Vol. 14, 1991, pp. 729–735.

[55] Fujii, H. A., Uchiyama, K., and Kokubun, K., "Mission function control of tethered subsatellite deployment/retrieval: in-plane and out-of-plane motion," *Journal of Guidance, Control, and Dynamics*, Vol. 14, 1991, pp. 471–473.

Appendix A

LIE GROUPS

To explain the terminology used in chapter 2, basic properties and definitions of Lie Groups are introduced here. References 43 and 44 present these concepts in detail.

Definition 1 [Group of transformations]. A group of transformations G is an aggregate set of transformations g_i such that the following properties are satisfied:

1. It contains the identity transformation.
2. Corresponding to each transformation g_l there is an inverse transformation g_l^{-1}.
3. The composition of transformations holds $g_l g_k \in G$ and the associativity rule $(g_i g_j)\, g_k = g_i\,(g_j g_k)$ is satisfied.

For instance, the set of nonsingular linear transformation matrices forms a group as all the above three properties are satisfied. Another important example is the symmetry group of a rigid body. To maintain the symmetry of a rigid body, symmetry groups or symmetry transformations gives rise to the set of all distance preserving transformations which transforms the position of the body but preserves the distance between all pairs of points of the rigid body.

Definition 2 [Lie group]. A Lie group is a smooth manifold G that has a group structure consistent with its manifold structure such that the group operation and its inversion are smooth maps between manifolds. A matrix representing a rotation about an axis through an angle is an example of a Lie group. The three-dimensional rotation group $\boldsymbol{SO}(3)$ is defined as

$$\boldsymbol{SO}(3) = \left\{\boldsymbol{C} : \mathbf{R^3} \rightarrow \mathbf{R^3} \text{ linear, } \boldsymbol{C}^T\boldsymbol{C} = E \text{ and } \det \boldsymbol{C} = 1\right\}$$

Lie groups describe continuous symmetries in physical systems using its Lie algebra $\boldsymbol{g}^*$ for its calculations. A Lie algebra is a vector space and uses linear algebra to study Lie groups. For example, $\boldsymbol{SO}(3)$ is a Lie group and is characterized by its Lie algebra. A Lie group G and its Lie algebra $\boldsymbol{g}^*$ are related in a manner similar to which a flow and the associated vector field are related. The corresponding vector field $\boldsymbol{v}$ on a flow $\boldsymbol{\Phi}\left(\boldsymbol{x},t\right)$ given by

$$\boldsymbol{v}\left(\boldsymbol{x}\right) = \frac{\mathrm{d}}{\mathrm{d}t}|_{t=0}\boldsymbol{\Phi}\left(\boldsymbol{x},t\right),$$

is called the infinitesimal generator of the flow.

Let $\boldsymbol{so}(3)$ be the set of skew-symmetric matrices defined by

$$\boldsymbol{so}(3) = \left\{\hat{\boldsymbol{\xi}} : \mathbf{R^3} \to \mathbf{R^3},\ \text{linear}\ \ \left|\hat{\boldsymbol{\xi}} + \hat{\boldsymbol{\xi}}^T\right| = 0\right\}$$

where $\boldsymbol{\xi} = (\xi_1, \xi_2, \xi_3)$ is a vector and $\hat{\boldsymbol{\xi}}$ is

$$\left[\hat{\boldsymbol{\xi}}\right] = \begin{bmatrix} 0 & -\xi_3 & \xi_2 \\ \xi_3 & 0 & -\xi_1 \\ -\xi_2 & \xi_1 & 0 \end{bmatrix}$$

This set $\boldsymbol{so}(3)$ forms the Lie algebra of $\boldsymbol{SO}(3)$ given as $\hat{\boldsymbol{\xi}}\boldsymbol{r} = \boldsymbol{\xi} \times \boldsymbol{r}$ for any $\boldsymbol{r} \in \mathbf{R^3}$. If we define the Lie algebra isomorphism between the space $\mathbf{R^3}$ and $\boldsymbol{so}(3)$ by $\boldsymbol{\xi} \mapsto \boldsymbol{so}(3)$ then the matrix exponential $e^{\hat{\boldsymbol{\xi}}t}$ is a rotation about $\boldsymbol{\xi}$ by the angle $\|\boldsymbol{\xi}\|\,t$ in the form

$$\boldsymbol{C}\left(t\right) = e^{\hat{\boldsymbol{\xi}}t}.$$

The action of the Lie group $\boldsymbol{SO}(3)$ on the configuration manifold Q is expressed as $\boldsymbol{C} \cdot \boldsymbol{q}$ where Q is given by

$$Q = \left\{\boldsymbol{q} = \left(\boldsymbol{q}_i \in \mathbf{R^3}, i = 1, \ldots, n\right)\right\}.$$

And the associated action of the infinitesimal generator $\boldsymbol{\xi}_Q$ on Q is a vector field defined as

$$\boldsymbol{\xi}_Q(\boldsymbol{q}) = \frac{\mathrm{d}}{\mathrm{d}t}\left(e^{\hat{\boldsymbol{\xi}}t} \cdot \boldsymbol{q}\right)_{t=0} = \hat{\boldsymbol{\xi}}\boldsymbol{q} = \boldsymbol{\xi} \times \boldsymbol{q}.$$

where $\boldsymbol{\xi}$ is the angular velocity vector.

The tangent space $\boldsymbol{T_q Q}$ is the collection of all tangent vectors to all possible curves passing through a given point $\boldsymbol{q}_i$. The set of all position-velocity pairs is a manifold and the tangent bundle $\boldsymbol{TQ}$ of the manifold is denoted by

$$\boldsymbol{TQ} = \{(\boldsymbol{q}, \boldsymbol{v}) : \boldsymbol{q} \in Q, \boldsymbol{v} \in \boldsymbol{T_q Q}\}$$

Similarly, in the phase space of position-momentum pairs the cotangent bundle $\boldsymbol{T^*Q}$ becomes

$$\boldsymbol{T^*Q} = \left\{(\boldsymbol{q}, \boldsymbol{p}) : \boldsymbol{q} \in Q, \boldsymbol{p} \in \boldsymbol{T_q^* Q}\right\}.$$

Every vector space V has a dual V^*: $V^* = \{l : V \to \boldsymbol{R} : l \text{ linear}\}$. The dual space to vector space V is defined as the vector space V^* consisting of all real-valued linear functions. As an example, for n point masses moving in a central force field, the dual pairing between $(\boldsymbol{q}, \boldsymbol{p}) \in \boldsymbol{T^*Q}$ and $(\boldsymbol{q}, \boldsymbol{v}) \in \boldsymbol{TQ}$ is given by the inner product

$$\langle \boldsymbol{p}, \boldsymbol{v} \rangle = \sum_{i=1}^{n} \boldsymbol{p}_i \boldsymbol{v}_i$$

This inner product structure identifies the vector space $\boldsymbol{v}$ and its dual $\boldsymbol{p}$. And the Legendre transformation $FL : \boldsymbol{TQ} \to \boldsymbol{T^*Q}$ gives rise to the linear momentum mapping

$$\boldsymbol{p}_i = m_i \boldsymbol{v}_i \qquad i = 1, \ldots, n$$

If all the point masses need to be rotated simultaneously then the $\boldsymbol{SO}(3)$ action on Q is

$$\boldsymbol{T_C q : q \mapsto C \cdot q := (C \cdot q_i)}. \tag{A.1}$$

The infinitesimal generators associated with this group action is given by

$$\boldsymbol{\omega}_Q := \hat{\boldsymbol{\omega}}\boldsymbol{q} = \boldsymbol{\omega} \times \boldsymbol{q} = (\boldsymbol{\omega} \times \boldsymbol{q}_i)\,. \tag{A.2}$$

Similarly to map the angular velocity and its dual, the angular momentum, consider the momentum map $\boldsymbol{J} : \boldsymbol{T^*Q} \to \boldsymbol{g}^*$ given by

$$\langle \boldsymbol{p}, \omega_Q(\boldsymbol{q})\rangle = \langle \boldsymbol{p}, \omega \times \boldsymbol{q}\rangle = \sum_{i=1}^{n} \boldsymbol{p}_i \cdot (\boldsymbol{\omega} \times \boldsymbol{q}_i) = \sum_{i=1}^{n} \boldsymbol{p}_i\,(\boldsymbol{q}_i \times \boldsymbol{p}_i) \cdot \boldsymbol{\omega} = \boldsymbol{J}\,(\boldsymbol{q}, \boldsymbol{p}) \cdot \boldsymbol{\omega} \tag{A.3}$$

That is,

$$\boldsymbol{J}\,(\boldsymbol{q}, \boldsymbol{p}) = \boldsymbol{q} \times \boldsymbol{p} := \Sigma_{i=1}^{n} \boldsymbol{q}_i \times \boldsymbol{p}_i \tag{A.4}$$

Which is the standard formula for angular momentum of a group of particles. And the Legendre transformation $FL : \boldsymbol{TQ} \to \boldsymbol{T^*Q}$ gives rise to the angular momentum mapping

$$\boldsymbol{so}\,(3) \to \boldsymbol{so}^*\,(3) : \boldsymbol{\omega} \mapsto \boldsymbol{J}\,(\boldsymbol{\eta}_Q\,(\boldsymbol{q})) = \boldsymbol{I}\,(\boldsymbol{q})\,\boldsymbol{\omega} \tag{A.5}$$

Where is $\boldsymbol{I}\,(\boldsymbol{q})$ the inertia tensor and is expressed in the rotational kinetic energy of the point masses as

$$2K_H\,(\boldsymbol{\xi}, \boldsymbol{\omega}) = \boldsymbol{\xi} \cdot \boldsymbol{I}\,(\boldsymbol{q})\,\boldsymbol{\omega} = \sum_{i=1}^{n} m_i\,(\boldsymbol{\xi} \times \boldsymbol{q}_i) \cdot (\boldsymbol{\omega} \times \boldsymbol{q}_i) \tag{A.6}$$